Measurement of transverse single-spin asymmetries in inclusive electroproduction at HERMES

Alejandro López Ruiz

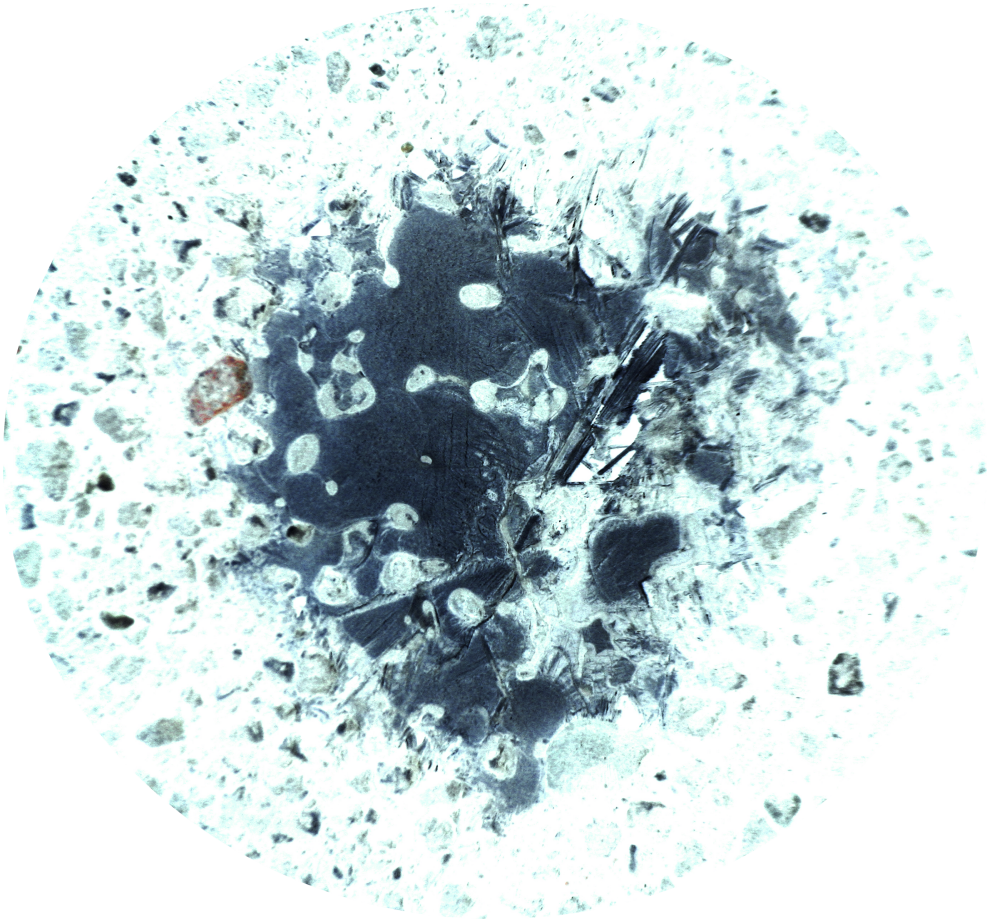

Promotor: Prof. Dr. Dirk Ryckbosch
Proefschrift ingediend tot het behalen van de graad van
Doctor in de Wetenschappen: Natuurkunde

Vakgroep Fysica & Sterrenkunde
Voorzitter: Prof. Dr. Dirk Ryckbosch
Faculteit Wetenschappen
Academiejaar 2012-2013

Faculteit Wetenschappen

UNIVERSITEIT GENT

Supervisor:
Prof. Dr. Dirk Ryckbosch

Research facility:
HERMES. DESY
Notkestrasse, 85
22607 Hamburg
Germany

Members of the examination committee:
(Defended on November, 30th, 2012, at the Universiteit Gent, Belgium)

Prof. Dr. Martin Grunewald	Universiteit Gent
Prof. Dr. Luc Van Hoorebeke	Universiteit Gent
Prof. Dr. Dirk Poelman (chairman)	Universiteit Gent
Prof. Dr. Klaus Rith	Universität Erlangen–Nürnberg
Prof. Dr. Dirk Ryckbosch (supervisor)	Universiteit Gent
Prof. Dr. Jan Ryckebusch	Universiteit Gent
Prof. Dr. Gunar Schnell	Universidad del Pais Vasco
Dr. Michael Tytgat	Universiteit Gent

The research presented in this dissertation was supported by a grant of the Research Foundation - Flanders (FWO).

Cover illustration:
A cracked heart beat

Foreword

To accomplish this doctoral thesis would not have been possible without the work, help and support from many people. I am indebted to all of you. Each one contributed in a way or another during these last years, and what I began as a young student, I finish now as a man. The full list is long. Here are some memory-filtered highlights.

First of all, Dirk Ryckbosch, for giving me the opportunity of working in his great group, for his leadership and supervision, for being an example to follow. Marco Contalbrigo, Klaus Rith and Gunar Schnell, possibly the most ambitious, instructive and rewarding working group ever – it was a delight to learn from/with you. Klaus, thanks for the careful reading, the always wise advice, and all the anecdotes. Gunar, you have been a *scientific father* (sometimes too picky!) and a good friend. Alberto Martínez de la Ossa, who programmed at least as many lines of code as me and who has been all these years a true mate. Lara De Nardo, for the early days of the two-photon exchange and the initiation on the refined art of cross-checks. Eduard Avetisyan, for the largest Monte Carlo production at HERMES known to date. Naomi Makins, for getting me on the good track and convincing me that you can *even* toast your bread with Emacs. Laura Manfre and Florian Sanftl, for the work they did as master students. All the people at the INW/DESY/Tokyo-Tech who made my days lighter with chats, drinks, unplanned lunches and coffee breaks, long car trips or quiet walks, football games and the pleasant crack of the ping-pong ball.

Not only has it been time. It has also been places. In Gent, Barbara & Wouter, Graciela & Hans, Arne, Kris – thank you all for your hospitality and friendship, for making me feel at home in your own homes. In Varenna, Ramona for that vivid summer, M. Anselmino and E. Leader for the unforgettable afternoon sessions under the magnolia tree. In Madrid as in Gent, Rafa, for the long nights under books and the discreet charm of music. In Hamburg, *ihr seid so viele!* Dirk, Juliana and Stefan for a splendid *endspurtgessellschaft*. Of course, Julia. Of course, Charlotte. And yet two recent episodes: Tristan and Loes, for getting me out of a tight spot in Rotterdam (*side note, thanks NMBS strikers for a wonderful evening!*), and Oscar, for the best reception I could have imagined for my defense.

Everywhere, my friends, some of whom I already mentioned.

Every time, my family, the present one, the already gone,
the one joined by blood, the one joined by soul.

And the music, that goes on...

Gent, December 2012,
Alejandro

Contents

1 Introduction **1**

1.1 Outline . . . 4

2 Physics **5**

2.1 Deep inelastic scattering . . . 5

2.1.1 Kinematics . . . 6

2.1.2 Cross section . . . 7

2.2 Quark-parton model . . . 11

2.2.1 PDFs . . . 12

2.2.2 Interpretation of the structure functions . . . 13

2.2.3 Spin crisis . . . 15

2.3 QCD formulation of the parton model . . . 16

2.3.1 QCD corrections . . . 18

2.3.2 Quark correlator . . . 20

2.3.3 Why transversity cannot be measured in inclusive DIS? . . . 25

2.4 Transverse spin physics . . . 27

2.4.1 A_N in hadronic interactions . . . 27

2.4.2 The problem with transverse SSAs . . . 28

2.5 Semi-inclusive DIS . . . 30

2.5.1 Kinematics . . . 31

2.5.2 Cross section . . . 31

2.5.3 Fragmentation correlator . . . 32

2.6 Parton model with intrinsic momentum . . . 34

2.6.1 TMDs . . . 35

2.6.2 Interpretation of the Sivers and Collins effects . . . 40

2.7 High-twist PDFs in collinear framework . . . 44

2.7.1 Other approaches . . . 44

2.8 Inclusive hadron production in ep scattering . . . 45

2.8.1 Kinematics . . . 46

2.8.2 Cross section . . . 46

2.8.3 Computation of A_N . . . 47

2.9 Outlook . . . 49

3 HERMES **51**
3.1 HERA and DESY . . . 51
3.1.1 The polarized lepton beam . . . 53
3.2 The polarized gas target . . . 55
3.3 The spectrometer . . . 58
3.3.1 Tracking . . . 59
3.3.2 Particle Identification . . . 60
3.3.3 Luminosity measurement . . . 63
3.3.4 Coordinate system . . . 64
3.4 The trigger system . . . 65
3.5 Data production chain . . . 66

4 Measurement **69**
4.1 Data quality . . . 69
4.2 Event selection . . . 70
4.2.1 Particle identification . . . 71
4.2.2 RICH hot spots . . . 77
4.3 Trigger Efficiencies . . . 79
4.3.1 Effect on the data . . . 82
4.4 Kinematic distributions . . . 83
4.4.1 Collected statistics . . . 85
4.5 Extraction of $A_{UT}^{\sin\phi}$ amplitudes . . . 86
4.6 Preliminary results . . . 90

5 Systematics **95**
5.1 Acceptance effects and misalignment . . . 96
5.2 Unpolarized Monte Carlo sample . . . 97
5.2.1 Event generator . . . 97
5.2.2 Generated statistics . . . 98
5.2.3 Comparison to data . . . 100
5.2.4 Zero asymmetry test . . . 102
5.3 Polarized Monte Carlo sample . . . 103
5.3.1 Model for the asymmetry . . . 104
5.3.2 Introduce spin dependence . . . 105
5.3.3 Reconstruction of $A_{UT,MC}^{\sin\phi}$ . . . 105
5.4 Systematic uncertainty . . . 107
5.4.1 All-in-one determination . . . 107
5.4.2 Target polarization error . . . 108
5.4.3 Target magnet correction . . . 109
5.4.4 Hadron misidentification . . . 109
5.4.5 Angular and momentum resolution . . . 109
5.4.6 Radiative corrections . . . 110
5.4.7 Cross-check of results . . . 110
5.4.8 Compatibility of data productions . . . 111

5.4.9 Total systematic uncertainty . . . 113

6 Results **115**
6.1 Discussion . . . 115
6.2 Contributing subprocesses . . . 120
6.2.1 Contribution from photoproduction . . . 122
6.2.2 Contribution from SIDIS . . . 124
6.2.3 Contribution from large z . . . 129
6.2.4 Contribution from low-Q^2 . . . 131
6.3 Conclusions . . . 132

7 Two-photon exchange in DIS **135**
7.1 Motivation . . . 136
7.2 Experimental access . . . 138
7.3 Formalism for DIS . . . 139
7.4 Measurement . . . 141
7.5 Results . . . 144
7.6 Outlook . . . 146

Appendices **147**

A Scattering basics **149**

B Derivation of formulae **155**

C Selection of DIS events **157**

D Wilson lines and universality **161**

E Extra figures **165**

Samenvatting **185**

Bibliography **187**

1 Introduction

When my friends ask me about the research topic of my PhD thesis, it always comes with one inevitable, simple question: *What is the use of a particle accelerator? – It accelerates particles*, I answer. To justify why accelerating particles is useful, I obviate part of the answer and take advantage that I work in a *deep inelastic scattering* experiment, HERMES at DESY. *We accelerate particles to crash them against other particles, like protons, in order to study their properties, just as you would throw stones to an apple tree to see how apples are on the inside*. Deep inelastic scattering (DIS) experiments are like a powerful microscope to *see* inside the proton.

Electrons as a tool for investigating the nucleon After more than 40 years of DIS experiments, we now have a rich and impressive knowledge of the structure of the proton, or nucleons in general. The idea is simple: very high energy leptons (electrons, positrons or muons) are collided against nucleons. The momentum of the lepton must be large enough such that the wavelength associated to the photon mediating the electromagnetic interaction is smaller than the nucleon's size; this way we know the photon gets *deep* in the nucleon. By detecting the lepton in the final state, and measuring its momentum and the angle at which it was scattered, one obtains information about the nucleon and its internal structure.

Parton distribution functions This information is encoded in *parton distribution functions* (PDFs), which represent the probability to find a *parton* (whatever the nucleon is made of) with certain properties inside of the nucleon. The building blocks of the nucleon, the quarks and gluons, were discovered this way. Data from DIS experiments show unequivocally that the nucleon possesses a charged substructure of a spatial size much smaller than the nucleon itself, and that its components behave like quasi-free objects when probed at high energies. These observations were formalized by Bjorken and Feynman in their *parton model* [19], that would later develop into the theory of Quantum Chromodynamics (QCD) [2], describing the interaction of *color* charged particles, the quarks and gluons. QCD is the basis for models that describe all particles made by these: the hadrons.

Spin crisis Another crucial observation from the early DIS experiments is the fact that quarks have spin-1/2. A nucleon made of three quarks can easily be accommodated in this picture by assuming that two of the quarks would have their spin aligned to the nucleon spin, and the remaining quark would have its spin anti-aligned. However, the results from *longitudinally polarized* DIS (where the spin of the nucleon is polarized along the same direction as the incoming beam) by the EMC collaboration [14] in the late 80's indicated that the spin of the quarks contributes only about 30% to the total spin of the nucleon. This striking observation was called a *spin crisis* [24] in the parton model, and led to a renewed interest in the nucleon substructure and other spin-related phenomena. In fact, the HERMES experiment was planned with the goal of studying in more detail the spin the contribution of the spin of the quarks [3].

A_N in hadronic collisions The *spin structure* of the nucleon, i.e., the means by which the quarks and gluons and their dynamics contribute to the total spin of the nucleon, is still nowadays an unresolved puzzle. In addition to the spin crisis, other polarization phenomena have been observed that deeply challenge the current understanding of the role of spin in particle physics [97]. Perhaps one of the most glaring examples is the case of the large left-right asymmetry A_N for pions produced in hadron-nucleon collisions with *transversely* polarized beam or targets, many times observed in different experiments but not yet fully understood [47–71]. Such a large *transverse* spin asymmetry was found surprising in the late 1970's, when it was observed for the first time, due to the wrong preconception that all transverse spin effects should be suppressed inside a relativistic proton [72]. However, inside of a nucleon, even a fast moving one, there is enough place for transverse motion of quarks and gluon radiations. Both cases are known nowadays to cause complex correlations between the spin of the nucleon and the momentum of the quarks, hence possibly giving rise to an asymmetrical distribution of the outgoing hadrons.

Transverse momentum of quarks Over the last two decades, two main approaches have been proposed that could generate transverse spin asymmetries. One [96] is based in the use of transverse-momentum dependent parton distribution and fragmentation functions (TMDs). In this context, two mechanisms exist that can explain the observed A_N: the Sivers and Collins effects. In the Sivers effect [74], an asymmetrical distribution of unpolarized quarks (having its origin in a correlation between the spin of the proton and the quark transverse momentum) is responsible for the preferred production of the outgoing hadrons in a certain direction. In the case of the Collins effect [75], the asymmetry is generated due to a correlation between the momentum of the produced hadron and the spin and momentum of the fragmenting quark. In the other approach [77], the transverse motion of quarks is ignored, but transverse SSAs arise from higher-order correlations between the quarks and gluons of the fragmenting proton. These two approaches are valid in separate kinematic regimes, but have been proven to be consistent with each other in the region of overlap [78]. In particular, both approaches predict that A_N should be zero for a sufficiently large value of the transverse momentum of the hadron, but more experimental data is needed in this region to check the validity of the models. In addition, a substantial number of theoretical predictions exist, which await experimental data [78, 79].

A_N in electroproduction In recent years, the interest of measuring the transverse spin asymmetry A_N in electron-proton reactions has been pointed out [5], with an unpolarized electron beam and a transversely polarized proton target. Since these reactions involve only the quark fields of one proton, they offer a much cleaner interpretation of A_N in terms of TMDs than for the hadronic data. A measurement of A_N in ep reactions can therefore be utilized to support or rule out some of the ideas discussed in this context. A theoretical prediction [89] exists for the kinematics of the HERMES experiment, suggesting that the Sivers effect could generate a sizable asymmetry for pions produced in the reaction $e\,p^{\uparrow} \to \pi^{\pm} X$.

Such a measurement of a transverse spin asymmetry in inclusive electroproduction does not exist up to date, and it is presented for the first time in this thesis[1].

Towards the complete picture of the nucleon The TMDs are a crucial step towards a complete picture of the parton structure of the nucleon in QCD. These distribution functions depend on the intrinsic motion of partons inside the nucleon, and allow the reconstruction of the nucleon structure in momentum space. With an increasing knowledge of TMDs, one expects to provide precise answers about e.g., the dynamics of the quarks in the nucleon and the correlation between the orbital motion of quarks, their spin, and the spin of the nucleon. The measurement and characterization of TMDs have generated an enormous amount of both experimental and theoretical work over the last years, and still are a high priority in the physics programs of accelerator facilities like DESY (HERMES), CERN (COMPASS), Jefferson Lab, and RHIC, as well as of forthcoming experiments like those planned for the Electron-Ion Collider (EIC).

The complementary aspect of the nucleon structure – the description of quarks in the *coordinate space* – is addressed by the Generalized Parton Distribution functions (GPDs) [6]. The GPDs are accessible in *exclusive* reactions, where all reaction products are detected. The transverse position of the parton on which the scattering took place is obtained by a Fourier transform from the transverse momentum of the scattered nucleon. A better understanding of the spatial distribution of partons would provide essential insight into the QCD dynamics inside hadrons. With the information from TMDs and GPDs combined, a complete multi-dimensional imaging of the nucleon could be achieved. A unified framework of parton distribution functions, from which both TMDs and GPDs can be derived, has been proposed recently [7]. This new set of *mother* distributions is referred to as Generalized Transverse-Momentum Dependent parton distribution functions (GTMDs).

[1] Preliminary HEMES results were shown previously at several conferences. See for instance Ref. [1].

1.1 Outline

The structure of this work is as follows:

- In Chapter 2, the relevant formalism for the study of SSAs is given, together with a selected overview of concepts and facts related to these. This Chapter can be considered as an extended version of the introduction given above.
- In Chapter 3, the HERMES experiment is described in detail.
- In Chapter 4, the selection of data and the method used to extract the asymmetries are discussed, and preliminary results for the asymmetries are shown, including only statistical error bars.
- Chapter 5 is dedicated to the estimation of systematic uncertainties that could affect the measurement of SSAs.
- Final results are presented in Chapter 6, together with an extended discussion of the measured asymmetries, and a possible interpretation in terms of the available theoretical knowledge.
- In Chapter 7, an additional study, reporting on the measurement of transverse SSAs in inclusive DIS is included. Such an asymmetry has been signaled as an indication for two-photon exchange effects in the ep reaction. This analysis was performed prior to the one described in the preceding chapters, and it was published in *Phys. Lett. B682* (2010) 351-354. See Ref. [158].
- Other relevant information is included in the Appendices. These are correspondingly linked from the main chapters.

So, what's the work you do for your thesis? – I count particles, I answer.

2 Physics

In this chapter, the relevant formalism for the discussion of transverse single spin asymmetries (SSAs) is considered. The starting point is the study of polarized deep inelastic scattering (DIS) reactions in Section 2.1 and the consequent formulation of the quark parton model (QPM) in Section 2.2, which subsequently led to the discovery and establishment of the theory of quantum chromodynamics (QCD), – Section 2.3. This framework provides a quite satisfactory understanding of the physics related to the nucleon's longitudinal spin. The transverse spin structure of the nucleon is more difficult to access. However, large transverse SSAs have been observed both in the inclusive production of hadrons from hadronic collisions (the controversial A_N discussed in Section 2.4) and in the polarized semi-inclusive DIS (SIDIS) – Section 2.5, a process which allows for a deeper exploration of the nucleon structure. Transverse-momentum dependent parton distribution and fragmentation functions (TMDs) are discussed in Section 2.6, and provide an explanation for transverse SSAs and point to the important role of the intrinsic motion of quarks, related to e.g., the Sivers and Collins effects. Other frameworks exist in which transverse spin effects can be accommodated, like for instance the high-twist collinear model, briefly discussed in Section 2.7. Based on the TMD formalism, a detailed discussion of transverse SSAs in the inclusive electroproduction of hadrons is presented in Section 2.8, where estimates of A_N are given for the HERMES kinematics.

2.1 Deep inelastic scattering

A schematic DIS reaction is depicted in Fig. 2.1. An incoming lepton with four-momentum k interacts with a target nucleon having four-momentum P. The interaction takes place by the exchange of a virtual photon γ^* with momentum q – the curvy line in between[1]. The term *virtual* refers to the fact that the photon is only the mediator, and not a detectable

[1]The interaction could be mediated as well by a weak boson Z^0 but at the energy scale of an experiment like HERMES, this is very improbable. Therefore, we just consider an electromagnetic interaction between both particles.

real photon. As a result of the collision, the proton fragments into new hadrons (typically, pions and kaons), and the beam lepton is scattered with a certain angle θ_e.

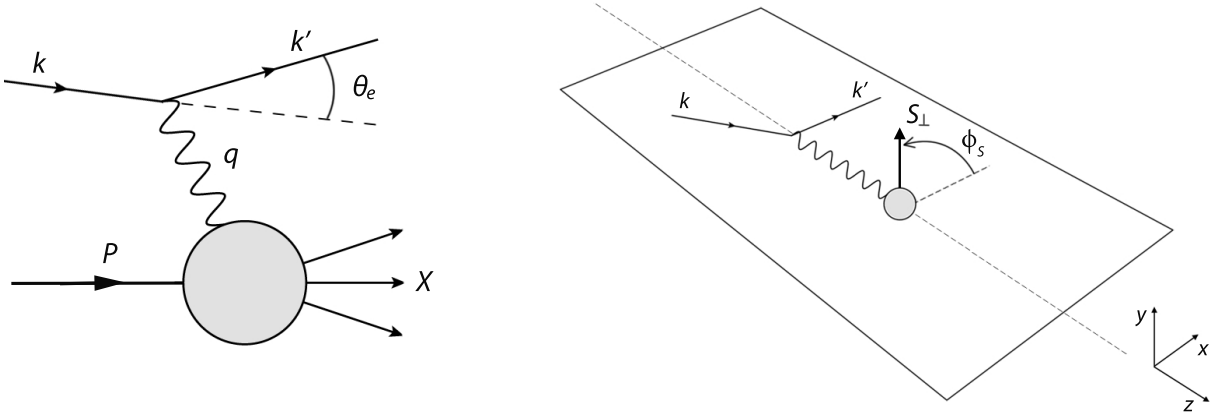

Figure 2.1. Diagram and kinematic plane for inclusive DIS.

2.1.1 Kinematics

With the three vectors given in Fig. 2.1, one can build six Lorentz invariant observables: k^2, P^2, q^2, $P \cdot q$, $k \cdot P$ and $k \cdot q$. The first two are the invariant masses of the lepton and nucleon, respectively. The invariants q^2 and $P \cdot q$ describe the interaction of the virtual photon with the nucleon. The last two depend on the energy of the lepton-nucleon system and the lepton scattering angle θ_e.

- The HERMES laboratory frame is defined such that the target nucleon is at rest $P \overset{\text{lab}}{=} (M, \mathbf{0})$.
- The four-momenta of the electron before and after the interaction are respectively $k = (E, \mathbf{k})$ and $k' = (E', \mathbf{k}')$.
- The four-momentum of the virtual photon is $q = k - k'$. The squared invariant mass of the virtual photon q^2 corresponds to the four-momentum transfer to the nucleon. The *virtuality* of the photon is expressed by negative values of $q^2 < 0$, in contrast to real photons, which are massless and therefore have $q^2 = 0$.

  For the analyses presented in this thesis, it suffices to characterize the scattered beam lepton by its energy and angle θ_e. In the lab system, neglecting the lepton mass, the momentum transfer becomes

$$q^2 \overset{\text{lab}}{\simeq} -4EE' \sin^2 \frac{\theta_e}{2} < 0, \tag{2.1}$$

  Usually, one rather takes $Q^2 = -q^2$ in order to avoid working with negative quantities.

- The energy transfer to the nucleon (ν) and the *dimensionless* fractional energy transfer (y) are defined

$$\nu = \frac{P \cdot q}{M} \overset{\text{lab}}{=} E - E', \qquad y = \frac{P \cdot q}{P \cdot k} \overset{\text{lab}}{=} \frac{\nu}{E}. \tag{2.2}$$

- The total energy available in the center of mass is $k + P$. The square of it is also Lorentz invariant $s = (P + k)^2 \overset{\text{lab}}{\simeq} M^2 + 2ME$.
- The squared invariant mass of the final state is $W^2 = (P + q)^2 \overset{\text{lab}}{=} M^2 + 2M\nu - Q^2$.
- Another useful dimensionless variable is

$$x = \frac{Q^2}{2\ P \cdot q} \overset{\text{lab}}{=} \frac{Q^2}{2M\nu}, \tag{2.3}$$

  known as the x-Bjorken variable. In the center-of-mass frame, x can be related to the fraction of the momentum of the nucleon carried by the nucleon's component that absorbs the virtual photon. It can also be used to indicate the degree of *inelasticity* of the process. A value of $x = 1$ means $Q^2 = 2M\nu$, which implies that all the available energy is transformed into kinetic energy $W^2 = M^2$.

In addition, another two important objects needed to describe the scattering process are the target polarization vector $\mathbf{S}$ and the azimuthal angle ϕ_S

$$\phi_S = \frac{\mathbf{q} \times \mathbf{k} \cdot \mathbf{S}}{|\mathbf{q} \times \mathbf{k} \cdot \mathbf{S}|} \cos^{-1} \frac{\mathbf{q} \times \mathbf{k} \cdot \mathbf{q} \times \mathbf{S}}{|\mathbf{q} \times \mathbf{k}||\mathbf{q} \times \mathbf{S}|}, \tag{2.4}$$

defined around the direction $\mathbf{q}$ of the virtual photon, between the lepton scattering plane (the plane containing both $\mathbf{q}$ and $\mathbf{k}'$) and the perpendicular component of the target spin vector $S_\perp$. See Fig. 2.1.

One-photon-exchange approximation This picture of a DIS reaction is based on the assumption that *only* one virtual photon is exchanged between both particles. This simplifies the calculations and it is generally accepted to be a good approximation. Contributions from two-photon exchange are discussed in more detail in Chapter 7.

2.1.2 Cross section

A general expression for the **elastic** cross section of two point-like charged particles can be derived form first principles by the use of the Feynman rules for QED. This is done in Appendix A. The idea to keep in mind is that the cross section implies the contraction of two tensors $L_{\mu\nu}$, given in Eq. (A.9), which describe the electromagnetic currents j_μ and j_ν of the two charged particles. This leads to a cross section expression

$$\sigma_{\text{elastic}} \sim L^a_{\mu\nu} L^{\mu\nu}_b. \tag{2.5}$$

The *leptonic* tensor can be expressed [9] as a sum

$$L_{\mu\nu} = L^{\text{S}}_{\mu\nu} + L^{\text{A}}_{\mu\nu}, \tag{2.6}$$

of a *symmetric* term $L^{S}_{\nu\mu}$ and an *anti-symmetric* term $L^{A}_{\nu\mu}$ according to their properties under the exchange of the μ, ν indexes[2]; only the anti-symmetric part depends on the nucleon spin.

In **inelastic** ep scattering, similarly, the cross section can be written as

$$\sigma_{\text{DIS}} \propto L_{\mu\nu} W^{\mu\nu}, \tag{2.7}$$

where the hadronic tensor $W_{\mu\nu}$, describes the interaction between the virtual photon and the nucleon and is formally defined in terms of scattering matrix elements of the hadronic electromagnetic current j^{h}_{μ} [10, 35]

$$\begin{aligned} 2MW_{\mu\nu}(q;P,S) &= \frac{1}{2\pi}\sum_{X}\int \frac{\mathrm{d}^3\mathbf{P}_X}{(2\pi)^3 2E_X}(2\pi)^4\delta^4(P+q-P_X), \\ &\quad \times\langle P,S|\, j^{h}_{\mu}(0)\,|X\rangle\langle X|\, j^{h}_{\nu}(0)\,|P,S\rangle. \end{aligned} \tag{2.8}$$

Here the sum is over all particles X in the final state, having four momenta $P_X = (E_X, \mathbf{P}_X)$. The δ^4 guarantees 4-momentum conservation[3]. Without any information about the nucleon internal dynamics, it is only possible to restrict the content of $W_{\mu\nu}$ using symmetry arguments, and write it in terms of *structure functions* [4], that parametrize our ignorance about the nucleon substructure. For inelastic ep scattering, assuming γ^* exchange, only *four* structure functions W_1, W_2, G_1 and G_2 are necessary

$$\begin{aligned} W_{\mu\nu}(q;P,S) &= W^{S}_{\mu\nu}(q;P) + iW^{A}_{\mu\nu}(q;P,S), \\ \text{such that} \quad & W^{S}_{\mu\nu} \propto W_1, W_2, \\ & W^{A}_{\mu\nu} \propto G_1, G_2. \end{aligned}$$

The structure functions $W_{1,2}$ contained in $W^{S}_{\mu\nu}(q;P)$ are unpolarized, and the $G_{1,2}$ depend on the proton spin. These functions depend mostly on the observables q^2 and $q\cdot P$, i.e., on Q^2 and x, see Eq. (A.25), and are all measurable quantities.

Bjorken scaling In the limit of large momentum transfer ($Q^2 \to \infty$), the structure functions become independent of Q^2

$$\begin{aligned} \lim_{Q^2\to\infty} M\, W_1(Q^2,x) &\equiv F_1(x), \\ \lim_{Q^2\to\infty} \nu\, W_2(Q^2,x) &\equiv F_2(x), \\ \lim_{Q^2\to\infty} \nu\, M^2\, G_1(Q^2,x) &\equiv g_1(x), \\ \lim_{Q^2\to\infty} \nu^2\, M\, G_2(Q^2,x) &\equiv g_2(x). \end{aligned}$$

Large Q^2 implies large ν and therefore the Q^2-independent functions $F_{1,2}$ and $g_{1,2}$ depend only on $x = Q^2/2M\nu$, which remains fixed. This phenomenon was originally predicted [11] by James Bjorken in 1968 and shortly afterwards confirmed experimentally at SLAC.The structure functions measured as a function of Q^2, see Fig. 2.2, are practically constant for different values of fixed x. See discussion further down in Section 2.2.2.

[2] $L^{S}_{\mu\nu} = L^{S}_{\nu\mu}$, but $L^{A}_{\mu\nu} = -L^{A}_{\nu\mu}$.
[3] See Appendix A for more details about other terms.
[4] Somewhat equivalent to the electric and magnetic *form factors* in elastic ep scattering.

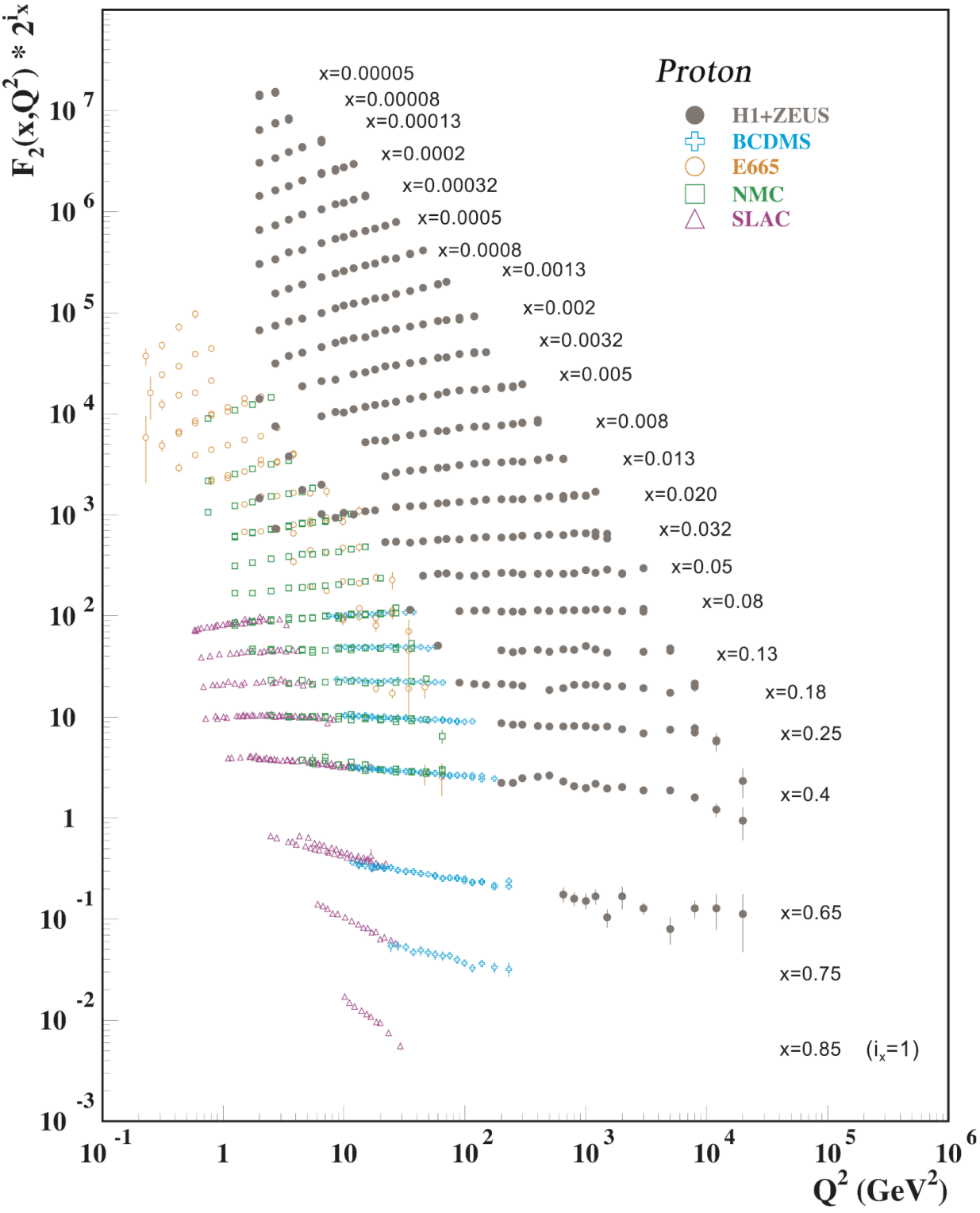

Figure 2.2. The proton structure function F_2 measured in electromagnetic scattering of electrons and positrons on protons (collider experiments H1 and ZEUS for $Q^2 \geq 2$ GeV^2), in the kinematic domain of the HERA data, and for electrons (SLAC) and muons (BCDMS, E665, NMC) on a fixed target. Statistical and systematic errors added in quadrature are shown. For the purpose of plotting F_2 has been multiplied by 2^{i_x}, where i_x is the number of the x bin, ranging from $i_x = 1$ ($x = 0.85$) to $i_x = 24$ ($x = 0.00005$). Figure taken from Ref. [12]. See references therein for the used data.

Measurement of structure functions The four structure functions can be measured in experiments by exploiting the symmetry behavior of the DIS cross section.

$$\sigma_{\text{DIS}} \propto L^{\text{S}}_{\mu\nu} W^{\mu\nu\text{S}} - L^{\text{A}}_{\mu\nu} W^{\mu\nu\text{A}}. \tag{2.9}$$

The determination of the spin-dependent structure functions g_1 and g_2 requires the use of a longitudinally polarized beam in addition to a polarized (longitudinal and transverse, respectively) target. In this case, the differential cross section is [9, 81]

$$\frac{\mathrm{d}^2\sigma}{\mathrm{d}x\,\mathrm{d}y} = \sigma_{UU} + |\mathbf{S}_L|\,\sigma_{LL} + |\mathbf{S}_\perp|\,\sigma_{LT}, \tag{2.10a}$$

$$\text{with} \quad \sigma_{UU} \equiv \frac{\mathrm{d}^2\sigma}{\mathrm{d}x\,\mathrm{d}y} = \frac{4\pi\alpha^2 s}{Q^4}\left[x\,y^2\,F_1 + (1-y)\,F_2\right], \tag{2.10b}$$

$$\sigma_{LL} \equiv \frac{\mathrm{d}^2\sigma^{++}}{\mathrm{d}x\,\mathrm{d}y} - \frac{\mathrm{d}^2\sigma^{+-}}{\mathrm{d}x\,\mathrm{d}y} = \frac{16\pi\alpha^2}{Q^2}\left[\left(1-\frac{y}{2}\right)\,g_1 - \frac{2M^2xy}{Q^2}\,g_2\right], \tag{2.10c}$$

$$\sigma_{LT} \equiv \frac{\mathrm{d}^2\sigma^{+\uparrow}}{\mathrm{d}x\,\mathrm{d}y} - \frac{\mathrm{d}^2\sigma^{+\downarrow}}{\mathrm{d}x\,\mathrm{d}y} = \frac{16\pi\alpha^2}{Q^2}\,\eta\sqrt{1-y-\eta\,\frac{y^2}{4}}\,\left[\frac{y}{2}\,g_1 + g_2\right], \tag{2.10d}$$

where $|\mathbf{S}_L|$ and $|\mathbf{S}_\perp|$ are the longitudinal and transverse components of the target spin with respect to the incoming beam direction; $\eta \equiv 2Mx/\sqrt{Q^2}$; σ_{UU} is the unpolarized cross section (with both target and beam unpolarized); σ_{LL} is the cross section difference for the parallel (σ^{++}) and antiparallel (σ^{+-}) longitudinal target spin configuration and a longitudinal beam; and σ_{LT} is the cross section difference for the case of a longitudinal polarized beam and a transversely polarized target in two opposite spin directions ($\sigma^{+\uparrow}$ and $\sigma^{+\downarrow}$).

- **Unpolarized case** Summing over the spins of the particles only the symmetric term $L^{\text{S}}_{\mu\nu} W^{\mu\nu\text{S}}$ survives. This allows to determine the structure functions F_1 and F_2 in unpolarized DIS from Eq. (2.10b). For a fixed target experiment, at a given (x, Q^2), Eq. (2.10b) implies at least two cross section measurements for two different values of y, i.e., beam energies.[5]
- **Longitudinally polarized case** The difference of cross sections with opposite target spin polarizations singles out the anti-symmetric term $L^{\text{A}}_{\mu\nu} W^{\mu\nu\text{A}}$, given by Eq. (2.10c). The spin-dependent structure function g_1 can be measured from the expression $g_1 = \sigma_{UU}\,A_\parallel + g_2$, where the *double-spin asymmetry* $A_\parallel \equiv \sigma_{LL}/\sigma_{UU}$ can be measured in inclusive DIS, and g_2 implies only small corrections. The first extraction of g_1 for the proton, neutron and deuteron was done in 1988 by the EMC collaboration [14]. Since then, the result has been improved several times from data by other collaborations [15], including HERMES [16].
- **Transversely polarized case** In the case of a transversely polarized target, Eq. (2.10d) is used to determine g_2, since g_1 is multiplied by a factor of y^2 and represents a small contribution to the cross section difference. The extraction of g_2 is reported in Ref. [17], and turns out to be much smaller than g_1. A very recent measurement of g_2 by HERMES can be found in Ref. [18].

[5] Alternatively, one can relate both structure functions to the ratio $\sigma_L/\sigma_T = R(x, Q^2) \sim F_2/(2xF_1)$ of longitudinal and transverse virtual-photon cross sections, for which parametrizations exist, and extract for instance F_2 from a single cross section measurement [10, 13].

2.2 Quark-parton model

The quark parton model (QPM) was devised in 1969 by Feynman and Bjorken [19] with the goal of providing an explanation, based on fundamental concepts, to the inelastic processes observed in the early DIS experiments. Not long afterwards it was linked to the ideas proposed a few years earlier by Gell-Mann [20] and Zweig [21], who had introduced the concept of quarks based on symmetry properties of mesons and baryons multiplets.

The basic idea of the parton model is that, when probed at high energies, the proton behaves as if it were made up of several point-like constituents or *parts*[6]. The DIS collisions $ep \to eX$ can then be regarded as the incoherent sum[7] for the elastic scattering of leptons off *free* quarks $eq \to eq$

$$\frac{\mathrm{d}\sigma^{\,ep\to eX}}{\mathrm{d}x\,\mathrm{d}Q^2} = \sum_q e_q^2\, q(x)\, \frac{\mathrm{d}\hat{\sigma}^{\,eq\to eq}}{\mathrm{d}Q^2}, \tag{2.11}$$

where the function $q(x)$ expresses the probability of finding a quark inside the proton with a certain momentum fraction x. The term $\mathrm{d}\hat{\sigma}/\mathrm{d}Q^2$ is the (computable) cross section for the scattering of two free, pointlike particles. The derivation of Eq. (2.11) is done in Appendix A.

Quarks can be considered as **free** particles in a reference frame where the proton is moving very fast, i.e., in an *infinite momentum frame* [8], where the interaction rate is slowed down by the relativistic time dilation. The Lorentz boost along the direction of motion also allows to neglect the transverse momentum of quarks: quarks can be assumed to move **collinear** with the proton[9].

> **Partons are pointlike!** *The scaling of the structure functions $F_{1,2}$ in the Bjorken limit, $Q^2 \to \infty$, implies that the inner structure of the proton consists of pointlike constituents. Large Q^2 means a high-energy virtual photon, i.e., with short wavelength and therefore high spatial resolution: The photon can resolve a finer substructure within the proton. The fact that the structure "seen" by the photon is independent of its invariant mass can only be explained if this is interacting with components without structure!*

[6] hence the name *partons*

[7] This is generally called the *impulse approximation*, namely that the virtual photon is absorbed by *only* one of the partons, and thus Eq. (2.11) can be summed *incoherently* over each quark species.

[8] In practice, just a "very high momentum" frame.

[9] This point will become relevant later in Sections 2.4 and 2.6 for the discussion of transverse spin effects.

2.2.1 PDFs

In the QPM model, the nucleon is described in terms of *Parton Distribution Functions* (PDFs). The most basic PDF is the *unpolarized* distribution function $q(x)$. In a proton with a given spin vector, we can study the project of the quarks along the same axis and study whether their spin is aligned $(+)$ or anti-aligned $(-)$ with the spin direction of the proton. Thus, the $q(x)$, expressed in terms of the *number densities* $q_{\pm}(x)$, is simply

$$q(x) = q_{+}(x) + q_{-}(x). \tag{2.12}$$

For a longitudinally polarized proton target, and following this notation, quarks can be found with the same spin direction (q_{+}^{+}), or opposite (q_{-}^{+}) to that of the proton, where now the superscript refers to the proton's spin.

> *Here, it is convenient to introduce the concept of* **helicity***: the projection of the spin of a particle along its direction of movement. This can take the values -1 or $+1$, simply indicated with $-$ or $+$. Note that, because of parity invariance, $q_{+}^{+} = q_{-}^{-}$ and $q_{-}^{+} = q_{+}^{-}$, meaning that the distribution of quarks with negative helicity in a proton with positive helicity is the same as that of quarks with positive helicity in a proton with negative helicity.*

The difference of cross sections with opposite longitudinal target polarization leads to[10]

$$\frac{\mathrm{d}\sigma^{+}}{\mathrm{d}x\,\mathrm{d}y} - \frac{\mathrm{d}\sigma^{-}}{\mathrm{d}x\,\mathrm{d}y} = \sum_{q} e_q^2\,\Delta q(x)\left[\frac{\mathrm{d}\hat{\sigma}^{+}}{\mathrm{d}y} - \frac{\mathrm{d}\hat{\sigma}^{-}}{\mathrm{d}y}\right], \tag{2.13}$$

where $\Delta q(x)$ is the *helicity distribution* of quarks

$$\Delta q(x) = q_{+}^{+}(x) - q_{-}^{+}(x). \tag{2.14}$$

Note that in double longitudinally polarized $e\,p$ scattering, the quark that absorbs the virtual photon must have its spin polarized opposite to the photon's spin, in order to conserve total angular momentum. Therefore a cross section measurement with reversed target polarization is sensitive to the difference Δq.

In the case of a transversely polarized target, the difference of cross sections is related to the transversity distribution $\Delta_T(x)$

$$\frac{\mathrm{d}\sigma^{+\uparrow}}{\mathrm{d}x\,\mathrm{d}y} - \frac{\mathrm{d}\sigma^{+\downarrow}}{\mathrm{d}x\,\mathrm{d}y} = \sum_{q} e_q^2\,\Delta_T q(x)\left[\frac{\mathrm{d}\hat{\sigma}^{+\uparrow}}{\mathrm{d}y} - \frac{\mathrm{d}\hat{\sigma}^{+\downarrow}}{\mathrm{d}y}\right] = 0, \tag{2.15}$$

which cannot be measured in inclusive DIS since $\mathrm{d}\hat{\sigma}^{+\uparrow} - \mathrm{d}\hat{\sigma}^{+\downarrow} \simeq 0$. The reason for this is the conservation of helicity – an intuitive explanation is given at the end of Section 2.3.3.

[10] See Appendix A for a derivation.

2.2.2 Interpretation of the structure functions

One great advantage of the QPM is that it provides a *partonic* interpretation of some of the structure functions. Starting from Eq. (2.11), calculating the cross section for the elastic $eq \to eq$ scattering process, and comparing to the expression of the DIS cross section in terms of structure functions in Eq. (2.10a), one finds that the structure functions become [9]

$$F_1(x) = \frac{1}{2}\sum_q e_q^2\ q(x), \qquad F_2(x) = x\sum_q e_q^2\ q(x) = 2xF_1(x), \tag{2.16}$$

$$g_1(x) = \frac{1}{2}\sum_q e_q^2\ \Delta q(x), \qquad g_2(x) = 0. \tag{2.17}$$

This means that one can determine the distribution $q(x)$ of quarks in the proton by a measurement of F_1 or F_2, i.e., from an unpolarized cross section measurement. Similarly, the polarized structure function g_1 gives information about the distribution of quarks with different *helicities*, i.e., with opposite longitudinal spin polarizations, inside a longitudinally polarized proton. The function g_2 is zero in the QPM and therefore does not have a partonic interpretation.

> **Partons have spin 1/2!** *The relationship between F_1 and F_2 given in Eq. (2.16) is known as the Callan-Gross relation [22] and implies that the unpolarized cross section is entirely described by only one of the structure functions, e.g., F_2. The experimental agreement with the Callan-Gross relation indicates that partons are spin $1/2$ particles, as this relation is only true in such case.*

Separately from the conclusions derived from DIS experiments, Gell-Mann and Zweig, based on the properties of the SU(3) symmetry group, concluded that the nucleons must be made from at least *three* quarks: point-like, electrically charged objects with spin $1/2$. In particular, a minimum of two different types of quarks are needed to explain the properties of nucleons, designated as the u (up) quark, with charge $+2/3$ and the d (down) quark, with charge $-1/3$. These quarks represent the quarks of the nucleon that determine its quantum numbers. In addition, other $q\bar{q}$ pairs, resulting from gluon interactions (see next section), are also present in the nucleon, called the *sea* quarks.

> **Partons are quarks!** *The experimental evidence that partons have no structure and that they are spin $1/2$ particles connected the DIS formalism by Bjorken and Feynman with the quark model.*

Results from neutrino data The above expressions for the structure functions are valid for all quark and anti-quark flavors. This implies that sea quarks are also "visible" in DIS experiments, since they do have an electric charge and therefore interact with the virtual photon. Assuming for simplicity that the *sea* inside the nucleon is only made of pairs of $u\bar{u}$, $d\bar{d}$, and *strange* quarks $s\bar{s}$ (these last ones also with charge $1/3$) the F_2 structure function can be calculated as a sum of the parton probabilities $u(x) \equiv q_u(x)$, $d(x) \equiv q_d(x)$ and

$s(x) \equiv q_s(x)$ for the nucleon. For example, for a proton target

$$F_2^{ep}(x) = \frac{4}{9}x[u(x) + \bar{u}(x)] + \frac{1}{9}x[d(x) + \bar{d}(x) + s(x) + \bar{s}(x)]. \tag{2.18}$$

Similarly, the structure function can be calculated from charged current DIS, which takes place by the exchange of a W^+ boson and consequently this can only hit quarks of charge $-1/3$ or antiquarks of charge $-2/3$, giving

$$F_2^{\nu p} = 2x[d(x) + s(x) + \bar{u}(x)]. \tag{2.19}$$

Another relevant observation in neutrino DIS comes from the determination of the F_2 structure function for the nucleon, which can be done by exploiting the isospin symmetric quark content of protons and neutrons. The expression for F_2 reads

$$\begin{aligned} F_2^{\nu N} &= \frac{1}{2}\,(F_2^{\nu p} + F_2^{\nu n}), \\ &= x\,[d(x) + s(x) + \bar{u}(x)] + x,[\bar{d}(x) + \bar{s}(x) + u(x)] \equiv x\,\Sigma(x). \end{aligned} \tag{2.20}$$

If the proton is only made of free quarks, the sum over all values of x and quark types must satisfy the momentum sum rule $\int \mathrm{d}x\,\Sigma(x) = 1$. However, from the measurement of $F_2^{\nu N}$ and F_2^{eN} it can be deduced that $\int \mathrm{d}x\,\Sigma(x) \sim 0.5$. This suggests that quarks carry only about 50% of the nucleon's momentum!

A comparison of neutrino and lepton scattering for isoscalar targets leads to a specific value of the ratio between the structure function measured in both cases $F_2^{eN}/F_2^{\nu N} \simeq 5/18$. The confirmation of this prediction by experimental data, together with the explanation of the Bjorken scaling, represented a great success of the QPM predictive power, and served to establish the validity of the model.

Violation of Bjorken scaling Possibly the strongest evidence against the naive QPM is the fact that the scaling of the unpolarized structure functions is only *approximate*. This can be seen in Fig. 2.2, A slight but significant Q^2-dependence is observed, such that the value of $F_2(x)$ increases at low x, and decreases at large x. *Does this mean that quarks have also a substructure?*

> **Partons interact!** *The two problematic facts introduced above can still be explained within the QPM if one takes into account interactions between partons. These interactions take place via the exchange of gluons, which can also fluctuate into $q-\bar{q}$ pairs. At large Q^2, as the resolution increases, gluons start to be resolved by the virtual photon, sharing therefore part of the nucleon's momentum. As a consequence, the probability of finding a parton with a large momentum fraction x decreases and the probability of finding one at low x increases. The breaking of Bjorken scaling is then explained in a fundamental way.*

2.2.3 Spin crisis

" where, oh where is the proton's spin? [24] "

In order to gain more insight from the role of the spin-dependent structure function g_1, one can take its first moment Γ_1, i.e., integrate the left hand side of Eq. 2.17 over x

$$\Gamma_1 = \int_0^1 g_1(x)\mathrm{d}x = \frac{1}{2}\sum_i e_i^2 \Delta q_i, \qquad \text{with } \Delta q_i = \int_0^1 \Delta q_i(x)\mathrm{d}x, \tag{2.21}$$

and write it in terms of the quark content of the proton

$$\begin{aligned} \Gamma_1^p &= \frac{1}{2}\left[\frac{4}{9}(\Delta u + \Delta\bar{u}) + \frac{1}{9}(\Delta d + \Delta\bar{d}) + \frac{1}{9}(\Delta s + \Delta\bar{s})\right], \\ &= \frac{1}{9}a_0 + \frac{1}{12}a_3 + \frac{1}{36}a_8, \end{aligned}$$

where the coefficients a_0, a_3, and a_8 are arranged [9] in terms of symmetry properties under $SU(3)$ such that

$$\begin{aligned} a_0 &= (\Delta u + \Delta\bar{u}) + (\Delta d + \Delta\bar{d}) + (\Delta s + \Delta\bar{s}) \equiv \Delta\Sigma, \\ a_3 &= (\Delta u + \Delta\bar{u}) - (\Delta d + \Delta\bar{d}), \\ a_8 &= (\Delta u + \Delta\bar{u}) + (\Delta d + \Delta\bar{d}) - 2(\Delta s + \Delta\bar{s}). \end{aligned} \tag{2.22}$$

The value of a_3 and a_8 can be measured experimentally in the beta decay of neutrons and hyperons [9]. This way, the contributions from the quarks to the spin of the proton, $\Delta\Sigma$, may be determined from the measurement of Γ_1^p. This was done for the first time in 1988 by the EMC collaboration at CERN, finding [25] $\Gamma_1^p \simeq 0.126 \pm 0.010 \pm 0.015$. Given the values of a_3 and a_8 of available at that time, this implied a value of $a_0 \simeq 0.098 \pm 0.076 \pm 0.113$.

Interpretation of the EMC results In the naive parton model, only the quarks are considered to be spin-polarized (gluons are ignored) and these move collinear with the nucleon such that their transverse momentum is zero. Thus their momenta do not contribute to the total angular momentum J_z along the direction of motion (say the z direction). The spin of the nucleon $S_z = 1/2$ can then be expressed as

$$(S_z^{\text{quarks}})_{\text{QPM}} = \int_0^1 \mathrm{d}x \left[\left(\frac{1}{2}\right) q_+(x) + \left(-\frac{1}{2}\right) q_-(x)\right], \tag{2.23}$$

since $q_\pm(x)$ count the number of quarks with momentum fraction x and spin component $\pm 1/2$. Using Eq. (2.14) and Eq. (2.22), one finds

$$(S_z^{\text{quarks}})_{\text{QPM}} = \frac{1}{2}\int_0^1 \mathrm{d}x\, \Delta q(x) \equiv \frac{1}{2}\Delta\Sigma = \frac{1}{2}a_0. \tag{2.24}$$

which together with the EMC result for the value of Γ_1^p, i.e., a_0, it implies that the spin of the quarks are just a small contribution to the proton's spin

$$(S_z^{\text{quarks}})_{\text{exp}} \simeq 0.03 \ll \frac{1}{2}. \tag{2.25}$$

This surprising fact was termed a "spin crisis in the parton model" [24] by E. Leader and M. Anselmino.

Resolution of the spin crisis The expression for Γ_1 in Eq. (2.21) is *only* true in the simple parton model. If QCD corrections are taken into account, there is a gluonic contribution coming from the split of a gluon into a $q\bar{q}$ pair. The virtual photon can then be absorbed by one of the radiated quarks, which probes the gluon longitudinal polarization instead. This leads to a new interpretation of a_0

$$a_0 = \Delta\Sigma - 2\frac{\alpha_s}{2\pi}\Delta g, \tag{2.26}$$

where Δg is the gluonic equivalent of Δq, i.e., the difference between the density of gluons with the same helicity as that of the nucleon and those with different helicity.[11]

This implies that the small measured value of a_0 does not necessarily imply that $\Delta\Sigma$ is small. The simple parton model formulae for a_0 and Γ_1 in terms of the Δq are therefore incorrect. A large value of the gluon polarization could then explain the small value measured for a_0, and yet keep a large value of $\Delta\Sigma$. Nevertheless, recent extractions of Δg seem to indicate a quite small value [41], which means that there must exist yet another *large* contribution to the nucleon spin.

Angular momentum sum rule The answer to the spin crisis possibly is in the transverse motion of partons, which is neglected in the collinear parton model. The transverse momentum can generate orbital angular momentum L_z, which would sum with the spin of quarks and gluons. This way, the angular momentum sum rule is

$$J_z = \frac{1}{2}\Delta\Sigma + \Delta g + L_z = \frac{1}{2}. \tag{2.27}$$

The study of inclusive and semi-inclusive DIS reactions with transversely polarized protons is the subject of the rest of the chapter. On the next section, the QCD formalism for the parton model is described, that will be useful later to discuss the transverse-momentum dependent PDFs.

2.3 QCD formulation of the parton model

The QPM led eventually to the formulation of quantum chromodynamics (QCD), the theory describing the properties of strongly-interacting particles, the quarks and gluons from which hadrons are made of. As a non-abelian gauge theory, QCD has two particular features: **confinement** and **asymptotic freedom**.

- *Confinement* refers to the property of the strong coupling constant, α_S, to grow exponentially at large distances or small-energies

$$\alpha_S(Q^2) \propto \frac{1}{\ln Q^2}, \tag{2.28}$$

[11] The gluonic correction to a_0 is often called in the bibliography the *axial anomaly* or *anomalous gluon contribution*, referring to the fact that it survives in the limit $Q^2 \to \infty$, where the effective strong coupling goes to zero and one would expect all QCD effects to be switched off.

explaining this way why quarks are bound together inside the nucleon. This dependence of α_S with the energy makes it rather difficult to perform exact calculations of processes, like for instance scattering amplitudes, since the number of gluon corrections grows "exponentially", making the calculations impossible to compute[12].

- *Asymptotic freedom*, in contrast, implies that at short distance or for high-energy interactions, α_S becomes smaller, which makes it possible to use **perturbation theory** in order to expand the object of interest in powers of the coupling constant

$$\sigma = \sigma_{LO}\,(1 + \alpha_S\, c_1 + \alpha_S^2\, c_2 + \ldots). \tag{2.29}$$

A certain magnitude can then be calculated at *leading order* (LO), corresponding to σ_{LO}, *next-to-leading order* (NLO), *next-to-next-to-leading order* (NNLO), etc. In this regard, asymptotic freedom can be seen as the prerequisite that permits us to study the nucleon structure. The simple QPM represents then the limiting case of QCD in which $Q^2 \to \infty$ and therefore there is *no* interaction between partons.

Perturbation theory is useful for the description of quantities that are either insensitive to long-distance physics, or that can be separated or *factorized* into short-distance (perturbative) and long-distance (non-perturbative) physics. An example of the latter is the DIS cross section, involving large momentum transfers ($Q^2 \to \infty, \alpha_S \to 0$), which allows to consider the quarks as quasi-free particles in the interaction of the nucleon with a high-energy electron.

The cross-section formula for the parton model, given in Eq. (2.11), can be written in a factorized form as a product of two parts

$$\mathrm{d}\sigma^{\,ep\to eX} = \sum_q f_q(x) \otimes \mathrm{d}\hat{\sigma}^{eq\to eq}(Q^2) \tag{2.30}$$

- a high-energy part, $\mathrm{d}\hat{\sigma}^{eq\to eq}$, describing the hard elastic scattering of the virtual photon off the quark; for high-energy transfers, $\mathrm{d}\hat{\sigma}^{eq\to eq}$ can be calculated in perturbation theory as

$$\hat{\sigma}_{\text{hard}} \sim (\hat{s}^{\,2} + \hat{u}^{\,2}), \tag{2.31}$$

with $\hat{s} = (p_i + q)^2$ and $\hat{u} = (k' - p_i)^2$ the usual Mandelstam variables, and $p_i = xP$ the parton momentum.

- a low-energy part, the parton distribution functions $f_q(x)$, containing all interactions and fluctuations of the quarks confined inside the proton. These low-energy interactions cannot be calculated, since they are typically non-perturbative, but can be measured in one type of process and applied to others[13].

At higher orders in perturbation theory, there are corrections of the order of powers of α_S to the hard-scattering cross section $\mathrm{d}\hat{\sigma}^{eq\to eq}$. One must consider virtual loop corrections to the $eq \to eq$ elementary process as well as the radiation of gluons from the outgoing quarks. This introduces a well-known Q^2 dependence on the PDFs (see Section 2.3.1)

$$f_q(x) \to f_q(x, Q^2). \tag{2.32}$$

[12] The radiation of gluons between quarks in two polarized protons involves about *half a million* diagrams! [26]

[13] A property known as *universality* of the PDFs. See Appendix D.

On the other hand, the parton distribution functions can be formally derived from the soft, non-perturbative part of the hadronic tensor. See Section 2.3.2.

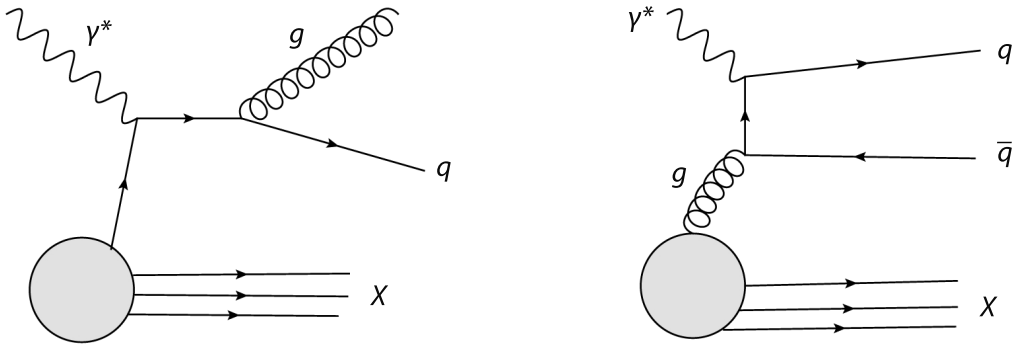

Figure 2.3. QCD corrections to the DIS cross section.

2.3.1 QCD corrections

The simplest QCD corrections are illustrated in Fig. 2.3. Gluons can be radiated from quarks, (*QCD-Compton scattering*) or they can absorb the virtual photon, turning into a $q\bar{q}$ pair (*photon-gluon fusion*). These processes can be calculated to a certain expansion order in pQCD, but one must pay some extra price. To illustrate this, let us consider the radiation of a gluon with momentum p_g by the quark with momentum k.

> *Note that in the previous sections, k and k' were use to designate the four-momenta of the electron before and after the scattering off the proton, respectively. From now on, we focus on the interaction of the virtual photon with the proton, i.e., with the quarks and gluons. The electron is therefore "left behind", and its momentum will not appear in the next sections unless stated. In the following, then, k is always used to denote quarks.*

The objects of interest are the quark-gluon vertices of Fig. 2.3. On the left hand diagram, it is considered the radiation of a quark by a gluon in the interaction with the virtual photon. On the right hand, a gluon emitted by the proton absorbs the virtual photon, converting afterwards in a quark-antiquark pair. The vertex contributions in each case are given respectively by

$$\frac{\not{k}\gamma_\mu(\not{k}-\not{p}_g)}{-2\,\mathbf{k}\cdot\mathbf{p}_g+i\epsilon} \quad \text{and} \quad \frac{\not{k}'\gamma_\mu(\not{k}'-\not{p}_g)}{2\,\mathbf{k}'\cdot\mathbf{p}_g-i\epsilon}. \tag{2.33}$$

These two vertices contain three types of singularities, coming from the way the denominators may vanish: *k-collinear*, *k'-collinear* and *soft*. The *soft* singularities arise from the fact that gluons are massless, and then all components of p_g may go to zero. Similarly, the k- and k'-singularities arise because the mass of quarks is usually neglected. Since there is no mass

term in the denominators, the scalar product $\mathbf{k} \cdot \mathbf{p}_g = k\, p_g \cos\theta$ vanishes for $\theta \to 0$. This corresponds to the gluon being emitted collinear with the initial parton direction.

> *The nature of the transverse quark momentum $\mathbf{k}_T$ can be perturbative, i.e., from the radiation of gluons like described in the previous section, or non-perturbative, usually called* **intrinsic** *parton momentum which merely arises from the spatial distribution of quarks inside the proton. Note that the radiation of a gluon naturally introduces a transverse momentum k_T of the partons!*

Renormalization of divergences The *collinear divergences* at $k_T = 0$ imply that the cross section cannot be integrated over $\mathrm{d}k_T^2$ from 0 to $k_T^2(\max)$ but rather starting at a cut-off value κ^2. As a consequence of the κ^2 integration, a residual term $\ln(Q^2/\kappa^2)$ is left. However, the physics of the process cannot depend on an arbitrary parameter like κ^2. A solution is to consider a certain *scale* μ^2, such that

$$\begin{aligned} \ln\left(\frac{Q^2}{\kappa^2}\right) &= \ln Q^2 - \ln\kappa^2 \\ &= \ln Q^2 - \ln\mu^2 + \ln\mu^2 - \ln\kappa^2 \\ &= \ln\left(\frac{Q^2}{\mu^2}\right) + \ln\left(\frac{\mu^2}{\kappa^2}\right). \end{aligned}$$

The new term $\ln(\mu^2/\kappa^2)$ is a trace of soft physics, and can be *incorporated* into the parton density $q_i(x) \to q_i(x, \mu^2)$, which is also of non-perturbative nature.

The parameter μ represents the *factorization scale* of the process, which can be set freely in order to specify which radiative corrections can be included in the PDFs – soft gluons, and which should be considered part of the hard quark-photon scattering – hard gluons. In DIS, the scale μ^2 is chosen conveniently to be equal to Q^2, a variable which has a physical meaning. Note that both the hard cross section and the parton distributions are in reality independent of μ, but it is only through this parameter that these objects can be assigned a *meaning* in the context of a quantum field theory like QCD [29].

Twist In addition to the perturbative corrections like the ones described above, related to the expansion on α_S, there are other corrections to Eq. (2.30) of non-perturbative nature. These are typically suppressed by inverse powers of the momentum transfer to the nucleon, $\mathcal{O}(1/Q^2)$. The order in $1/Q^2$ at which a certain observable appears is indicated by the concept of *twist*. If it is seen at $(1/Q^2)^p$, this corresponds to twist $t = 2 + 2p$. Thus, *leading-twist* means $t = 2$. Formally, the twist can be regarded as a new quantum number, related to the dimension and spin of field operators [27]. Most spin effects known to date are related to leading-twist observables, like the three PDFs introduced in the previous section. Higher-twist PDFs have also been proven to play a significant role – see Section 2.7.

Evolution equations for parton densities The rescaled or *renormalized* parton density $q_i(x, \mu^2)$ cannot be calculated perturbatively but its variation with $\ln \mu^2$ is given by

$$\frac{\partial q_i(x,\mu^2)}{\partial \ln \mu^2} = \frac{\alpha_s}{2\pi} \int_x^1 \frac{d\xi}{\xi} \left[q_i(\xi,\mu^2) P_{qq}(x/\xi) + g(\xi,\mu^2) P_{qg}(x/\xi) \right], \tag{2.34}$$

where P_{qq} is the (calculable) probability that a quark radiates a gluon and P_{qg}, similarly, the probability that a gluon converts into a $q\bar{q}$ pair. An equivalent equation is found for the gluon density

$$\frac{\partial g_i(x,\mu^2)}{\partial \ln \mu^2} = \frac{\alpha_s}{2\pi} \int_x^1 \frac{d\xi}{\xi} \left[\sum_i q_i(\xi,\mu^2) P_{gq}(x/\xi) + g(\xi,\mu^2) P_{gg}(x/\xi) \right], \tag{2.35}$$

where P_{gq} is equivalent to P_{qg} and P_{gg} represents a 3-gluon vertex.

The Eqs. 2.34 and 2.35 are known as the DGLAP evolution equations, also known as the Altarelli-Parisi equations[14]. They describe the Q^2 dependence of the parton distribution functions, which implies that if the PDF is known at a certain scale Q_0^2, it is possible to calculate it at any given Q^2. The DGLAP equations represent one of the milestones of perturbative QCD, due to the very good agreement of their solutions with experimental data [32].

2.3.2 Quark correlator

The momentum $q(x)$, helicity $\Delta q(x)$ and transversity $\Delta_T q(x)$ distribution functions were introduced in Section 2.2.1 to provide a partonic interpretation of the DIS interactions. These and other PDFs can be formally derived from the hadronic tensor $W_{\mu\nu}$ describing the hadronic current.

Definition The general form of the hadronic tensor was defined in Eq. (2.8) without any assumption on the hadron structure. Considering now that the ep scattering process takes place via the hard scattering off a quark, the final state $|X\rangle$ in Eq. (2.8) can then be split into a quark with momentum $k' = k + q$ and a remnant. See Fig. 2.4.

Using the rules for Feynman diagrams, the tree-level Feynman amplitude is given by[15]

$$\mathcal{M}^\mu = \bar{u}(k')\gamma^\mu A_q(k; P, S), \tag{2.36}$$

including a free-quark spinor $\bar{u}(k')$ for the outgoing quark, the photon-quark vertex $ie_q\gamma^\mu$, and a matrix element $A_q(k; P, S)$ describing the extraction of a quark with momentum k from the nucleon and the nucleon's remnant with momentum P and spin S.

[14] Dokshitzer in 1977, Gribov and Lipatov in 1972, and Altarelli and Parisi in 1977 wrote independently the first formulation of these equations [30]. An accessible review by Altarelli can be found in Ref. [31].

[15] In the following, k is used to denote quarks, instead of leptons. This is an unfortunate convention used in most of the relevant literature.

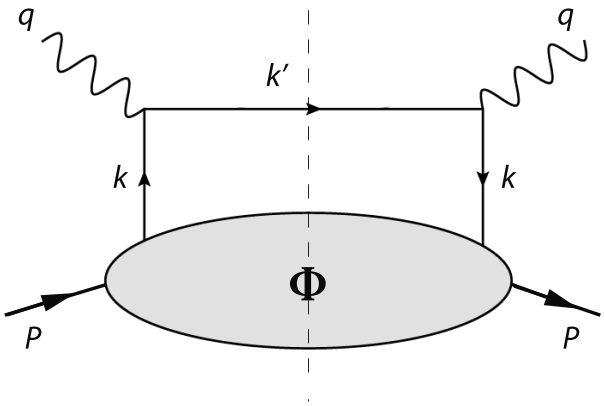

Figure 2.4. The schematic representation of the correlator.

In order to expand the hadronic tensor using Feynman diagrams, factorization into a hard and a soft part must be assumed. Another approach for the quantum field formulation of the hadronic tensor is based on the Operator Product Expansion (OPE) technique, in which factorization is actually proven. See Ref. [33] for a review of both approaches. In the diagrammatic approach chosen here, the diagram of Fig. 2.4 is just the tree-level contribution. A complete handling implies corrections to the hard scattering by gluons, in which case the results are equivalent to those provided by the OPE.

The hadronic tensor can be written as [16]

$$
\begin{aligned}
2MW^{\mu\nu}(q;P,S) \;=\; & \frac{1}{2\pi}\sum_q e_q^2 \sum_X \int \frac{\mathrm{d}^3\mathbf{P}_X}{(2\pi)^3\,2E_X} \int \frac{\mathrm{d}^4k}{(2\pi)^4} \int \frac{\mathrm{d}^4k'}{(2\pi)^4}\,\delta(k'^2) \\
& \times \left[\bar{u}(k')\gamma^\mu A_q(k;P,S)\right]^* \left[\bar{u}(k')\gamma^\nu A_q(k;P,S)\right] \\
& \times (2\pi)^4\,\delta^4(P-k-P_X)\,(2\pi)^4\,\delta^4(k+q-k')\,. \qquad (2.37)
\end{aligned}
$$

Here, k' is the momentum of the quark after absorbing the virtual photon; the $\delta(k'^2)$ arises from the condition that the scattered quark is *on-shell*, i.e., it is a free particle satisfying the energy-mass relation $E'^2 = \mathbf{k}'^2 + m_q^2$. The quark mass can be neglected in the calculation. The $[\ldots]^*$ indicates the complex conjugate of the amplitude, that can be replaced with an hermitian conjugate † since this is a real number. The matrix element can be written as $A_{qi}(k,X;P,S) = \langle X|\,\psi_i(0)|P,S\rangle$, where the $\psi(\xi)$ are the local quark fields, describing one type of quark, which depend on the space-time coordinate[17] ξ. Similarly, $A^\dagger_{qi}(k,X;P,S) = \langle P,S|\,\bar{\psi}_i(0)|X\rangle$ with $\bar{\psi}(\xi)$ describing anti-quarks. On the other hand, the product of the two spinors is $u(k')\bar{u}(k') = \not{k}' + m_q \simeq \not{k} + \not{q}$, again neglecting the quark

[16] The derivation in Refs. [34–36] were used in this section.

[17] The variable ξ is used to indicate the space-time four vector to avoid confusion with the x-Bjorken variable.

mass[18].Then Eq. (2.37) becomes

$$
\begin{aligned}
2M W^{\mu\nu}(q;P,S) &= \frac{1}{2\pi}\sum_q e_q^2 \sum_X \int \frac{\mathrm{d}^3\mathbf{P}_X}{(2\pi)^3\,2E_X}\int\frac{\mathrm{d}^4k}{(2\pi)^4}\int\frac{\mathrm{d}^4k'}{(2\pi)^4}\,\delta(k'^2)\\
\textit{soft part}\rightarrow &\quad \times \langle P,S|\bar\psi_i(0)|X\rangle\,\langle X|\psi_j(0)|P,S\rangle \qquad (2.38)\\
\textit{hard part}\rightarrow &\quad \times [(-i\gamma^\mu)(\not k+\not q)(i\gamma^\nu)] \qquad (2.39)\\
&\quad \times (2\pi)^4\,\delta^4(P-k-P_X)\,(2\pi)^4\,\delta^4(k+q-k')\,,
\end{aligned}
$$

where the separation into the hard and soft parts has been emphasized. All information about the nucleon internal structure and soft non-perturbative interactions is contained in the *quark-quark correlation matrix* $\Phi_{ij}(k;P,S)$, defined as

$$
\begin{aligned}
\Phi_{ij}(k;P,S) &= \sum_X \int \frac{\mathrm{d}^3\,\mathbf{P}_X}{(2\pi)^3\,2P_X^0}\,\delta^4(P-k-P_X)\\
&\quad \times\langle P,S|\bar\psi_j(0)|X\rangle\,\langle X|\psi_i(0)|P,S\rangle. \qquad (2.40)
\end{aligned}
$$

The hadronic tensor can then be rewritten as

$$
\begin{aligned}
2M W_{\mu\nu} &= \sum_q e_q^2 \int\frac{\mathrm{d}^4k}{(2\pi)^4}\int\frac{\mathrm{d}^4k'}{(2\pi)^4}\,\delta(k'^2)\,(2\pi)^4\,\delta^4(k+q-k')\,\mathrm{Tr}\left[\Phi\,\gamma^\mu\not k'\gamma^\nu\right]\\
&= \sum_q e_q^2 \int\frac{\mathrm{d}^4k}{(2\pi)^4}\,\delta\left((k+q)^2\right)\mathrm{Tr}\left[\Phi\,\gamma^\mu(\not k+\not q)\gamma^\nu\right], \qquad (2.41)
\end{aligned}
$$

The $\Phi_{ij}(k;P,S)$ correlation matrix (simply called the *quark-quark correlator*) characterizes the *soft*, non-perturbative interactions inside the proton. This is graphically illustrated by the grey "blob" in Fig. 2.4.

A more compact form of the correlator can be found by applying a Fourier transformation[19] and using the completeness relation $|X\rangle\langle X| = \mathbb{1}$ to eliminate the unobserved X states, which leads to

$$
\Phi_{ij}(k;P,S) = \frac{1}{(2\pi)^4}\int \mathrm{d}^4\,\xi\; e^{-i\,p\cdot\xi}\;\langle P,S|\bar\psi_j(\xi)\;\psi_i(0)|P,S\rangle. \qquad (2.42)
$$

The quark correlator Φ can be regarded as a *bilocal* operator $\bar\psi(0)\,\psi(\xi)$ that relates the initial state of the nucleon $|P,S\rangle$ to the struck quark, integrated over all possible separations ξ in space-time the quark might have [20].

Integration For further exploration of the correlator, it is convenient to use light-cone variables[21], such that the quark momentum can be parametrized as [35][22]

$$
k = [k^+,k^-,\mathbf{k}_T] = \left[xP^+,\;\frac{k^2+|\mathbf{k}_T|^2}{2xP^+},\;\mathbf{k}_T\right]. \qquad (2.43)
$$

[18]The Feynman *slash notation* for a four-momentum A corresponds to $\not A \equiv \gamma^\mu A_\mu$.
[19]See Eq. (A.5).
[20]The above definition of Φ_{ij} does not take into account the presence of Wilson lines, see Appendix D.
[21]See definition of $k^\pm$ at the end of Appendix D.
[22]Note that in Ref. [35], light-cone vectors are written with the *minus* component first $k = [k^-,k^+,\mathbf{k}_T]$.

Assuming that the virtuality of the quark k^2 and its transverse momentum $\mathbf{k}_T$ are both small in comparison to Q^2, the relevant component of the quark momentum respect to the proton momentum becomes $k^+ = xP^+$, and the quark correlator is effectively a function of only x and S. The correlator can then be integrated over the other variables, depending on the case of interest:

- If only the momentum of the scattered lepton is known (in inclusive DIS), the scattered electron does not carry any information on the intrinsic motion of quarks and the quark correlator can be integrated over both $\mathrm{d}k^-$ and $\mathrm{d}^2\mathbf{k}_T$

$$\Phi_{\mathrm{DIS}}(x, S) = \int \mathrm{d}^2\mathbf{k}_T \, \mathrm{d}k^- \Phi(k; P, S), \tag{2.44}$$

  which leads to the *three* leading-twist PDFs described in the next paragraph.

- If in addition, one hadron is detected in coincidence with the lepton (in semi-inclusive DIS), the hadron transverse momentum $\mathbf{p}_{h\perp}$ can be related to the parton intrinsic motion. One can then investigate the $\mathbf{k}_T$-dependent correlator

$$\Phi_{\mathrm{SIDIS}}(x, \mathbf{k}_T, S) = \int \mathrm{d}k^- \Phi(k; P, S), \tag{2.45}$$

  which leads to the transverse-momentum dependent (TMDs) parton distribution functions. See Section 2.6.1.

Distribution functions The quark-quark correlator $\Phi(x, S)$ is constrained by the hermiticity properties of the fields, and by parity and time reversal invariance. This allows to expand Φ in terms of *twelve* scattering amplitudes for leading-twist, which are real scalar functions $A(p \cdot P,\, p^2)$[23]. Imposing such symmetry requirements, they can be reduced to just *three* [34]

$$\Phi(x, S) = \frac{1}{2}\left[f_1(x)\, \not{P} + S_L\, g_{1L}(x)\, \gamma^5 \not{P} + h_{1T}\, i\sigma_{\mu\nu}\gamma^5 P^\mu\, S_\perp^\nu\right]. \tag{2.46}$$

The three functions $f_1(x)$, $g_{1L}(x)$ and h_{1T} correspond to the three distribution functions already introduced, just with different notation[24]. These can be *projected* out of the quark correlator by means of the corresponding Dirac matrices [34]

$$\frac{1}{2}\,\mathrm{Tr}\left[\gamma^+\,\Phi(x, S)\right] = f_1(x, k_\perp) \equiv q(x)\,, \tag{2.47}$$

$$\frac{1}{2\,S_L}\,\mathrm{Tr}\left[\gamma^+\gamma_5\,\Phi(x, S)\right] = g_{1L}(x, k_\perp) \equiv \Delta\, q(x)\,, \tag{2.48}$$

$$\frac{1}{2\,S_\perp^j}\,\mathrm{Tr}\left[i\sigma^{j+}\gamma_5\,\Phi(x, S)\right] = h_{1T}(x, k_\perp) \equiv \Delta_T q(x)\,. \tag{2.49}$$

[23] Just like the four structure functions describing $W_{\mu\nu}$ were a function of $q \cdot P$ and q^2.

[24] There are different symbols used to denote the most common distribution functions, due to the different authors. A good summary can be found in Ref. [38].

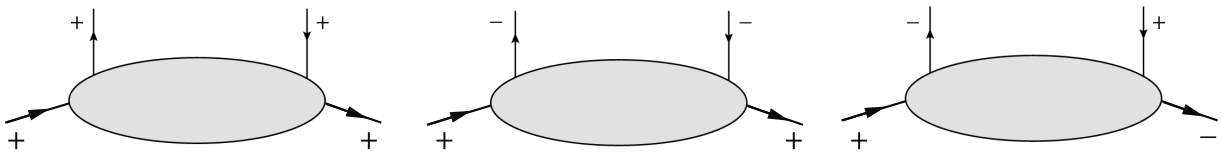

Figure 2.5. The three quark-nucleon helicity amplitudes.

Probabilistic interpretation The hadronic tensor can be related to forward virtual Compton scattering, i.e., the probability amplitudes of a virtual photon scattering off a proton, by means of the optical theorem [34]. These amplitudes are of the form $\mathcal{A}_{\Lambda\lambda,\Lambda'\lambda'}$, representing different ways in which the helicities of the quark (λ) and proton (Λ) can change in the scattering process. This can happen in 16 different ways, which, after imposing the conservation of helicity and parity invariance, leads to just three independent amplitudes[25]

$$\mathcal{A}_{++,++}\,, \quad \mathcal{A}_{+-,+-}\,, \quad \mathcal{A}_{+-,-+}\,. \tag{2.50}$$

Using the optical theorem, the three leading-twist PDFs can be related to these amplitudes in the following way

$$q(x) = \; q_+(x) + q_-(x) \;\sim \mathrm{Im}(\mathcal{A}_{++,++} + \mathcal{A}_{+-,+-})\,, \tag{2.51a}$$
$$\Delta q(x) = \; q_+(x) - q_-(x) \;\sim \mathrm{Im}(\mathcal{A}_{++,++} - \mathcal{A}_{+-,+-})\,, \tag{2.51b}$$
$$\Delta_T q(x) = \; q_\uparrow(x) - q_\downarrow(x) \;\sim \mathrm{Im}\mathcal{A}_{+-,-+}\,. \tag{2.51c}$$

The probability amplitudes are represented graphically in the diagrams of Fig. 2.5. The transversity distribution, related to the right-most diagram, implies a mix of both helicity states, and is therefore off-diagonal in the helicity basis. For this reason, it only admits an interpretation in terms of probability densities in the *transverse polarization basis*

$$\Delta_T q(x) = q_\uparrow(x) - q_\downarrow(x) \sim \mathrm{Im}(\mathcal{A}_{\uparrow\uparrow,\uparrow\uparrow} - \mathcal{A}_{\uparrow\downarrow,\uparrow\downarrow})\,. \tag{2.52}$$

As shown in the next section, this mixing of helicity states is the origin of the reason why transverse spin effects are absent in inclusive DIS.

Determination of PDFs The unpolarized PDFs are by now the best known partonic distributions. They can be extracted from DIS data using the DGLAP equations (see Section. 2.3.1). There is extensive bibliography about this, see for example the first section of Ref. [90]. One possibility, for instance, is to exploit the simple relation of F_2 with the quark distributions $q(x)$, given in Eq. (2.18). One starts with possible parametrization of the parton dependence, usually with a large (10-30) number of free parameters. This set of parameters is then fit to available cross section and F_2 data. By using large sets of data from several experiments, e.g., obtained with different beams and targets, the fits can be optimized.

[25] If the $\mathbf{k}_T$ dependence is taken into account, a total of *six* independent helicity amplitudes are needed to describe the TMDs contained in the $\Phi(x, \mathbf{k}_T, S)$ correlator.

The quark **helicity** distributions have been measured by several experiments, including HERMES [39], and are also well known. Their evolution with Q^2 is not completely studied, and more experimental data are needed. The gluon helicity presents more difficulties to be accessed, as it is measured through scaling violations of g_1. See Refs. [40, 90] for more information. The evolution of the g_1 structure function is sensitive to the helicity density of **gluons** Δg through the Q^2 evolution given by the DGLAP equations. At first order, the splitting of gluons into quark pairs $g \to q\bar{q}$ contributes weakly to g_1. At next-to-leading order, additional sensitivity arises from the photon-gluon fusion process (see Fig. 2.3), which produces a $q\bar{q}$ pair resulting in two jets of hadrons. This signature can be used to access Δg in the detection of hadron pairs at large transverse momentum, or in inclusive hadron production, from double-spin cross section asymmetries. The quantity $\Delta g/g$ was determined this way by the HERMES and COMPASS collaborations [41].

The **transversity** distribution is the least known of the three leading-twist integrated PDFs, partially due to the fact that it cannot be accessed in DIS. This is discussed next.

2.3.3 Why transversity cannot be measured in inclusive DIS?

In terms of scattering amplitudes introduced in Section 2.3.2, the transversity distribution can be regarded as

$$\Delta_T q = |\langle \uparrow X| \uparrow\rangle|^2 - |\langle \downarrow X| \uparrow\rangle|^2, \tag{2.53}$$

where the term $\langle \downarrow X| \uparrow\rangle$ is the transition probability of a transversely polarized proton with spin *up* $|\uparrow\rangle$ resulting in a quark with spin *down* $\langle\downarrow|$ plus X more particles in the final state. The $|\uparrow\rangle$ and $|\downarrow\rangle$ states can be represented in the helicity basis as

$$|\uparrow\rangle = \frac{1}{\sqrt{2}}(|+\rangle + i\,|-\rangle), \qquad |\downarrow\rangle = \frac{1}{\sqrt{2}}(|+\rangle - i\,|-\rangle). \tag{2.54}$$

Inserting these expressions into Eq. (2.53), it is easy to prove that the transversity distribution implies a **helicity flip**

$$\Delta_T q = \langle +X|+\rangle \langle -X|-\rangle. \tag{2.55}$$

This is shown in Fig. 2.6. The lower diagram represents the term in Eq. (2.55) and the upper part represents a generic DIS diagram with possible loop corrections. If the helicity of the quark in the initial state is, e.g., $+1$ there is no way, by means of photon or gluon couplings, of flipping the helicity to -1 in the final state, as QED and QCD interactions conserve helicity[26]. Both diagrams are therefore incompatible: transversity decouples from DIS. The parton model result for the difference of transversely polarized cross sections leads to $\mathrm{d}\sigma^{+\uparrow} - \mathrm{d}\sigma^{+\downarrow} = 0$.

A function that does not conserve the helicity or *chirality* is called to be **chiral-odd**, in contrast to *chiral-even* functions, that do conserve it. Given its chiral-odd nature, a possibility to access the transversity distribution is that it comes together with another chiral-odd process. A *double* helicity flip would turn into a conservation of the total helicity.

[26] Helicity conservation is only guaranteed for hard scattering, i.e., very high energies, in all strong and electroweak interactions in the standard model. However, helicity flips are allowed at low energies.

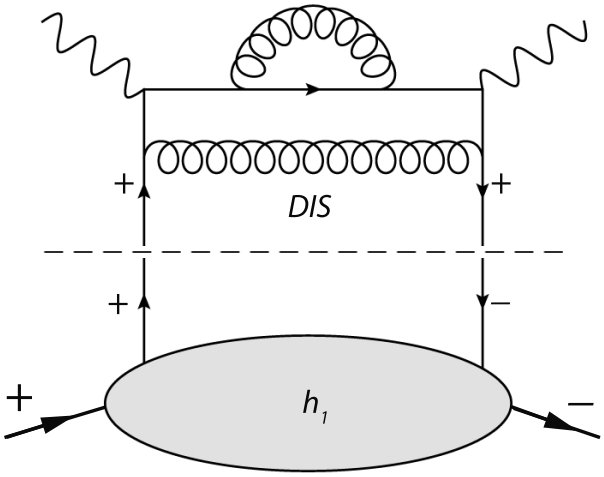

Figure 2.6. Decoupling of transversity from DIS due to the helicity flip.

Why gluons cannot carry transversity? Gluons are gauge bosons and hence have spin 1, i.e., they exist with helicity ± 1. In terms of the helicity amplitudes, the transversity distribution for gluons h_1^g would imply a helicity flip of 2 units, which cannot take place in a spin-1/2 nucleon. In DIS reactions using targets with higher spin, like deuterium, this could be allowed.

Access to transversity The cleanest and most direct way to measure transversity is [42] via the double transversely polarized Drell-Yan process, $p^\uparrow \bar{p}^\downarrow \to e^+ e^- X$, which couples *two* transversity distributions. See Fig. 2.7. This process does not violates helicity: one has $-+$ both in the initial and final state. However, the single helicities of the proton and quark states change, thus probing transversity via the double transverse spin asymmetry

$$A_{TT} = \frac{\mathrm{d}\sigma^{\uparrow\uparrow} - \mathrm{d}\sigma^{\uparrow\downarrow}}{\mathrm{d}\sigma^{\uparrow\uparrow} + \mathrm{d}\sigma^{\uparrow\downarrow}}, \tag{2.56}$$

$$= \frac{\sum_q e_q^2 \left[h_{1q}(x_1)\, h_{1q}(x_2) + h_{1\bar{q}}(x_1)\, h_{1\bar{q}}(x_2)\right]}{\sum_q e_q^2 \left[q(x_1)\, q(x_2) + \bar{q}(x_1)\, \bar{q}(x_2)\right]} \frac{\mathrm{d}\hat{\sigma}^{\uparrow\uparrow} - \mathrm{d}\hat{\sigma}^{\uparrow\downarrow}}{\mathrm{d}\hat{\sigma}^{\uparrow\uparrow} + \mathrm{d}\hat{\sigma}^{\uparrow\downarrow}}, \tag{2.57}$$

Unfortunately, such a process is difficult to achieve experimentally, and no data is available yet to test the available lattice and model calculations. Data are expected to be collected from the collisions at RHIC and at GSI.

At the moment, the most reasonable way to measure h_1 is in SIDIS processes, in which the transversity distributions is coupled to a chiral-odd fragmentation function, called the Collins function $H_1^\perp$. This is shown in the right hand diagram of Fig. 2.7. The first extraction of the transversity distribution for the u and d quarks was recently done by Anselmino et al. [43] from a global analysis of the results from the HERMES [44] and COMPASS [45] collaborations, together with the measurement of the Collins fragmentation function by the BELLE [46] collaboration from $e^+e^- \to hhX$ collisions at KEK.

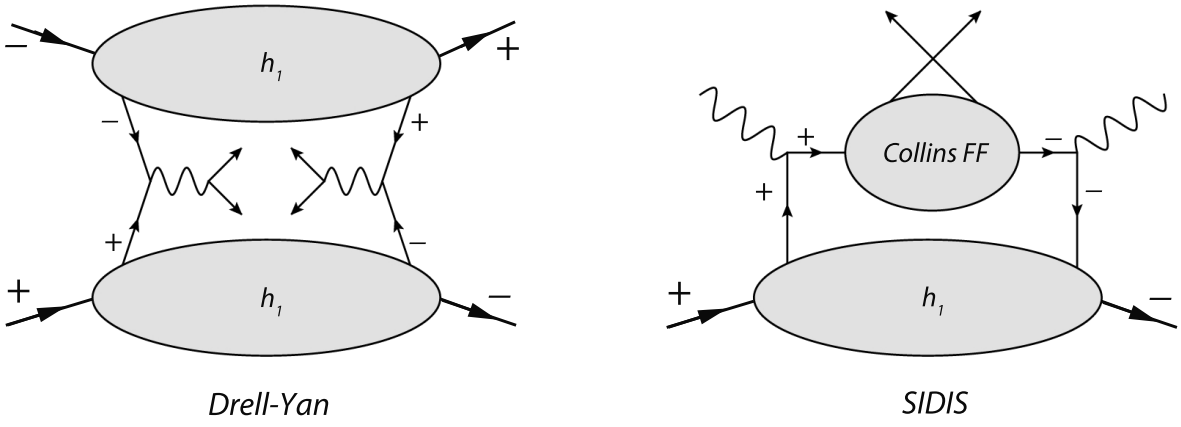

Figure 2.7. Experimental access to transversity. *Left:* The combination of two transversity distributions in polarized Drell-Yan processes. *Right:* Transversity coupled to a chiral-odd fragmentation function in polarized SIDIS.

2.4 Transverse spin physics

In the previous section, it has been discussed how the structure of the nucleon can be explained in terms of the PDFs, the parton distribution functions. These are introduced in the context of the QPM and can also be derived from the quark-quark correlator describing the non-perturbative part of the $\gamma^* q$ cross section. In particular, the longitudinal spin structure of the nucleon is very well understood and the agreement between experimental data and theory, excellent.

The transverse spin structure is much more challenging, and less studied. The fact that the transversity distribution cannot be accessed in DIS, as discussed in Section 2.3.3, and that in general all spin effects associated to the transverse polarization of the proton are very small, like the polarized structure function g_2, kept the study of transverse spin effects away from the general interest for a long time. Moreover, as argued in Section 2.4.2, it was believed for a long time that any large transverse SSAs would be forbidden in pQCD.

The observation, however, of large transverse SSAs in the inclusive production of hadrons from hadronic collisions, discussed in Section 2.4.1, led to a deeper revision of the subject. In particular, the essential role that the *intrinsic* motion of quarks plays both in the distribution of quarks inside the nucleon and in the final hadronization processes was understood.

Note that a distinction between longitudinal and transverse spin effects makes only sense in the context of a relativistic nucleon, i.e., in a nucleon at rest the helicity and transversity distributions are the same.

2.4.1 A_N in hadronic interactions

The transverse single-spin asymmetry A_N is one of the simplest spin observables in particle collisions. One scatters a beam of transversely polarized protons off unpolarized protons and measures the number of pions (or mesons in general) produced to the left and to the right of the transverse spin, in the plane defined by the azimuthal projection of the momentum

p of the detected particle and the spin vector $\mathbf{S}_\perp$ of the polarized particles. An equivalent experiment can be performed with an unpolarized beam scattering off a transversely polarized target. A *left-right* asymmetry is defined this way, related to the spin-dependent part of the cross section

$$A_N \equiv \frac{\mathrm{d}\sigma^\uparrow(p,\mathbf{S}_\perp) - \mathrm{d}\sigma^\uparrow(p,-\mathbf{S}_\perp)}{\mathrm{d}\sigma^\uparrow(p,\mathbf{S}_\perp) + \mathrm{d}\sigma^\uparrow(p,-\mathbf{S}_\perp)} = \frac{\Delta\sigma(p,\mathbf{S}_\perp)}{\sigma(p)}. \tag{2.58}$$

Such asymmetries have been measured over the last four decades in several experiments [47–71], for the inclusive production of several hadron types in hadron-nucleon collisions, at center-of-mass energies in the range 5–200 GeV. In most cases, surprisingly large asymmetries were observed, up to 40%, with a clear kinematic dependence on the transverse momentum of the hadron p_T as well as on the Feynman variable x_F, related to the longitudinal momentum of the hadron – see Eq. (2.98). Some of the measurements of A_N are summarized in Fig. 2.8.

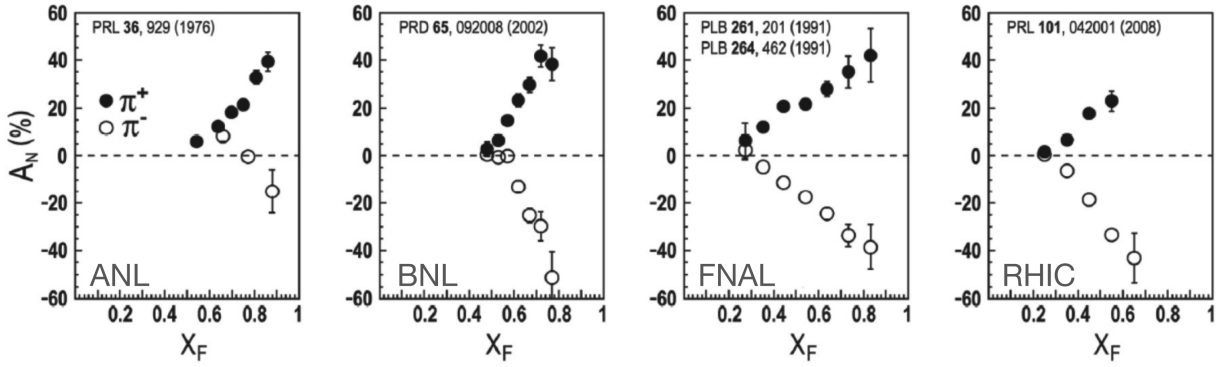

Figure 2.8. Measurements of A_N for charged pions in $p^\uparrow p \to h X$ collisions. The center-of-mass energies correspond respectively (from left to right) to $\sqrt{s} = 4.9$ GeV, 6.6 GeV, 19.4 GeV, 62.4 GeV.

2.4.2 The problem with transverse SSAs

The conceptual simplicity of A_N contrasts with the complexity of the theoretical analysis. In fact, an explanation for the large values observed for this asymmetry has represented a challenge for theoretical spin physics over the last decades. The reason for this is that the asymmetry for an inclusive process like $A^\uparrow B \to h X$ is related to effects that go beyond the leading-twist framework based on a collinear factorization theorem, where cross sections can be written as convolutions of leading-twist parton distributions, fragmentation functions, and hard elementary cross sections, and where observables are not sensitive to intrinsic transverse parton momentum, $k_\perp$. This can be seen by considering the difference of cross sections with opposite spin polarization of hadron A

$$\mathrm{d}\sigma^\uparrow - \mathrm{d}\sigma^\downarrow = \sum_{abcd;s_a s_c} \Delta_T f_{a/A}(x_a,s_a) \otimes f_{b/B}(x_b) \otimes [\mathrm{d}\hat{\sigma}^\uparrow - \mathrm{d}\hat{\sigma}^\downarrow] \otimes D_{h/c}(z). \tag{2.59}$$

The above equation involves the convolution of

- the transversity distribution

$$\Delta_T f_{a/A}(x_a) = f_{a_+/A^\uparrow}(x_a) - f_{a_+/A^\downarrow}(x_a) = f_{a_+/A^\uparrow}(x_a) - f_{a_-/A^\uparrow}(x_a), \tag{2.60}$$

  which is suppressed for the process considered, where only one proton (beam or target) is transversely polarized, since pQCD interactions conserve chirality. This leads to power suppressions of A_N,

- the difference of cross sections $[\mathrm{d}\hat{\sigma}^\uparrow - \mathrm{d}\hat{\sigma}^\downarrow]$ for the elementary hard scattering of quarks a and b, which at leading order, is related to the partonic asymmetry $\hat{a}_N$ [72]

$$\hat{a}_N \equiv \frac{\mathrm{d}\hat{\sigma}^\uparrow - \mathrm{d}\hat{\sigma}^\downarrow}{\mathrm{d}\hat{\sigma}^\uparrow - \mathrm{d}\hat{\sigma}^\downarrow} \propto \alpha_S \frac{m_q}{\sqrt{s}} \underset{m_q=0}{\longrightarrow} 0, \tag{2.61}$$

  which strongly depends on the strong coupling constant, α_S and the mass m_q of the quarks, and since it is inversely proportional to the energy of the collision, it should vanish at high energies,

- a fragmentation function $D_{h/c}(z)$ which, if assumed to be independent of the spin of the partons, $D_{h/c}(z, s_c) = D_{h/c}(z, -s_c) \equiv D_{h/c}(z)$, cancels in the cross section ratio.

For transversity to contribute, the hard-scattering functions need to involve a transversely polarized quark scattering off an unpolarized quark, for which the hard-scattering cross section vanishes. In addition, a non-vanishing SSA requires the presence of a relative interaction phase between the interfering amplitudes for the different helicities. At leading twist, this phase can only arise through loop corrections, which are of high order in α_S and thus lead to a further suppression.

For a long time, it was believed that this small asymmetry at partonic level $\hat{a}_N$ should also translate into a vanishing asymmetry at hadronic level A_N [72]. Following this reasoning, the observation of a large transverse SSA was signaled by the authors of Ref. [72], as either an indication that QCD is not valid in this region, or it cannot be applied perturbatively because α_S turns out to be too large, or "conceivable, something is wrong with the present formulation of QCD itself". The failure of Eq. (2.59) in explaining transverse SSAs indicates the limitation of the collinear factorization in QCD at leading twist, and the need to look for other alternatives.

Explanations for A_N There are three different scenarios in which this situation can be improved, related to the three factorized terms of Eq. (2.59)

(i) Use transverse momentum dependent PDFs $f_{a/A^\uparrow}(x_a, \mathbf{k}_\perp)$. Within the parton model, considering only the elementary interaction $qq \to qq$ at leading order, the final $\mathbf{p}_T$ of the hadron can originate from the transverse intrinsic motion of partons $\mathbf{k}_\perp$.

(ii) Take higher order pQCD corrections like $qq \to qqg$ or $qg \to qq\bar{q}$ in the elementary cross section, which also leads to hadrons produced at large $\mathbf{p}_T$.

(iii) Consider a spin-dependent fragmentation process, in which the final hadron obtains a transverse motion respect to the direction of the fragmenting quark.

The calculation of A_N including next-to-leading order terms in the elementary cross-section – case *(ii)*, leads to a partonic asymmetry $\hat{a}_N$ still negligible at high energies [73]. Note that, in a purely collinear configuration, the struck quark would fragment only in the forward direction, which strongly suppresses by rotational invariance any transverse momentum dependent asymmetry [85].

The cases *(i)* and *(iii)* were first considered by Sivers [74] and Collins [75], respectively, and imply taking into account $k_\perp$-dependent parton distribution and fragmentation functions. Such observables can be accessed in semi-inclusive DIS (SIDIS) scattering, characterized by a large scale Q^2, and by a smaller transverse momentum $p_{h\perp}$ of the produced hadron. In this case, one can prove a factorization theorem for the spin-dependent part of the cross section into $k_\perp$-dependent functions describing the distribution of quarks and gluons in the polarized proton and that of hadrons in the fragmenting partons, and a partonic hard-scattering cross section that can be calculated in pQCD. Large transverse SSAs can be obtained this way, present at leading twist (i.e., not power suppressed). This is discussed in more detail in Section 2.6.

A non-vanishing asymmetry A_N can also be obtained in collinear QCD (where the intrinsic motion of the partons is ignored) by taking into account higher-twist contributions. A collinear factorization theorem can then be proven in terms of quark-gluon correlation functions for single inclusive processes, like $p^\uparrow p \to h X$, where the only hard scale is the transverse momentum of the detected hadron p_T. The transverse SSA in such case is power-suppressed by $1/p_T$. The calculation of A_N at twist-3 was done by Qiu and Sterman [77], and is briefly considered in Section 2.7.

In the next section, the process of semi-inclusive deep-inelastic scattering (SIDIS) is described, which provides a convenient framework in order to study the intrinsic partonic motion and related transverse-spin effects.

2.5 Semi-inclusive DIS

A one-particle semi-inclusive DIS reaction is shown in Fig. 2.9. In addition to the scattered lepton[27], detected with momentum k', one of the outgoing hadrons, resulting from the fragmentation of the proton, is detected with momentum p_h. All other reaction products (X) are undetected. In the following, we consider only correlations between the scattered lepton and *one* detected hadron, i.e., between the angles ϕ_S and ϕ_h. In practice, events with more than one hadron in the final state are usually detected, in which case only angular correlations between the lepton and each one of the hadrons are considered separately. [28]

[27] Now k is again the lepton variable!

[28] Although not considered here, the case of two-hadron SIDIS can also be used to access the transversity distribution [80].

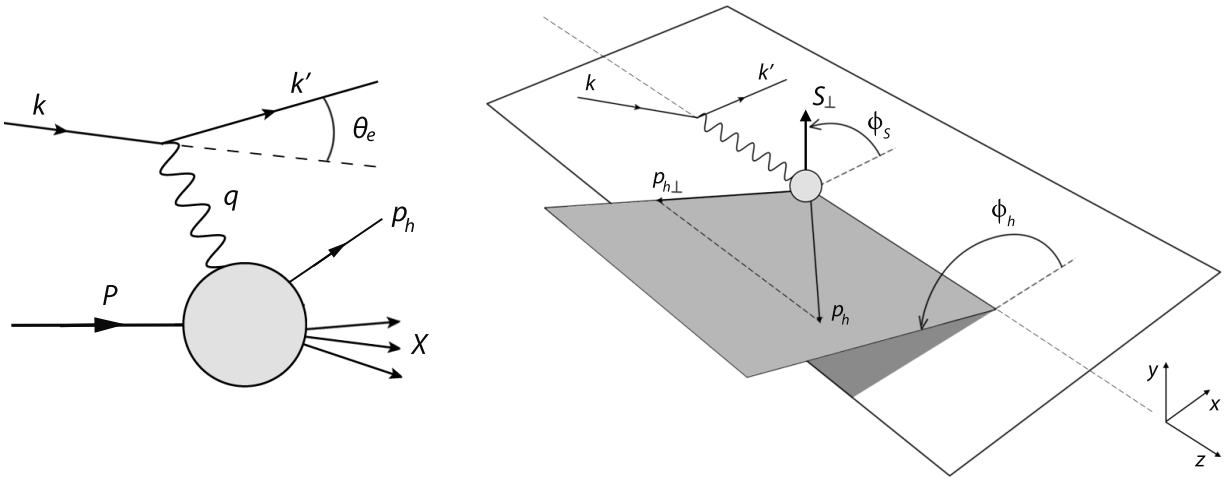

Figure 2.9. Schemmatic diagram and reaction plane in semi-inclusive DIS.

2.5.1 Kinematics

In addition to the DIS observables, described in Section 2.1.1, additional variables are needed to characterize the hadron detected in the final state with momentum $p_h = (E_h, \mathbf{p}_\mathrm{h})$. As $\mathbf{p}_h$ can point in any direction, it is better to work with its longitudinal and perpendicular components defined with respect to the virtual photon momentum $\mathbf{q}$, since this determines the direction of the Lorentz boost. One then has the following three variables

- z, which indicates the longitudinal fraction of the energy transferred to the proton carried by the final state hadron

$$z = \frac{P \cdot p}{P \cdot q} \overset{\text{lab}}{=} \frac{E_h}{\nu}, \tag{2.62}$$

  and therefore can be in the range $z \in [0, 1]$,

- $\mathbf{p}_{h\perp}$, the transverse component of the hadron momentum with respect to $\mathbf{q}$,

- ϕ_h, the azimuthal angle around the direction of the virtual photon, defined between the lepton scattering plane and the hadron direction, see Fig. 2.9, as

$$\phi_h = \frac{\mathbf{q} \times \mathbf{k} \cdot \mathbf{p}_\mathrm{h}}{|\mathbf{q} \times \mathbf{k} \cdot \mathbf{p}_\mathrm{h}|} \cos^{-1} \frac{\mathbf{q} \times \mathbf{k} \cdot \mathbf{q} \times \mathbf{p}_\mathrm{h}}{|\mathbf{q} \times \mathbf{k}||\mathbf{q} \times \mathbf{p}_\mathrm{h}|}. \tag{2.63}$$

2.5.2 Cross section

Similarly to the case of inclusive DIS, a full analytical expression for the differential SIDIS cross section cannot be written out explicitely, but it can be decomposed in terms of several polarized and unpolarized structure functions. For the general case of a polarized proton target with spin vector $\mathbf{S}$, where $\mathbf{S}_\parallel$ is the longitudinal component and $\mathbf{S}_\perp$ is the transverse

component, relative to the virtual photon direction, one finds [81]

$$\begin{aligned}\frac{\mathrm{d}\sigma}{\mathrm{d}x\,\mathrm{d}y\,\mathrm{d}\phi_S\,\mathrm{d}z_h\,\mathrm{d}\phi_h\,\mathrm{d}p_{h\perp}^2} \propto \Big\{ & F_{UU,T} + \epsilon\, F_{UU,L} + \epsilon\, \cos(2\phi_h)\, F_{UU}^{\cos 2\phi_h} \\ & + |\mathbf{S}_\parallel|\, \epsilon\, \sin(2\phi_h)\, F_{UL}^{\sin 2\phi_h} + |\mathbf{S}_\parallel|\, \lambda_e \sqrt{1-\epsilon^2}\, F_{LL} \\ & + |\mathbf{S}_\perp| \Big[\sin(\phi_h - \phi_S) \left(F_{UT,T}^{\sin(\phi_h-\phi_S)} + \epsilon\, F_{UT,L}^{\sin(\phi_h-\phi_S)} \right) \\ & \quad + \epsilon\, \sin(\phi_h + \phi_S)\, F_{UT}^{\sin(\phi_h+\phi_S)} + \epsilon\, \sin(3\phi_h - \phi_S)\, F_{UT}^{\sin(3\phi_h-\phi_S)} \Big] \\ & + |\mathbf{S}_\perp|\, \lambda_e \sqrt{1-\epsilon^2}\, \cos(\phi_h - \phi_S)\, F_{LT}^{\cos(\phi_h-\phi_S)} + \dots \Big\}. \end{aligned} \tag{2.64}$$

Here, the subscripts of the structure functions $F_{\mathrm{x\,y,z}}$ indicate the longitudinal (L) or transverse (T) polarizations of the beam and target, respectively, or if these are unpolarized (U); the third subscript indicates the polarization of the virtual photon. The variable ϵ is the degree of longitudinal polarization of the virtual photon, and λ_e is the helicity of the electron. See Eq. (2.7) of Ref. [81] for more details. Note that the DIS cross section formula in Eq. (2.10a) can be obtained from Eq. (2.64) by performing the integrals over $\mathbf{p}_{h\perp}$ and z and summing over all hadrons in the final state [81].

2.5.3 Fragmentation correlator

In Section 2.3.2, the formalism to study the interaction of the virtual photon with the quarks was presented. This formalism can be extended to take into account the final state fragmentation of the nucleon into hadrons. The tree-level Feynman amplitude in this case is[29]

$$\mathcal{M}^\mu = A_h(k'; p_h, s_h)\gamma^\mu A_q(k; P, S), \tag{2.65}$$

where the free quark spinor is now replaced by a matrix element describing the a-priori unknown fragmentation of the quark into a hadron with momentum p_h and spin S_h

$$A_q(k'; p_h, s_h) = \langle 0|\, \psi(0)\, |p_h, s_h, X\rangle. \tag{2.66}$$

Similarly to Eq. (2.41), the hadronic tensor now includes a new soft structure $\Delta(k'; p_h, s_h)$

$$2M\,W^{\mu\nu} = \sum_q e_q^2 \int \frac{\mathrm{d}^4 k}{(2\pi)^4} \int \frac{\mathrm{d}^4 k'}{(2\pi)^4}\, \delta^4(k + q - k')\, \mathrm{Tr}[\Phi\, \gamma^\mu\, \Delta\, \gamma^\nu]\,, \tag{2.67}$$

see also Fig. 2.10. The $\Delta(k'; p_h, s_h)$ is the *fragmentation correlator* defined as [34]

$$\begin{aligned}\Delta_{ij}(k'; p_h, s_h) \;=\; & \sum_X \int \frac{\mathrm{d}^3\mathbf{P}_X}{(2\pi)^3\, 2E_X} \int \mathrm{d}^4\xi\, e^{ik'\cdot\xi} \\ & \times \langle 0|\, \psi_i(\xi)\, |p_h, s_h, X\rangle\langle p_h, s_h, X|\bar{\psi}_j(0)|0\rangle. \end{aligned} \tag{2.68}$$

[29] From now on, k and k' are used again to denote the quarks momenta before and after absorbing the virtual photon, respectively.

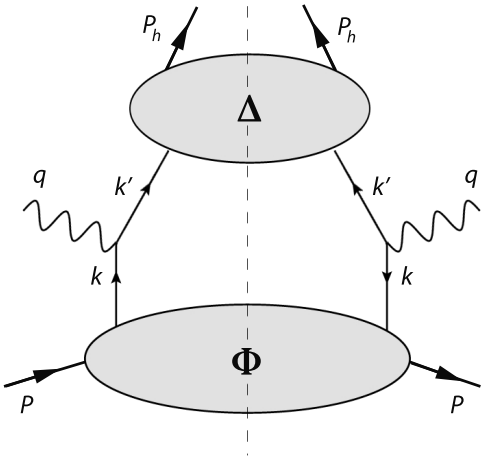

Figure 2.10. Diagram showing the factorization of semi-inclusive DIS.

In the collinear case, where both $\mathbf{k}_T = 0$ and $\mathbf{k}'_T = 0$, the momenta of the quarks in the initial and final state can be represented by their "plus" and "minus" components, respectively

$$k^+ = xP^+, \qquad k'^- = p_h^-/z, \tag{2.69}$$

the fragmentation matrix can be expressed as the sum of three-leading twist fragmentation functions

$$\Delta(z) = \frac{1}{2}\left\{D(z)\,\not{p}_h + S_{hL}\,\Delta D(z)\,\gamma_5\not{p}_h + \Delta_T D(z)\,\not{p}_h\gamma_5\not{s}_{hT}\right\}. \tag{2.70}$$

These functions are absent in inclusive DIS, where none of the produced hadrons are detected; they play, however, an important role in SIDIS. The *unpolarized* fragmentation function $D(z) \equiv D_q^h$ describes the number density of hadrons of type h with longitudinal momentum fraction z in the fragmenting quark. For spinless hadrons in the final state, e.g., pions, the hadronization processes is described by just this function. The other two fragmentation functions, $\Delta D(z)$ and $\Delta_T D(z)$, are related to the production of hadrons with spin polarization, e.g., in the case of spontaneous polarization of Lambda particles [83].

The fragmentation functions are related to the probability $\mathcal{N}_{h/q}$ of finding a hadron with longitudinal momentum fraction z inside a quark q, depending of the polarization states [34]

$$D(z) = \mathcal{N}_{h/q}(z), \tag{2.71a}$$
$$\Delta D(z) = \mathcal{N}_{h/q+}(z) - \mathcal{N}_{h/q-}(z), \tag{2.71b}$$
$$\Delta_T D(z) = \mathcal{N}_{h/q\uparrow}(z) - \mathcal{N}_{h/q\downarrow}(z). \tag{2.71c}$$

Experimental determination Fragmentation functions are mostly determined from cross section measurements in e^+e^- annihilation data, in which one hadron is detected in the final state, coming from photon or Z-boson decay [84]

$$\frac{\sigma^h}{\sigma_{\text{total}}} \equiv F^h(x,s) = \sum_q \int_x^1 \frac{\mathrm{d}z}{z} C_q\, D_{h/q}(x/z, s), \tag{2.72}$$

where $\sigma^h \equiv \mathrm{d}\sigma^{e^+e^-\to\gamma(Z)\to hX}/\mathrm{d}x$, F^h are the *hadron* fragmentation functions, and the coefficients C_q are related to the electroweak coupling, or to the squared parton charge e_q^2 if weak effects can be neglected. The absence of hadrons in the initial state make the e^+e^- processes very suitable for a clean determination of the parton FFs, although it is only sensitive to combinations of $D_{h/q} + D_{h/\bar{q}}$ via $\gamma(Z) \to q\bar{q} \to h + X$.

In semi-inclusive DIS, information about $D_{h/q}$ can be obtained from an unpolarized cross section measurement

$$\frac{\mathrm{d}^3\sigma^h}{\mathrm{d}x\,\mathrm{d}z\,\mathrm{d}Q^2}(x,z,Q^2) \propto \sum e_q^2 q(x,Q^2) D_{h/q}(z,Q^2), \tag{2.73}$$

which requires knowledge on the unpolarized quark distributions $q(x,Q^2)$. See, e.g., Ref. [82].

2.6 Parton model with intrinsic momentum

There is enough evidence, both theoretical and experimental, to consider the intrinsic transverse motion of quarks inside the nucleon [85]

- Since the size of the nucleon is about 1 fm, an intrinsic transverse momentum of the quarks of about $\langle k_\perp \rangle \sim 0.2$ GeV is allowed by the Heisenberg uncertainty principle.
- The radiation of gluons by massless collinear quarks naturally introduces a transverse motion (cf. Sec. 2.3).
- The production of hadrons in SIDIS processes with respect to the virtual photon direction is clearly non-collinear, and hadrons with large transverse momentum are observed.
- The process of hadronization of quarks into jets has also been observed to be non-collinear.
- The experimental observation of the Cahn effect [86], which predicts a $\cos\phi_h$ dependence of the elementary cross section $eq \to eq$ in unpolarized SIDIS processes. This angular dependence originates from the angle of the vector $\mathbf{k}_\perp$, vanishing when $k_\perp = 0$, and has been observed experimentally [87] in SIDIS processes. A fit to the data assuming a Gaussian $k_\perp$ dependence of the PDFs gives $\langle k_\perp \rangle = 0.25$ GeV, as expected from elementary arguments.

The quark transverse motion cannot be accessed in inclusive DIS, given the impossibility of the scattered lepton to "remember" that information. In a SIDIS reaction, with at least one of the produced hadrons detected in coincidence with the lepton, the transverse momentum of the hadron $\mathbf{p}_{h\perp}$ can be related to $\mathbf{k}_\perp$. The factorization of the cross section for SIDIS can be expressed as

$$\mathrm{d}\sigma^{\,ep\to ehX} = \sum_q f_q(x,\mathbf{k}_\perp;Q^2) \otimes \mathrm{d}\hat{\sigma}^{eq\to eq}(y,\mathbf{k}_\perp;Q^2) \otimes D_{h/q}(z,\mathbf{p}_{h\perp};Q^2). \tag{2.74}$$

Here, the $f_q(x, \mathbf{k}_\perp; Q^2)$ correspond to Transverse-Momentum Dependent parton distribution functions (TMDs), and the $D_{h/q}(z, \mathbf{p}_{h\perp}; Q^2)$ to fragmentation functions (FFs) describing the hadronization of a quark q into a hadron h carrying a longitudinal momentum fraction z of the virtual photon's momentum. Both types of functions are usually referred to as TMDs.

2.6.1 TMDs

The TMDs contain information on the intrinsic motion of quarks and gluons inside a fast moving proton. Moreover, they indicate *correlations* between the spin $\mathbf{S}$ and momentum $\mathbf{P}$ of the proton, the spin $\mathbf{s}_q$ and transverse momentum $\mathbf{k}_\perp$ of the partons, and/or the spin $\mathbf{s}_h$ and transverse momentum $\mathbf{p}_{h\perp}$ of the hadrons in the final state.

Sivers The first TMD was historically introduced by Dennis Sivers in 1990 [74] as a possible explanation for the transverse asymmetry A_N observed in the inclusive production of pions from hadronic collisions (see Section 2.4.1). Sivers proved that if the unpolarized partons inside a transversely polarized proton could have an asymmetric $\mathbf{k}_\perp$ distribution

$$f_{q/p^\uparrow}(x, \mathbf{k}_\perp) \neq f_{q/p^\uparrow}(x, -\mathbf{k}_\perp) = f_{q/p^\downarrow}(x, \mathbf{k}_\perp), \tag{2.75}$$

this would lead to a correlation between the transverse momentum of unpolarized partons and the transverse spin of the nucleon. Such correlation can only be of the form

$$\mathbf{S} \cdot (\hat{\mathbf{P}} \times \hat{\mathbf{k}}_\perp), \tag{2.76}$$

since this is the only combination of these three vectors that conserves parity.

> *Under parity transformation, the momenta of the proton and quark change respectively as* $\mathcal{P}(\hat{\mathbf{P}}) = -\hat{\mathbf{P}}$ *and* $\mathcal{P}(\hat{\mathbf{k}}_\perp) = -\hat{\mathbf{k}}_\perp$*, while the spin is a pseudo-vector and therefore gives* $\mathcal{P}(\mathbf{S}) = \mathbf{S}$*; this can also seen considering that the spin changes as an angular momentum* $\mathbf{L} = (\mathbf{r} \times \mathbf{p}) \to (-\mathbf{r}) \times (-\mathbf{p}) = \mathbf{r} \times \mathbf{p}$*.*

This asymmetric distribution of quarks leads to a new reinterpretation of the unpolarized parton distribution function inside a transversely polarized proton

$$f_{q/p^\uparrow}(x, \mathbf{k}_\perp) = f_{q/p}(x, k_\perp) + \frac{1}{2}\Delta^N f_{q/p^\uparrow}(x, k_\perp)\, \mathbf{S} \cdot (\hat{\mathbf{P}} \times \hat{\mathbf{k}}_\perp). \tag{2.77}$$

Here, the $\Delta^N f_{q/p^\uparrow}$ is the so-called Sivers function, also sometimes found in the literature as $f_{1T}^\perp = -\Delta f^N_{q/p^\uparrow} M/2|\mathbf{k}_\perp|$.

$$\begin{aligned} \Delta f_{q/p^\uparrow}(x, \mathbf{k}_\perp) &= f_{q/p^\uparrow}(x, \mathbf{k}_\perp) - f_{q/p^\uparrow}(x, -\mathbf{k}_\perp) \\ &\equiv \Delta^N f_{q/p^\uparrow}(x, k_\perp)\, \mathbf{S}_\perp \cdot (\hat{\mathbf{P}} \times \hat{\mathbf{k}}_\perp) \\ &= -2\,\frac{k_\perp}{M}\, f_{1T}^\perp(x, k_\perp)\, \mathbf{S}_\perp \cdot (\hat{\mathbf{P}} \times \hat{\mathbf{k}}_\perp)\,. \end{aligned} \tag{2.78}$$

The Sivers distribution function leads to sizable transverse SSAs, present at leading-twist. These are discussed, as measured from HERMES data, together with an interpretation of the Sivers effect, in Section 2.6.2.

Collins The second TMD was introduced in 1993 by John Collins [75], now, in the quark fragmentation scheme. Following the works initiated by Efremov *et al.* [76], Collins proposed a new way of determining the transverse polarization state of a parton undergoing a hard scattering, i.e., as a tool to measure the transversity distribution, which in turn could also explain the origin of large transverse SSAs. For this purpose, Collins pointed out the relevance of polarized SIDIS reactions. He showed how a spin transfer from a *transversely* polarized quark to an *unpolarized* (or spinless) hadron should lead to a significant azimuthal asymmetry in the distribution of hadrons in the transverse plane. Such effect would manifest itself at *leading* twist, described by a function

$$\Delta D_{h/q^\uparrow}(z, \mathbf{k}'_\perp) \equiv D_{h/q^\uparrow}(z, \mathbf{k}'_\perp) - D_{h/q^\uparrow}(z, -\mathbf{k}'_\perp), \tag{2.79}$$

$$\text{with} \qquad D_{h/q^\uparrow}(z, -\mathbf{k}'_\perp) = D_{h/q^\downarrow}(z, \mathbf{k}'_\perp), \tag{2.80}$$

leading to a non-zero $\Delta D_{h/q^\uparrow}$. This function, now called the Collins function, appears in the fragmentation function for an *unpolarized* hadron generated in the fragmentation of a *polarized* quark due to a correlation between the spin $\mathbf{s}_q$ of the fragmenting quark, its momentum $\mathbf{p}_q$, and the transverse momentum of the produced hadron $\mathbf{p}_{h\perp}$

$$D_{h/q^\uparrow}(z, \mathbf{k}'_\perp) = D_{h/q}(z, \mathbf{k}'_\perp) + \frac{1}{2}\,\Delta D_{h/q^\uparrow}(z, \mathbf{k}'_\perp)\,(\hat{\mathbf{p}}_q \times \hat{\mathbf{p}}_{h\perp}) \cdot \mathbf{s}_q. \tag{2.81}$$

This (again) is the only possible combination of these three vectors conserving parity. Notice the similarity with Eq. (2.77). Another common notation for the Collins function is $H_1^\perp = z m_h\, \Delta D_{h/q^\uparrow}/2p_{h\perp}$, with m_h the mass of the produced hadron.

$$\begin{aligned} \Delta D_{h/q^\uparrow}(z, \mathbf{k}'_\perp) &= D_{h/q^\uparrow}(z, \mathbf{k}'_\perp) - D_{h/q^\downarrow}(z, \mathbf{k}'_\perp) \\ &\equiv \Delta^N D_{h/q^\uparrow}(z, k'_\perp)\, \mathbf{s}_q \cdot (\hat{\mathbf{p}}'_q \times \hat{\mathbf{k}}'_\perp) \\ &= \frac{2\,k_\perp}{z\,m_h} H_1^\perp(z, k'_\perp)\, \mathbf{s}_q \cdot (\hat{\mathbf{p}}'_q \times \hat{\mathbf{k}}'_\perp)\,, \end{aligned} \tag{2.82}$$

Note that here $\mathbf{k}'_T$ is defined with respect to the direction of the produced hadron. A more extended discussion on the Collins fragmentation function is given in Section 2.6.2.

Leading-twist TMDs These and other TMDs can be formally derived from the quark correlator Φ, defined in Eq. (2.40). By means of combinations of the Dirac matrices γ^+, γ_5 and σ_{+j}, expanding the correlator in powers of $1/Q^2$ and taking only the leading order, the following terms contributing to Φ can be selected [88]

$$\frac{1}{2}\,\mathrm{Tr}\left[\gamma^+\,\Phi(x, \mathbf{k}_\perp, \mathbf{S})\right] = f_1(x, k_\perp) - \frac{\epsilon^{jk}\,k_\perp^j\,S_T^k}{M}\,f_{1T}^\perp(x, k_\perp), \tag{2.83}$$

$$\frac{1}{2}\,\mathrm{Tr}\left[\gamma^+\gamma_5\,\Phi(x, \mathbf{k}_\perp, \mathbf{S})\right] = S_L\,g_1(x, k_\perp) + \frac{\mathbf{k}_\perp \cdot \mathbf{S}_\perp}{M} g_{1T}(x, k_\perp), \tag{2.84}$$

$$\begin{aligned} \frac{1}{2}\,\mathrm{Tr}\left[i\sigma^{j+}\gamma_5\,\Phi(x, \mathbf{k}_\perp, \mathbf{S})\right] &= S_\perp^j\,h_1(x, k_\perp) + S_L\,\frac{k_\perp^j}{M}\,h_{1L}^\perp(x, k_\perp) \\ &\quad + \frac{(k_\perp^j\,k_\perp^k - \frac{1}{2}\,\mathbf{k}_\perp^2\,\delta^{jk})S_\perp^k}{M^2}\,h_{1T}^\perp(x, k_\perp) \\ &\quad + \frac{\epsilon^{jk}\,k_\perp^k}{M}\,h_1^\perp(x, k_\perp), \end{aligned} \tag{2.85}$$

leading to a total of eight *leading-twist* TMDs:

- $f_1(x, k_\perp)$ is the **unpolarized**, $k_\perp$-dependent momentum distribution of partons inside a nucleon. Integrated over $k_\perp$ this is the unpolarized PDF, $q(x)$ for quarks (and $g(x)$ for gluons).
- $g_1(x, k_\perp)$ is the $k_\perp$-dependent **helicity** distribution, relating partons with opposite spin along the direction of motion in a nucleon longitudinally polarized. The integrated version corresponds to $\Delta q(x)$ and $\Delta g(x)$, discussed in Sections 2.2.1 and 2.3.2.
- $h_1(x, k_\perp)$ is the **transversity** distribution of quarks with opposite transverse spin direction inside a nucleon with transversely polarized spin. As in the $k_\perp$-integrated case, there is no transversity distribution of gluons in a spin 1/2 hadron.
- $f_{1T}^\perp(x, k_\perp)$ is the **Sivers** function, related to the momentum distribution of *unpolarized* partons q inside a transversely *polarized* proton $p^\uparrow$, which links the parton intrinsic motion $k_\perp$ to the proton momentum and spin in the way given by Eq. (2.77). In semi-inclusive DIS, the Sivers effect leads to an azimuthal asymmetric distribution of the hadrons produced, and represents a clear indication of parton orbital motion. This effect has been observed by the HERMES [91] and COMPASS [92] collaborations.
- $h_1^\perp$ is the **Boer-Mulders** function [93], which describes the momentum distribution of *transversely polarized quarks* inside an *unpolarized* proton

$$f_1(x, \mathbf{k}_\perp; \mathbf{s}_q) = \frac{1}{2} f_1(x, k_\perp) - \frac{k_\perp}{2M} h_1^\perp(x, k_\perp)\, \mathbf{s}_q \cdot (\hat{\mathbf{P}} \times \hat{\mathbf{k}}_\perp) \,. \tag{2.86}$$

  This function singles out polarized quarks in unpolarized nucleons and therefore might give rise to unexpected spin effects in unpolarized processes. A spin asymmetry originating from $h_1^\perp$ was recently measured by the HERMES collaboration [94].
- The other TMDs appearing in Eq. (2.83) – (2.85) are related to double spin correlations in the PDFs: $g_{1T}(x, k_\perp)$ indicates the distribution of longitudinally polarized partons in a transversely polarized proton, $h_{1L}^\perp(x, k_\perp)$ the amount of transversely polarized quarks in a longitudinally polarized proton, and $h_{1T}^\perp(x, k_\perp)$ of transversely polarized quarks in a proton polarized transversely but in a different direction. At leading twist, these three functions can be expressed approximately in terms of the other TMDs, and have rather a secondary role.

The partonic picture of the leading-twist TMDs is summarized in Fig. 2.11. At higher twist, the corresponding TMDs appear in observables which are suppressed by inverse powers of Q^2 and are therefore less likely to be measured. After integration over $k_\perp$, these eight functions lead to the three leading-twist PDFs of Eqs. (2.47)-(2.49).The notation used here to denote TMDs follows the one in Ref. [37]. See also the Trento conventions [38].

In addition to the spin-$k_\perp$ correlations given by these eight TMDs, similar correlations can occur in the fragmentation of a quark with spin vector $\mathbf{s}_q$ and momentum $\mathbf{k}_q$ into a hadron. In this case, the fragmentation of a quark into an unpolarized hadron is described by two independent leading-twist transverse-momentum dependent fragmentation functions

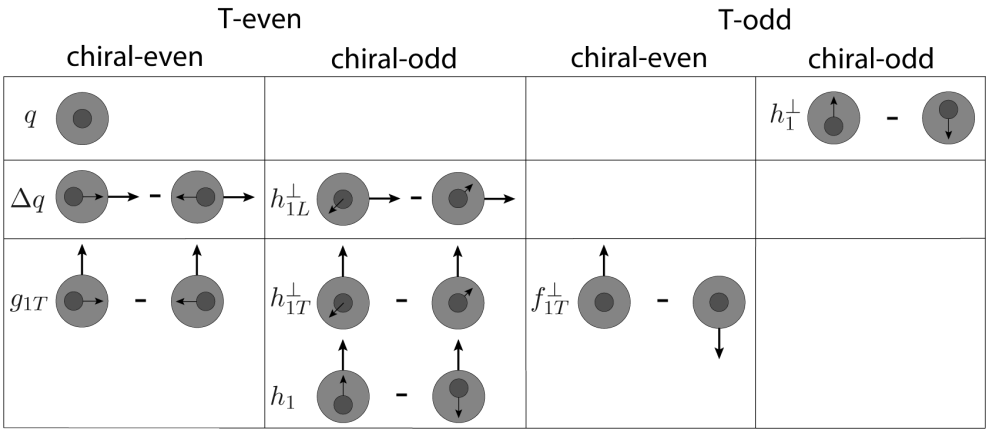

Figure 2.11. Partonic interpretation of the eight unintegrated leading-twist TMDs. Nucleon and quark are represented with the light and dark circles, respectively. The arrows indicate their spin orientations with respect to the virtual photon direction, which is assumed to enter the figure from the left side.

- $D_{1h}^q(z, \mathbf{p}_{h\perp})$ (also denoted as $D_{h/q}$) is the unpolarized, $p_{h\perp}$ dependent, **fragmentation** function describing the fragmentation of a parton a into a hadron h independently of the spins. Its $p_{h\perp}$-integrated version is $D_{1h}^q(z) = \int d^2\mathbf{p}_{h\perp}\, D_{1h}^q(z, \mathbf{p}_{h\perp})$.
- $H_1^{\perp q}(z, \mathbf{p}_{h\perp})$ is the **Collins** function, describing the fragmentation of a transversely polarized quark into an unpolarized hadron, in the only possible way given by Eq. (2.81). The Collins effect leads as well to an azimuthal SSA in SIDIS. This was observed by the HERMES collaboration [95] and also by the COMPASS collaboration [92].
- Another six leading-twist fragmentation functions should exist, equivalent to the TMDs of Fig. 2.11, given the similarity of the formalisms describing both sets of functions. These could, in principle, be measured in future or ongoing experiments.

Chirality An important feature of some of the TMDs is that they change the helicity (or *chirality*) of the partons in the reaction. This is the case for the transversity function h_1, the Boer-Mulders function $h_1^\perp$ and the Collins fragmentation function $H_1^\perp$. For these reason, these distribution functions are called to be **chiral-odd**, in contrast to the *chiral-even* TMDs, that conserve chirality. Since the total chirality of the SIDIS reaction must be conserved, in the scheme of Eq. (2.74) a chiral-odd PDF (h_1 or $h_1^\perp$) must always appear accompanied by a chiral-odd fragmentation function ($H_1^\perp$) (see right-hand side of Fig. 2.7) or another chiral-odd PDF (see left-hand side of Fig. 2.7). An example of chiral-even PDF is the Sivers function $f_{1T}^\perp$, which therefore can be convoluted with the chiral-even unpolarized fragmentation function D_1. Such correspondences can be further seen in Eqs. (2.88 – 2.91).

Applicability of TMDs The factorization of the SIDIS cross section into TMDs has been only proven for the kinematic range in which the transverse momentum of the hadron $p_{h\perp}$ is small in comparison to the Q^2 scale of the reaction

$$p_{h\perp} \simeq \Lambda_{QCD} \ll Q. \tag{2.87}$$

If $p_{h\perp}$ is small (i.e., in the presence of a soft scale) the hadronization processes can be considered along the same direction as the quark motion, which simplifies the calculation of the contribution from the unintegrated PDFs. For hadrons with larger transverse momentum, however, other mechanisms might become significant, arising from quark-gluon correlations and higher pQCD contributions [89]. The hard scale (large Q^2), on the other hand, guarantees that one remains in the region of validity of the QCD parton model.

TMD factorization in one-scale processes The situation is different for processes where only one scale is present, e.g., in the inclusive detection of hadrons from $e\,p^\uparrow$ or $p^\uparrow\,p$ reactions. A large-enough hadron transverse momentum is needed to ensure a large momentum transfer. In the case of $e\,p$ production, discussed in Section 2.8, the ratio p_T^2/Q^2 should in addition be kept small to guarantee the applicability of the TMDs.

TMD factorization for such processes was first suggested by Sivers [74] and then phenomenologically adopted [96] to reproduce the large values of A_N measured by the E704 collaboration [8], and in Ref [97] for the RHIC data [98]. However, a definite proof of the validity of the TMD factorization for hadronic processes with only one scale is still lacking [89]. Several alternatives have been proposed in this regard.

In particular, in Ref. [89], a phenomenological test of the TMD factorization for processes with just one large scale was proposed by considering the spin asymmetries in inclusive electroproduction of hadrons, $ep^\uparrow \to hX$, where only one hadron (and not the scattered beam lepton) is detected in the final state. Given the impossibility of reconstructing the direction $\mathbf{q}$ of the virtual photon, such analysis must be performed in the $e-p$ center-of-mass frame. In this case, the transverse momentum of the outgoing hadron $\mathbf{p}_T$ is defined with respect to the beam direction, in contrast to $\mathbf{p}_{h\perp}$, defined with respect to the γ^* direction. Such an analysis is a close analogue to that for $p^\uparrow p \to hX$ processes, with the advantage that it is a cleaner channel, involving only the parton distributions of the polarized proton, while using a point-like electromagnetic probe. This is covered in Section 2.8 in more detail.

SIDIS structure functions revisited In the kinematic region where the TMDs are defined, the structure functions of the SIDIS cross section in Eq. (2.64) become, for the case of an spinless (or unpolarized) outgoing hadron [90]

$$F_{UU} \sim \sum_q e_q^2\, f_1 \otimes D_1 \qquad F_{LT}^{\cos(\phi_h-\phi_S)} \sim \sum_q e_q^2\, g_{1T} \otimes D_1\,, \tag{2.88}$$

$$F_{LL} \sim \sum_q e_q^2\, g_1 \otimes D_1 \qquad F_{UT}^{\sin(\phi_h-\phi_S)} \sim \sum_q e_q^2\, f_{1T}^\perp \otimes D_1\,, \tag{2.89}$$

$$F_{UU}^{\cos(2\phi_h)} \sim \sum_q e_q^2\, h_1^\perp \otimes H_1^\perp \qquad F_{UT}^{\sin(\phi_h+\phi_S)} \sim \sum_q e_q^2\, h_1 \otimes H_1^\perp\,, \tag{2.90}$$

$$F_{UL}^{\sin(2\phi_h)} \sim \sum_q e_q^2\, h_{1L}^\perp \otimes H_1^\perp \qquad F_{UT}^{\sin(3\phi_h-\phi_S)} \sim \sum_q e_q^2\, h_{1T}^\perp \otimes H_1^\perp\,. \tag{2.91}$$

This factorization of the structure functions as a convolution of TMDs holds *only* in the parton model approximation. Most analyses of TMDs performed to date are based on this assumption, providing a quite satisfactory general view of their features. However, for

studies involving a higher precision, i.e., higher energy, radiation of soft gluons should be included [90], which modifies the above expressions.

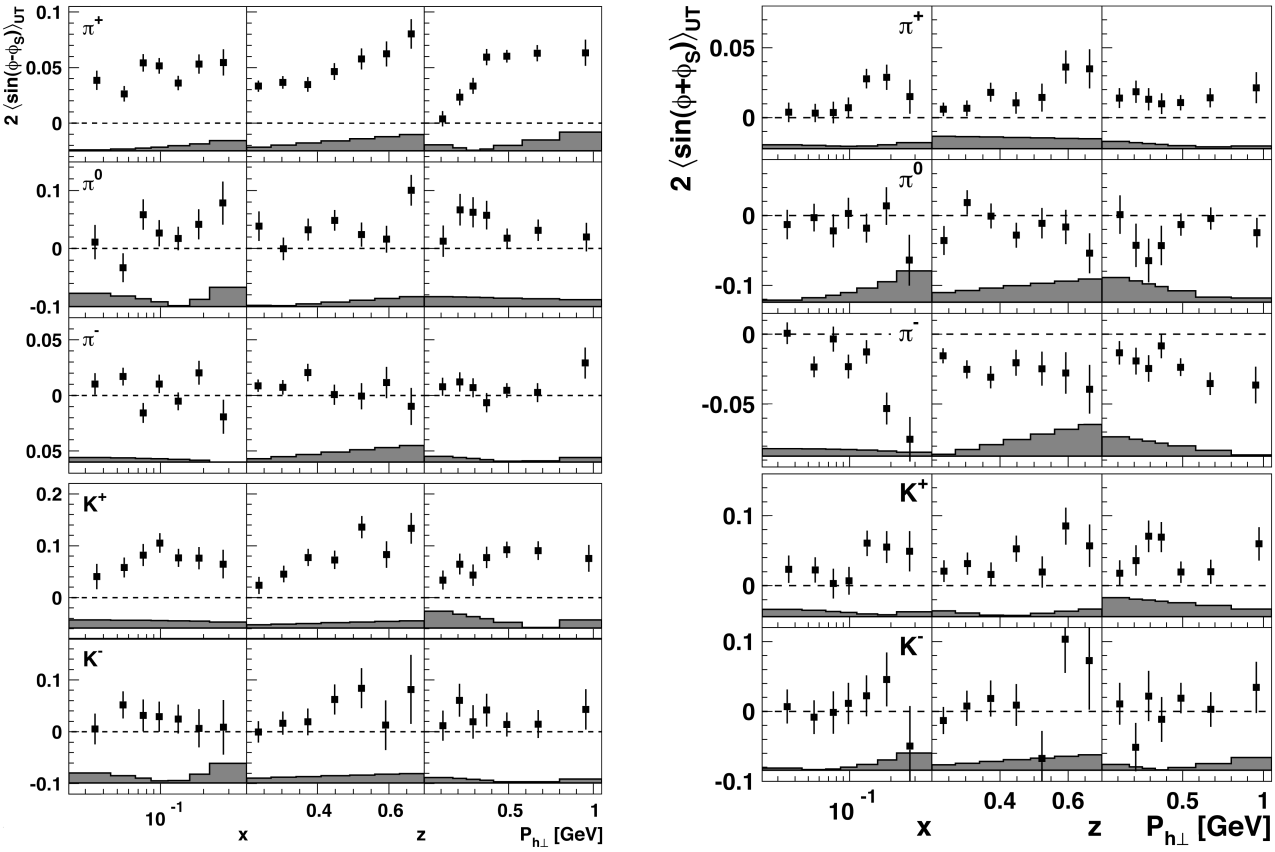

Figure 2.12. Sivers (left) and Collins (right) amplitudes for π^+, π^0, π^-, K^+ and K^- as a function of x, z and $p_{h\perp}$, measured at HERMES from SIDIS data with a transversely polarized proton target and a 27.6 GeV electron beam. The figures are taken from Refs. [91] and [95], respectively.

2.6.2 Interpretation of the Sivers and Collins effects

Transverse SSAs associated with the Sivers and Collins effects can be measured from SIDIS data by exploiting the azimuthal angular modulations present in the SIDIS cross section. From Eq. (2.64) and Eqs. (2.89-2.90), it is clear that the following azimuthal amplitudes are sensitive to these TMDs

$$\sin(\phi_h - \phi_S) \sim f_{1T}^{\perp}(x) \otimes D_1(z) \quad \text{(Sivers + unpolarized FF)} \tag{2.92}$$

$$\sin(\phi_h + \phi_S) \sim h_1(x) \otimes H_1^{\perp}(z) \quad \text{(transversity + Collins).} \tag{2.93}$$

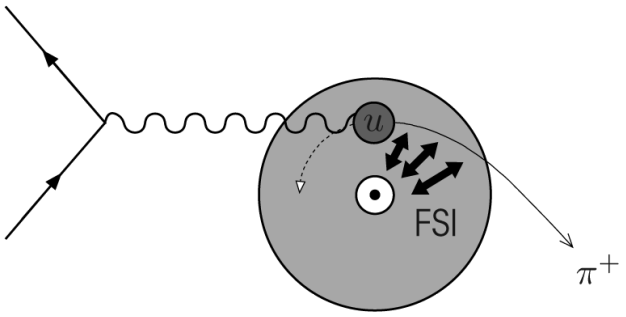

Figure 2.13. Interpretation of the Sivers effect, in the production of a π^+ from the scattering off an u quark in a transversely polarized proton. The attractive final state interactions (FSI) deflect the struck quark, resulting in a transverse SSA. Figure taken from Ref. [101].

Sivers asymmetries In the QCD parton model, the $\sin(\phi_h - \phi_S)$ amplitude can be interpreted as [91]

$$2\big\langle \sin(\phi_h - \phi_S)\big\rangle_{\mathrm{UT}} = -\frac{\sum_q e_q^2 f_{1T}^{\perp} \otimes_{\mathcal{W}} D_1}{\sum_q e_q^2 f_1 \otimes D_1}, \tag{2.94}$$

where symbol $\otimes$ ($\otimes_{\mathcal{W}}$) represents a (weighted) convolution integral over intrinsic and fragmentation transverse momenta.

The HERMES results for the Sivers amplitudes for several mesons are shown in the left hand panel of Fig. 2.12. Non-zero asymmetries were measured for π^+, π^0 and K^+, demonstrating for the first time the existence of T-odd distribution functions in DIS. The existence of such functions, and in particular the fact that they depend on the quark transverse momentum suggests that these quarks carry a significant amount of orbital angular momentum. These results are of great relevance, as the orbital angular momentum of quarks is one of the missing pieces of the *spin puzzle*, mentioned in Section 2.2.3. An attempt to connect the Sivers function, or other similar function describing spin-orbit correlations, with the angular momentum contribution of the quarks to the nucleon spin has been made in Refs. [99, 100].

Interpretation of the Sivers effect The Sivers effect can be visualized in Fig. 2.13. Following the ideas presented in Ref. [99], the parton distribution function can be expressed in the impact parameter space $\mathbf{b}_\perp$, defined as the transverse distance of the quark to the transverse center of longitudinal momentum. The distribution $q(x, \mathbf{b}_T)$ of unpolarized quarks is axially symmetric for an unpolarized or longitudinally polarized nucleon, but in the case of a transversely polarized nucleon, due to the $\mathbf{S}\cdot(\mathbf{P}\times\mathbf{k}_\perp)$ correlation, it is distorted perpendicular to both the spin and the momentum of the nucleon. Such distortion makes the quark densities to appear enhanced on one side of the nucleon or another depending on the orbital angular momentum $\mathbf{L}_q$, but vanishes if there is no $\mathbf{L}_q$ of quarks parallel to the nucleon spin.

The distortion can be understood, in a semi-classical model, by considering the orbital motion of quarks with orbital momentum parallel to the proton spin. In the interaction with the virtual photon, these quarks appear to be moving towards the photon on the left side of the proton spin, for the case of a transversely polarized proton, and away from it on the right side. Thus, they are probed with momentum fractions x_{obs} different than the ones in an unpolarized proton, i.e., smaller on the left side and larger on the right side. Since the unpolarized PDF decreases very rapidly with x at large momenta[30], this implies that the smaller x_{obs} observed at the left side of the proton corresponds to a larger value of the PDF, i.e., there are effectively more quarks of that type at the left side of the proton spin than at the right side. This is the case for the u quarks in a transversely polarized proton as seen in Ref. [99]. Thus the probability of the virtual photon to struck an u quark is larger for the left hemisphere of the proton. For quarks with orbital angular momentum anti-parallel to the proton spin, the case of d quarks [99], the distortion reflects into an enhancement on the right hemisphere. Once the quark is struck, the presence of *final state interactions* (FSI), i.e., the exchange of gluons between the struck quark and the color-charged proton remnant, which are expected to be in average attractive [99], cause the quark to be deflected towards the center of momentum before its fragmentation. Thus, an u quark in a transversely polarized proton (this corresponds to $\phi_S = \pi/2$), fragmenting into a π^+ has a higher probability to be struck on the left hemisphere of the proton, and therefore be deflected by FSI to the right ($\phi_h = \pi$) , leading to a positive Sivers asymmetry ($\sin(\phi_h - \phi_S) = \sin \pi/2 > 0$), as observed at HERMES. On the contrary, d quarks fragmenting into π^- are deflected into the opposite direction, thus leading to a negative Sivers amplitude. In the case of π^- production at HERMES, however, scattering off both u and d must be taken into account due to the abundance of u quarks in the proton target. This would lead to a cancellation of effects, thus explaining the vanishing π^- asymmetry in Fig. 2.12.

It should be emphasized that the Sivers distribution function needs the existence of a net orbital angular momentum of the quarks to be non-zero. In addition, the asymmetric distribution resulting from the $\mathbf{S} \cdot (\mathbf{P} \times \mathbf{k}_\perp)$ term is forbidden by time reversal invariance. It is by the presence of FSI that a non-vanishing Sivers function is allowed. The non-conservation of time reversal invariance makes the Sivers function a **naive T-odd** distribution function. See note on Wilson lines in Appendix D for more details.

Based on a combined fit from HERMES and COMPASS data, and on the available parametrizations for the unpolarized fragmentation function $D_1(z)$, well known from electron-positron annihilation processes, a extraction of the Sivers distribution function $f_{1T}^{\perp}$ for the u and d quarks was done in Ref. [102]. The extracted parametrization describes well both the HERMES and COMPASS data.

[30] See e.g., Fig. 18.4 of Ref. [12].

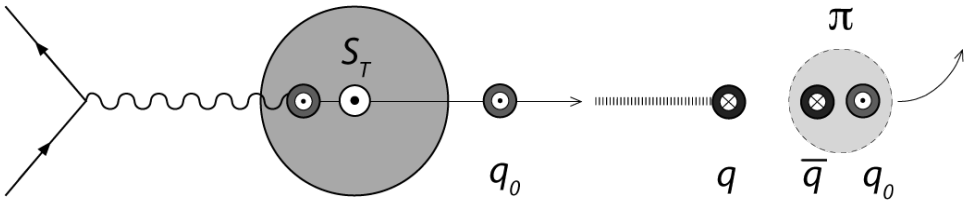

Figure 2.14. Interpretation of the Collins effect by Artru [103]. See text for details.

Collins asymmetries The Collins amplitude, in turn, can be interpreted as [95]

$$2\left\langle \sin(\phi_h+\phi_S)\right\rangle_{\mathrm{UT}} = \frac{(1-y)}{(1-y+y^2/2)}\frac{\mathcal{C}\left[-\dfrac{\mathbf{P}_{h\perp}\cdot\mathbf{k}'_{\mathrm{T}}}{|\mathbf{P}_{h\perp}|\,M_h}\,h_1\,H_1^{\perp}\right]}{\mathcal{C}\left[f_1\,D_1\right]}, \tag{2.95}$$

where the symbol $\mathcal{C}[...]$ stands for the convoluted integral [31]

$$\mathcal{C}[...] = x\sum_q e_q^2 \int d^2\mathbf{k}_{\mathrm{T}}\,d^2\mathbf{k}'_{\mathrm{T}}\,\delta^{(2)}\left(\mathbf{k}_{\mathrm{T}}-\mathbf{k}'_{\mathrm{T}}-\frac{\mathbf{P}_{h\perp}}{z}\right)[...]. \tag{2.96}$$

The $\sin(\phi_h+\phi_S)$ amplitudes measured by the HERMES collaboration are shown in the right hand panel of Fig. 2.12 for charged pions and kaons, and π^0. The large asymmetries measured for charged pions represented the first proof of non-vanishing transversity and Collins distribution functions.

An intuitive explanation for the Collins effect was suggested by Artru in Ref. [103]. This is illustrated in Fig. 2.14. The struck quark q_0, with transverse spin polarization, is kicked out of the nucleon after absorbing the virtual photon. A $q\,\bar{q}$ pair is created as a consequence of the color string break. The new pair must be in a $J^P = 0^+$ state in order to preserve the vacuum quantum numbers[32]. The positive parity forces the spin of the new quark and the antiquark to be aligned ($S = 1$), and thus the pair obtains an orbital angular momentum $L = 1$ to compensate the total spin[33]. The struck quark q_0 recombines with the newly created antiquark, with their spins antiparallel, to form a pion ($S = 0$). This way, the angular momentum of the $q\,\bar{q}$ pair is transferred to the pion, acquiring a certain transverse momentum with respect to the virtual photon.

The fragmentation of an u quark is said to be *favoured* if the produced hadron contains an u quark as a valence quark (e.g., π^+) and *unfavoured* in the opposite case (e.g., π^-). The large π^- asymmetries measured at HERMES, given the u quark dominance in the ep scattering, suggests therefore that the *favoured* and *unfavoured* Collins fragmentation functions are of similar magnitude but with opposite sign [104].

[31] In this equations, $\mathbf{k}'_T$ refers to the transverse momentum of the fragmenting quark with respect to the direction of the produced hadron, like in Eqs. (2.79) – (2.82), while $\mathbf{k}_T$ is used to denote the transverse momentum of the quark with respect to the momentum on the nucleon, like it is the case of the PDFs.

[32] The + sign indicates that under a parity transformation, the vacuum state does not change.

[33] According to $|L-S| < J < |L+S|$.

2.7 High-twist PDFs in collinear framework

In a collinear framework, where partons move parallel with the proton and therefore $\mathbf{k}_\perp = 0$, large spin effects are also found if higher-twist contributions to the cross section are considered. In this case, the kinematical dependence of the spin asymmetries on the hadron transverse momentum $\mathbf{p}_T$ arises from high-order quark-gluon correlations, absent at leading twist where only the quark-quark correlator discussed in Section 2.3.2 contributes.

The first calculation[34] of a sizable SSA in collinear pQCD came out in 1991 by Qiu and Sterman [105], for the case of direct photon production in $p^\uparrow p$ collisions, and was subsequently also done for the case of inclusive pion production [77]. In both cases, the formalism is based on the use of a generalized factorization theorem that allows to write the transverse spin-dependent cross-section as a sum of several terms, involving twist-3 parton distribution functions for the polarized initial proton $f^{(3)}_{a/A^\uparrow}(x_1, x_2)$, convoluted with standard twist-2 PDFs for the non-polarized proton $f_{b/B}(x')$, and a short-distance hard-scattering part calculable in perturbative QCD [77] $\hat{\sigma}$, plus the corresponding fragmentation functions

$$\begin{aligned} \Delta\sigma_{A+B\to\pi} &= \sum_{abc} f^{(3)}_{a/A^\uparrow}(x_1, x_2) \otimes f_{b/B}(x') \otimes \hat{\sigma}_{a+b\to c} \otimes D_{c\to\pi}(z) \\ &+ \sum_{abc} \delta q^{(2)}_{a/A}(x) \otimes f^{(3)}_{b/B}(x'_1, x'_2) \otimes \hat{\sigma}''_{a+b\to c} \otimes D_{c\to\pi}(z) \\ &+ \sum_{abc} \delta q^{(2)}_{a/A}(x) \otimes f_{b/B}(x') \otimes \hat{\sigma}'_{a+b\to c} \otimes D^{(3)}_{c\to\pi}(z_1, z_2) \\ &+ \text{higher power corrections.} \end{aligned} \tag{2.97}$$

The twist-3 PDFs involve quark-gluon correlations, related to the interaction of quarks with the color fields of the hadron remnant. Such correlations are absent at leading twist where only the quark-quark correlator discussed in Section 2.3.2 contributes.

2.7.1 Other approaches

Apart from the TMD approaches and the high-twist collinear model, there exist other QCD-based theoretical frameworks in which transverse SSAs (in particular, A_N) can be reproduced. One example is the "orbiting valence quark model" of Liang and Boros [73], in which the fragmentation into mesons can be calculated from the fusion of a quark from the target hadron with an antiquark of the projectile hadron (a process that cannot be calculated using pQCD). The orbital angular momentum of the quarks, together with hadronic surface effects due to the spatial extension of the colliding hadrons, would be responsible for the spin asymmetry of the produced mesons. Another non-perturbative approach is the model of Troshin and Tyurin [107], in which the valence quarks inside the colliding hadrons are considered to be *composite* objects, i.e., multi-quark condensates made of so-called *current* quarks; the origin of the asymmetry is attributed to the orbital angular momentum of these.

[34] In the literature, the seeds of this idea can already be found in the works of Kane et al. [72] and Efremov and Teryaev [106]. These realized that pQCD can be used to study the effects of transverse spin, but were unable to explain the large magnitude of the observed transverse SSAs. In particular, in Ref. [106] it was pointed out that a non-zero A_N could be obtained in pQCD beyond the leading power expansion.

2.8 Inclusive hadron production in ep scattering

In the last sections, possible mechanisms have been discussed that can give rise to large transverse spin asymmetries. In the following, we focus on the goal for the work done in this thesis: the measurement of transverse SSAs in the inclusive production of hadrons from $e\,p^{\uparrow}$ collisions.

Motivation Transverse SSAs in hadron inclusive electroproduction are appealing. On the one hand, it is an alternative measurement of A_N, never done before in contrast to the various results coming from $p^{\uparrow}\,p$ scattering. On the other hand, as already commented in Section 2.6.1, it can provide relevant insight into the validity of TMD factorization for processes with only one large scale (in this case, the transverse momentum p_T of the detected hadron). Such transverse SSAs are deeply connected with the asymmetries associated to the Sivers and Collins functions, shown in Fig. 2.12, as they represent the general case in which the lepton variables (i.e., ϕ_S) are integrated over. The spin mechanisms behind both types of asymmetries - the inclusive and the SIDIS ones, should therefore be very related in the kinematic region of overlap. Note that, since the lepton track is not required, it is therefore not possible to cut on the usual DIS kinematic variables. In particular, this implies that the total inclusive sample contains a significant proportion of hadrons produced at very low Q^2, i.e., in *quasi-real photoproduction* ($Q^2 \simeq 0$). A transverse SSA for hadrons in this low-Q^2 region cannot be explained, in principle, by the TMD formalism, which is only valid for events with $p_T^2/Q^2 < 1$. Other mechanisms, for example connected to higher-twist PDFs, could play a role there. See further discussion in Chapter 6.

In Ref. [89], the formalism for the study of SSAs in $ep^{\uparrow} \to hX$ assuming TMD factorization is presented, and numerical estimates are given based on the contributions of the Sivers and Collins effects to A_N at different kinematic regimes (HERMES, COMPASS, ENC, JLab). This paper can be therefore regarded as the theoretical background on which the analyses presented in this thesis are based on. The main ideas are outlined next.

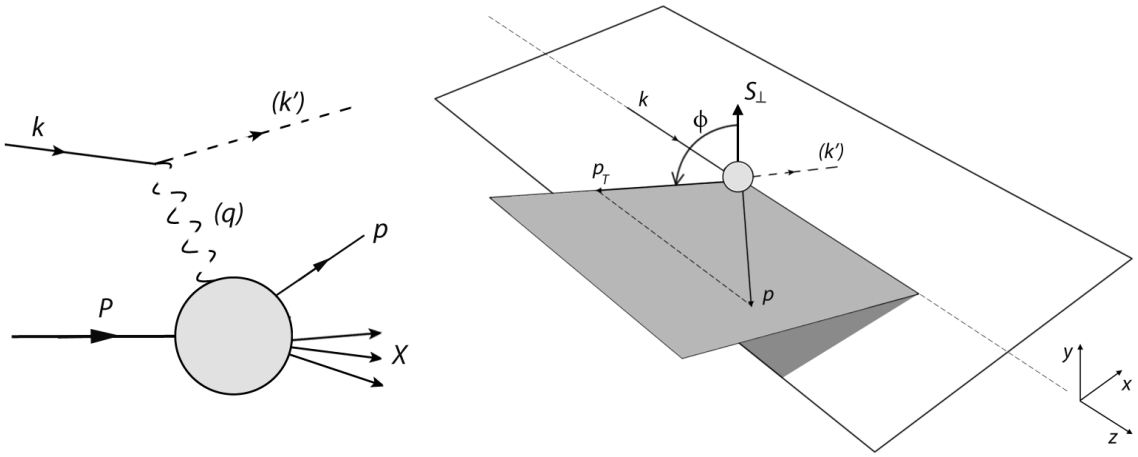

Figure 2.15. Reaction plane for inclusive detection of hadrons in $e\,p^{\uparrow}$ collisions. The 4-momenta in parentheses correspond to undetected particles.

2.8.1 Kinematics

The reaction of interest is depicted in Fig. 2.15. An incoming electron (or positron) with momentum $\mathbf{k}$ collides against a static proton target with mass M and zero momentum in the laboratory frame. The spin $\mathbf{S}$ of the proton is polarized along the y_{lab} direction (up or down), transversely to the direction of the beam. In addition to $\mathbf{k}$ and $\mathbf{S}$, the only other known direction is the momentum $\mathbf{p}$ of one outgoing hadron, produced as a result of the hadronization of the proton after the collision with the electron.

Since the scattered beam lepton is not detected, it is *not* possible to reconstruct the direction $\mathbf{q}$ of the virtual photon, necessary for the calculation of the relevant DIS variables, like x and Q^2 (see Section 2.1.1). The beam direction, along the z_{lab} axis, is taken as the direction of reference and the following observables are used instead

- $x_F = 2\,p_z^{\text{CM}}/\sqrt{s}$, known as the x-Feynman variable, related to the longitudinal fraction of the hadron momentum p_z^{CM}, calculated in the center-of-mass system as

$$\begin{aligned} p_z^{\text{CM}} &= \gamma\,(p_z^{\text{lab}} - \beta\,E), \\ \text{with} \qquad \beta &= \frac{E_{\text{beam}}}{M + E_{\text{beam}}}, \\ \gamma &= \frac{1}{\sqrt{1-\beta^2}}, \end{aligned}$$

  and $E = \sqrt{p^2 + m^2}$ is the energy of the hadron with mass m.
- $\mathbf{p}_T$, the transverse momentum of the hadron,
- ϕ, the azimuthal angle around the beam direction, between the hadron production plane, containing $\mathbf{k}$ and $\mathbf{p}$, and the target spin vector $\mathbf{S}$, defined as

$$\phi = \frac{\mathbf{k}\times\mathbf{S}\cdot\mathbf{p}}{|\mathbf{k}\times\mathbf{S}\cdot\mathbf{p}|}\cos^{-1}\frac{\mathbf{k}\times\mathbf{S}\cdot\mathbf{k}\times\mathbf{p}}{|\mathbf{k}\times\mathbf{S}||\mathbf{k}\times\mathbf{p}|}. \tag{2.98}$$

Notice the difference between p_T and $p_{h\perp}$. The latter is defined with respect to the direction of the exchanged virtual photon, for which the scattered lepton must be detected. As this is not the case in the inclusive detection of the produced hadrons, p_T is defined with respect to the direction of the beam.

2.8.2 Cross section

The cross section for the process $p^\uparrow e \to hX$ can be written as [89]

$$\mathrm{d}\sigma = \sum_{q,\{\lambda\}} \int \frac{\mathrm{d}x\,\mathrm{d}z}{16\,\pi^2 x\,z^2 s}\,\mathrm{d}^2\mathbf{k}_\perp\,\mathrm{d}^3\mathbf{p}_\perp\,\delta(\mathbf{p}_\perp\cdot\hat{\mathbf{p}}'_q)\,\delta(\hat{s}+\hat{t}+\hat{u})\,\Sigma(S)^{qe\to qe}\,, \tag{2.99}$$

where[35],

[35] Note that the formalism in Ref. [89] considers the case of a transversely polarized proton beam colliding against a static electron target, $p^\uparrow\,e \to h\,X$, which is the opposite case of the HERMES experiment.

- the summation in Eq. (2.99) runs over all helicity indices λ and parton types q,
- x and z are the fraction of the proton momentum carried by the parton, and by the outgoing hadron, respectively[36]
- $\mathbf{k}_\perp$ is the transverse momentum of the parton in the proton,
- $\mathbf{p}_\perp$ is the transverse momentum of the final hadron with respect to the fragmenting quark,
- $\mathbf{p}'_q$ is the momentum of the fragmenting parton, which can be expressed as a function of the final hadron kinematics (See (Eq. A6) of Ref. [89]),
- $\hat{s}, \hat{t}, \hat{u}$ are the usual Mandelstam variables,
- $\Sigma(S)^{qe\to qe}$ is the spin-dependent term of the cross section, describing the elementary quark-lepton interaction. It depends on the target proton spin S. Its exact expression is [89]

$$\Sigma^{qe\to qe} = \left\{ \rho^{q/p^\uparrow}_{\lambda_q,\lambda'_q}\, \hat{f}_{q/p^\uparrow}(x, k_\perp)\, \frac{1}{2}\, \hat{M}_{\lambda_q,\lambda_e;\lambda_q,\lambda_e}\, \hat{M}^*_{\lambda'_q,\lambda_e;\lambda'_q,\lambda_e}\, \hat{D}^{\lambda_h,\lambda_h}_{\lambda_q,\lambda'_q}(z, p_\perp) \right\} \tag{2.100}$$

  where

  - $\rho^{q/p^\uparrow}_{\lambda_q,\lambda'_q}$ is the helicity density matrix of parton q inside the transversely polarized proton $p^\uparrow$,
  - $\hat{f}_{q/p^\uparrow}(x, k_\perp)$ is the PDF of unpolarized partons q inside the transversely polarized proton $p^\uparrow$,
  - $\hat{M}_{\lambda_q,\lambda_e;\lambda_q,\lambda_e}$ and $\hat{M}^*_{\lambda'_q,\lambda_e;\lambda'_q,\lambda_e}$ are the helicity amplitudes for the process $qe \to qe$,
  - $\hat{D}^{\lambda_h,\lambda'_h}_{\lambda_q,\lambda'_q}(z, p_\perp)$ is the product of *fragmentation amplitudes* for the $q \to h + X$ process, such that the unpolarized fragmentation function $D_{h/q}(z)$ is given by

$$D_{h/q}(z) = \frac{1}{2} \sum_{\lambda_q,\lambda_h} \int \mathrm{d}^2 p_\perp\, \hat{D}^{\lambda_h,\lambda_h}_{\lambda_q,\lambda_q}(z, p_\perp)\,. \tag{2.101}$$

2.8.3 Computation of A_N

The transverse SSA can be measured by looking at the production of hadrons at different values of p_T and x_F, by reversing the target polarization $\mathbf{S}_\perp$ between the *up* ($\uparrow$) and *down* ($\downarrow$) states

$$A_N = \frac{\mathrm{d}\sigma^\uparrow(\mathbf{S}_\perp) - \mathrm{d}\sigma^\downarrow(\mathbf{S}_\perp)}{\mathrm{d}\sigma^\uparrow(\mathbf{S}_\perp) + \mathrm{d}\sigma^\downarrow(\mathbf{S}_\perp)}. \tag{2.102}$$

Inserting Eq. (2.99) in the above expression, for the two proton polarization states, leads to

$$A_N = \frac{\displaystyle\sum_{q,\{\lambda\}} \int \frac{\mathrm{d}x\,\mathrm{d}z}{16\,\pi^2 x\, z^2 s}\, \mathrm{d}^2 k_\perp\, \mathrm{d}^3 p_\perp\, \delta(p_\perp \cdot \hat{p}'_q)\, \delta(\hat{s} + \hat{t} + \hat{u})\, [\Sigma(\uparrow) - \Sigma(\downarrow)]^{qe\to qe}}{\displaystyle\sum_{q,\{\lambda\}} \int \frac{\mathrm{d}x\,\mathrm{d}z}{16\,\pi^2 x\, z^2 s}\, \mathrm{d}^2 k_\perp\, \mathrm{d}^3 p_\perp\, \delta(p_\perp \cdot \hat{p}'_q)\, \delta(\hat{s} + \hat{t} + \hat{u})\, [\Sigma(\uparrow) + \Sigma(\downarrow)]^{qe\to qe}}\,. \tag{2.103}$$

[36] In Ref. [89], x and z are actually defined as the light-cone momentum fractions of partons in hadrons and of hadrons in partons, respectively.

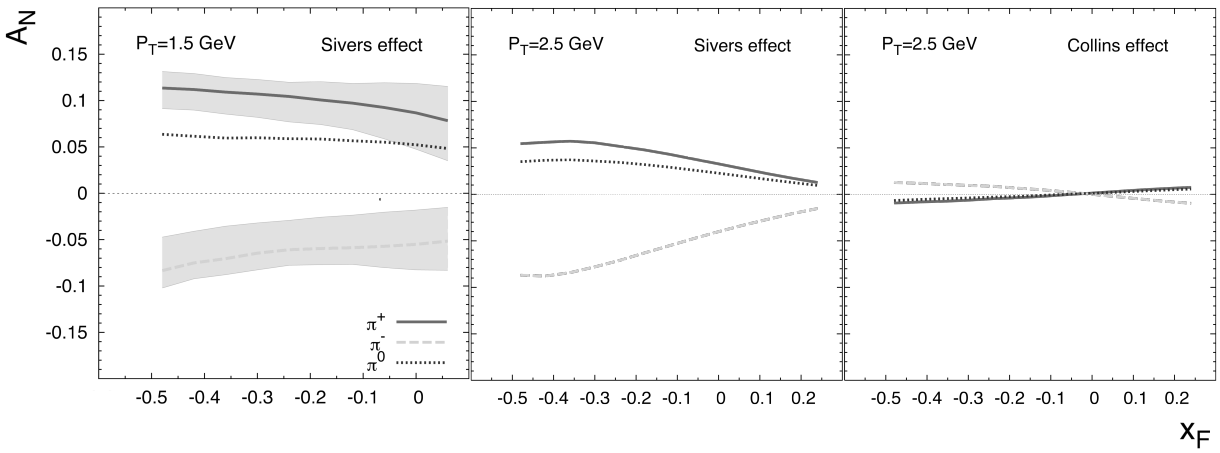

Figure 2.16. Estimates of A_N vs. x_F for the $p^\uparrow e \to \pi X$ process at HERMES, taken from Ref. [89]. Left panel: Sivers effect at $p_T = 1.5$ GeV; central panel: Sivers effect at $p_T = 2.5$ GeV; right panel: Collins effect at $p_T = 2.5$ GeV.

Using the TMD formalism, the spin-dependent terms can be expressed as

$$\sum_{\{\lambda\}} [\Sigma(\uparrow) - \Sigma(\downarrow)]^{qe\to qe} = \frac{1}{2}\,\Delta^N f_{q/p^\uparrow}(x, k_\perp)\cos\phi\,\left[|\hat{M}_1^0|^2 + |\hat{M}_2^0|^2\right]\,D_{h/q}(z, p_\perp) + h_{1q}(x, k_\perp)\,\hat{M}_1^0\hat{M}_2^0\,\Delta^N D_{h/q^\uparrow}(z, p_\perp)\,\cos(\phi' + \phi_q^h), \quad (2.104)$$

where the first term contains the Sivers function $\Delta^N f_{q/p^\uparrow}(x, k_\perp)$ and the unpolarized fragmentation function $D_{h/q}(z, p_\perp)$. The second term of Eq. (2.104) shows the contribution to A_N of the transversity distribution $h_1(x, k_\perp)$ coupled to the Collins function $\Delta^N D_{h/q^\uparrow}(z, p_\perp)$. Similarly, one has

$$\sum_{\{\lambda\}} [\Sigma(\uparrow) + \Sigma(\downarrow)]^{qe\to qe} = f_{q/p}(x, k_\perp)\,\left[|\hat{M}_1^0|^2 + |\hat{M}_2^0|^2\right]\,D_{h/q}(z, p_\perp)\,. \quad (2.105)$$

Contributions to A_N from other TMDs were dropped from the above equations, as they turn out to be negligible [89]. Moreover, numerical calculations show that the dominating contribution to A_N comes from the Sivers function, while the term containing the Collins and transversity functions represent only a *modest* contribution.

The numerical computation of A_N can be done from Eqs. (2.103)–(2.105). For this, one needs a expression for the elementary interaction amplitudes ($\hat{M}_1^0$, $\hat{M}_2^0$), which are calculable, as well as an expression for the contributing TMDs. As the latter cannot be derived from first principles, one can use available parametrizations extracted from data (see below).

Theory predictions Based on the above formalism, the authors of Ref. [89] give estimates of A_N for the kinematics of the HERMES experiment, for the inclusive production of either a π^+, a π^- or a π^0. These are shown in Fig. 2.16, where the contributions from the Sivers and Collins effect are shown separately. The predictions for A_N are presented as a function of x_F, for two different fixed values of p_T (1.5, 2.5 GeV) in the case of the Sivers contribution,

and for a fixed value of $p_T = 2.5$ GeV for the contribution of the Collins function. These values of p_T should be taken as the hard scale of the process, ensuring a large momentum transfer in the proton–electron hard collision ($Q^2 > 1$ GeV). It was checked that a value of $p_T = 2.5$ GeV guarantees a safe Q^2 region in the whole x_F range, while $p_T = 1.5$ GeV implies it only for backward production, $x_F \lesssim 0$.

- The Collins effect, shown on the right-most panel, is almost negligible in this kinematical region. This is due to the dynamical suppression of the Collins effect in the backward region ($x_F < 0$), where the partonic spin transfer cross section[37] becomes smaller, which is in addition reinforced by the integration over the azimuthal angles.
- The Sivers contribution are significantly higher, and showing a clear dependence on both x_F and p_T. The estimates for A_N indicate a larger asymmetry for large negative values of x_F, for $p_T = 2.5$ GeV
- For this calculation of A_N, the parametrization for the Sivers function from Ref. [108] was used, extracted from SIDIS data; the parametrization for the transversity and Collins functions of Ref. [109], extracted from SIDIS and e^+e^- data, the unpolarized PDFs of Ref. [110] and the FFs of Ref. [111]. In the left panel, the statistical uncertainty bands for charged pions are shown, coming from the parametrization of the Sivers functions [108].
- These results are for $p^\uparrow e$ scattering. Nevertheless they can be easily adapted to the HERMES case ($e\,p^\uparrow$), taking into account that, because of rotational invariance,

$$A_N^{e\,p^\uparrow \to h\,X}(x_F, p_T) \;=\; -A_N^{p^\uparrow\, e \to h\,X}(-x_F, p_T)\,. \tag{2.106}$$

2.9 Outlook

In this chapter, the formalism of deep inelastic scattering (DIS) was reviewed (Sec. 2.1–2.3), with special emphasis on the study of reactions using a transversely polarized proton target (Sec. 2.4–2.8). In particular, the relevance of transverse single-spin asymmetries (SSAs) associated to the Sivers and Collins effect was discussed in Section 2.6, together with the theoretical framework of transverse-momentum dependent parton distribution and fragmentation functions (TMDs), in which these and other SSAs can be interpreted. Other approaches to sizable transverse SSAs were briefly discussed in Section 2.7. Finally, in Section 2.8, the measurement of transverse SSAs in the inclusive electroproduction of hadrons, $e\,p^\uparrow \to h\,X$, was proposed as a test of the validity of the factorization of the $e\,p^\uparrow$ cross section into TMDs. No experimental data on this channel have been published until now, but theoretical calculations, done for the kinematics of the HERMES experiment, indicate that the Sivers function leads to large asymmetries in the production of several mesons species. The measurement of such transverse SSAs has been done for the first time in the work presented in this thesis, and will be covered in detail in the next chapters.

[37] Related to the helicity amplitudes $\hat{M}^0_1\hat{M}^0_2$, which enter the Collins contribution to A_N in Eq. (2.104).

3
HERMES

The HERMES[1] experiment took place between the years 1995 and 2007 at the DESY research center in Hamburg, Germany. With the goal of studying in detail the nature of the nucleon spin, the experiment performed high energy electron-nucleon collisions using the electron beam from the HERA accelerator and an atomic gas target with spin-polarized nucleons. Information about the spin of the proton components could be obtained by measuring spin asymmetries.The experiment was originally planned in 1988, motivated by the astonishing observation of the EMC experiment at CERN, that quarks only carry a small fraction of the nucleon's spin – the so-called *spin-crisis*. In addition to the spin physics program, the HERMES collaboration has been able to provide the particle physics community with a rich variety of results over the last 16 years. The possibility of using different beam and target polarizations together with the very precise particle identification system were some of the key elements to move from the initially planned measurement of inclusive spin asymmetries to the more advanced semi-inclusive measurements.

In this chapter, the main features of the experimental setup of the HERMES experiment are reviewed, with particular emphasis on the components involved in the analysis described in the next chapters of this thesis. For a complete review of the HERMES setup, as well as for more technical details, see the cited bibliography.

3.1 HERA and DESY

The idea of building a hadron-electron ring accelerator (HERA) at the *Deutsches Elektronen-Synchrotron* (DESY) laboratory was originally suggested in the late 70s [112] as a powerful *electron microscope* to investigate the structure of the proton. Approved for construction in 1984 and with the first electron-proton collisions taking place in 1991, HERA was successfully operating for more than 15 years until its final shutdown in 2007. The accelerator devices for both particle beams resided in a 6.3 km long underground ring at the city of Hamburg, in the north of Germany.

[1] **HER**A **me**asurement of **s**pin

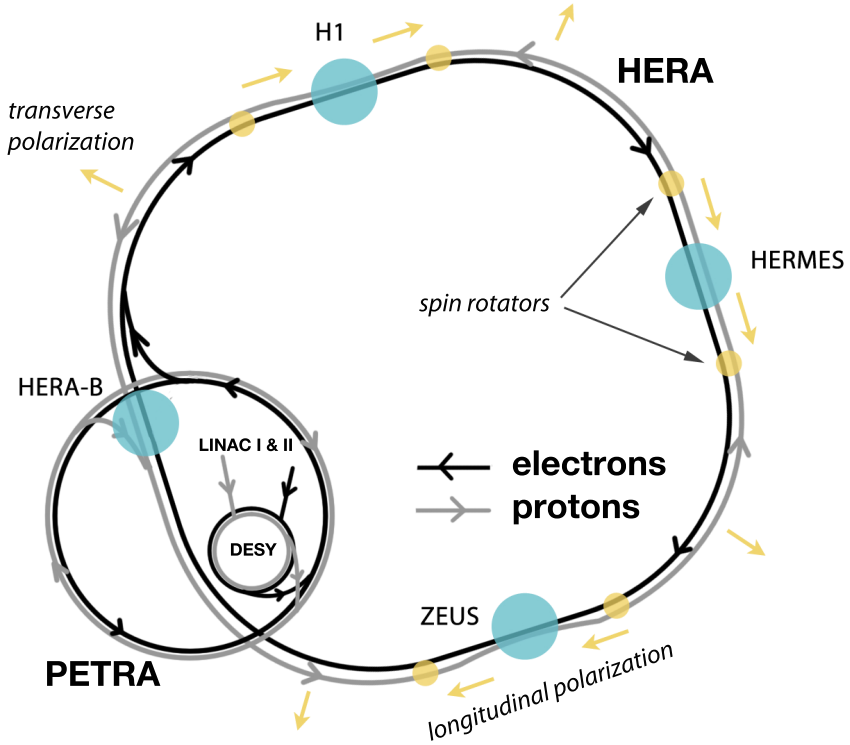

Figure 3.1. Schematic view of the HERA accelerator.

A schematic view of HERA is shown in Fig. 3.1. The tunnel consisted of four circular arcs joined by four straight segments (each 360 m long) where four large experimental halls housed the H1, HERA-B, HERMES and ZEUS detectors. The proton beam with energy of 920 GeV and the 27.6 GeV electron beam were originally used by the collider experiments H1 and ZEUS to obtain direct head-on electron-proton collisions at center-of-mass energies of about 300 GeV. After 1995, the fixed-target experiment HERMES in addition studied the nucleon spin by making the electron beam traverse a gas with spin-polarized nucleons. For a shorter time, at the HERA-B experiment, CP-violation in the decay of B-mesons was aimed to be measured by colliding the HERA protons with the atomic nuclei of a fast moving thin target wire. The electrons and protons were pre-accelerated before their injection into the HERA rings. This was done by a couple of linear accelerators (LINAC and LINAC II) plus a synchrotron accelerator (named originally DESY) and the PETRA ring, the other main accelerator at DESY. The protons were obtained from a source of H^- ions with an energy of 50 MeV provided by the LINAC, accelerated to about 7.5 GeV in the synchrotron and then injected into the PETRA ring after removing the electrons. The electron beam was initially accelerated up to 200 MeV in the LINAC II and then up to 7.5 GeV in the synchrotron. At the PETRA ring, electrons reached an energy of 14 GeV, and protons of about 40 GeV, before their final injection into HERA.

The broad physics program of the four involved experiments made the HERA accelerator a pioneering one in various aspects [113], most remarkably in the use of two colliding beams of particles with different masses. The development of the technology necessary for

accelerating protons and electrons at such high energies in two separate rings and colliding them in flight was a major challenge at DESY. In the two collision points, where both beams interacted at a small angle, the protons were deflected into the electron pipe by guiding magnets and brought back to their trajectory after the interaction. The geometry and energy requirements planned for HERA also made necessary the use of superconducting magnets for deviating the proton beam in the sharp bends. These were able of providing a magnetic field with a strength of about 4.7 T, cooled down with liquid helium to temperatures of only 4.5 K. HERA was, together with the Tevatron at the Fermilab research center in Chicago, the first superconducting accelerator[2].

The DESY research center was established in Hamburg in 1959 with the goal of helping the development, construction and operation of particle accelerator facilities. The main research tool before the construction of the HERA collider was the acceleration of electron and positron beams at the storage rings DORIS and PETRA. Still nowadays, and for over 50 years, the HASYLAB laboratory uses the synchrotron radiation generated at these to carry on investigation in various fields of physics, chemistry, material science, molecular biology and medicine. The near future of DESY seems to go in fact into these latter directions, with the current construction of the European X-ray laser project XFEL.

3.1.1 The polarized lepton beam

Another new technique developed at HERA was the longitudinal polarization of an electron beam in an accelerator ring. This was required by the HERMES experiment in order to perform measurements of spin asymmetries, and later also used by the H1 and ZEUS collider experiments. Back in the early 1990s, polarized electron and muon beams were being or had been used at SLAC and the SMC experiments at CERN, respectively. In the first case, polarized electrons were obtained from photo-ionization of Li atoms [114] or from photoelectric emission from a Ga-As surface excited by a polarized laser light [115]; in the latter, weak decay of pions or kaons was used to achieve a naturally polarized muon beam [116]. Such experimental set-ups presented much less problems than the polarization of an electron beam circulating in a ring like HERA.

The beam-polarization technique was based on the previously known Sokolov-Ternov effect [117]. Transverse polarization of electrons had been discovered in the late 1960s[3] to happen spontaneously when these are accelerated in a ring. The emission of synchrotron radiation causes an accelerating electron to flip its spin in order to conserve total angular momentum. The self-polarization of the beam comes from the fact that the probability of emitting radiation is slightly bigger for the electrons with spin parallel to the magnet field than for the ones with anti-parallel spin, thus populating more the latter state. For positrons, the opposite is true. This small effect produced transverse polarizations of about 55 % in

[2]The technology was invented in the 1960s at the Rutherford-Appleton Laboratory, UK and first used at Fermilab in 1987, with magnets reaching 4.4 T at a temperature of 4.6 K.

[3]The effect carries since them the name of their discoverers, the Russian physicists A. A. Sokolov and I. M. Ternov.

nearly 20 minutes time – a quite optimal time scale for the lifetime of about 10 hours of the electron beam.

Longitudinal polarization was achieved by rotating the spin of the electrons right before the interaction points. This was a crucial point in the physics program of the collaborations, as spin effects caused by the transverse polarization of an electron beam are strongly suppressed by the mass of the electron. The *spin rotator* consisted of a series of magnets that, by applying small corrections to the direction of the electron spin, were able of switching from transverse to longitudinal polarization over about 60 m distance. After its passing through the experimental halls, the beam polarization was set back to transverse before entering the arcs in order to favor the self-polarization process. The transverse and longitudinal polarizations of the beam were constantly measured by analyzing the Compton scattering of laser light off the beam. Longitudinal polarizations ranging between 40% and 60% were obtained at HERA for the electron beam.

The HERA beam could be operated with both electrons and their antiparticles, positrons. The data selected for these analyses were obtained with the positron beam used between the years 2002 and 2004, while for the complete year 2005, from which most data originate, electrons were employed. In the following, unless leading to confusion, the term *electron*, or more generically *lepton*, will refer to both types of beam. The use of a polarized beam did not restrict the physics analyses to spin-related subjects. A data sample with zero average beam polarization could be easily arranged by balancing the data sets taken with the different orientation of the beam spin.

Some characteristics of the HERA electron beam are summarized in Table 3.1.

Length of the ring	6.3 km
Number of bunches	189
Injected beam current	~ 50 mA
Energy	27.6 GeV
Lifetime	~ 10 h
Bunch density	5×10^{10} $e^{\pm}$
Time interval between bunches	$\Delta t = 96$ ns
Number of times a bunch flies through the HERA ring in a second	47000
Time width of a bunch	$\sigma_t \sim 35$ ps
Beam size (elliptical)	$\sigma_x = 0.26$ mm
	$\sigma_y = 0.07$ mm
	$\sigma_z = 11$ mm

Table 3.1. Features of the HERA lepton beam.

3.2 The polarized gas target

The HERMES target was designed to fulfill two main experimental requirements: *(i)* achieve effective lepton-nucleon scattering with a high polarized target source, and *(ii)* guarantee a high lifetime of the HERA lepton beam after the interaction, so that it could be further used by the two collider experiments H1 and ZEUS. The solution was an innovative approach, not seen before at other polarized deep-inelastic scattering experiments: the use of a gas target with spin polarized nucleons in an internal storage cell through which the electron beam passes. The target could also be operated with unpolarized gases. Hydrogen and deuterium gases were mainly used with the polarized setup, as the spin of their nucleons is easier to keep under control, while the unpolarized target ran as well on ^{4}He, N, Kr, Ne and Xe-gases. The data analyzed in this thesis were taken exclusively with the transversely polarized hydrogen gas target.

An schematic view of the HERMES target region can be seen in Figure 3.2, consisting of three main parts responsible for the storage, injection and monitoring of the spin polarized target gas, plus a magnet. These are described in more detail in the next sections. For a complete description of the HERMES polarized target, see Ref. [118].

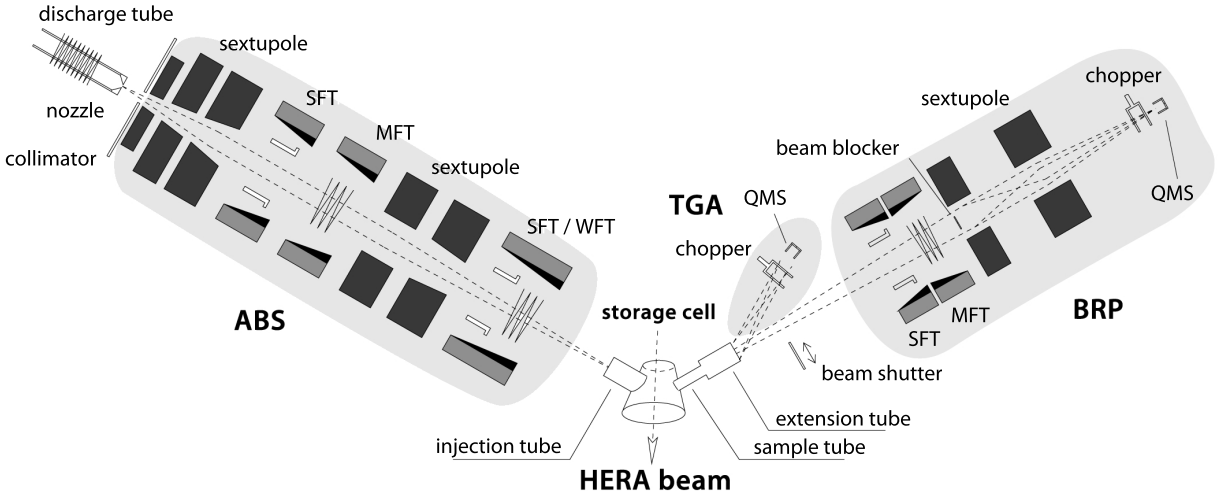

Figure 3.2. Diagram of the polarized gas target with on the left the Atomic Beam Source (ABS) in the middle the target cell and on the right the Target Gas Analyzer (TGA) and the Breit-Rabi Polarimeter (BRP).

Target cell The storage cell consisted of a 400 mm long aluminum tube with an elliptical cross section of 21×8.9 mm^2, made of two aluminum sheets 75 μm thick welded together. Both extremes were open, such that the cell was directly connected to the HERA electron beam pipe.The target gas was injected at the center of the cell by the atomic-beam source (ABS) and removed at the extremes by two powerful turbo-molecular pumps. This resulted in a triangular distribution of the target atoms, with maximum at the center of the cell. Gas densities of about $1 - 2 \times 10^{14}$ nucleons/cm^2 were reached during the polarized target runs. As the target cell was directly attached to the HERA lepton beam pipe, two collimators

upstream protected the cell from synchrotron radiation and scattered leptons hitting the cell walls. The transition from the beam pipe to the cell was also made RF-smooth by a thin perforated titanium tube which confined the electromagnetic field of the bunched HERA beam and avoided the generation of *wake fields* that could cause heating. Two cooling rails along the cell kept the temperature at 100 K to minimize depolarization effects.

Target magnet The target region was placed within a magnetic field obtained by a surrounding magnet. Such field determined the geometrical axis of the spin of the gas nucleons. Two different target magnets were employed to obtain a polarized spin target at HERMES. During the years 1997-2000, longitudinal spin polarization was achieved by a set of superconducting magnet coils, while on the period 2002-2005 it was replaced by a conventional dipole magnet to obtain a transverse spin. The target magnetic field served as well to reduce the depolarization of the nucleons inside the target cell: *spin relaxation* can undergo by collision of the polarized atoms with the walls of the target cells, or between them, and by the transient magnetic fields generated at the passage of the lepton beam bunches. These depolarization effects can be minimized by applying a strong magnetic field of high uniformity. The field value of the transverse target magnet was of about 300 mT.

Polarized atomic gas injection The injection of spin polarized nucleons into the target cell was accomplished at HERMES by an atomic-beam source (ABS), capable of dissociating and polarizing hydrogen (H) or deuterium (D) atoms from their molecular gases. Injection rates of about 6.5×10^{16} atoms/s were reached with nuclear polarization above 97%. The principle of operation of the ABS is the following: Molecules are dissociated into atoms by a radio-frequency electric discharge, achieving a degree of dissociation up to 80%. The dissociated gas expands through a conical nozzle of 2mm of diameter into a vacuum chamber, where a set of sextupole magnets, based on the Stern-Gerlach principle, focuses the atoms with electron spin $+\frac{1}{2}$ and deflects those with electron spin $-\frac{1}{2}$. Nuclear polarization is then obtained by a proper recombination of the four hyperfine energy levels that atomic hydrogen exhibits in the presence of a magnetic field[4].

By applying high-frequency magnetic fields, those atoms with nucleon spin *up* or *down* can be selected such that the total electron polarization vanishes. The apparatus for these fields consisted of a resonator cavity in the case of the strong field transition (SFT) or a high-frequency coil in the case of the weak field and medium field transition (WFT and MFT) [119]. This way, atoms with spin-polarized nucleons and unpolarized shell electrons were injected into the target cell. The spin state of the nucleons was flipped at 1-3 min time interval, in order to provide data in both spin states, essential for the calculation of spin asymmetries.

The vacuum inside the ABS chamber was provided by a powerful pumping system with a power higher than 15000 l/s. This high vacuum suppressed the scattering of the atomic beam and guaranteed a low flux of atoms into the vacuum of the HERA lepton pipe.

[4]Resulting from the *up* and *down* spin states of the nucleon and the shell electron.

Year	Polarization
2002	0.783 ± 0.041
2003	0.795 ± 0.033
2004	0.737 ± 0.055
2005	0.705 ± 0.065

Table 3.2. Target polarization values for each year of transverse polarization data.

Measurement of target polarization With the use of an internal gas target, an additional challenging requirement was to determine the effective target polarization seen by beam. This is in principle different from the polarization of the injected beam, as a result of the several interactions that the atoms of the target may undergo inside the storage cell. Two main categories of processes take place in the target chamber: recombination of atoms into molecules by collisions with the cell walls and spin relaxation processes. The effect of these could have been measured by scattering processes from beam leptons if the cross sections involved were higher. Instead, a sampling technique was employed by analyzing a sample of the target gas contained in the storage cell with a Breit-Rabi polarimeter (BRP) and a target gas analyzer (TGA). Both devices were fed by a common tube, providing a sample of about 5 % of the target gas. The feed was connected to the center of the storage cell at the same angle but opposite side as the injection tube from the ABS, in order to ensure that the analyzed gas would not stem directly from the injected beam.

The BRP measured the population of the hyperfine states of hydrogen atoms. Its logic is similar to the ABS injection device: a set of hyperfine transition units and sextupole magnets allows to focus or deflect atoms into a detector chamber where a quadrupole mass spectrometer (QMS) and an electron multiplier provide flux rates. The TGA provided the degree of dissociation of the target gas by measuring the atomic and molecular content. It was mounted inside the BRP vacuum, 7° off-axis with respect to the BRP to not interfere with the beam entering the polarimeter, and made use of an detector similar to the one in the BRP to measure the atomic and molecular flux.

Target polarization values The average target polarization P_T as seen by the lepton beam is given by the expression

$$P_T = \alpha_0(\alpha_r + (1-\alpha_r)\beta)P_a, \tag{3.1}$$

where α_0 is the initial atomic fraction in the gas injected by the ABS, α_r is the fraction of nucleons in atoms after recombination in the storage cell, P_a is the nuclear polarization of atoms and $\beta = P_m/P_a$ is the ratio of the nuclear polarization in molecules to the one in atoms. These quantities were calculated using the measurements from the TGA and BRP in combination with various calibrations. From this analysis, a systematic uncertainty to P_T was correspondingly assigned.

Using Eq. 3.1, the average degree of the target spin polarization was determined for each data period. This is summarized in Table 7.1 together with the uncertainties. See Ref. [120] for more information. For the transversely polarized data set used in this analysis, the target spin vector was polarized either *up* or *down* along the y_{lab} axis (see Sec. 3.3.4).

3.3 The spectrometer

The big *forward-angle* spectrometer [121] used by the HERMES experiment was located in the east hall of the HERA tunnel. Seven floors below ground level, behind a thick concrete wall that protected the outside from the radiation of the HERA beams, the $7 \times 5 \times 4$ m^3 detector was placed along the HERA beams, right behind the target region described before. A forward-angle spectrometer is generally used by experiments with a fixed target, as the particles resulting from the collision with a high-energy beam are most probably emitted in the forward direction.

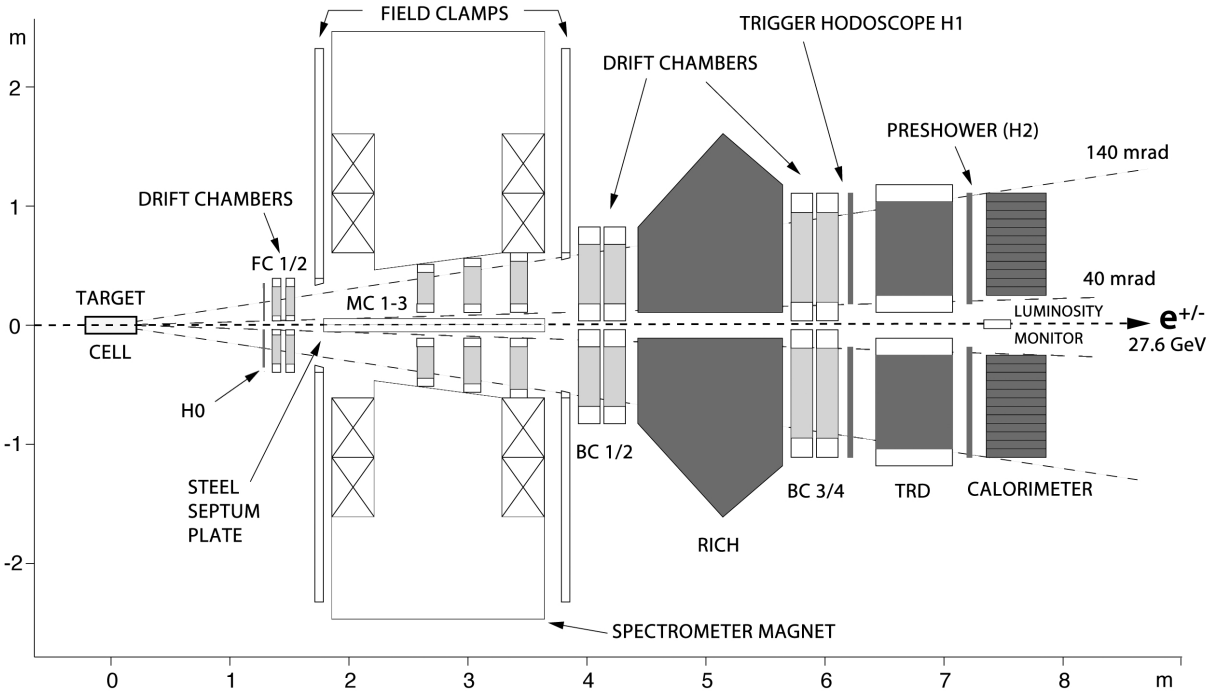

Figure 3.3. Side view of the HERMES spectrometer. Particle identification detectors and tracking devices are depicted in dark and light gray, respectively. The dashed lines delimitates the detection acceptance.

A schematic view of the HERMES experiment is shown in Fig. 3.3. The spectrometer consisted mainly of two types of detectors, namely tracking devices and particle identification detectors, that permitted detecting and identifying both the scattered lepton and the produced particles resulting from the hadronization of the broken target proton. All detectors were divided in two parts, a *top* and a *bottom* part, with a horizontal gap in between them such that the HERA beam pipes could go through.

- The wire chambers located at the front (FC), back (BC) or in between (MC) the poles of the spectrometer magnet were used for the tracking of charged particles.
- The dipole magnet consisted of several tons of iron, providing a magnetic field with a deflecting power of $\int BdI = 1.3$ Tm. The two poles of the magnet delimited the maximum angle of 140 mrad at which tracks were detected in the vertical direction,

whereas the minimum acceptance corresponded to 40 mrad due to a 11 cm thick iron plate that shielded the HERA beam pipes from the strong field of the magnet. In the horizontal direction, the maximum acceptance was 170 mrad. This *acceptance gap* at low angles implied that in many of the recorded events, the beam lepton would not be detected after colliding with the target, as it often was scattered at angles smaller than 40 mrad.

- Particle identification (PID) was carried out by the combination of several detectors: a ring-imaging Cherenkov (RICH) detector, a transition radiation detector (TRD), a pre-shower/hodoscope detector (H2) and an electromagnetic calorimeter.
- The hodoscopes H1 and H2 provided the signal for the trigger system. They were made of several paddles of scintillator, a material which emits light at the passage of a charged particle, read out by photomultiplier tubes. An additional small hodoscope H0, made of two paddles and placed before the magnet, helped to discriminate against background events mainly caused by the proton beam and so reduce the trigger rates.
- The luminosity detector, placed at the rear end of the spectrometer, very close to the electron beam pipe, determined the luminosity of the experiment during each period of data taking.

More information about the tracking and PID detectors as well as the luminosity measurement is given in the next sections.

3.3.1 Tracking

Two types of tracking chambers were employed at HERMES, either *proportional wire chambers* (MC) or *drift chambers* (FC and BC). Wire chambers have been used in particle detectors for more than half a century. They are based on an array of thin wires, operating at a certain electric potential, that collect the ionization produced by charged particles traversing a gas volume. The more advanced drift chambers originated in the 1970s and provide a finer spatial resolution by using the drift time of the ionization products inside the detector volume.

The front chambers (FC) [122] served to determine the vertex of the interaction at the target cell from the initial trajectory of the tracks. In combination with the back chambers (BC) [123], the momentum of the charged tracks was calculated from the bending in the magnetic field provided by the spectrometer magnet, using momentum look-up tables. The BC were also used to identify the hits in the PID detectors.

Tracks were reconstructed by a *fast tree*-based search algorithm, selecting combinations of hits in the FC and BC that would intersect at the center of the magnet. The magnet chambers (MC) [124] were used to track low-momentum particles, strongly deflected in the magnetic field and therefore not reaching the BC. The momenta of particles was determined with a resolution finer than 2%, and the angles within ± 1.8 mrad.

3.3.2 Particle Identification

The precise identification of pions, kaons and protons, and the efficient separation of these hadrons from leptonic tracks was one of the main features of the HERMES spectrometer. The four components used by the PID system are reviewed on the next paragraphs. The way their signals were combined to actually perform the identification of particles is described in Section 4.2.1.

RICH The ring imaging Cherenkov (RICH) detector [125] was installed in 1998 to improve hadron identification over a wide momentum range as part of the plan of the collaboration to measure semi-inclusive spin asymmetries. This represented an upgrade with respect to the previously operating threshold gas-Cherenkov detector.

Like any Cherenkov detector, the RICH detector is based on the effect discovered [126] by P. A. Cherenkov in 1937[5] that radiation is emitted by charged particles when these travel in a medium at a speed higher than the speed of light in that medium. Cherenkov photons are emitted in a cone of angle θ_C about the direction of motion of the particle. The opening angle is related to the relativistic speed β of the particle and the refractive index n of the material as $\cos\theta_C = 1/\beta n$. A radiator material (typically gas) and a set of photomultiplier tubes (PMTs) are used to produce and detect the Cherenkov photons.

An schematic drawing of the RICH detector used at HERMES can be seen in the left-hand side of Fig. 3.4. In this case, two radiators were used instead of one: *(i)* an aerogel radiator with refraction index $n = 1.03$, covering the pion momentum range $1 - 10$ GeV/c, and *(ii)* a pure C_4F_{10} gas radiator with $n = 1.0014$, optimal for hadrons with momentum between 10 and 17 GeV/c. The HERMES RICH detector was one of the first ones to make use of aerogel tiles, shortly after their use was demonstrated in a test setup [127] at CERN [6]. A panel of 1934 PMTs of 15 mm diameter each collected the emitted light, after reflection and focusing by a spherical mirror. The separation of pions, kaons and protons is shown in the right-hand side of Fig. 3.4.

The ring pattern recognition is usually done at other RICH detectors by a fit to the circular hit pattern. This was not possible at HERMES as the spherical mirror produces elliptical rings. Two different reconstruction algorithm were used on this analysis. The *direct ray tracing* (DRT) is based on the comparison of the detected pattern to simulations of the several particle hypotheses, assigning a probability to each hypothesis. For events containing more than one track, an *event level tracking* (EVT) algorithm improves the identification of close tracks whose Cherenkov rings overlap, by performing combinations of all expected DRT patterns.

[5] and awarded in 1958 with the Nobel Prize in physics, together with I. Y. Tamm and I. M. Frank,
[6] Already in 1983 EMC used an aerogel counter with blocks of $18 \times 18 \times 2.7$ cm^3 [128].

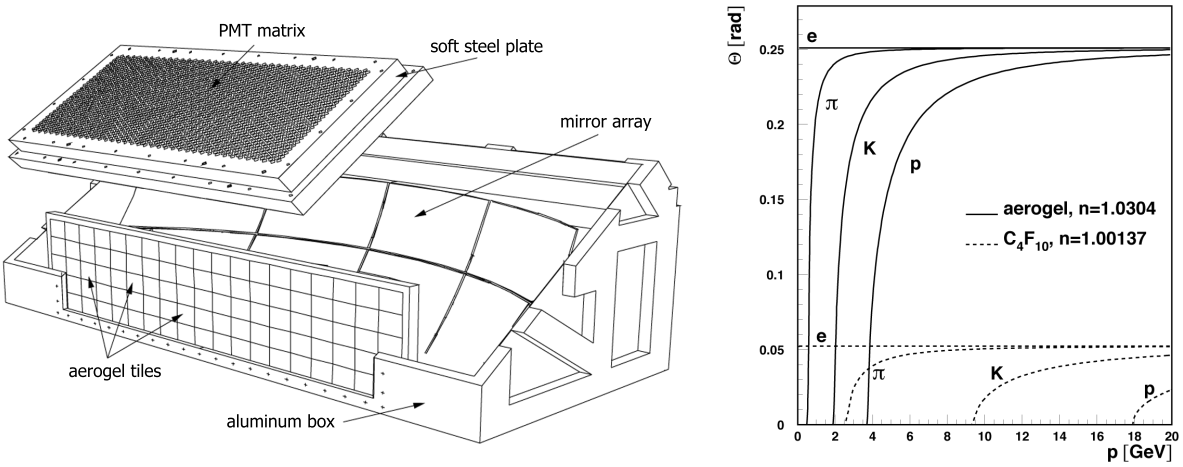

Figure 3.4. *Left:* Schematic picture of the RICH detector at HERMES. Charged particles traversing the RICH detector produce Cherenkov photons when they pass through the radiators (the aerogel tiles and the C_4F_{10} gas filling the inner volume of the detector). These photons are projected onto a matrix of PMTs by a spherical mirror. *Right:* The Cherenkov angle as a function of the particle's momentum, showing the achieved separation for the both radiators.

TRD The transition radiation detector (TRD) at HERMES provided a highly efficient discrimination of hadrons and leptons. Its operating mechanism is based on the phenomenon[7] that highly relativistic charged particles emit radiation in a cone with opening angle $\theta \sim 1/\gamma$ when they go through two media with different dielectric constant. Here, $\gamma = 1/\sqrt{1-\beta^2}$ is the Lorentz factor. This transition radiation is emitted due to the reorganization of the Coulomb field, that must satisfy the condition of continuity at the boundary between the two media.

The TRD at HERMES consisted of a set of radiator blocks and multi-wire proportional chambers, optimized for the frequencies[8] of the produced photons. The radiator would ideally be an arrangement of thin layers of a material (*medium* 1) with high photon transparency separated by vacuum (*medium* 2), but this is not technically achievable in large dimensions. An array of polypropylene fibers was used instead such that the ~ 20 μm cylindrical fibers approximate the foil layers.

As the probability of emitting a photon is directly proportional to γ, essentially only leptons (with $\gamma \sim 10^4$ at HERMES energies) and not hadrons ($\gamma \sim 10^1$) produced transition radiation. A track detected in coincidence with a photon signal was then a clear signature of a lepton track. For a complete description of the TRD at HERMES, see Ref. [131].

[7] Originally predicted in 1946 [129] and first demonstrated for experimental use in the early 70's [130].
[8] For the HERMES energies, in the x-ray region.

Calorimeter and pre-shower The electromagnetic calorimeter measured the energy of leptons and photons and also provided a separation between hadrons and leptons. As depicted in Fig. 3.5, it consisted of 420 lead-glass blocks of 9×9 cm^2 cross section and 50 cm long, stacked in a 42×10 array. The principle of an electromagnetic calorimeter is quite simple: leptons and photons lose their energy in *electromagnetic showers*.

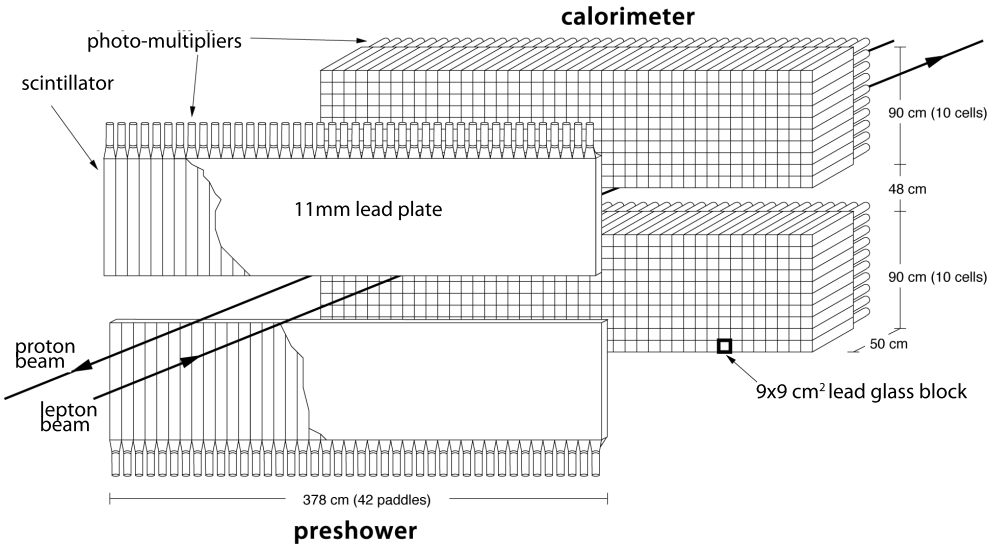

Figure 3.5. Schematic view of the pre-shower detector (H2) and the electromagnetic calorimeter.

An electromagnetic shower originates right after a high-energy electron, positron or photon enters a material. For energies above 100 MeV, the dominating processes are *bremsstrahlung* for electrons and positrons, as a result of their interaction with the Coulomb field of the material, and e^+e^- pair production for photons. These processes successively generate a cascade of particles until the energy of the produced particle is low enough, in which case they primarily lose their energy by ionization. The longitudinal development of the shower is characterized by the *radiation length* of the material, defined as the mean distance over which the electron loses all but $1/e$ of its energy by bremsstrahlung [132]. The block dimensions were chosen to be 18 radiation lengths long and such that 99% of the energy of an electromagnetic shower would be deposited into a set of 3×3 blocks. A measurement of the deposited energy was done based on the Cherenkov photons radiated by the many lower energy constituents of the shower that are still highly relativistic. These Cherenkov photons traveled through the mirror shielded blocks, to be finally collected by a PMT at the rear end. Lepton and photon showers are not distinguishable, but they can be differentiated by the existence of a charged track in the tracking system associated to the shower.

The use of the calorimeter as a PID detector to separate hadrons from leptons was possible thanks to the topological difference between electromagnetic and hadronic showers. The radiation length for hadrons is much higher than for leptons, as their large mass suppresses significantly the energy lost by bremsstrahlung ($\propto 1/m^2$). The hadronic showers usually initiate when a hadron collides with a nucleus, producing pions and nuclear fragments which

eventually decay themselves. Neutral pions decay into photons which start electromagnetic cascades within the hadronic shower. Hadronic showers typically started only in the second half of the calorimeter and spread over the boundaries of a 3×3 block array, but still deposited a smaller amount of energy than leptons or photons.

In order to improve the lepton-hadron separation at the calorimeter, a 1.1 cm thick lead plate was installed at the front side of the hodoscope H2, that would make leptons (and not hadrons) initiate showers, leaving a large signal in the hodoscope. The electromagnetic calorimeter was used to provide a first level trigger on the scattered beam leptons, based on a minimum energy deposition in a localized spatial region – 1.4 GeV for the polarized data set.

3.3.3 Luminosity measurement

In a fixed target experiment, the luminosity is given by the product of the target density n_t and the beam current I_b, integrated over the time of measurement. These can be measured separately, or their product determined more accurately by measuring the reaction rates R of a process of well determined cross section $\mathrm{d}\sigma/\mathrm{d}\Omega$ in a detector with acceptance region Ω,

$$\mathcal{L} = \int \mathrm{d}t \; n_t I_b = \frac{R}{\int \mathrm{d}\Omega \; \dfrac{\mathrm{d}\sigma}{\mathrm{d}\Omega}}. \tag{3.2}$$

The precise determination of the collected luminosity is essential for the measurement of spin asymmetries, as this is used to normalize the particle yields taken with each orientation of the target spin and to weight the different data sets used.

At HERMES, the luminosity detector was based on the coincident collection of particle pairs coming from the elastic scattering of the beam leptons off the electrons of the gas atoms stored in the target cell. . The cross section for these elastic processes are well known, being either Møller scattering ($e^-e^- \to e^-e^-$) for an electron beam, or Bhabha scattering ($e^+e^- \to e^+e^-$) for a positron beam. In the last case, also photon pairs resulting from e^+e^- annihilation can be produced. With a beam energy of 27.6 GeV, the elastic scattering angle is 6.1 mrad, making the pair of particles leave the beam pipe at 7.2 m from the center of the target cell. This was the exact location of the luminosity monitor [133], consisting of two small calorimeter blocks read out by PMTs. Each block consisted of a 3×4 matrix of lead-glass crystals with size $22 \times 22 \times 200$ mm^3. An independent trigger system fired in case an energy deposition bigger than 4.5 GeV was found simultaneously in both calorimeter blocks. This way, background events were filtered, as they typically deposit energy in only one detector. The trigger was calibrated with signals from beam leptons scattered elastically off the target nucleons, depositing an energy approximately equal to the beam energy of 27.6 GeV in one of the blocks of the luminosity monitor.

In practice, the luminosity was measured from the event rate collected over 10 s of data taking, a *burst*, from the relation

$$\mathscr{L} = \langle R_{\mathrm{Lumi}} \rangle \cdot C_{\mathrm{Lumi}} \cdot N_n \cdot \tau_{\mathrm{DAQ}} \cdot t_{\mathrm{Burst}}, \tag{3.3}$$

where $\langle R_{\text{Lumi}} \rangle$ is the average rate measured by the luminosity monitor, C_{Lumi} is a proportionality constant which varies year-to-year relating the rate to the luminosity per nucleon, N_n is the number of nucleons per nucleus in the target gas, τ_{DAQ} is the fractional life-time of the data acquisition system (in %) and t_{Burst} is the length of the burst.

3.3.4 Coordinate system

The HERMES coordinate system was chosen such that the beam pipe runs along the z_{lab} axis, with its origin starting at the center of the target cell. The target cell extended therefore over the range -20 cm to 20 cm. The x_{lab} and y_{lab}-coordinates had their origin at the center of the electron beam pipe. The x_{lab}-coordinate has its positive values pointing to the left looking downstream, towards the proton HERA pipe. The y_{lab}-coordinate is defined positive for the top half.

In addition to the geometrical coordinates, the angles ϕ and θ are used to define the position of tracks. The polar angle θ_{lab} is defined as the angle between the track momentum $\mathbf{p}$ and the z_{lab}-axis, being positive for $y_{\text{lab}} > 0$ and negative for $y_{\text{lab}} < 0$. The azimuthal angle ϕ_{lab} is defined as the angle between the track and the positive half of the x_{lab}-axis.

The HERMES *lab* coordinate system is shown schematically in Figure 3.6. The *left* and *right* parts of the detector are indicated with respect to the orientation of the target spin vector. This will be relevant later in Section 4.5 for the definition of spin asymmetries.

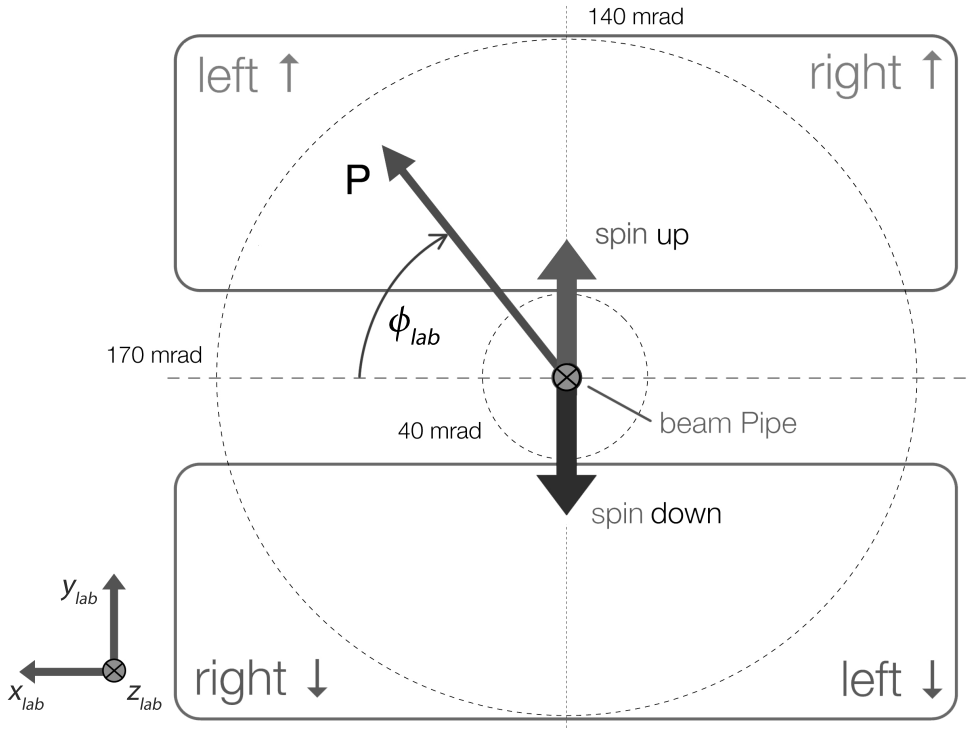

Figure 3.6. Transverse section of the HERMES spectrometer.

3.4 The trigger system

The trigger system selects events of interest for physics analyses or detector monitoring and calibration. This is done by the combination of signals from various detectors (typically hodoscopes, drift/wire chambers, calorimeter) within a certain time window after an event (i.e., collision) occurs.

At HERMES, the first level trigger decision was taken 400 ns after the passage of the lepton beam bunch signal (every 96 ns), synchronized with the HERA clock. Several trigger schemes were used at HERMES over the years of data taking. Some of them served to indicate potential events of interests for certain analysis, while other triggers were used merely for calibration of the detectors.

The main **physics trigger**, trigger 21, guaranteed a clean sample of events, suitable for most DIS analysis performed at HERMES, consists of the responses in coincidence of the hodoscopes H0, H1, H2, and the electromagnetic calorimeter

$$\text{trig21} = (H0 \cdot H1 \cdot H2 \cdot calo)_{top} + (H0 \cdot H1 \cdot H2 \cdot calo)_{bot},$$

where the signals from both the top and bottom halves are taking into account. Two independent triggers for each half also exist, trigger 24 (top), and 25 (bottom):

$$\begin{aligned} \text{trig24} &= (H0 \cdot H1 \cdot H2 \cdot calo)_{top} \\ \text{trig25} &= (H0 \cdot H1 \cdot H2 \cdot calo)_{bot}, \end{aligned}$$

such that $\text{trig21} = \text{trig24} + \text{trig25}$ can be built from a logical *OR* from both triggers.

Some observations:

- A typical DIS event at HERMES was characterized by a lepton track leaving a signal in the hodoscopes and depositing a large amount of energy in the calorimeter, in coincidence with some hadronic tracks, seen by the tracking and PID detectors.
- High-energy photons also start electromagnetic showers in H2 and the calorimeter with large energy depositions. By including the hodoscopes H0 and H1 (where only charged tracks leave a signal), these could be discarded as not being DIS events.
- The energy deposition in the pre-shower hodoscope H2 and the calorimeter is much higher for leptons than for hadrons. This implies that a hadron track has a higher probability of firing trigger 21 if a lepton was simultaneously detected in the calorimeter acceptance.
- The energy threshold for the calorimeter was 1.4 GeV for the polarized data set used for the analyses of this thesis. In other data-taking periods, the calorimeter threshold was increased to 3.5 GeV ($y < 0.87$) to discard hadronic showers, or to reduce trigger rates in the case of runs with high-density unpolarized gas targets.

For the analysis of hadron tracks, where other detected tracks, like leptons, are ignored, the simultaneous detection of a lepton in the calorimeter increased therefore the chance

that the trigger fired and the event was recorded. This happens with higher probability in certain kinematic regions, e.g., at high transverse momentum where the lepton escapes the septum acceptance gap, and can therefore lead to an artificial abundance of hadron tracks at such kinematics. One way to avoid this problem is by correcting the particle yields for the trigger efficiency. This is discussed in detail in Section 4.3.

The other relevant trigger for the discussion of inclusive hadron tracks is trigger 28, called the **photoproduction trigger**, formed from the responses of the hodoscopes H_0, H_1 and the back chambers

$$\text{trig28} = (H0 \cdot H1 \cdot BC)_{top} \times (H0 \cdot H1 \cdot BC)_{bot}. \tag{3.4}$$

As it does not involve the calorimeter, trigger 28 could be use to select hadron tracks not necessarily originating from DIS events, usually produced at low angles, corresponding to low four-momentum transfers ($Q^2 \to 0$), hence the label *photoproduction*. Note that trigger 28 requires the presence of at least one track in each detector half, while trigger 21 fires always that trigger 24 and/or 25 does. This will become relevant in Section 4.3 for the estimation of trigger efficiencies.

3.5 Data production chain

The data acquisition (DAQ) at HERMES consisted of various stages. The first step started at the electronics trailer, a few meters away from the spectrometer. A wealth of cables, under the thick concrete walls protecting from the HERA radiation, connected each detector with the readout electronics, responsible for the digitization of the detector responses. At the command of the trigger system, all detector signals necessary for reconstructing an event were collected from their various components. Simultaneously, and independently of the trigger, information from the status of the detectors and other experimental conditions was recorded every 10 s. These *slow data* contained for instance the beam and target polarizations, luminosity scalars and detector temperatures or operating voltages, and it is used later in Sec 4.1 to decide if the data were taken under optimal running conditions. Both types of data were sorted by the DAQ software and written in EPIO format into DLT data tapes, by a small Linux cluster at the HERMES control room, in the same experimental hall. The EPIO data files were then copied to a taping robot at the DESY main site.

The second part of the data processing was to convert the raw detector data into a format suitable for physics analyses. First, the HERMES decoder software (HDC) interpreted the electronic detector signals as, e.g., hit positions or energy depositions, storing them in an ADAMO database. This decoded detector information was translated into actual tracks by the HERMES reconstruction code (HRC). Finally, by synchronizing the track information with the slow control data, final ADAMO tables were created containing all necessary information for the analyzers. These ready-to-use data files were (and still are nowadays) updated periodically by incorporating latest information on detector calibration, PID parent distributions, tracking efficiencies, etc. Every updated iteration of the HRC data represents a μDST production, named after the year when the data were taken plus a subscript consisting of a letter and a cypher.

The data used in this analysis come from the μDST productions 02d1, 03d1, 04d1, 05d1. One particular improvement of the d1 productions with respect to the μDST productions done before 2009 is the use of a new tracking algorithm, the HERMES tracking code (HTC) based on the Kalman filter method. HTC uses the track information from HRC and performs a new parametrization of the tracks in terms of quality parameters and vertexing probabilities, by taking into account the target magnetic field, the passage through materials and the beam position.

The μDST files are organized into three data levels: *events*, *bursts* and *runs*. The *event* level contains all relevant information from the reconstructed tracks, like momentum, angles, PID, etc. All tracks within the 10 s lap where slow control data are taken form a *burst*. A *run* is the collection of bursts corresponding to a raw EPIO data volume of about 450 Mb, that was collected in about 10 minutes of polarized data taking.

4 Measurement

In this chapter, the measurement of the asymmetries from the detected hadron tracks is discussed in detail. This is done in three steps. First, data are discarded that were taken under bad operating conditions of the spectrometer, beam and target – see Section 4.1. Second, good hadron tracks are selected by imposing the kinematic and geometric cuts described in Section 4.2. One major correction on the data yields is to account for the low efficiency of the electromagnetic calorimeter for triggering on single hadron tracks. This is discussed in Section 4.3. Kinematic distributions of the selected events are shown in Section 4.4. Finally, in Section 4.5, the asymmetries are calculated from their azimuthal moments $A_{UT}^{\sin\phi}$, by a fit of the expected target-spin angular dependence to the data. Different fitting methods are discussed in that section, and their outcome briefly commented in Section 4.6. The calculation of the associated systematic uncertainties will be performed in Chapter 5. Further discussion of the measured asymmetries can be found in Chapter 6.

4.1 Data quality

The information provided by the DAQ system, described in Section 3.5, is used to decide on the quality of the data to be analyzed. In particular, the following criteria were used to select good events:

- Good operating conditions of the PID and tracking detectors. Data were discarded if at least one block of the calorimeter, preshower or the luminosity monitor was not operating properly. These three detectors were constantly monitored online during the data taking runs by the *gain monitoring system* (GMS). Events for which voltage spikes were seen in any detector were discarded.
- The target polarization must be in either the *up* or *down* state, defined with respect to the HERMES coordinate system. The degree of nuclear polarization must be between 30% and 80% as injected by the ABS system (Sec. 3.2) and consistent with the one determined by the TGA/BRP. Values higher than 80% were in any case not achieved experimentally.

- Reasonable beam current (2 mA $\leq I_B \leq$ 50 mA) and luminosity rates (1 Hz $\leq L \leq$ 50 Hz). The lower cut of the beam current discards data resulting in very small counting rates and therefore with a very high statistical uncertainty.
- Data were also discarded if no DAQ information was available.

In addition to the beam current, the DAQ also checked the value of the longitudinal polarization of the beam, necessary for other analysis at HERMES. The beam polarization is only used for this analysis in order to guarantee a helicity-balanced data set, i.e., with no net beam polarization.

In practice, the DAQ information is coded in a list of 32 bit patterns, set to 1 if the good conditions were satisfied. These *bad bits* were checked every 10 seconds by the DAQ system during the data taking. All events recorded within this 10 s interval represent a *burst* of data and share therefore the same data quality parameters.

4.2 Event selection

Events were selected containing at least one charged-hadron track, $ep^{\uparrow} \rightarrow hX$, with h being either a pion or a kaon. Tracks were reconstructed using the HTC method (see Sec. 3.5). The quality of each track was ensured by a set of pre-defined criteria or *cuts*, common to most HERMES analyses:

- The track must originate in the target cell. The origin vertex is calculated by HTC from the crossing of the track with the electron beam. The z_{lab} position of the vertex was required to be within $\pm$18 cm, to avoid events coming from the very end of the target cell where the target gas densities were very low.
- The track must be contained within a trustable or *fiducial* volume of the spectrometer, where proper tracking and identification can be guaranteed. This excludes a few mm of the edges at the calorimeter, the regions around the metal septum plate shielding the electron beam, and the field clamps at both sides of the magnet, where the particles might have undergone interactions with the metal atoms. The precise values of these geometrical cuts are summarized in Table 4.1.
- The momentum of the hadron tracks must be in the range $2 - 15$ GeV where the RICH detector has the highest efficiency for identifying hadrons. Pion tracks with momentum down to 1 GeV were also identified with accuracy, but a common cut at 2 GeV was chosen for all analyzed hadron tracks for consistency.
- The sum of the momenta of all tracks within an event cannot be higher than the beam momentum 27.6 GeV. As the track momentum was reconstructed with an accuracy of 2%, the sum is required to be smaller than 28.2 GeV.
- An energy cluster associated to the track is found in the calorimeter blocks, with a minimum energy deposition of 1.4 GeV. This threshold was set originally such as to detect the scattered lepton from DIS events, but was low enough to trigger on events

	front track	**back track**
vertex position	$\lvert z_{\text{lab}}\rvert \leq 18$ cm	–
front field clamp ($z_{\text{lab}} = 172$ cm)	$\lvert x_{\text{lab}}\rvert \leq 31$ cm	–
septum plate ($z_{\text{lab}} = 181$ cm)	$\lvert y_{\text{lab}}\rvert > 7$ cm	–
rear field clamp ($z_{\text{lab}} = 383$ cm)	$\lvert y_{\text{lab}}\rvert < 54$ cm	$\lvert y_{\text{lab}}\rvert \leq 54$ cm $\lvert x_{\text{lab}}\rvert \leq 100$ cm
calorimeter ($z_{\text{lab}} = 783$ cm)	–	$\lvert x_{\text{lab}}\rvert \leq 175$ cm 30 cm $\leq \lvert y_{\text{lab}}\rvert \leq 108$ cm

Table 4.1. Geometrical requirements for the selected tracks.

consisting of only charged hadrons and no leptons in its geometrical acceptance. The efficiency of the calorimeter is studied in detail in Section 4.3.

- The main physics trigger (21) must fire for the tracks in the event.
- Short tracks not reaching the back chambers after being bent in the magnet were discarded, given the impossibility to identify them.
- Hadron and lepton tracks were differentiated by making use of the PID variable, described in the next section. Hadrons were identified as having a value of PID < 0.
- In an inclusive analysis of hadron tracks, the lepton tracks are in in principle ignored. However, lepton tracks can be used to *tag* the events produced in DIS reactions. The selection of the DIS candidate is done according to a set of kinematic requirements. This is discussed in detail in Appendix C. When reconstructed, lepton tracks were required $PID > 2$ in order to reduce misidentification.

4.2.1 Particle identification

The responses of the PID detectors described in Section 3.3.2 are combined to provide a criterium to discriminate against different particle types. Hadrons are distinguished from leptons by using the combination of the TRD, RICH and preshower detectors with the electromagnetic calorimeter. The RICH detector provides as well a clear distinction between several hadron types, namely pions, kaons and protons.

The idea behind the PID system is connected to Bayes' theorem [134], which relates the *conditional probability* $P(A \mid B)$ of an event A under the condition that event B was observed to its inverse probability $P(B \mid A)$:

$$P(A \mid B) = \frac{P(B \mid A)\ P(A)}{P(B)}. \tag{4.1}$$

This is an useful relation in case that the probabilities $P(B|A)$ and $P(A)$ are known a priori. The term $P(B)$ can be regarded in practice as a normalization factor.

General case Let us consider a particle detector. A certain signal X in the detector can be attributed to several particle types. The conditional probability $P(i \mid X)$ that the signal was caused by a particle of type i is given by Bayes' theorem as

$$P(i \mid X) = \frac{P(X \mid i)\ P(i)}{\sum_i P(X \mid i)\ P(i)}. \tag{4.2}$$

Here,

- $P(i)$ is the probability to observe a particle of type i in the detector. This is given by the *flux factor* ϕ^i of the particle, which is usually a function of the momentum and angle of the particle, and can be measured;
- $P(X \mid i)$ is the probability that a particle of type i leaves a specific signal X in the detector D. This probability distribution is characteristic of each particle type and detector type and is usually referred to as the *parent distributions* $\mathcal{L}^i_D$. These can be measured for example using test beams, or in Monte Carlo simulations [135]. The parent distributions from several detectors D can be combined into a single probability distribution $\mathcal{L}^i = \prod_D \mathcal{L}^i_D$.
- The sum of all probabilities is normalized to unity $\sum_i P(i \mid X) = 1$.

Using then the notation

$$\begin{aligned} \mathcal{P}^i &\equiv P(i \mid X) \\ \phi^i &\equiv P(i) \\ \mathcal{L}^i &\equiv P(X \mid i) \end{aligned}$$

and assuming that all particle fluxes ϕ^i and parent distributions $\mathcal{L}^i$ of n different particle types in the detector set are known, the probability $\mathcal{P}^i$ that a certain signal was caused by a particle i is then given by

$$\mathcal{P}^i = \frac{\phi^i \mathcal{L}^i}{\sum_n \phi^n \mathcal{L}^n}. \tag{4.3}$$

Hadron - lepton separation The discrimination of hadrons against leptons can be effectively done with the PID detectors at HERMES as the responses of these detectors to leptons and hadrons are significantly different. The parent distributions of leptons $\mathcal{L}^e$ and hadrons $\mathcal{L}^h$ are well defined as analytical expressions fitted to test beams or HERMES data. The hadron and electron fluxes are determined from an iterative procedure [135] and are usually combined into the flux ratio

$$\Phi = \frac{\phi^h}{\phi^e}. \tag{4.4}$$

The probabilities of detecting a hadron or lepton can be expressed then as

$$\mathcal{P}^e = \frac{\mathcal{L}^e}{\mathcal{L}^e + \Phi \mathcal{L}^h} \qquad \mathcal{P}^h = \frac{\mathcal{L}^h}{\Phi^{-1}\mathcal{L}^e + \mathcal{L}^h}, \tag{4.5}$$

such that the sum of both is normalized to unity

$$\mathcal{P}^e + \mathcal{P}^h = 1. \tag{4.6}$$

The most important particle identification quantity at HERMES is defined by the logarithmic ratio

$$\begin{aligned} \mathrm{PID} &= \log_{10} \frac{\mathcal{P}^e}{\mathcal{P}^h} \\ &= \log_{10} \frac{\mathcal{L}^e}{\Phi \mathcal{L}^h} \\ &= \log_{10} \frac{\mathcal{L}^e}{\mathcal{L}^h} - \log_{10} \Phi. \end{aligned} \tag{4.7}$$

The use of a logarithmic ratio to combine both probabilities is very convenient and provides a probability distribution that intuitively resembles the response of the PID detectors. Positive values of the PID variable indicate that the particle is most probably a lepton, while negative values identify hadrons. For a ratio equal to zero, the particle is with equal probability a hadron or a lepton.

The responses from the several detectors can be combined as

$$\mathrm{PID} = \log_{10} \left(\prod_D \frac{\mathcal{L}^e_D}{\mathcal{L}^h_D} \right) = \sum_D \log_{10} \frac{\mathcal{L}^e_D}{\mathcal{L}^h_D}. \tag{4.8}$$

This is calculated separately for the six modules of the TRD detector and combined under the variable

$$\mathrm{PID}_5 = \log_{10} \left(\prod_{i=1}^{6} \frac{\mathcal{L}^e_{TRD_i}}{\mathcal{L}^h_{TRD_i}} \right) \tag{4.9}$$

and for the parent distributions of the calorimeter, preshower and RICH detectors as

$$\mathrm{PID}_3 = \mathrm{PID}_{\mathrm{calo}} + \mathrm{PID}_{\mathrm{pre}} + \mathrm{PID}_{\mathrm{RICH}} = \log_{10} \frac{\mathcal{L}^e_{\mathrm{calo}} \mathcal{L}^e_{\mathrm{pre}} \mathcal{L}^e_{\mathrm{RICH}}}{\mathcal{L}^h_{\mathrm{calo}} \mathcal{L}^h_{\mathrm{pre}} \mathcal{L}^h_{\mathrm{RICH}}}. \tag{4.10}$$

The PID variable becomes then

$$\mathrm{PID} \equiv \mathrm{PID}_3 + \mathrm{PID}_5 - \log_{10} \Phi, \tag{4.11}$$

and a convenient hadron-lepton separation is obtained by cutting on the zero value

$$\begin{aligned} \mathrm{PID} > 0 : &\quad \text{leptons} \\ \mathrm{PID} < 0 : &\quad \text{hadrons.} \end{aligned}$$

The PID distribution of events from the selected data is shown in Fig. 4.1, from which is clear that the probability distributions of hadrons and leptons are well distinguished by using the PID variable. The tails of the distributions can nevertheless extend beyond the zero value, contaminating the other sample. This can be be conveniently studied with the formalism described below.

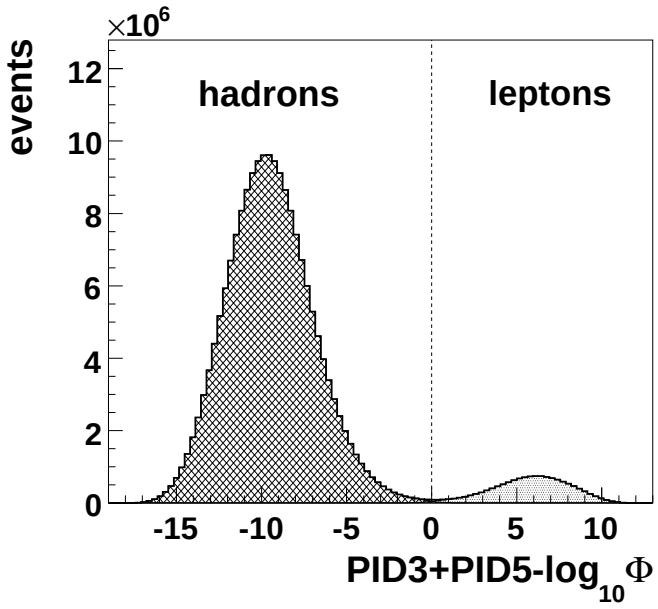

Figure 4.1. The PID distribution of events. The dotted vertical line represents the cut at PID = 0 used to distinguish hadrons.

In terms of the PID variable, the probabilities for detecting a lepton and hadron can be written, using equations 4.6 and 4.8, as

$$\mathcal{P}^e = \frac{10^{\mathrm{PID}}}{1+10^{\mathrm{PID}}} \qquad \mathcal{P}^h = \frac{1}{1+10^{\mathrm{PID}}}. \tag{4.12}$$

These distributions are plotted in Fig. 4.2. The use of a logarithmic y-axis allows to see the mixing of both distributions around the cut value. The black thick line is the same PID distribution as Fig. 4.1, the line-shaded histogram represents $N_{\mathrm{PID}} \cdot \mathcal{P}^h$ and the gray-shaded histogram, $N_{\mathrm{PID}} \cdot \mathcal{P}^e$, where N_{PID} is the total number of events in each PID bin.

The *lepton contamination* $\mathcal{C}_e$ of the hadron sample accounts for the events of $\mathcal{P}^e$ below $\mathrm{PID}_{cut} = 0$, and can be calculated as

$$\mathcal{C}_e = \frac{\int_{-\infty}^{\mathrm{PID}_{cut}} \mathcal{P}^e d\mathrm{PID}}{\int_{-\infty}^{\mathrm{PID}_{cut}} (\mathcal{P}^e + \mathcal{P}^h) d\mathrm{PID}} = \frac{\int_{-\infty}^{\mathrm{PID}_{cut}} \mathcal{P}^e d\mathrm{PID}}{\int_{-\infty}^{\mathrm{PID}_{cut}} d\mathrm{PID}}. \tag{4.13}$$

In practice, these integrals can be calculated by summing over the event sample, for all events that satisfy $\mathrm{PID} < \mathrm{PID}_{cut}$

$$\mathcal{C}_e = \frac{\sum_{\mathrm{PID}<0} \frac{10^{\mathrm{PID}}}{1+10^{\mathrm{PID}}}}{\sum_{\mathrm{PID}<0} 1}. \tag{4.14}$$

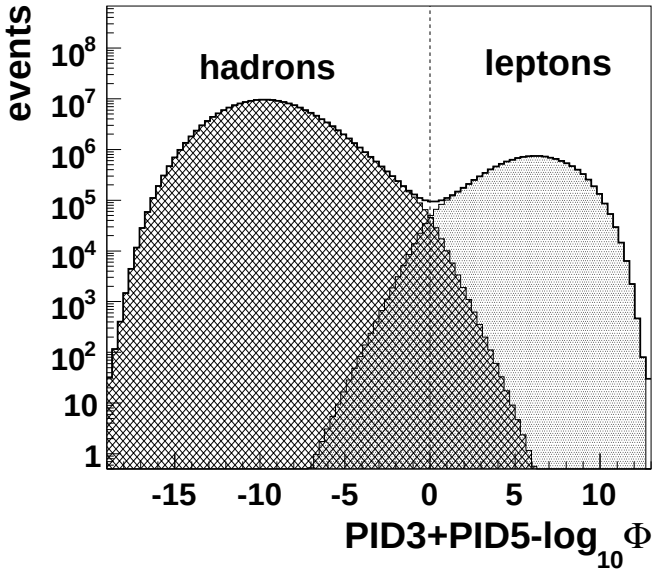

Figure 4.2. The PID distribution of hadronic and leptonic events. The dotted vertical line represents the cut at PID = 0 used to distinguish hadrons.

In the same fashion, the *hadron detection efficiency* $\mathcal{E}_h$ accounts for the events of $\mathcal{P}^h$ with PID $>$ PID$_{cut}$ and therefore discarded by the cut on the PID value

$$\mathcal{E}_h = \frac{\int_{-\infty}^{\mathrm{PID}_{cut}} \mathcal{P}^h d\mathrm{PID}}{\int_{-\infty}^{\infty} \mathcal{P}^h d\mathrm{PID}} \longrightarrow \frac{\sum_{\mathrm{PID}<0} \frac{1}{1+10^{\mathrm{PID}}}}{\sum_{\mathrm{PID}<0} \frac{1}{1+10^{\mathrm{PID}}}}. \tag{4.15}$$

For the sample of analyzed hadron tracks, the lepton contamination was smaller than 0.06%, with a hadron detection efficiency of 99.94%. The same formalism can be applied to the lepton sample. As the total number of collected leptonic events is significantly smaller, a cut of PID < 2 was chosen to guarantee a clean sample with misidentification below 2%.

Identification of charged hadrons Pions and kaons resulting from interactions in the target cell were identified with high precision over the momentum range $2 - 15$ GeV by the RICH detector. In order to account for possible misidentification of the detected hadrons, the efficiency of the RICH detector was investigated by determining the probability $P(h_{id}|h_{\mathrm{true}})$ that a hadron of a particular species h_{true} is identified as h_{id}. This can be accomplished by using a PYTHIA simulation, where both variables (the real hadron type and the reconstructed) are known.

Taking into account the three hadron types distinguishable by the RICH detector, pions, kaons and protons, the yield of hadrons N_h^{id} identified as type h can be related to the yield

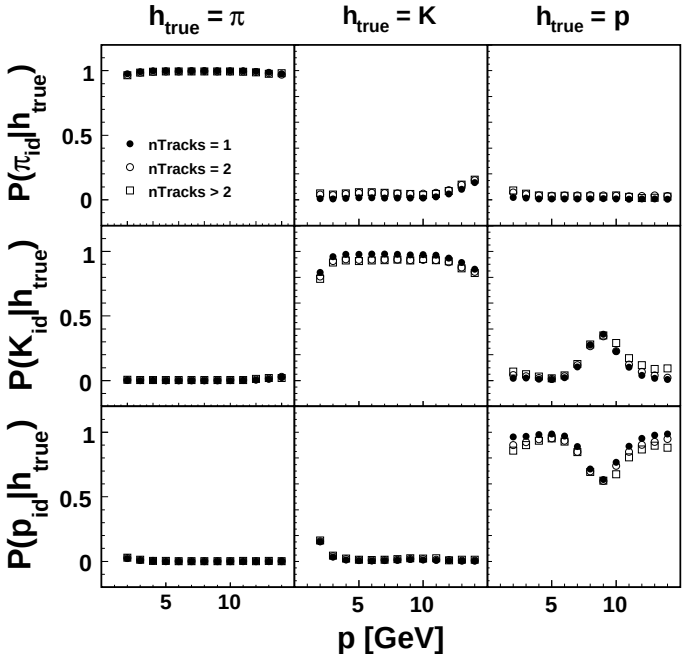

Figure 4.3. $\mathcal{P}$-matrices, i.e., the probability that a hadron of type h_{true} is identified as h_{id}, as a function of momentum. Columns represent true hadron type, and rows identified type.

of true hadron types N_h^{true} by the, so called, $\mathcal{P}$-matrix

$$\begin{pmatrix} N_\pi^{id} \\ N_K^{id} \\ N_p^{id} \end{pmatrix} = \begin{pmatrix} P(\pi_{id}|\pi_{\text{true}}) & P(\pi_{id}|K_{\text{true}}) & P(\pi_{id}|p_{\text{true}}) \\ P(K_{id}|\pi_{\text{true}}) & P(K_{id}|K_{\text{true}}) & P(K_{id}|p_{\text{true}}) \\ P(p_{id}|\pi_{\text{true}}) & P(p_{id}|K_{\text{true}}) & P(p_{id}|p_{\text{true}}) \end{pmatrix} \cdot \begin{pmatrix} N_\pi^{\text{true}} \\ N_K^{\text{true}} \\ N_p^{\text{true}} \end{pmatrix}, \tag{4.16}$$

where the elements of the off-diagonal are the probabilities that hadrons are misidentified.

Inverting the $\mathcal{P}$-matrix, the true yield of hadrons can then be calculated from the measured yields. This procedure is known as **RICH unfolding**. A track identified as being of type h_{id} is weighted in the true pion yield by the element $P^{-1}(\pi_{\text{true}}|h_{id})$ of the $\mathcal{P}^{-1}$-matrix, and as $P^{-1}(K_{\text{true}}|h_{id})$ in the true kaon yield. The *true* total number of hadron tracks of each species is then obtained by summing these weights (w_h^{true}) over all tracks

$$N_h^{\text{true}} = \sum_{\text{tracks}} w_h^{\text{true}} = \sum_{\text{tracks}} P^{-1}(h_{\text{true}}|h_{id}). \tag{4.17}$$

The $\mathcal{P}$-matrix was calculated specifically with the set of data selection cuts used for this analysis from the PYTHIA sample described in Section 5.2. Possible kinematic dependences were taken into account by calculating the $\mathcal{P}$-matrix separately in bins of 1 GeV of the hadron momentum. Also the number of hadrons detected in each detector half was considered, as this determines the algorithm used in the ring pattern recognition, see Section 3.3.2. The resulting probabilities for each case are plotted in Fig. 4.3.

4.2.2 RICH hot spots

During the analysis of inclusive data, an excess of events was found in the distribution of kaons in the θ_x-θ_y plane[1]. This is most noticeable for kaons with transverse momentum larger than 1 GeV. This can be seen in Fig.4.4. Such excess is located in two well-defined geometrical areas of the top part of the detector, from now on referred to as *hot spots*. A shortage of events is found in the same areas for the pion distributions, thus being a clear sign of misidentification of pions into kaons. These events must then be removed from the data sample.

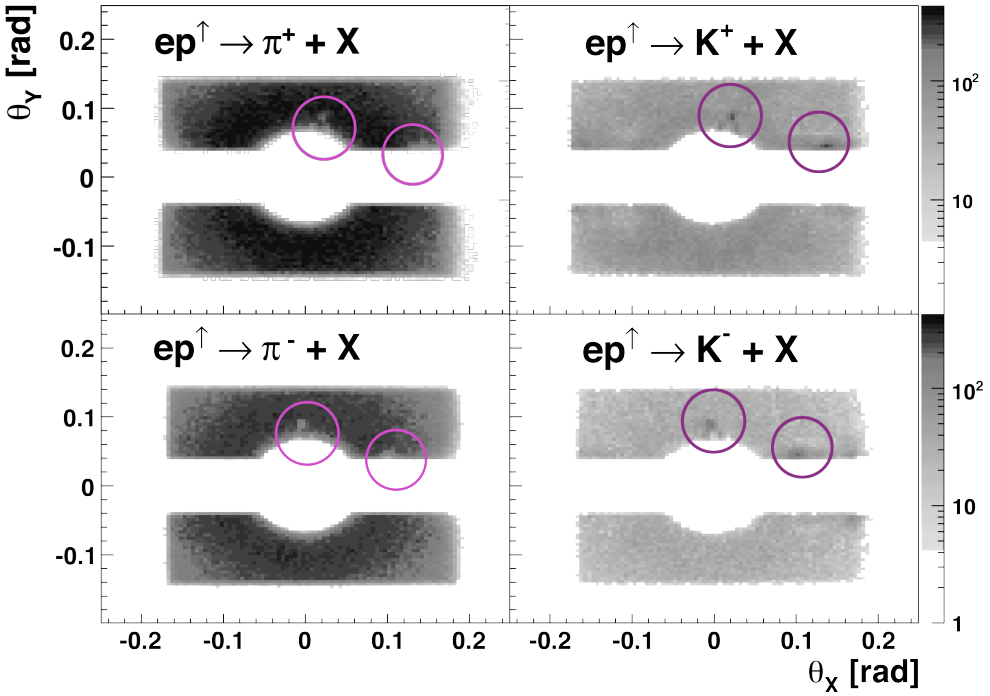

Figure 4.4. Distribution of events in the transverse plane, defined by the polar coordinates θ_x and θ_y.

The reason for this misidentification was found to be in two malfunctioning PMTs which, during the time period in which the data were taken, were located in the corresponding regions of the top part of the RICH detector where the hot spots are found. The distribution of events at the front face of the PMT matrix ($z_{\text{lab}} = 550$ cm) of the RICH is shown in Fig. 4.5 for hadrons with $p_T > 1$ GeV. The hot spots are clearly visible in this case as well. Note, in this figure, the effect of the deflection of charged particles in the magnetic field of the spectrometer magnet.The problem of malfunctioning PMTs at these positions was known from online control plots and monitoring during the data taking period, but this is the first time that such an effect was noticed in the hadron distributions. Several tests were done in order to gain insight in possible kinematical dependences of the events within the hot spots. No particular dependences were found, supporting the idea that these events are misidentified due to hardware problems.

[1]The variables θ_x and θ_y are defined in Eq. (4.22).

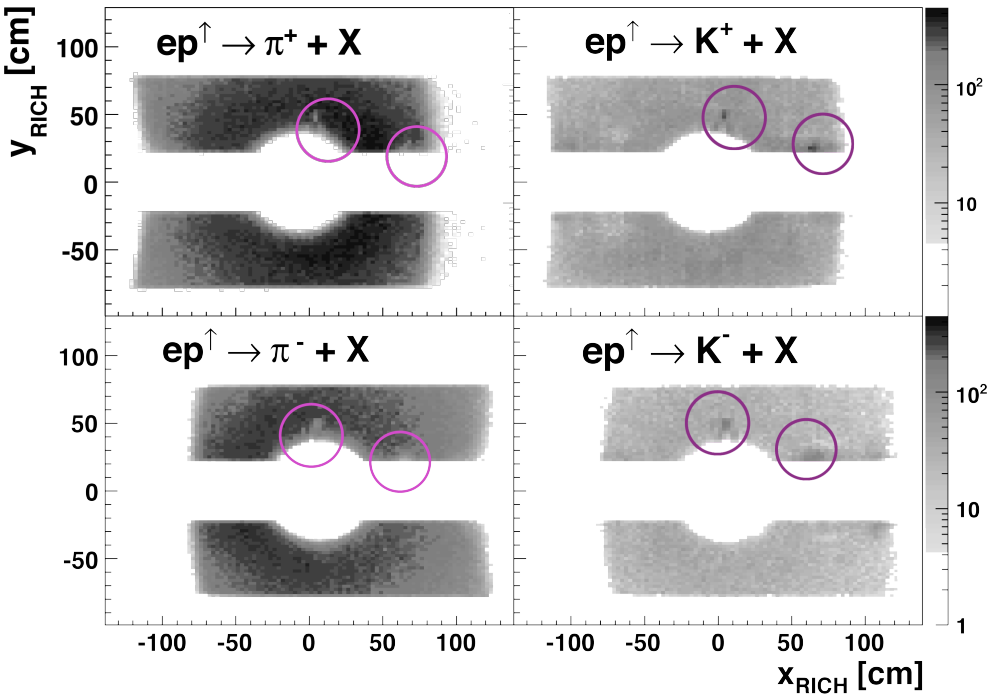

Figure 4.5. Distribution of events in the transverse plane at the coordinates of the PMT matrix of the RICH detector ($z = 550$ cm).

Removal of hot spots The hot spots are present at all values of the momentum of the hadrons, although due to the large statistics at lower momentum values, they are most visible in the range $p \in [8, 10]$ GeV or for hadrons with transverse momentum larger than 1 GeV. Events were removed according to the following ellipses, optimized to cover the surface of each spot

$$\frac{(x_{\text{RICH}} - 4)^2}{9^2} + \frac{(y_{\text{RICH}} - 45)^2}{12^2} = 1 \qquad \text{for the upper spot,} \tag{4.18}$$

$$\frac{(x_{\text{RICH}} - 65)^2}{15^2} + \frac{(y_{\text{RICH}} - 25)^2}{5^2} = 1 \qquad \text{for the lower spot.} \tag{4.19}$$

The same ellipses were used for pions and kaons since the mis-identification stems from a geometrically well defined hardware problem. Note that the circles drawn in the above figures are only for visual reference. The ellipses used to cut the events are much narrower, fitted to the hot spots.

4.3 Trigger Efficiencies

Trigger efficiencies account for the effectivity of a detector in detecting a particle of a certain type. The efficiency of the main physics trigger (21) is the product of the efficiencies of each detector involved, namely

$$\epsilon(\text{trig}\,21) = \epsilon(H_0) \cdot \epsilon(H_1) \cdot \epsilon(H_2) \cdot \epsilon(\text{calo}). \tag{4.20}$$

The hodoscopes H_0, H_1 and H_2 are known to have a good response ($\epsilon \sim 1$) to both hadron and lepton tracks [138,139]. The calorimeter, on the other hand, relies on the energy deposition in its lead-glass blocks. In the case of lepton tracks, the energy deposition is generally much larger than the minimum threshold of 1.4 GeV, thus leading to $\epsilon_{\text{leptons}}(\text{calo}) \sim 1$. Hadrons, however, deposit much less energy in the calorimeter blocks than leptons, often smaller than 1.4 GeV. A lower efficiency of the calorimeter is thus expected for events with only hadron tracks and no leptons. This happens generally at low-Q^2 events, where the beam lepton is scattered at low angles ($\theta_e^2 \propto Q^2$) and therefore not entering the calorimeter geometry.

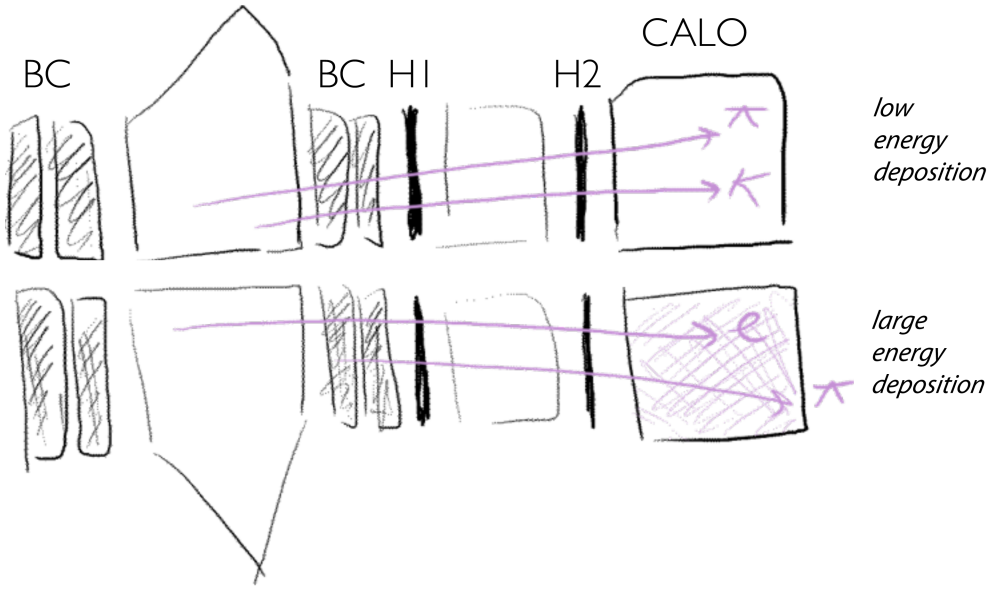

Figure 4.6. Schematic picture of the energy deposition in the calorimeter

Why correcting by the trigger efficiency? In the measurement of a cross section ratio, trigger efficiencies are expected to cancel out as they do not depend on the target polarization but rather on the kinematics and spatial configuration of the event [138]. In our particular case, however, since Q^2 is correlated with the hadron transverse momentum p_T, we *know* that more hadrons are collected at large transverse momentum, where a larger number of events containing a lepton are expected. This excess of hadrons at large p_T is artificially induced by the operating conditions of the calorimeter. In such case, the trigger efficiency is *folded* with the detector acceptance. In other words, the trigger efficiency for hadron tracks depends, in addition to the hadron kinematics and position, on the kinematics and geometrical distribution of lepton tracks. This is in principle a complex dependence, and

may not cancel out in the asymmetry ratio, thus affecting the measured asymmetries. For this reason, the data yields must be corrected by the calorimeter efficiency. The way to proceed is the following:

1. Calculate calorimeter efficiency for single hadron tracks The trigger efficiency of the calorimeter is calculated from events containing only *single* hadron tracks. This is done without requiring any of the data quality cuts described in Section 4.2, as these would interfere with the actual efficiency.

The calorimeter efficiency can be obtained, given the HERMES trigger scheme (Section 3.4), by comparing the cases in which both trigger 21 and 28 fired to the cases in which only trigger 28 did

$$\epsilon(\text{calo}) = \frac{N_{28\&21}}{N_{28}}. \tag{4.21}$$

Note that trigger 28 requires the simultaneous detection of a track in the top and bottom parts of the spectrometers, and that the BC chambers are also required to fire. Optimally one would use trigger equivalent to trigger 21 but without the requirement on the calorimeter. But this is the best we can do[2].

In order to increase the sensibility of the correction procedure, the calorimeter efficiency is calculated as a function of the momentum of the hadron and its spatial coordinates. The latter can be properly characterized by the θ_x and θ_y coordinates, defined as

$$\begin{aligned} \theta_x &= \arctan(\tan\theta \cdot \sin\phi) \\ \theta_y &= \arctan(\tan\theta \cdot \cos\phi). \end{aligned} \tag{4.22}$$

The bins in p, θ_x, θ_y used are defined in Table 4.2. The resulting values for the efficiency are kept in a file, that will later serve as a **look-up** table for the calorimeter efficiency. The calorimeter efficiency for single hadron tracks in the central region of the calorimeter is essentially the same for all hadron types, being about 0.2 for the lowest bin in momentum, and rising in a kind of logarithmic way up to 0.6 for the larger momentum bins. Kaons have slightly smaller values than pions and protons. In the detector edges, due to the bending of the particles in the magnet field, the efficiency is different for positive and negative charged particles, i.e., for the left-end side of the detector ($\theta_x \sim -0.2$) the efficiency for π^+ is about twice the efficiency for π^- – towards the right-end side, this trend is reversed. A graphical representation of the efficiency as a function of the hadron momentum, averaged over the 8×8 bins of θ_x and θ_y can be found in Fig. E.28.

An uncertainty can be assigned to the trigger efficiency, according to the formula

$$\delta\epsilon = \sqrt{\frac{(N_{28\&21}+1)(N_{28}-N_{28\&21}+1)}{(N_{21}+2)^2(N_B+3)}}, \tag{4.23}$$

that takes into account that the error should be smaller for efficiencies approaching the unity value. Additionally, it was also checked whether the efficiencies had any dependence on the target spin, as this could create artificial asymmetries. No significant dependence was found within the uncertainties..

[2]When the HERMES trigger scheme was planned back in the 90s, the goal of the collaboration was not really to perform analyses of inclusive hadrons!

Variable	Bins	Bin borders
p	8	$[2, 2.8, 3.1, 4, 5, 6.5, 8, 10, 15]$
θ_x	8	$[-0.2, -0.09, -0.04, -0.01, 0, 0.01, 0.04, 0.09, 0.2]$
θ_y	8	$[-0.15, -0.09, -0.06, -0.05, 0, 0.05, 0.06, 0.09, 0.15]$

Table 4.2. Bins used for calculation and correction of the data yields by the calorimeter efficiency.

2. Correct data yields With the efficiency look-up table in hand, one can proceed to correct the particle yields. This is done at extraction level, i.e., in the same piece of analysis code as described in Section 4.2. Each hadron track is weighted by the calorimeter efficiency associated to *that* event.

Note that correcting each track separately by *its* associated trigger efficiency would be wrong, as this only accounts for the efficiency of *single* tracks[3]. If several hadrons deposit energy at the same turn, the efficiency of the calorimeter correspondingly must increase.

A solution to this is to take into account all other tracks detected simultaneously. One must calculate then the trigger efficiency separately for each track according to its p, θ_x, θ_y, and then combine the trigger efficiencies for all tracks in that event into an average efficiency $\langle\epsilon\rangle$. Each track in the same event is then weighted by the same $\langle\epsilon\rangle$.

The average is actually done in two steps

1. First, one must consider the different probabilities for a given track to be of a certain hadron species, according to the PID identification of the RICH detector. This turns into a RICH-weighted efficiency, for each single track, given by

$$\epsilon_w = \frac{\alpha_\pi\,\epsilon_\pi + \alpha_K\,\epsilon_K + \alpha_p\epsilon_p}{\alpha_\pi + \alpha_K + \alpha_p}, \tag{4.24}$$

   where $\epsilon_{\pi,K,p}$ are the trigger efficiencies, as read from the look-up table, for the p, θ_x, θ_y of a given track, according to the hypotheses of that track being a pion, kaon or proton.

2. Second, once the ϵ_w are calculated for each track in the event, these are combined into an average efficiency for the whole event as

$$\langle\epsilon\rangle = 1 - \prod_{\text{event}} (1 - \epsilon_w). \tag{4.25}$$

   This operation corresponds to a logical-OR, i.e., the inverse of the product of the inverses. In the cases that a lepton track is also found in the event, the trigger efficiency for *all* tracks in the event is set manually to 1.

The calorimeter efficiency in each kinematical bin, averaged over the entire data sample, is shown in Fig. 4.7. These average values represent the average over all tracks, calculated according to Eq. (4.25), and are therefore generally larger than the efficiencies for triggering

[3]The multiplicity of tracks was checked to be larger than one in a significant fraction of events, particularly for hadrons with large transverse momentum.

on single hadron tracks. The average efficiency shows a clear dependence on the hadron energy, i.e., on both p_T and x_F. Notice that, at large p_T and x_F, where it is more likely to detect the scattered electron (which contributes with $\langle\epsilon\rangle = 1$), a "boost" of the average efficiency values is seen. These average values are only shown for illustrative purposes, but they are *not* used anywhere in the analysis. See also Figs. E.26, E.27 and E.28.

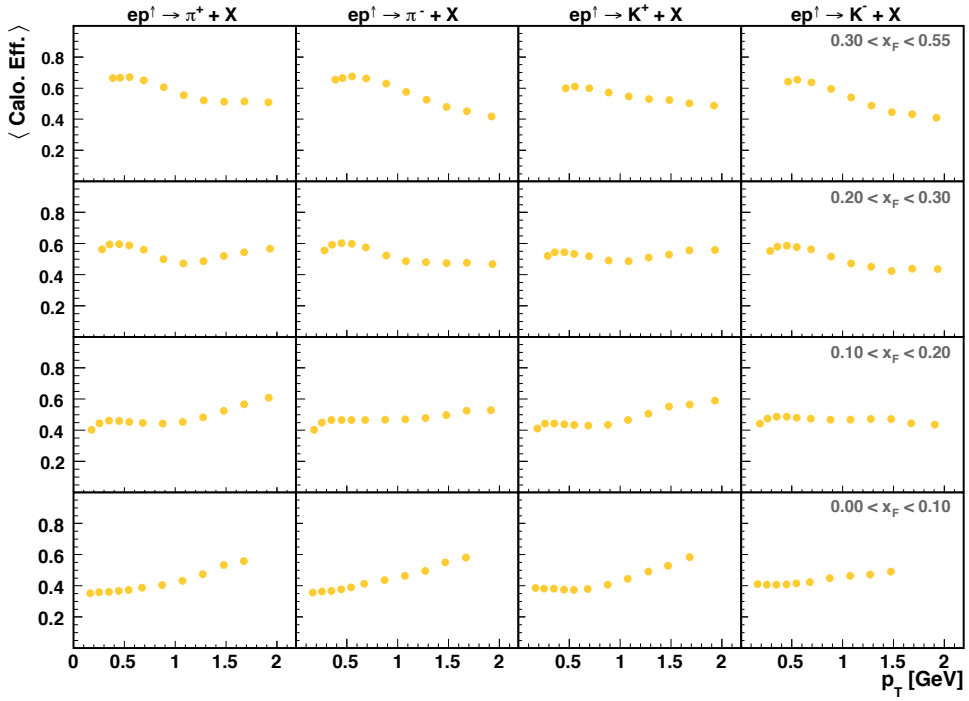

Figure 4.7. Average calorimeter efficiency in each bin of the hadron transverse momentum used in the analysis.

4.3.1 Effect on the data

The comparison between the data yields before and after the correction by the calorimeter efficiency can be seen in Fig. 4.8 as a function of p_T and x_F. The kinematical distributions of the corrected data are slightly shifted towards smaller values of p_T and x_F. This reflects the fact that at large hadron momenta, for which it is more likely that the scattered lepton ends up in the calorimeter acceptance, more hadrons are detected due to the influence of the energy deposited by the lepton on the trigger system. The impact of the calorimeter efficiency is more noticeable in the angular distributions of Fig. 4.10. The detected hadrons are shifted towards lower polar angles. Lower θ implies lower momentum transfer Q^2, reflecting again the influence of the lepton tracks, typically detected in collisions at large Q^2. The comparison of the ϕ distributions is particularly interesting, showing how the data are shifted from the center of the detector towards the outer sides.

4.4 Kinematic distributions

The selected hadronic events are plotted in the left panel of Fig. 4.8 as a function of the transverse momentum of the hadrons, and in the right panel as a function of x_F. The majority of events are distributed at both low p_T and x_F, the fraction of those with $p_T > 1$ GeV or $x_F > 0.3$ being significantly small. Both kinematic variables are related to the momentum of the hadron and are therefore correlated, as can be seen in Fig. 4.9.

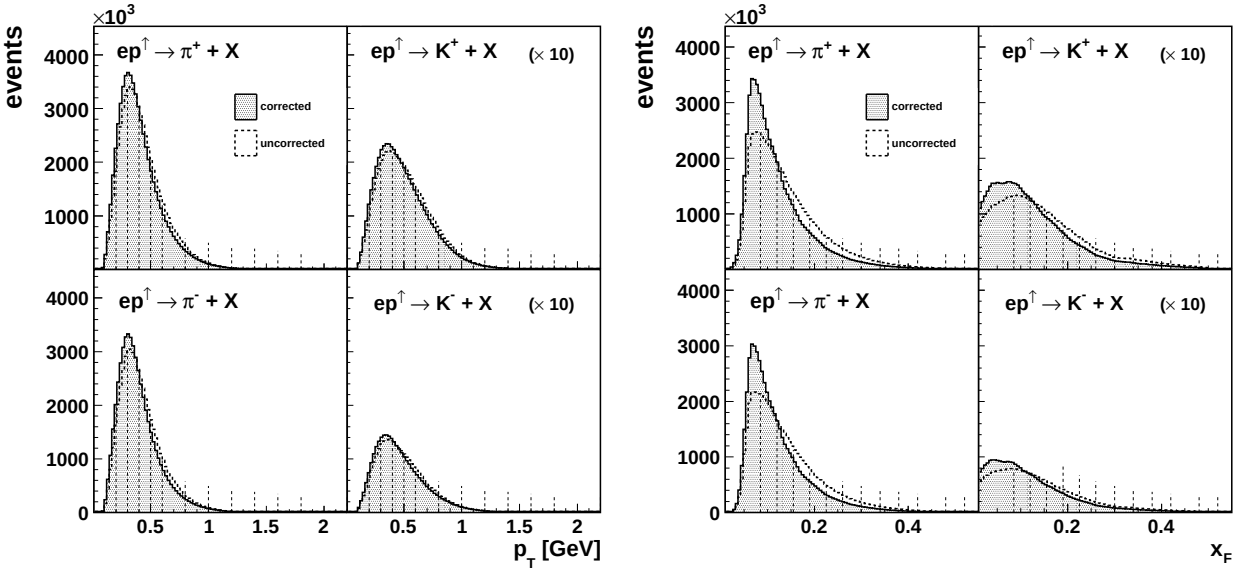

Figure 4.8. Distribution of collected events as a function of p_T (left) and x_F (right). The vertical dotted lines correspond to the bins defined in the first two rows of Table 4.3, respectively. The histograms for kaons are multiplied by a factor of 10. The histograms with the black (dotted) line represent the data after (before) correction by the calorimeter efficiency.

Variable	Bins	Bin borders
p_T	12	[0, 0.2, 0.3, 0.4, 0.5, 0.6, 0.8, 1.0, 1.2, 1.4, 1.6, 1.8, 2.2] GeV
x_F	12	[0, 0.085, 0.120, 0.155, 0.190, 0.225, 0.26, 0.30, 0.34, 0.38, 0.42, 0.48, 0.55]
x_F	4	[0, 0.1, 0.2, 0.3, 0.55]
p_T	12	[0, 0.2, 0.3, 0.4, 0.5, 0.6, 0.8, 1.0, 1.2, 1.4, 1.6, 1.8, 2.2] GeV
p_T	4	[0, 0.33, 0.66, 1.0, 2.2] GeV
x_F	12	[0, 0.085, 0.120, 0.155, 0.190, 0.225, 0.26, 0.30, 0.34, 0.38, 0.42, 0.48, 0.55]
ϕ	20	[0.0, 0.27, 0.54, 0.81, 1.08, 1.35, 2.02, 2.29, 2.56, 2.83, 3.10, 3.37, 3.64, 3.91, 4.18, 4.45, 5.17, 5.44, 5.71, 5.98, 6.29] rad

Table 4.3. Kinematic bins used in the analysis.

Kinematic binning The dotted lines in the above mentioned figures illustrate the chosen bins in which the asymmetries are calculated. The exact value for each bin boundary is given in Table 4.3. The bins for the p_T and x_F distributions are chosen to be finer in the region where the statistics are larger in order to increase the sensibility of the measurement to the kinematical dependence of the asymmetries. A *two-dimensional* analysis was also performed, using the bins defined in the two bottom rows of Table 4.3. In this case, the asymmetry are calculated as a function of p_T in *four* different slices of x_F, and as a function of x_F in four different slices of p_T.

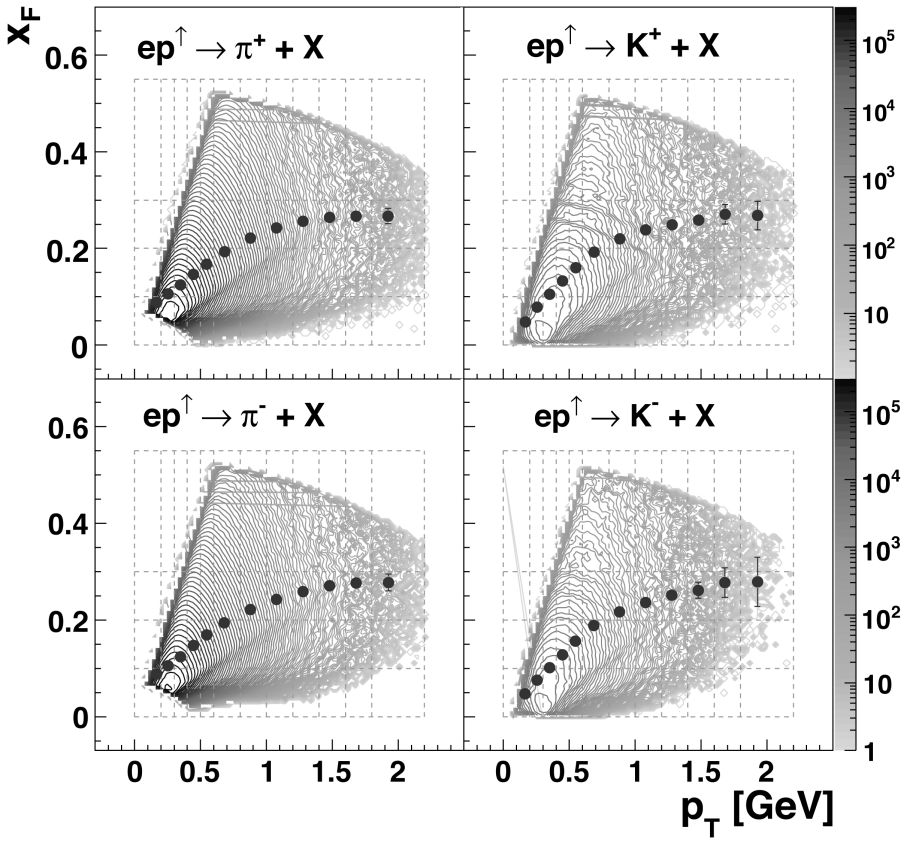

Figure 4.9. Distribution of events in the p_T-x_F kinematic plane. The dotted lines correspond to the bins defined in the third row of Table 4.3. The points represent the average x_F value in each bin of p_T.

Angular dependence The distribution of the collected data as a function of the relevant angular variables, ϕ and θ, is plotted in Fig. 4.10. The azimuthal angle ϕ is crucial for the calculation of spin asymmetries, done in the next section. Note that the ϕ distribution has been shifted by $\pi/2$ to show the actual azimuthal acceptance of the HERMES spectrometer. The polar angle θ is used to determine the hadron transverse momentum from the expression $\mathbf{p}_T = \mathbf{p}\ \cos\theta$. These angular distributions reveal the acceptance of the HERMES spectrometer. The empty area around $\phi \sim \pi$ corresponds to the gap between the top and bottom parts of the spectrometer, which are separated by a corresponding polar angle $\theta = 40$ mrad.

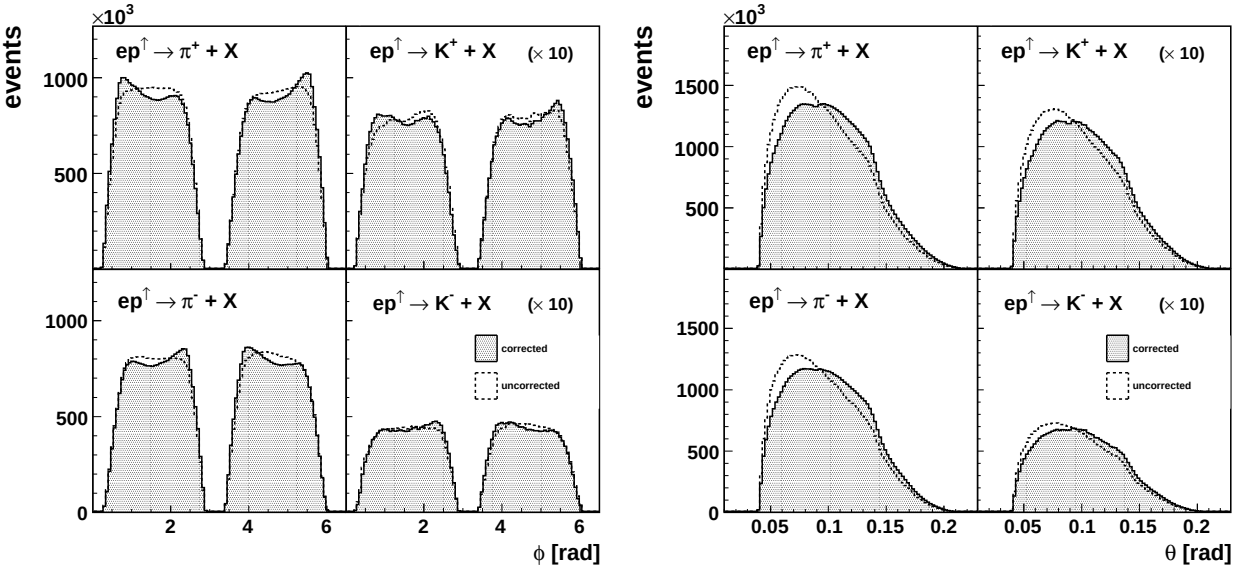

Figure 4.10. Distribution of collected events as a function of ϕ (left) and θ (right). The histograms for kaons are multiplied by a factor of 10. The histograms with the black (dotted) line represent the data after (before) correction by the calorimeter efficiency.

4.4.1 Collected statistics

The total statistics collected amount to about 120 million pion tracks and 8 million kaon tracks. Exact numbers are given in Table 4.4, corresponding to N_h^{true}, see Eq. (4.17), i.e.,

	π^+	π^-	K^+	K^-	all hadron tracks
02d1	5.027.166	4.308.669	457.901	255.121	10.704.173
03d1	2.926.625	2.491.391	254.928	140.805	6.378.049
04d1	17.628.295	15.066.379	1.533.550	856.286	37.950.221
05d1	36.426.365	31.146.723	3.175.454	1.789.987	78.443.265
all data	62.008.451	53.013.161	5.421.833	3.042.200	133.475.708

Table 4.4. Collected hadron tracks for each data production.

corrected by the RICH unfolding technique. The above given yields do not include the correction by the trigger efficiency. These hadron tracks are well defined and their relevant properties (momentum, direction and particle type) precisely determined, and are therefore the starting point of the data analysis itself.

4.5 Extraction of $A_{UT}^{\sin\phi}$ amplitudes

As it was already discussed in Section 2.8, a dependence on the target spin in inclusive particle production, $e\,p^{\uparrow} \to h\,X$, can result into a spin asymmetry A_{UT} of the particles produced, related to the azimuthal angle ϕ

$$A_{UT} \equiv \frac{\sigma_{UT}(\phi)}{\sigma_{UU}}. \tag{4.26}$$

With the use of a transversely polarized target and the spin pointing in the direction of $\mathbf{S}_\perp$, and only one reaction plane defined by the transverse momentum $\mathbf{p}_T$ of the produced/scattered particle and the momentum of the incoming beam particle $\mathbf{k}$, the only possible dependence of the spin-dependent part of the cross section on these magnitudes is

$$\sigma_{UT} \propto \mathbf{S}_\perp \cdot (\mathbf{k} \times \mathbf{p}_T). \tag{4.27}$$

This is the only combination of these three vectors that conserves parity[4]. As the cross product $(\mathbf{k} \times \mathbf{p}_T)$ results in a vector perpendicular to the hadron production plane, parity invariance allows A_{UT} to be different from zero only if the target spin has a component $S_\perp$ perpendicular to such plane. Working out the mixed product, the term becomes

$$\mathbf{S} \cdot (\mathbf{k} \times \mathbf{p}_T) = S_\perp \ \cos\left(\frac{\pi}{2} - \phi\right) \ (k\,p_T) = S_\perp\, k\, p_T \ \sin\phi, \tag{4.28}$$

such that the $\sin\phi$ dependence of the polarized cross section produces an asymmetrical distribution of the outgoing particles in the plane transverse to the beam direction. If the distribution of particles is analyzed in symmetric bins of the azimuthal angle ϕ with respect to the target spin, this results into a **left-right** asymmetry. An equivalent asymmetric distribution must be observed when comparing data, for the same bin of ϕ, when reversing the target spin between two opposite directions, thus resulting into a **target-spin** asymmetry.

Left-right asymmetry A_{UT} can be measured from the count rates of particles produced to the left (N_L) and the right (N_R) of the target spin vector[5]

$$A_{UT} = \frac{1}{\langle P\rangle}\frac{N_L^{\uparrow} - N_R^{\uparrow}}{N_L^{\uparrow} + N_R^{\uparrow}} \equiv A_N, \tag{4.29}$$

with $\langle P\rangle$ the average target polarization that accounts for the fact that, in practice, not all target centers have their spin polarized in the same direction. A left-right asymmetry defined this way is conventionally called A_N, for it is an asymmetry in the plane *normal* to the target spin. The asymmetry is then determined by comparing the data yields in different bins of ϕ, which span symmetrical regions of the detector with respect to the target spin. In the case of HERMES, the data taken with opposite target spin polarizations ($\uparrow$ and $\downarrow$) can be combined into

$$A_N = \frac{1}{\langle P\rangle}\frac{(N_L^{\uparrow} + N_R^{\downarrow}) - (N_R^{\uparrow} + N_L^{\downarrow})}{(N_L^{\uparrow} + N_R^{\downarrow}) + (N_R^{\uparrow} + N_L^{\downarrow})}. \tag{4.30}$$

[4] See note under Eq. (2.76).
[5] See Fig. 3.6.

Here it is taken into account that the geometrical region spanned by a ϕ bin changes from the left to the right part of the detector as the target spin polarization changes between the up and down states. In other words, the *total* number of particles collected being scattered at the left of the target spin is $N_L = N_L^{\uparrow} + N_R^{\downarrow}$. In the above expression of A_N, the particle yields must be properly normalized by the corresponding luminosities collected with each target spin orientation.

When measured this way, A_N can suffer from the limited detector acceptance, especially in cases of miscalibration or displacement of the detectors involved in the detection of the outgoing particles, which could induce a fake left-right asymmetry.

Target-spin asymmetry A better alternative to measure A_{UT} is by keeping the azimuthal angle ϕ fixed, and comparing the yields obtained with opposite target spins. Using Eq. (4.27) and Eq. (4.28), the polarized cross section σ_{UT} for the $e\,p \to h\,X$ reaction can be expressed as

$$\sigma_{UT} = \sigma_{UU}\ S_{\perp}\ A_{UT}^{\sin\phi}\ \sin\phi, \tag{4.31}$$

such that all possible kinematic dependences are included in the term $A_{UT}^{\sin\phi}$. This term is the amplitude of the $\sin\phi$ form that describes the angular dependence of the data, and therefore, it can be extracted from a fit of the data to a $\sin\phi$ functional form. The $A_{UT}^{\sin\phi}$ **amplitudes** are related to A_N in the way given by

$$A_N = -\frac{\int_0^{\pi} d\psi\, \sigma_{UT} \sin\psi}{\int_0^{\pi} d\psi\, \sigma_{UU}} = -\frac{2}{\pi} \cdot A_{UT}^{\sin\psi}, \tag{4.32}$$

whose derivation is done in detail in Appendix B. Both measurements, $A_{UT}^{\sin\phi}$ and A_N, are therefore equivalent. The extraction of the azimuthal moments, however, offers the advantage that it is less sensitive to the acceptance of the detector, since the kinematical dependence is extracted from a fit over all ϕ bins. This method was thus preferred in this work in order to determine the SSA in the production of inclusive hadrons in $ep^{\uparrow}$ collisions. On the following, it is described in detail how the $A_{UT}^{\sin\phi}$ amplitudes can be extracted from a fit to data.

Two alternatives were tested concerning the fitting procedure. One is based on the method of *least squares*, which requires the data points (e.g. the events) to be Gaussian distributed with a known variance, and therefore the events must be grouped into bins with sufficiently high statistics. The other alternative is based on the *maximum likelihood estimation*, which can be applied to unbinned data. Both methods are discussed below.

1. Binned least-squares fit One possibility is to bin the data in bins of the azimuthal angle ϕ and perform a conventional χ^2 fit to the data using the MINUIT package [136]. In this case, and given the divided geometry of the HERMES spectrometer, the ϕ bins must be defined such that the gap around the beam pipe is incorporated into the adjacent bins. The distribution of events in ϕ is shown in Fig. 4.10. The acceptance gap is located around the values of $\phi = \pm\pi/2$. The binned fit is an easy alternative from the computational point of view, but it has the disadvantage that in the bins with lower statistical power, it might lead to a lack of precision.

The asymmetry was calculated as

$$A_{UT}(p_T, x_F, \phi) = \frac{\frac{N^{\uparrow}}{L_P^{\uparrow}} - \frac{N^{\downarrow}}{L_P^{\downarrow}}}{\frac{N^{\uparrow}}{L^{\uparrow}} + \frac{N^{\downarrow}}{L^{\downarrow}}}, \tag{4.33}$$

where $N^{\uparrow(\downarrow)}$ are the number of events measured in bins of p_T, x_F and ϕ, contained in Table. 4.3. The differential yield for a given target spin direction ($\uparrow$ upwards or $\downarrow$ downwards) can be expressed as

$$\begin{aligned}\frac{\mathrm{d}^3 N^{\uparrow(\downarrow)}}{\mathrm{d}p_T\ \mathrm{d}x_F\ \mathrm{d}\phi} = \\ \left[L^{\uparrow(\downarrow)}\ \mathrm{d}^3\sigma_{UU} + (-)L_P^{\uparrow(\downarrow)}\ \mathrm{d}^3\sigma_{UT}\right]\ \Omega(p_T, x_F, \phi) \\ = \mathrm{d}^3\sigma_{UU}\left[L^{\uparrow(\downarrow)} + (-)\right. \\ \left. L_P^{\uparrow(\downarrow)}\ A_{UT}^{\sin\phi}(p_T, x_F)\sin\phi\right]\ \Omega(p_T, x_F, \phi).\end{aligned} \tag{4.34}$$

Here, σ_{UU} is the unpolarized cross section, $L^{\uparrow(\downarrow)}$ is the total luminosity in the $\uparrow$ ($\downarrow$) polarization state, $L_P^{\uparrow(\downarrow)} = \int L^{\uparrow(\downarrow)}(t)\ P(t)\ \mathrm{d}t$ is the integrated luminosity weighted by the magnitude P of the target polarization, and Ω is the detector acceptance efficiency.

If the average polarizations of both target spin states are the same [6], $\langle P^{\uparrow}\rangle = \langle P^{\downarrow}\rangle$, the asymmetry becomes

$$A_{UT}(p_T, x_F, \phi) = A_{UT}^{\sin\phi}(p_T, x_F)\ \sin\phi. \tag{4.35}$$

The $A_{UT}^{\sin\phi}$ amplitudes were extracted with a binned χ^2 fit of the functional form $p_1 \sin\phi$ to the measured asymmetry. These are plotted with open points in Figs. 4.11 – 4.14.

2. Unbinned maximum-likelihood fit A more sophisticated alternative is to perform a maximum likelihood fit of a $\sin\phi$ form to the data. The dependence of data on the azimuthal angle ϕ is extracted in this case from each collected event directly by an iterative procedure. Maximum likelihood fits are useful in the case of sparse data and rapidly varying distribution of data, and particularly in the case of low statistics[7].

In the maximum likelihood fit approach, the data set is assumed to follow, in every bin of p_T and x_F, the following probability density function

$$pdf(\phi) = 1 + S_{\perp} \cdot (a + A_{UT}^{\sin\ \phi}\ \sin\ \phi), \tag{4.36}$$

and the best values of the parameters $\alpha = \{a,\ A_{UT}^{\sin\phi}\}$ are found by maximizing the likelihood function $\mathcal{L}$ in the total sample of N events

$$\mathcal{L}(\alpha) = \prod_i^N pdf(\phi_i; \alpha). \tag{4.37}$$

[6] For the case of small differences between $\langle P^{\uparrow}\rangle$ and $\langle P^{\downarrow}\rangle$, consult Appendix B.

[7] With enough statistical power and a sufficiently large number of bins in ϕ, both binned and unbinned methods should provide a similar result.

In practice, this is done by minimizing the quantity $-2\ \ln\mathcal{L}$, which has the same minimum values for the set of parameters α as $\mathcal{L}$ its maximum values. The minimum, and therefore the value of the parameters α, is found with the MIGRAD command of MINUIT [136]. The exact form of the likelihood function used to extract the $A_{UT}^{\sin\phi}$ amplitudes is

$$-2\ \ln\mathcal{L} = -2\sum_{i}^{N} \ln\left[\frac{pdf(\phi_i;\alpha)}{C_S}\right] w_i, \tag{4.38}$$

where the coefficients C_S are a normalization factor to the total luminosity L_T collected for every spin state S *up* ($\uparrow$) or *down* ($\downarrow$) of the polarized target: $C_S = L^{\uparrow(\downarrow)}/L_T$. The weight w_i takes into account the probability of a track of being a hadron of true type h, given by the RICH unfolding procedure in Eq. (4.17), and the calorimeter efficiency, given by Eq. (4.25), in the following way

$$w_i = w_h^{\text{true}}/\langle\epsilon\rangle. \tag{4.39}$$

Note that weighting data by w_i changes the effective number of hadrons for a given kinematic point, and therefore this affects the statistical uncertainty of the asymmetry amplitudes. In order to avoid this, the following procedure has to be used to get the correct error estimation

1. using the above defined likelihood function, $\mathcal{L}$, run the HESSE command of MINUIT at the same minimum given my MIGRAD, to obtain the corresponding covariance matrix $\mathcal{C}$,
2. define a new likelihood function $\mathcal{L}_{\text{err}}$ as

$$-2\ \ln\mathcal{L}_{\text{err}} = -2\sum_{i}^{N} \ln\left[\frac{pdf(\phi_i;\alpha)}{C_S}\right] w_i^2, \tag{4.40}$$

   where the weight now enter squared w_i^2,
3. run HESSE again by using $\mathcal{L}_{\text{err}}$; this provides a new covariance matrix $\mathcal{C}_{\text{err}}$,
4. the correct values for the parameters uncertainty is given by the *corrected* covariance matrix $\mathcal{C}_{\text{corr}} = \mathcal{C}\cdot\mathcal{C}_{\text{err}}^{-1}\cdot\mathcal{C}$.

This procedure is based on the prescription given by F. T. Solmitz [137], although not exactly the same[8].

[8] In Ref. [137], a different quantity is used instead of $\mathcal{C}_{\text{err}}^{-1}$ which in some cases coincide.

4.6 Preliminary results

The measured $A_{UT}^{\sin\phi}$ amplitudes for charged pions and kaons are shown in Fig. 4.11 as a function of the hadron transverse momentum, and in Fig. 4.13 as a function of x_F. A multidimensional extraction of $A_{UT}^{\sin\phi}$ is shown in Fig. 4.12 as a function of p_T for four different slices of x_F, and in Fig. 4.14 as a function of x_F in four different regions of the transverse momentum. Only statistical error bars are included in these figures. The open points in the figures show the result of using the least squares fit approach. The larger error bars in this case are a consequence of binning the data, which implies a loss of precision and it is reflected in the statistical uncertainty. For this reason, maximum likelihood fits were preferred to extract the asymmetry amplitudes, and only this approach is used in all results shown later unless explicitly stated. Only data points whose statistical uncertainty is smaller than 0.1 are plotted.

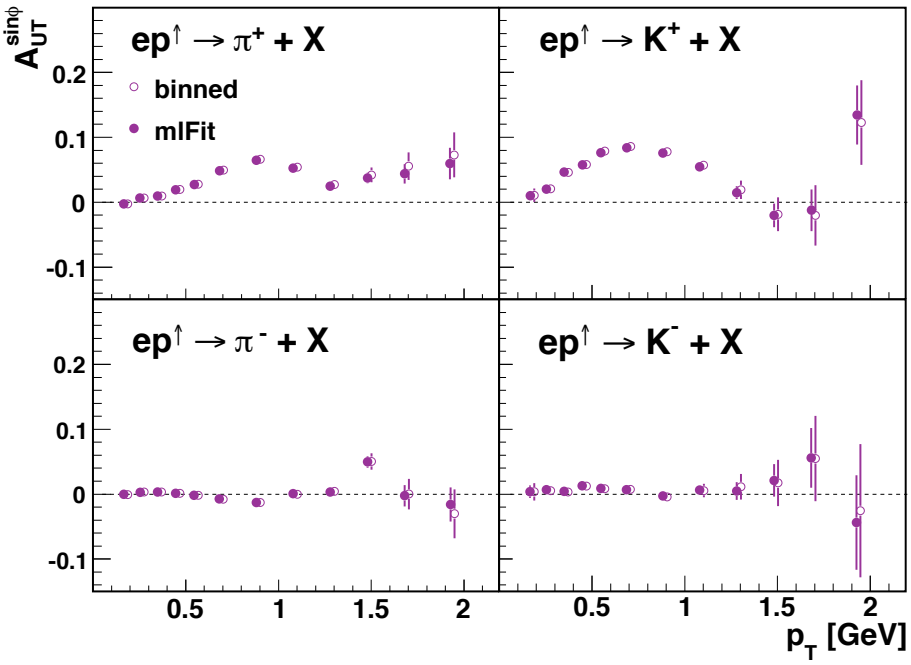

Figure 4.11. The $A_{UT}^{\sin\phi}$ amplitudes extracted by two different fit methods as a function of p_T.

Dependence on p_T The $A_{UT}^{\sin\phi}$ amplitudes for positive hadrons show a a clear dependence on the transverse momentum of the hadron. The asymmetry for π^+ increases with the transverse momentum, within the range $0 < p_T < 1$ GeV, up to a value of about 6%, then decreases for $p_T > 1$ GeV down to 2% and rises again for the largest p_T bin up to a value of about 5%. For K^+, a similar behavior is observed, although the lack of statistics at large transverse momentum makes it difficult to conclude if there is a second rise after $p_T > 1$ GeV. The asymmetries for π^- are nearly zero for the entire p_T range investigated. For K^-, these are also consistent with zero.

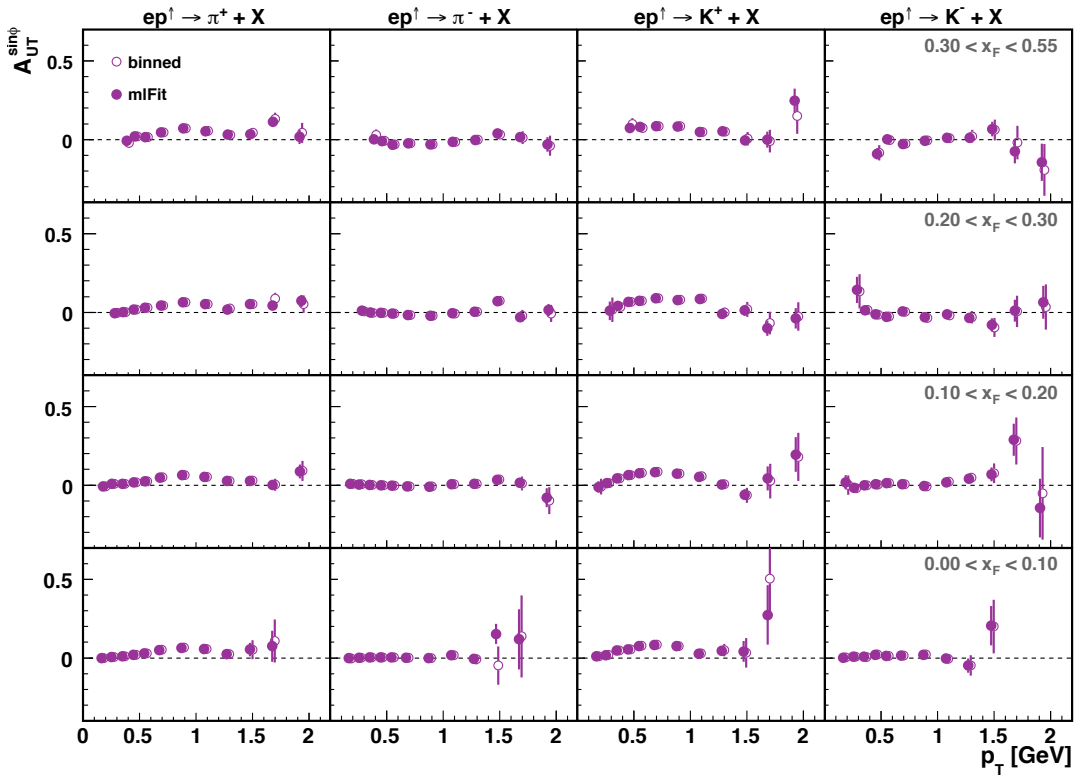

Figure 4.12. The $A_{UT}^{\sin\phi}$ amplitudes for the four different types of hadrons, extracted as a function of p_T, in four different bins of x_F.

In the case of the two-dimensional results, shown in Fig. 4.12, a similar message holds for the π^+ and K^+ as in the monodimensional case. Besides, no strong dependence on x_F is observed, as it can be concluded from the comparison of the $A_{UT}^{\sin\phi}$ points for each p_T bin over the four rows, indicating four different slices of x_F. Only the points at large p_T seem to depend on x_F. The situation is quite different for the negative hadrons. The π^- amplitudes clearly change sign within the range $p_T < 1$ GeV over the four x_F regions, being nearly zero, but positive, for the lowest row in x_F and of larger magnitude, and negative, for the highest row. In the range $0.30 < x_F < 0.55$, the amplitudes for π^-, in addition, change sign with p_T, being negative for $p_T < 1$ GeV and positive for $p_T > 1$ GeV. A similar tendency is observed for the K^- amplitudes, but with larger error bars.

Dependence on x_F The evolution of the $A_{UT}^{\sin\phi}$ amplitudes with x_F is much smoother than with p_T, as it can be seen in Fig. 4.13. For positive pions, they increase with x_F up to a value of 10% for the largest x_F bin. For positive kaons, asymmetries between 5% and 8% are observed, with a small dependence on x_F. The π^- amplitudes are symmetric to the π^+ but smaller in magnitude, reaching only about -4% for the largest x_F bin. The K^- amplitudes, on the contrary, are essentially zero for the entire x_F range, with certain trend towards negative values (down to 3%) for the range 0.25 GeV $< p_T <$ 3.5 GeV.

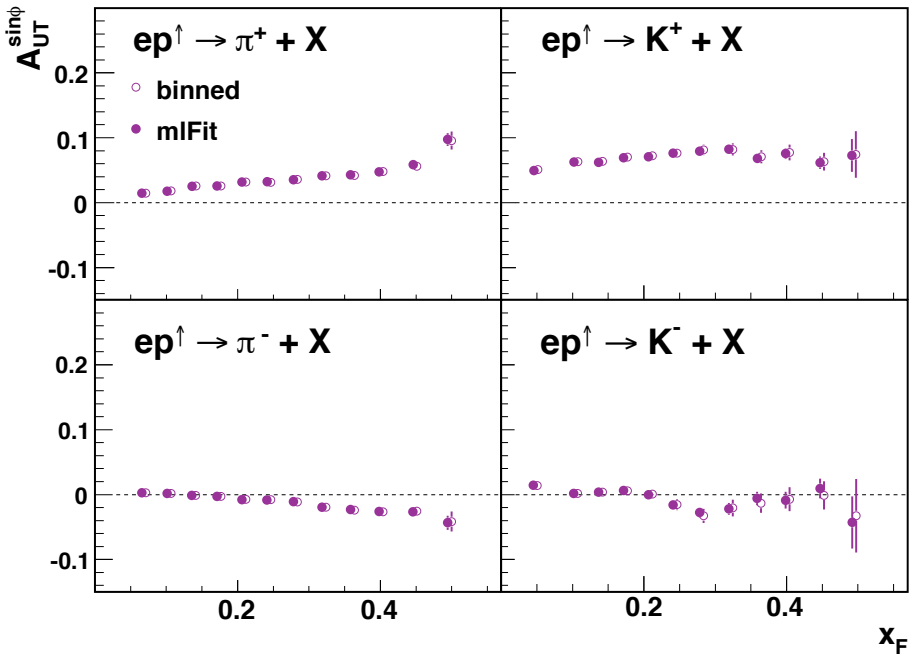

Figure 4.13. The $A_{UT}^{\sin\phi}$ amplitudes extracted by two different fit methods as a function of x_F.

The apparent dependence on x_F of these asymmetries becomes less evident when observing the multidimensional extraction of the amplitudes in Fig. 4.14. In this case, the π^+ amplitudes are rather flat over the entire x_F range, and show a clear dependence with the transverse momentum, i.e., the four vertical plots on the column corresponding to π^+. The moderate slope of the π^+ amplitudes at large x_F can be attributed to the residual dependence of x_F on the transverse momentum due to the sizable width of the bins in p_T. A similar message can be drawn for all other hadron types.

Conclusion The dominating kinematic dependence of the amplitudes is then on the transverse momentum of the hadron. The dependence of the asymmetries on x_F, as seen in Fig. 4.13 is probably just a reflection of the correlation between these two variables, shown in Fig. 4.9. The determination of the systematic uncertainty associated to the $A_{UT}^{\sin\phi}$ amplitudes is done in the next chapter. A more extended discussion and interpretation of the presented results will be done after that, in Chapter 6.

Effect of the calorimeter efficiency on the $A_{UT}^{\sin\phi}$ amplitudes The correction of the hadron yields by the calorimeter efficiency, described in Section 4.3, has a significant impact on the extracted asymmetry amplitudes, particularly for the bins at high p_T. See Figures E.29 – E.32.

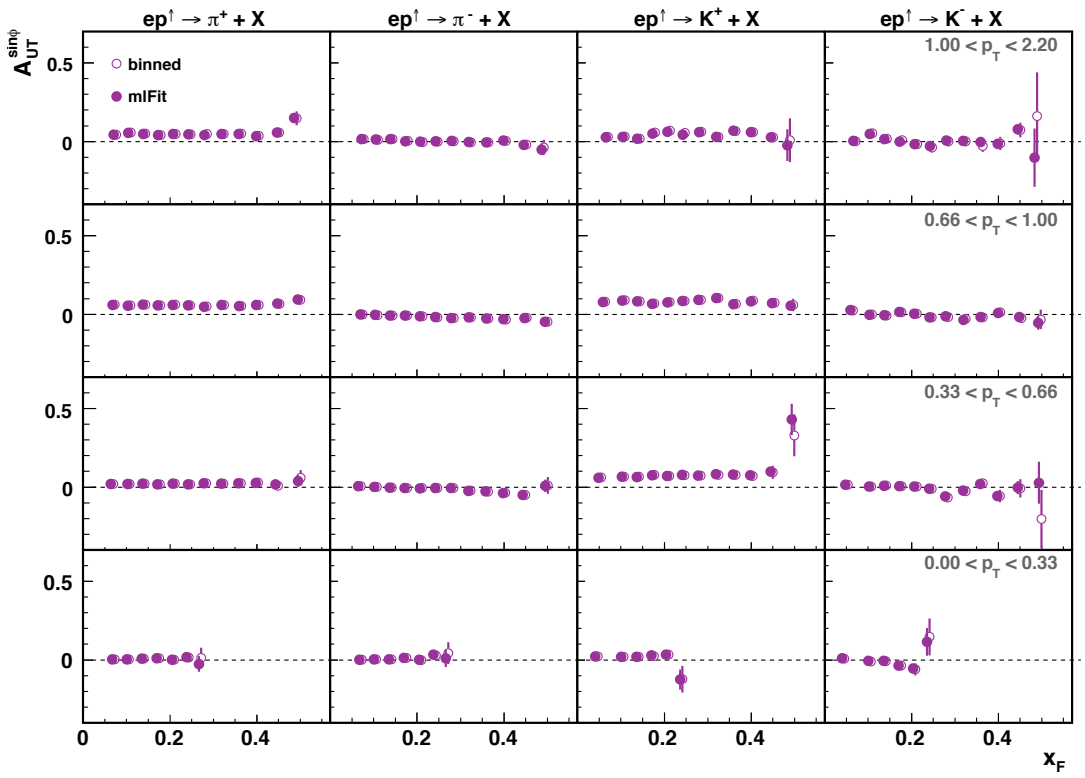

Figure 4.14. The $A_{UT}^{\sin\phi}$ amplitudes for the four different types of hadrons, extracted as a function of x_F, in four different bins of p_T.

5 Systematics

Systematic effects are all sources of uncertainty arising from inadequate knowledge of the experimental setup that lead to a measurement that differs from the real value by a fixed amount. Some examples are the mis-calibration of the detectors, changes in the data-taking conditions or malfunctioning detector parts. Unlike statistical uncertainty, the error associated with systematic effects does not decrease with the statistical power. A systematic effect can be identified by a steady trend in the difference of two data sets obtained with two different experimental configurations.

The definition of the SSA (see Section 4.5) offers the advantage that many systematic effects cancel in the ratio of cross sections. In addition, the fully differential extraction of the $A_{UT}^{\sin\phi}$ amplitudes was chosen such that it minimizes the impact of other non-vanishing effects. In this chapter, the potential influence of several sources of error is investigated, and a systematic uncertainty is correspondingly assigned to the asymmetry amplitudes presented in the previous chapter.

One important case is the problem originating from the limited acceptance of the HERMES spectrometer, introduced in Section 5.1. Most systematic studies, and in particular the estimation of the *acceptance effects* were done with the help of a Monte Carlo simulation. The idea is to reconstruct the asymmetry from a Monte Carlo sample where the generated events exhibit the same target spin dependence as the one observed in data. These events are then run through a simulation of the HERMES spectrometer that reproduces the way real particles are detected. Deviations of the reconstructed asymmetry from the input used at generation level represent the actual effect of the measurement, and can be taken as the systematic uncertainty on $A_{UT}^{\sin\phi}$.

The general features of the Monte Carlo production are reviewed in Section 5.2. The implementation of the target spin dependence describing $A_{UT}^{\sin\phi}$ into this sample is described in Section 5.3. The influence on the measured $A_{UT}^{\sin\phi}$ moments is summarized in Section 5.4, where other sources of systematic uncertainty are also considered, most of them being negligible or their effect already accounted for in the acceptance studies.

5.1 Acceptance effects and misalignment

The limited acceptance of the HERMES spectrometer implies that not all particles produced in a collision are necessarily being detected. The hadron yields of Section 4.4.1 represent therefore a certain, *a priori* unknown fraction of the original particle rate. The limited kinematic distribution of the collected events might influence the $A_{UT}^{\sin\phi}$ amplitudes. One example is the case discussed in Section 4.3. There are other ways in which artificial asymmetries can be induced in the data, as mentioned below. For this reason, the acceptance studies are highly relevant for the correct interpretation on the measured asymmetries.

In practice, the number of events collected in a particular kinematic bin is convoluted with the **acceptance function** ϵ of the detector, that may depend on the relevant kinematic variables

$$N^{\uparrow\downarrow}(p_T, x_F, \phi) = \int \epsilon(p_T, x_F, \phi)\ \sigma(p_T, x_F, \phi), \tag{5.1}$$

such that $\epsilon(p_T, x_F, \phi)$ does not necessarily cancel out in the cross section ratio (Eq. (4.26)). This implies that the process of measuring might lead itself to a false detector asymmetry.

Something similar happens in the case of an off-centered, inclined or curved beam not properly aligned with the longitudinal z_{lab}-axis of the spectrometer. This is illustrated in Fig. 5.1. In the aligned case, the scatter products are symmetrically distributed in both detector halves, thus leading to a null left-right asymmetry. If the beam and the detector are misaligned with respect to each other, however, an asymmetric distribution of events is found. In simple cases, reversing the target spin direction and combining the particle yields as described in Section 4.5 would help canceling out such misalignment effects. More generally, the effects of the HERMES acceptance can be conveniently estimated with the Monte Carlo description of the next sections.

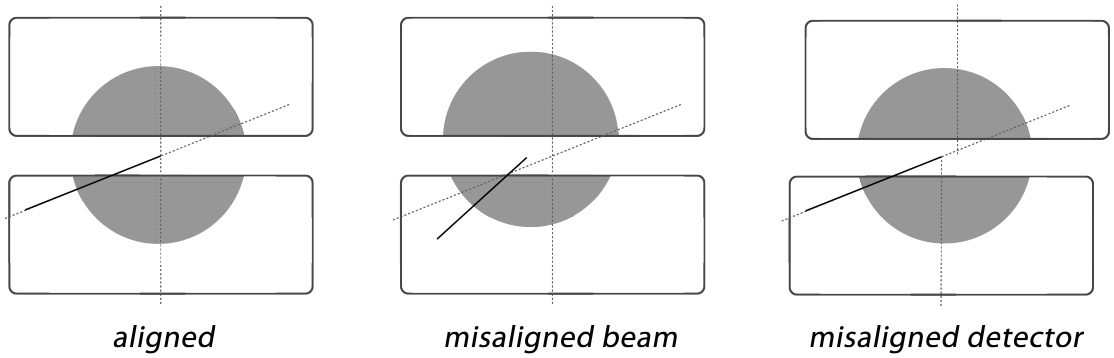

Figure 5.1. Examples of misalignment between the beam and the detector that can lead to fake *left-right* asymmetries.

5.2 Unpolarized Monte Carlo sample

The acceptance studies are performed on a large production of Monte Carlo events generated purposely for this analysis. The systematic uncertainty associated to $A_{UT}^{\sin\phi}$ is related to the statistical power of the Monte Carlo sample (cf. Section 5.4). Enough statistics must be generated to bring the systematic uncertainty down to a reasonable value in comparison to the statistical uncertainties of the data asymmetry amplitudes. This is no trivial task, given the small statistical error bars of the measured $A_{UT}^{\sin\phi}$ and the fact that, as it happens also in the case of real data, most of the generated events have very low p_T and Q^2, thus making the region at large p_T and x_F quite unaccessible from the point of view of the generation of events in those bins.

5.2.1 Event generator

The general scheme of the Monte Carlo production chain (HMC) is depicted in Fig. 5.2. The starting point is the simulation of the electron-proton collisions. This is done with a version of PYTHIA [140], where the cross section of all implemented processes was tuned to HERMES data. Some of these processes are for instance DIS, QCD-Compton and photon-gluon fusion reactions or the exclusive formation of vector mesons. The kinematics of the scattered lepton are then generated according to the relative cross sections.

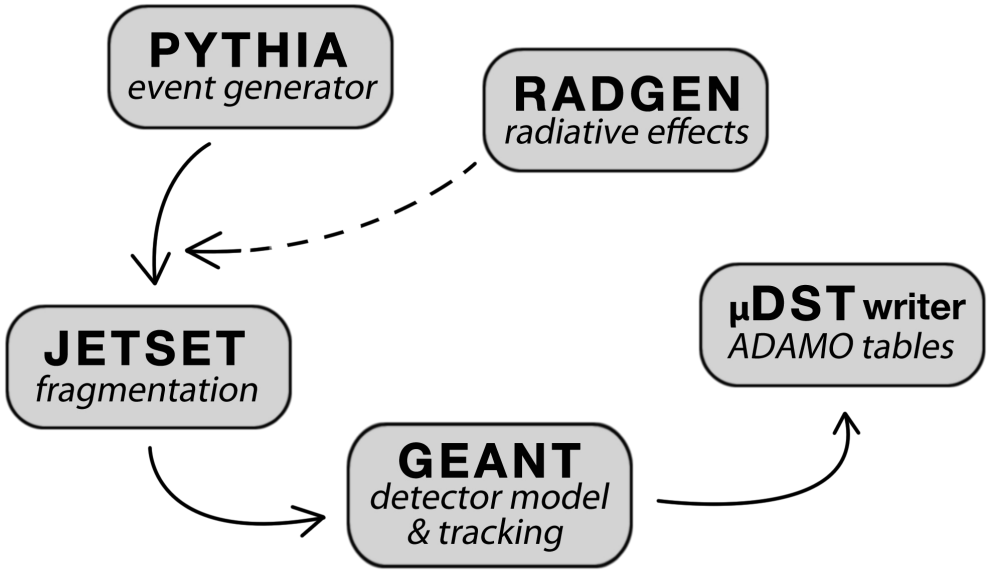

Figure 5.2. The HERMES Monte Carlo production chain (HMC).

Radiative corrections, i.e., Bremsstrahlung in the initial or final state of the scattering process, can be included at this point by the RADGEN software [141]. The fragmentation of the proton into hadrons is described by JETSET [140] based on the LUND string model [142], modified to describe the hadron multiplicities measured at HERMES [143].

The final kinematics of the total event are then run through a simulation of the HERMES detector done with the GEANT package [144]. A precise description of the dimensions

and materials of every component of the spectrometer is contained in a *geometry file*. A parametrization of the HERMES magnetic field, measured in experimental surveys, is included in a similar way. Finally tracks are reconstructed, accounting for the detector smearing and resolution due to the passage of the particles through the different materials and detector components. After 2005, the HMC code included as well the new HTC tracking method, used to reconstruct tracks in real data.

A μDST writer converts the generated data into ADAMO tables with a similar structure to the ones done for data. The main difference with the data tables is that all information about the generated values is also conserved. The tables are written to files, ready to use in analyses.

Why PYTHIA? The choice of PYTHIA over other Monte Carlo generators used at HERMES like *disNG* or *gmc_trans* was preferred as it can generate events down to $Q^2 \sim 0$ GeV^2 and $W^2 > 4$ GeV^2, which is of crucial importance as the biggest fraction of the events in the analyzed inclusive data set comes from quasi-real photoproduction, with very low Q^2 (cf. Chapter 6).

The use of *gmc_trans* can be particularly useful for the study of SSA in semi-inclusive analysis, since it can simulate azimuthal distributions based on the available knowledge of TMDs [145]. For the inclusive measurement presented in this thesis, however, there might be other significant contributions to the spin-dependent cross section σ_{UT} beyond the results from SIDIS measurements. For this reason, it was preferred to use an unpolarized generator like PYTHIA, and implement by hand the target spin dependence seen for the $A_{UT}^{\sin\phi}$ amplitudes.

5.2.2 Generated statistics

Three sets of Monte Carlo data were generated, amounting to a total of nearly 1100 million events. As indicated in Table 5.1, a PYTHIA sample was first generated containing approximately 1020 million events, from which only about 315 million were useful for the analysis. This implies a *reconstruction* efficiency of just 30%. Of the remaining 70%, it was found out that ∼20% are rejected as the hadrons have momentum smaller than 2 GeV, and about 10% are discarded by requiring the 'fiducial volume' and 'short track' cuts and the track's vertex to be in the target cell. The remaining 40% is lost after track reconstruction, mainly because they escape the HERMES acceptance. In addition, a very small percentage of events at high-p_T is generated.

Two other samples of smaller size were produced with the goal of reducing the systematic uncertainty of the large p_T bins. This was done by only writing to disk those final state hadrons whose p_T were larger than a certain cut (0.9 GeV and 1.5 GeV, respectively). This way, no *selector* is used at the generation stage. A selector is a common trick to generate only events of interest, i.e., with Q^2 bigger than 1 GeV^2, but which could result into a sample with altered kinematic properties and in turn affect the $A_{UT,MC}^{\sin\phi}$ amplitudes. The last two columns of Table 5.1 show how the events generated this way are more efficiently produced regarding the data quality cuts imposed in the analysis code. In prod_pt0.9, up to 64% of the events pass the analysis cuts in comparison with the 30% of prod[44]. The main reason

Production	prod[44]	prod_pt0.9	prod_pt1.5
cut	–	$p_T > 0.9$ GeV	$p_T > 1.5$ GeV
generated statistics	1021 M	73 M	680 K
from which			
selected events	315 M	47 M	340 K
reconstruction efficiency	30%	64%	50%
events with $p_T > 1$ GeV	0.56%	28%	60%
events with $p_T > 1.6$ GeV	0.02%	0.86%	51%

Table 5.1. Monte Carlo productions generated for the study of systematic effects.

for this is that, by requiring a larger p_T, many events produced at low Q^2, and therefore with not a sufficiently large angle θ to escape the HERMES acceptance gap, are discarded.

The distribution of *all* produced MC data in the p_T– x_F plane can be seen in Fig. 5.3.

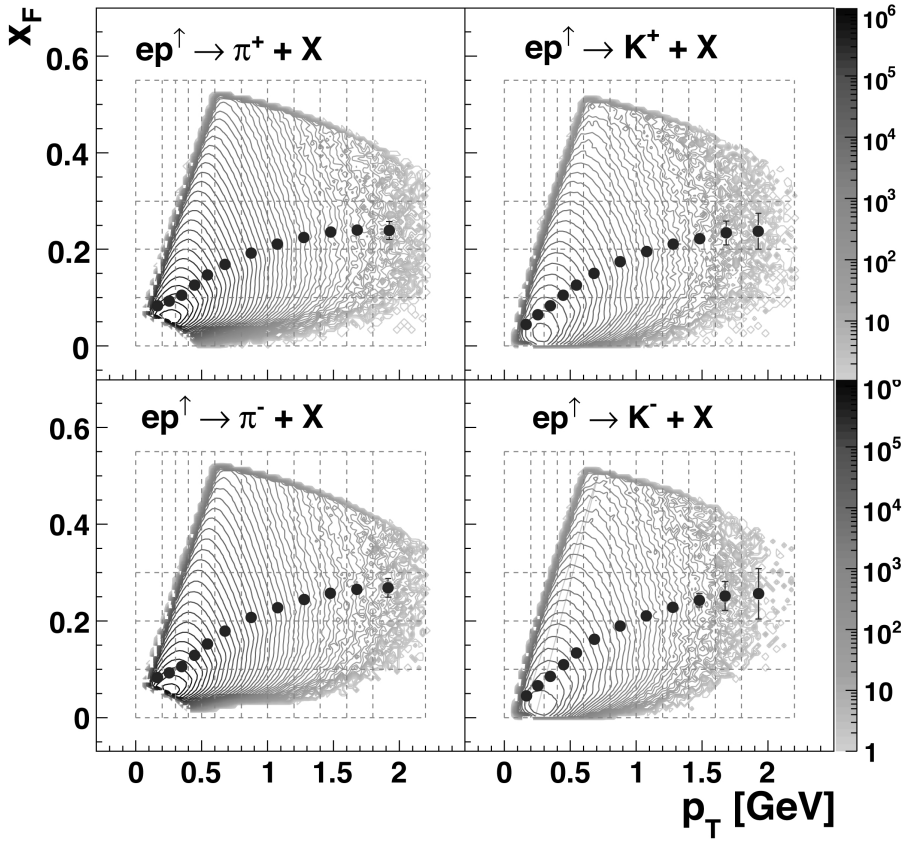

Figure 5.3. Distribution of Monte Carlo data in the p_T-x_F kinematic plane. The dotted lines correspond to the bins defined in Section 4.4. The points represent the average x_F value in each p_T bin.

5.2.3 Comparison to data

The MC productions are used to estimate the systematic uncertainty. Therefore the relevant properties of the MC data are *(i)* that it reproduces well the kinematic distribution of the analyzed data (cf. Section 4.4), and *(ii)* that it does not generate by itself any fake asymmetry. The latter is inspected in the next section.

The comparison between the kinematic distributions of MC and data events as a function the relevant kinematic variables p_T, x_F and ϕ, and the azimuthal (ϕ) and polar angles (θ) is shown in Fig. 5.4. The amount of MC data is about 3 times bigger than the analyzed data from the 02-05 productions, therefore the MC histograms were normalized to the data ones. As it can be seen in the above mentioned figure, the distribution of *data* and *Monte Carlo* events are quite consistent with each other. Some differences are found at low p_T and low x_F, where more events are found for the Monte Carlo data, being particularly noticeable in the case of the K^+. Such deviations are known from other analyses of kaon data at HERMES. The origin of this seems to be intrinsic to the simulation software and it could not be improved. Only MC data from *prod[44]* are plotted in these one-dimensional representations. Including the other two MC productions (*prod_pt0.9* and *prod_1.5*) adds two corresponding excesses of events at large p_T to the histograms, which hampers the comparison of the tales of the data and MC distributions. The two-dimensional distribution of *all* Monte Carlo events in the $p_T - x_F$ plane is shown in Fig. 5.3. The average values, represented by the black points, did not change when including the two large-p_T productions, indicating that the average kinematics are well reproduced also by these productions. Regarding the comparison to data distribution in Fig. 4.9, it is observed these average values are slightly shifted to lower values of x_F for the same p_T bins.

It is worth noting that the correction of the data yields by the calorimeter efficiency significantly improved the agreement between the Monte Carlo and data distributions. This can be concluded from a quick look to the one-dimensional distributions of data with and without correction by the trigger efficiency (see Section 4.4), and the comparison of the Monte Carlo and corrected data distributions shown on the next page.

Fraction of DIS events in Monte Carlo Besides, there was found a significant discrepancy in the fraction of DIS events between Monte Carlo and real data. The fraction of DIS events was found to be similar both in both cases only for the range of $p_T < 0.8$ GeV. For larger values of the transverse momentum, the fraction of DIS events in Monte Carlo was more than twice as large as for real data. This trend was somehow reversed when comparing Monte Carlo data with real data *uncorrected* by the trigger efficiency. In this case, the agreement seemed to be better at large values of p_T, and worse at low p_T values. A reasonable explanation for this effect was not found. However, this could be related to the fact that the kinematical configuration of these Monte Carlo data was originally tuned to reproducing available HERMES data from quasi-real photoproduction events, and not to DIS data. The disagreement between Monte Carlo and data concerning the fraction of DIS events – an essential parameter, and the lack of time and manpower to improve this, prevented us from using the Monte Carlo data for other studies, i.e., estimation of $\langle Q^2 \rangle$ or $\langle p_T^2/Q^2 \rangle$ for each measured value of the $A_{UT}^{\sin\phi}$ amplitudes.

Nevertheless, given the good agreement between the kinematical distribution of the data with the Monte Carlo events, the Monte Carlo sample can be safely used for the estimation of systematic uncertainties.

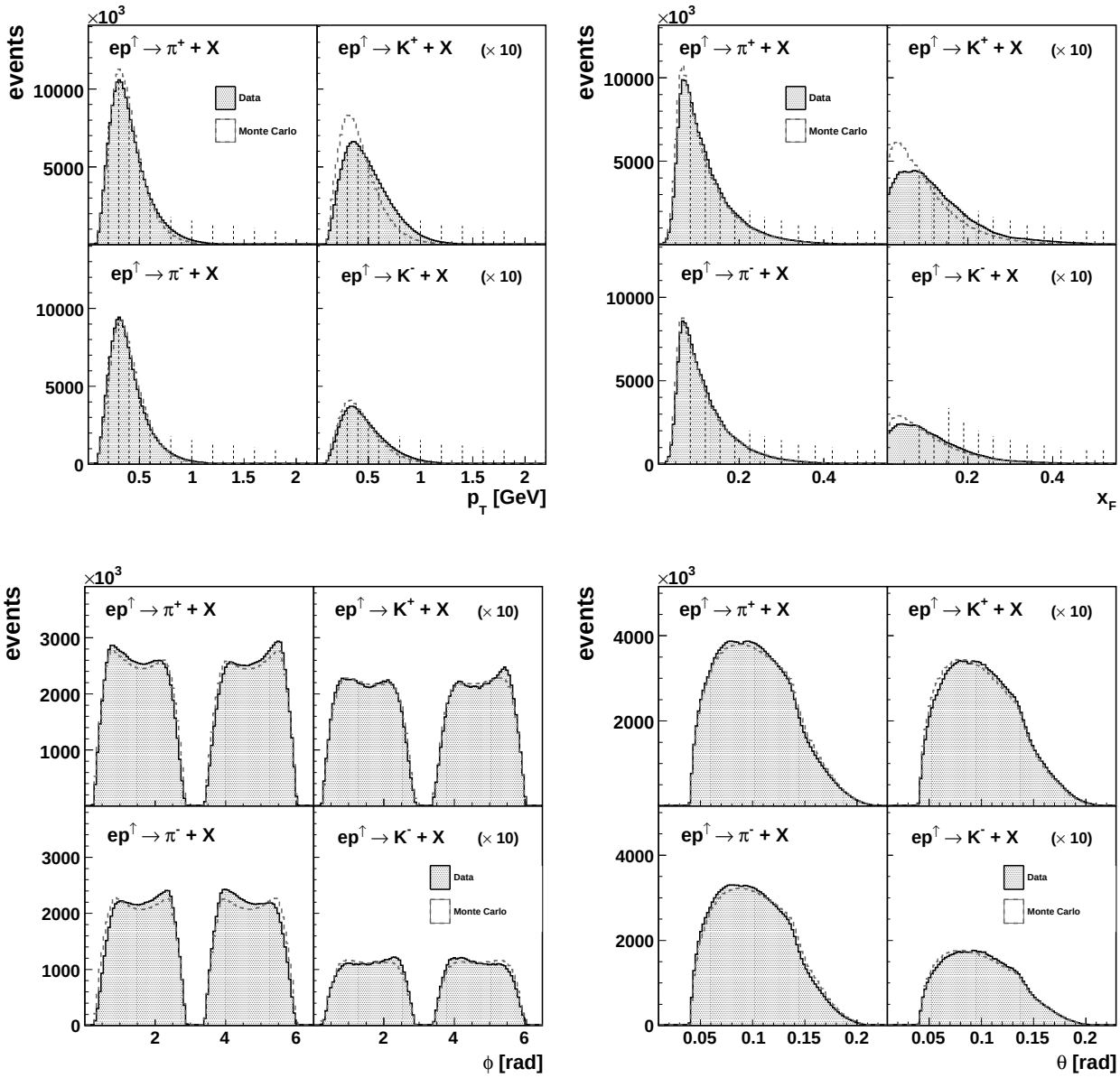

Figure 5.4. Distribution of Monte Carlo events (dotted line) as a function of p_T (top left), x_F (top right), ϕ (bottom left) and θ (bottom right) compared to the distribution of real data (black line). The dotted vertical lines in the histograms of the upper panels correspond to the bins defined in the first two rows of Table 4.3, respectively. All kaon histograms are multiplied by a factor of 10.

5.2.4 Zero asymmetry test

Before implementing a target spin dependence on the PYTHIA events, it is crucial to check whether this unpolarized sample can generate an asymmetry. In such case, this asymmetry can be attributed exclusively to the limited acceptance and detector effects. Applying the technique described in Section 4.5, the asymmetry amplitudes can be extracted from this unpolarized Monte Carlo sample in an equivalent way as done for data.

The results of this *zero input* test can be seen in Fig. 5.5. The extracted amplitudes are consistent with zero within 1%, which indicates that the limited acceptance of HERMES does not generate artificial asymmetries by itself. As it is shown in the next section, the acceptance effects become only relevant through the convolution with a real nonzero asymmetry (cf. Eq. 5.1). Nevertheless, smalls deviations from the zero line are observed for certain bins. See, for example, the fourth p_T bin in the upper x_F row for the K^+, or the same bin one row below. These deviations are also found later in Section 5.3.2 when the target spin dependence is implement in the Monte Carlo sample. As it will be explained then, such deviations are accounted for in the final systematic uncertainty.

On the next sections, all Monte Carlo asymmetries are plotted with orange points, while the data asymmetries are plotted with the same color as in the last Chapter.

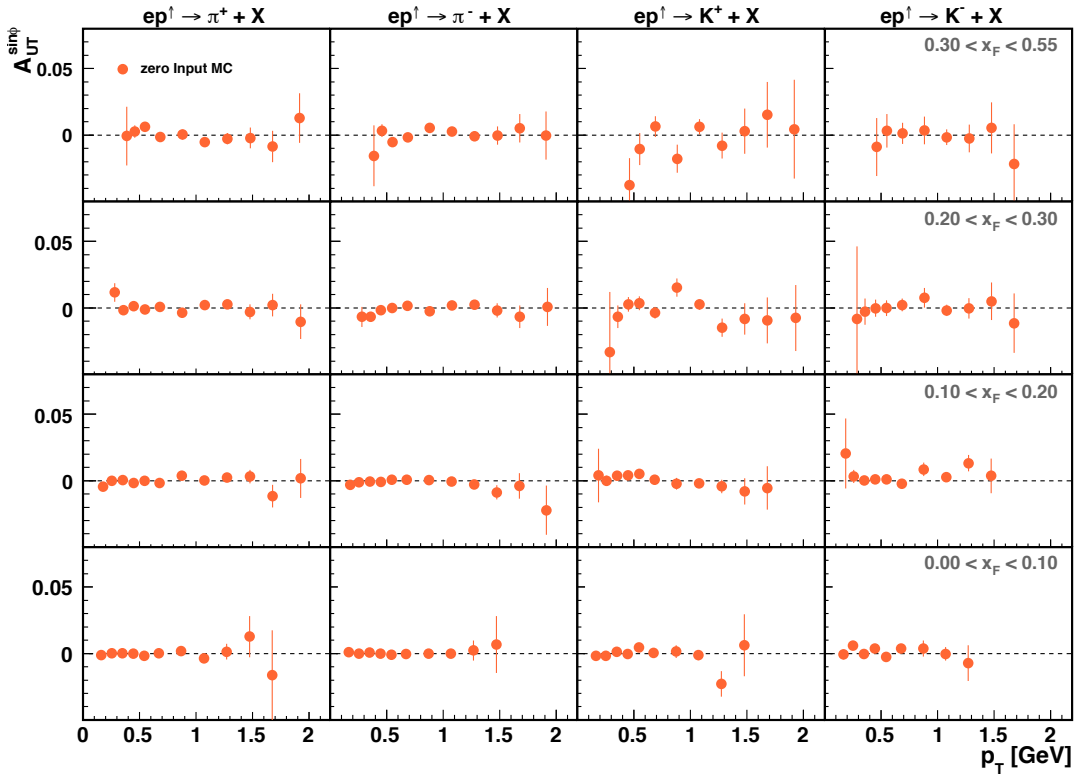

Figure 5.5. Extraction of the azimuthal amplitudes as a function of p_T, from the unpolarized Monte Carlo sample, leading to zero asymmetries.

5.3 Polarized Monte Carlo sample

The incorporation of the target spin effects was done by a sophisticated method [146] used recently in other analyses of spin asymmetries at HERMES [147]. This method is based on two steps:

- First, the kinematic dependence of the $A_{UT}^{\sin\phi}$ amplitudes is extracted from data by a maximum-likelihood fit procedure, based on a fully differential probability density function (pdf), defined in Section 5.3.1.
- Second, a target spin dependence is introduced in the Monte Carlo events by assigning their polarization state according to the distribution of probability given by the above mentioned *pdf*. See Section 5.3.2.

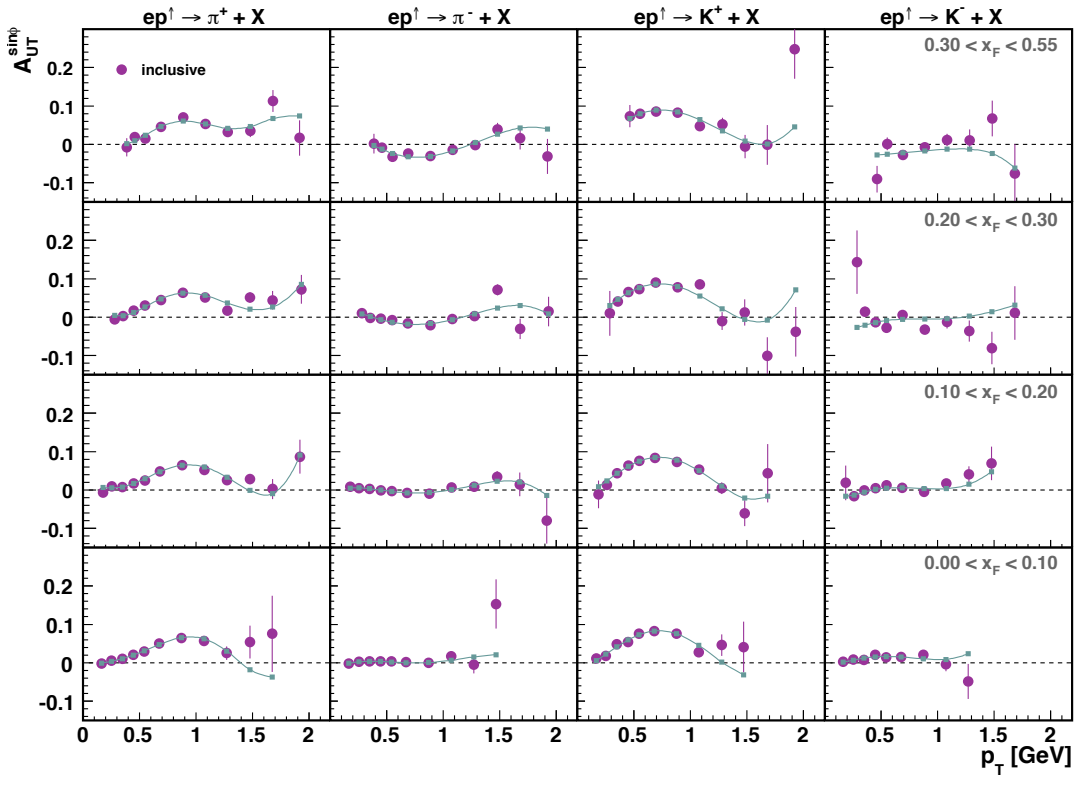

Figure 5.6. The $\mathcal{A}_{UT}^{\sin\phi}$ fit function (with squares) evaluated at the average bin kinematics $\langle p_T \rangle$, plotted together with the $A_{UT}^{\sin\phi}$ amplitudes as a function of p_T in four different slices of x_F.

5.3.1 Model for the asymmetry

The full dependence of the $A_{UT}^{\sin\phi}$ amplitudes on the kinematic variables p_T, x_F and the azimuthal angle ϕ was extracted from data by a fit based on a fully differential probability density function (pdf):

$$\text{pdf}(p_T, x_F, \phi) = 1 + S_\perp \cdot \mathcal{A}_{UT}^{\sin\phi}(p_T, x_F) \cdot \sin\phi, \tag{5.2}$$

where

- $S_\perp$ is the degree of transverse polarization of the target, see table 7.1
- $\mathcal{A}_{UT}^{\sin\phi}(p_T, x_F)$ is a Taylor expansion in p_T and x_F around the average kinematics of the data sample. The Taylor expansion was truncated at fifth order in p_T and first order in x_F, giving a total of 12 parameters:

$$\mathcal{A}_{UT}^{\sin\phi}(p_T, x_F) = \sum_{i=0}^{5} \hat{p}_T^i c_i + \hat{x}_F^i \sum_{i=0}^{5} \hat{p}_T^i d_i. \tag{5.3}$$

  Here, $\hat{p}_T^i \equiv p_T^i - \langle p_T \rangle$ and $\hat{x}_F^i \equiv x_F^i - \langle x_F \rangle$, where $\langle p_T \rangle$ and $\langle x_F \rangle$ are the average kinematic values of the **whole** data set[1]. The set of 12 parameters c_i and d_i for each hadron species was obtained from a maximum-likelihood fit to the entire data sample. The number of terms in the expansion was optimized to reproduce the observed $A_{UT}^{\sin\phi}$ amplitudes. The π^- and K^+ asymmetries were fitted with 10 parameters (4th order in p_T, 1st in x_F). In the case of the K^- asymmetries, it was seen that these were well described by using a total of 8 parameters (3th order in p_T, 1st in x_F). Using higher orders in the expansion was not seen to have an effect on the fitted parameters, or made the fit procedure not to converge in MINUIT. The low order considered for x_F can be understood from the discussion of Section 4.6.

Figure 5.6 shows the $\mathcal{A}_{UT}^{\sin\phi}$ functions for the four hadron types, denoted with square symbols, evaluated at the average bin kinematics $\langle p_T \rangle$, $\langle x_F \rangle$. A line matching the $\mathcal{A}_{UT}^{\sin\phi}$ points is also drawn to guide the eye. In all cases, and most noticeably for pions where the collected statistics are higher, the agreement between $\mathcal{A}_{UT}^{\sin\phi}$ and the data asymmetries is remarkably good, reproducing the trends and various changes in slope. Nevertheless, a couple of *outlaying* points are not perfectly matched. The one-dimensional projections of $\mathcal{A}_{UT}^{\sin\phi}$ as a function of p_T and x_F can be seen in Fig. E.2 and Fig. E.4, and the two-dimensional projection as a function of x_F, in four different slices of p_T, in Fig. E.6. Note that the fit function is the same one in all cases, but projected in a different kinematic region.

The main advantage of this method lies in the fact that the asymmetries are *not* directly fit to a certain functional form, thus lacking any physical meaning. The kinematic and target spin dependence of the *data* themselves is extracted in the event-level fit. The only constraint is therefore the truncation of the Taylor expansion, which was seen to not have any impact on the extracted parameters.

[1] These average values define the function for a specific data set, and always the same values should be used to evaluate the function in another sample, i.e., Monte Carlo or data from another experiment.

5.3.2 Introduce spin dependence

The target spin dependence must be *folded* with the unpolarized cross section. Optimally, one would do this at the stage where the events are generated by PYTHIA, before these are passed to the hadronization and tracking software, and most importantly before reconstruction through the HERMES acceptance. This way, events would be reconstructed the same way as happens for real data, where the kinematics of the produced hadrons are determined by the interaction of the beam electron with the spin polarized target proton.

The modification of the PYTHIA code to include the parametrization of $A_{UT}^{\sin\phi}$ would be a very time consuming task and is also not strictly necessary. In practice, the target spin dependence does not change the number of resulting events, but implies only a redistribution of events into other kinematic bins. On the other hand, it is no large approximation to assume that the parametrization of the observed $A_{UT}^{\sin\phi}$ amplitudes is also valid in a 4π, acceptance-free volume.

The target spin dependence is then implemented by assigning manually the target spin state of every *reconstructed* event, i.e., observed in the HERMES acceptance, according to the distribution given by the *pdf* described in the previous section, evaluated at the *generated* kinematics. A random number *rnd* is drawn between 0 and 1 and compared to the value of the *pdf* evaluated at the **generated** values of p_T, x_F and ϕ and for each hadron species.

$$\text{spin} = \begin{cases} +1 & \text{if} \quad \text{rnd} < 0.5\ (1 + \mathcal{A}_{UT}^{\sin\phi}(p_T, x_F)_{\text{gen}} \cdot \sin\phi_{\text{gen}}), \\ -1 & \text{if} \quad \text{rnd} > 0.5\ (1 + \mathcal{A}_{UT}^{\sin\phi}(p_T, x_F)_{\text{gen}} \cdot \sin\phi_{\text{gen}}). \end{cases}$$

5.3.3 Reconstruction of $A_{UT,MC}^{\sin\phi}$

With the target spin effects introduced in the generated sample, the asymmetries amplitudes can be extracted in the same way as described in Section 4 for real data. Monte Carlo events are required to fulfill the same requirements as the real data, when applicable. These are

- Reject short tracks,
- Fiducial volume cut,
- 2 GeV $< p <$ 15 GeV,
- Production vertex within the target cell.

Results for the reconstructed $A_{UT,MC}^{\sin\phi}$ are shown in Fig. 5.7. The $\mathcal{A}_{UT}^{\sin\phi}$ functions are also shown, evaluated at the average bin kinematics of this sample in order to guarantee that the comparison to $A_{UT,MC}^{\sin\phi}$ can be done, for every bin, at the *same* kinematic point. The resemblance to the data asymmetries is evident. The small deviations from the model, depicted with the grey squares, indicate the difference between the spin asymmetry carried by the hadrons as they are produced after the collisions in the target and after they are detected. This deviation represents the effect of the actual detection process and it is used in the next section to determine the systematic uncertainty introduced by the HERMES spectrometer.

The one-dimensional extractions of $A_{UT,MC}^{\sin\phi}$ as a function of p_T and x_F can be seen in Fig. E.3 and Fig. E.5, respectively, together with the corresponding projections of $\mathcal{A}_{UT}^{\sin\phi}$ evaluated in the average bin kinematics of the Monte Carlo sample. Similarly, Fig. E.7 shows the two-dimensional extraction of $A_{UT,MC}^{\sin\phi}$ as a function of x_F, in four different slices of p_T. Note that the fit function is in these cases the same one as extracted from data (i.e., in Section 5.3.1), but evaluated in the Monte Carlo sample.

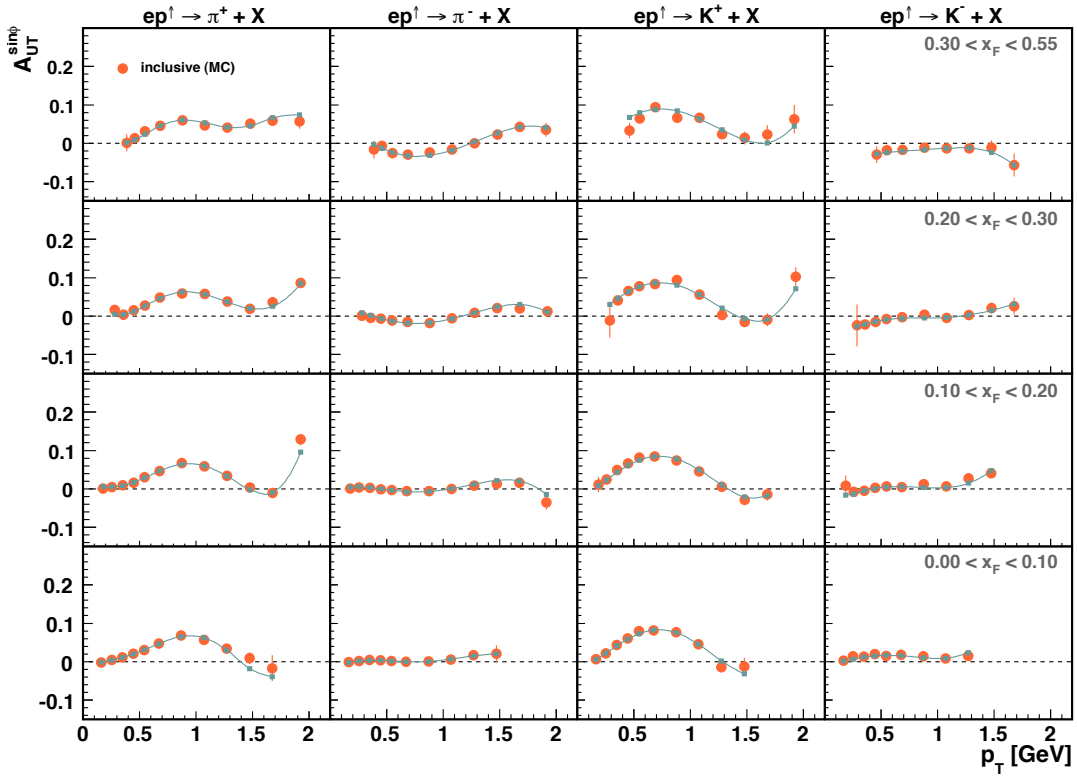

Figure 5.7. The $A_{UT,MC}^{\sin\phi}$ amplitudes extracted from the polarized PYTHIA sample as a function of p_T in four slices of x_F. The $\mathcal{A}_{UT}^{\sin\phi}$ function is also shown for comparison; this is evaluated at the average bin kinematics $\langle p_T \rangle_{MC}$, $\langle x_F \rangle_{MC}$ for each hadron species.

5.4 Systematic uncertainty

In this section, several contributions to the systematic uncertainty on the extraction of the $A_{UT}^{\sin\phi}$ amplitudes are considered. The contribution from the acceptance studies described in the last sections is calculated in Section 5.4.1. This represents the biggest source of uncertainty, as it involves many experimental effects included in the Monte Carlo simulation. Another significant contribution is the one coming from the uncertainty on the measurement of the target transverse polarization, discussed in Section 5.4.2. The effect of other considered sources is reviewed in the following subsections, and turned out to be negligible or already accounted for in the *all-in-one* systematic uncertainty.

5.4.1 All-in-one determination

The deviation of the reconstructed $A_{UT,MC}^{\sin\phi}$ asymmetry amplitudes from the model $\mathcal{A}_{UT}^{\sin\phi}$, shown in Fig. 5.7, is caused by the convolution of the HERMES acceptance with the target spin dependence and it accounts for the uncertainty on $A_{UT}^{\sin\phi}$ originating from all systematic effects included in the Monte Carlo simulation. The statistical uncertainty of $A_{UT,MC}^{\sin\phi}$ is determined by the number of events in the Monte Carlo sample. The deviation between the input model and the reconstructed asymmetry was seen to decrease with increasing Monte Carlo statistics. Therefore, enough data were generated to bring down such deviation to a smaller size than the statistical uncertainty of $A_{UT,MC}^{\sin\phi}$ in most of the kinematical bins.

The systematic uncertainty is taken then as the biggest of either

(i) the deviation

$$|\mathcal{A}_{UT}^{\sin\phi}(p_T, x_F)_{av} - A_{UT,MC}^{\sin\phi}(p_T, x_F)| \tag{5.4}$$

between the model function $\mathcal{A}_{UT}^{\sin\phi}$ evaluated at the average bin kinematics and the asymmetry $A_{UT,MC}^{\sin\phi}$ reconstructed in Monte Carlo, or

(ii) the statistical error of the Monte Carlo asymmetry $A_{UT,MC}^{\sin\phi}$. See Fig 5.7 for both cases.

The resulting systematic uncertainty is then *smoothed*, in order to avoid abrupt changes. This can be done for instance by fitting the resulting distribution of uncertainty (i.e., the value of the systematic uncertainty on each kinematic bin) to a linear or second-order polynomial. The *new* systematic uncertainty is taken then as the absolute value of the polynomial in each kinematic bin. The ROOT [148] software offers a convenient way of doing this, by filling a histogram with the values of the systematic uncertainty (the *original* one) and using the TH1F::Smooth() function. This last option was preferred. In any case, the result is similar. As a result of the smoothing procedure, bins with large (smaller) systematic uncertainty contribute to a larger (small) uncertainty of the adjacent bins.

5.4.2 Target polarization error

The degree of polarization of the protons in the target gas is determined with a precision smaller than $< 10\%$ by the BRP and the TGA polarimeters, described in Section 3.2. This uncertainty propagates directly to $A_{UT}^{\sin\phi}$, e.g., via the $1/\langle P\rangle$ term in Eq. (4.29), via the L_P term in Eq. (4.33), and via the $S_\perp$ term in Eq. (4.36), for the different definitions.

The average polarization and uncertainty for the complete data set are obtained, for each target spin orientation, with the integrals

$$\begin{aligned}\langle P^{\uparrow(\downarrow)}\rangle = \frac{L_P^{\uparrow(\downarrow)}}{L^{\uparrow(\downarrow)}} &= \frac{1}{L^{\uparrow(\downarrow)}}\int L^{\uparrow(\downarrow)}(t)\; P(t)\; \mathrm{d}t,\\ \langle \Delta P^{\uparrow(\downarrow)}\rangle &= \frac{1}{L^{\uparrow(\downarrow)}}\int L^{\uparrow(\downarrow)}(t)\; \Delta P(t)\; \mathrm{d}t,\end{aligned}$$

which in practice are calculated as a sum over the total number of collected bursts[2]. The resulting values are shown in Table 5.2. No difference between the net polarization of each target spin state is found. The systematic uncertainty on $A_{UT}^{\sin\phi}$ coming from the measurement of the target polarization is then given by the formula of standard error propagation. Writing $P = \langle P^{\uparrow(\downarrow)}\rangle$ and $\Delta P = \langle \Delta P^{\uparrow(\downarrow)}\rangle$ for brevity, one obtains

$$(\Delta A_{UT}^{\sin\phi})_{\text{pol}} = \left[\left(\frac{\partial A_{UT}^{\sin\phi}}{\partial P}\right)^2 (\Delta P)^2\right]^{1/2} = \Delta P/P \tag{5.5}$$

This is given in the right column of Table 5.2. Notice that this uncertainty is a constant factor or *scale uncertainty*, relative to the absolute value of the asymmetry in each bin, and independent of the kinematics.

Production	$\langle P^{\uparrow}\rangle$	$\langle P^{\downarrow}\rangle$	$\langle \Delta P\rangle$	$(\Delta A_{UT}^{\sin\phi})_{\text{pol}}$
02d1	0.783	0.783	0.041	5.2%
03d1	0.795	0.795	0.033	4.1%
04d1	0.737	0.737	0.056	7.5%
05d1	0.705	0.705	0.065	9.2%
all	0.713	0.713	0.063	8.8%

Table 5.2. Average target polarizations for the data sets used in this analysis. The last two columns contain the average uncertainty on the measurement of the target polarization, and the relative uncertainty which is transferred to the asymmetries.

[2]The target polarization and the luminosity are both scalers recorded only every 10 s (cf. Sec 3.2)

5.4.3 Target magnet correction

The magnetic field provided by the target magnet deflected the produced charged hadrons and the scattered electron in the target region. For the transversely polarized target the field was directed along the negative y_{lab}-axis and thus had a large component perpendicular to the particle momentum. This affected the reconstruction of the tracks and their kinematics at the scattering vertex.

The HTC tracking algorithm accounts for this effect based on a mapping of the magnetic field in the target area. For real data, the deflection of the tracks is corrected and the angular and vertex resolution are recovered as in the case of the target magnet switched off [101]. Therefore, no significant influence on the $A_{UT}^{\sin\phi}$ amplitudes is expected from this source.

The effect is in any case accounted for in the extraction of the *all-in-one* systematic uncertainty, since both the target magnetic field and the correction by HTC are included in the Monte Carlo simulation.

5.4.4 Hadron misidentification

The true type of the hadron tracks identified by the RICH detector was determined in Section 4.2.1 by an unfolding procedure such that each track is given a certain probability for being a pion, a kaon or a proton track. The equivalent transformation, from the *generated* true type to the *reconstructed* type identified by the RICH detector, is included in the analysis of the PYTHIA sample and the extraction of $A_{UT,MC}^{\sin\phi}$. This way, the effect of the *mis*-identification of the hadron candidates is included in the all-in-one systematic uncertainty.

The elements of the $\mathcal{P}$ and $\mathcal{P}^{-1}$ matrixes, however, are also determined in Monte Carlo within a certain uncertainty, which propagates to the asymmetry measurement. This correction is known to be very small [149] from other analyses performed at HERMES, and in any case of order of the statistical uncertainty of the Monte Carlo sample. Therefore, no extra source of error was assigned.

5.4.5 Angular and momentum resolution

The momenta of the particles is determined by HERMES with a good momentum resolution of $\Delta P/P < 2.6\%$, and an angular resolution of $\Delta\theta < 1.8$ mrad. The resolution of the angle ϕ that enters the extraction of $A_{UT}^{\sin\phi}$ is directly related to these, and therefore also good. This single contribution can also be estimated from the available PYTHIA simulation, where the exact values of the generated and reconstructed angle ϕ are known. The effect of this small uncertainty in the measured asymmetries is automatically accounted for in the estimation of the *all-in-one* systematic uncertainty. of Section 5.4.1.

5.4.6 Radiative corrections

The electrons of the beam are free particles and can therefore undergo radiation processes. The emission of a real photon changes the kinematics of the process and consequently the angles at which the new hadrons are produced. If a photon with four-momentum q_{rad} is radiated in the *initial* state, e.g., before the collision with a proton in the target gas, the actual energy of the beam electron is $k_{\text{true}} = E_{\text{beam}} - q_{\text{rad}}$ smaller than the 27.6 GeV of the HERA beam. If, on the contrary, the radiative process takes place in the final state, the detected electron has less energy than right after the collision. This is illustrated in both graphics of Fig. 5.8. In both cases, it implies a correction on the calculation of the virtual photon four-momentum

$$q_{\text{true}} = k - k' - q_{\text{rad}}, \tag{5.6}$$

which can be estimated using the PYTHIA production, where radiative corrections have been previously implemented. The impact on the reconstruction of the hadronic tracks was found to be negligible.

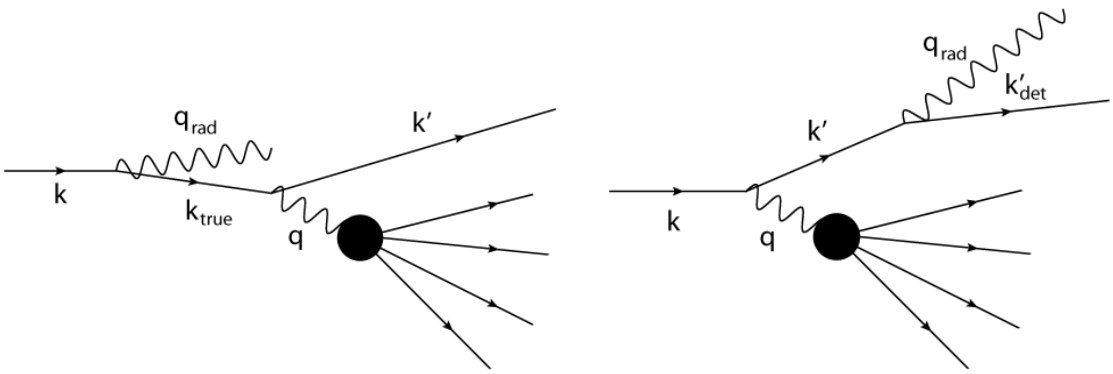

Figure 5.8. Radiative effects in the initial (left) and final (right) states.

5.4.7 Cross-check of results

The results presented in this and the previous chapter were cross checked using two independent analysis codes. This is required by the guidelines of the HERMES collaboration for all published data. In particular, the agreement between two analyzers must be larger than 95% in order to be accepted for publication.

In our case, the discrepancy in the total amount of analyzed inclusive data, i.e., the selected hadron tracks, was smaller than 0.1%. The differences in the selection of SIDIS events, relevant for the discussion of the asymmetries in Chapter 6, were also brought down to this level. The two analysis codes provided therefore nearly identical results for the measured asymmetries, in all cases within the 95% confidence level.

5.4.8 Compatibility of data productions

The data used in this analysis were collected between the years 2002 and 2005. Within such a long period, and especially after long breaks in which some components of the accelerator or the detectors were replaced or upgraded, some experimental conditions may change as for instance the alignment of detectors or their calibrations. This in turn may influence the asymmetry measurement. The compatibility of asymmetries calculated from data of two different productions can be estimated with a Student's t-test for two samples with unequal size and variance (also known as Welch's t-test) [150]. In this case, the t variable indicating the deviation between the asymmetry values ($A^{\sin\phi}_{UT,\,1}$, $A^{\sin\phi}_{UT,\,2}$) of two different data sets is

$$\text{Deviation} = \frac{A^{\sin\phi}_{UT,\,1} - A^{\sin\phi}_{UT,\,2}}{\sqrt{\sigma_1^2 + \sigma_2^2}}, \tag{5.7}$$

where σ_1 and σ_2 are the corresponding statistical uncertainties of the asymmetries. Optimally, one expects the deviation to be between the values of -1 and 1, and to not indicate any systematic trend, i.e., the asymmetry being systematically bigger for one of the two sets.

Several t- tests were performed, i.e., between data from the different productions, in order to check for possible discrepancies, and in that case, assign a corresponding systematic uncertainty to the measured asymmetries. For this discussion, it will suffice to consider the result of the t-test for the 05d1 and 04d1 data, plotted in Fig. 5.9 for each p_T–$x_F$bin and each hadron type. These productions represent the largest parts of the analyzed data, as can be seen from Table 4.4. Since the 04d1 data were taken with a positron beam, and the 05d1 data with an electron beam, this test also allows to check the possible influence of the charge of the beam. A beam with the same particle type but opposite charge bends in opposite directions in the strong magnetic field of the target. This can lead to corrections to the asymmetry amplitudes.

The deviation of the asymmetries in this case is in most cases within the optimal $[-1, 1]$ boundaries, denoting 1σ deviations. No strong systematic trends are seen, although the 05d1 asymmetries, e.g., for π^+, show a certain tendency towards larger values than the 04d1 in some kinematic regions. Most worrying are the cases in which the deviations are large for asymmetry points at small values of the transverse momentum, where the statistics are larger and therefore the statistical uncertainties of the asymmetries are small.

In order to check the possible impact of the asymmetry, an estimation of the systematic uncertainty arising from the deviations of the 05d1 and 04d1 data was performed, based on the following steps

1. Calculate the difference, in every kinematical bin of Fig. 5.9, of the asymmetry for each year ($A^{\sin\phi}_{UT,\,1} - A^{\sin\phi}_{UT,\,2}$). Standard error propagation allows to assign an uncertainty to each point as $\sqrt{\sigma_1^2 + \sigma_2^2}$.
2. Fit the resulting spectrum with a polynomial. A first-order polynomial ($f(p_T) = a + b\,p_T$) was seen to work well for this purpose.
3. With the set of parameters (a, b) obtained from the fit, evaluate the polynomial at the average p_T of every bin.

4. The deviation of the polynomial from the zero line can be taken, for each bin, as a systematic uncertainty to the measured $A_{UT}^{\sin\phi}$ amplitudes.

The result of this procedure is plotted in Fig. 5.10. The grey square points denote the difference of the asymmetries with error bars according to the item *1.* above. The little squares matched with a line denote the fitted polynomial, evaluated at the average p_T of every bin. In all cases, the deviations of the fitted function from the zero line is smaller than the statistical uncertainty of the $A_{UT}^{\sin\phi}$ amplitudes. Therefore, differences between the data from the 05d1 and 04d1 productions can be considered as statistical fluctuations, in all cases smaller than 1σ, showing that the productions are compatible, and no systematic uncertainty must be assigned from this source.

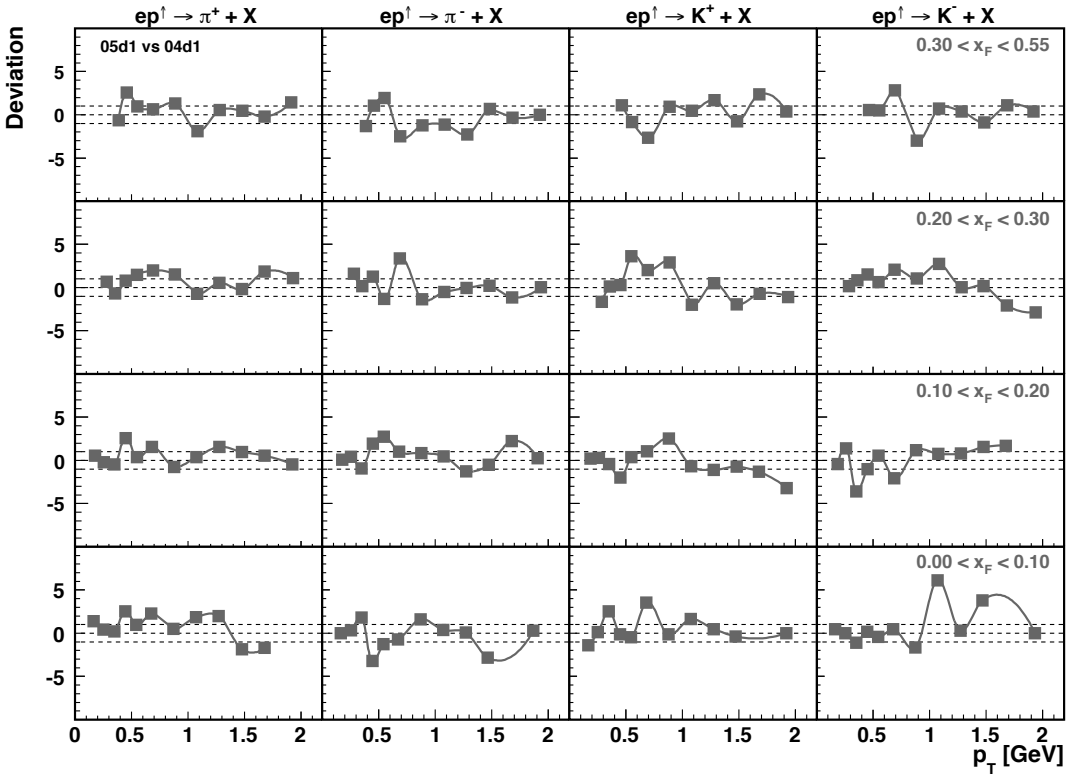

Figure 5.9. Student's *t*-test for the $A_{UT}^{\sin\phi}$ amplitudes of 05d1 and 04d1 data.

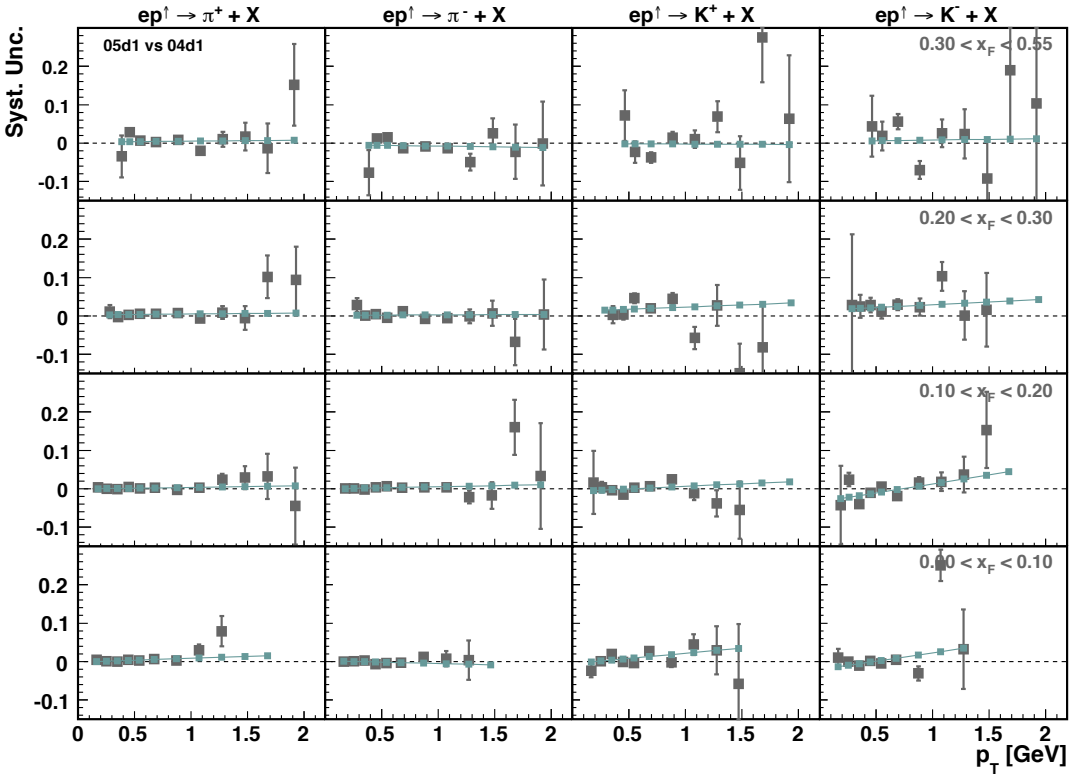

Figure 5.10. Systematic uncertainty associated to the $A_{UT}^{\sin\phi}$ amplitudes from the differences of the 05d1 and 04d1 data. See text for details.

5.4.9 Total systematic uncertainty

Most of the sources of systematic error considered above are accounted for in the all-in-one determination of the systematic uncertainty, described in Sections 5.3.1 – 5.4.1, or found to be negligible. This is summarized in Table 5.3. The total uncertainty indicated in last row is an average over all 1D bins of p_T.

Source	Size
Target polarization error	8.8%
Misalignment & acceptance	all-in-one
Target magnet correction	all-in-one
Hadron misidentification	all-in-one
Angular & momentum resolution	all-in-one
Radiative corrections	negligible
Compatibility of data productions	negligible

Table 5.3. Sources of systematic uncertainty considered.

6 Results

The final results for the measured $A_{UT}^{\sin\phi}$ amplitudes in the inclusive electroproduction of π^+, π^-, K^+ and K^- are shown in Fig. 6.1 for the one-dimensional extraction of the amplitudes as a function of p_T and x_F. The two-dimensional extraction of the amplitudes is plotted in Fig. 6.2 as a function of p_T in four slices of x_F, and in Fig. 6.3 as a function of x_F in four slices of p_T. In all figures, the systematic uncertainty, estimated as described in the previous chapter, is added in quadrature to the statistical uncertainty of the asymmetry points. The inner error bars represent the statistical uncertainty and the outer bars, when visible, the total uncertainty. Only data points whose statistical uncertainty is smaller than 0.1 are plotted. In this chapter, the measured $A_{UT}^{\sin\phi}$ amplitudes are discussed in detail, and a possible interpretation is offered.

6.1 Discussion

A description of the measured asymmetries based solely on the kinematic evolution of the data was already provided in Section 4.6, according to the experimental uncertainty given by statistical error bars. The inclusion of the systematic uncertainties constitutes in most cases just a small correction to the statistical uncertainty[1] and does not change this description.

In order to gain more insight into the origin of the measured asymmetries, we will focus on the general evolution of these with the transverse momentum, which exhibits a richer kinematic structure. Let us consider in the first place the π^+ asymmetries as a function of p_T, plotted in the left upper panel of the top part of Fig. 6.1. The asymmetry is zero for the lowest p_T-bins, then rises up to a maximum of 10% for a value of the transverse momentum of about 0.8 GeV, after which it decreases to nearly zero for $p_T \sim 1.3$ GeV. Such trend is also observed over all four slices of x_F, as seen in the right column of Fig. 6.2.

[1] Only in the case of the K^+ asymmetries as a function of x_F, the systematic uncertainty is larger than the statistical uncertainty. This can be understood from a look at the upper-right panel of Fig E.5, where all $A_{UT,MC}^{\sin\phi}$ points are quite far from the input function, in contrast to all other cases.

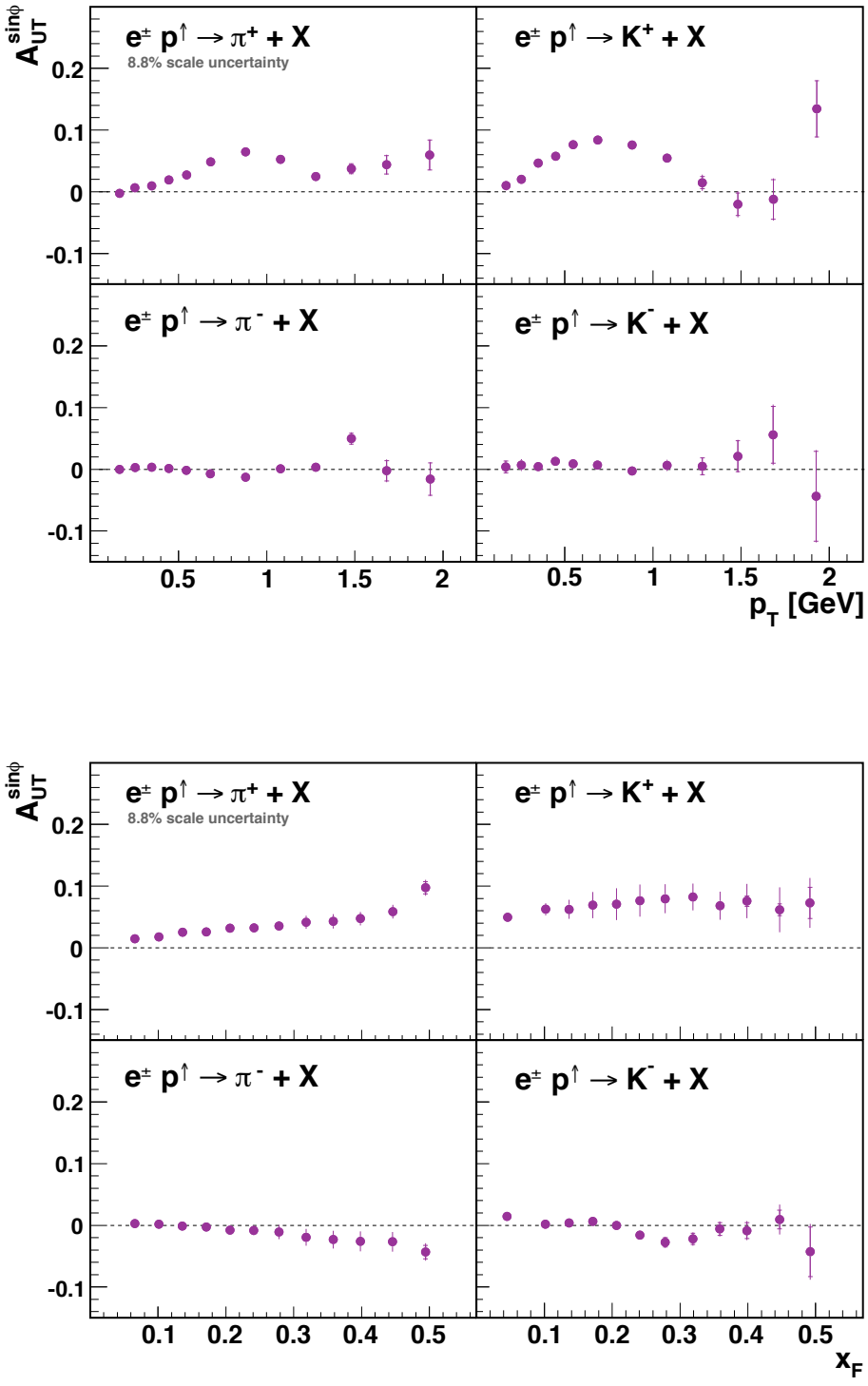

Figure 6.1. The $A_{UT}^{\sin\phi}$ amplitudes extracted as a function of p_T (top) and as a function of x_F (bottom). The inner error bars represent the statistical uncertainty of the measurement; the outer error bars indicate the total error obtained by adding the statistical and systematic uncertainties in quadrature.

The evolution of the π^+ asymmetries at high p_T, as it can be seen from the four left panels of Fig. 6.2, is rather uncertain. Data points do not show a clear trend in this case, and the larger error bars allow a variety of interpretations. However, in the one-dimensional results of Fig. 6.1, an evident tendency of the asymmetry to increase with p_T for the last points at high p_T is observed. This tendency is also found for the $0.20 < x_F < 0.30$ data (second upper panel on the left column of Fig. 6.2), and is also compatible, within the error bars, with the asymmetries extracted for the lower x_F data. In the case of the upper (large x_F) panel, it is difficult to conclude whether the π^+ asymmetry rises at large p_T (this could be compatible with the large error bar of the last data point), or whether the asymmetry vanishes, in which case, the second-last data point could be considered as resulting from a statistical fluctuation of the data. However, an inspection of the asymmetry values for these large-x_F, large-p_T region separately for each data production (02-05), seems to support the idea of an increasing asymmetry[2].

Bearing this in mind, and after the discussion of Section 4.6 on the other hadron species and the evolution of $A_{UT}^{\sin\phi}$ with x_F, the following conclusions can be drawn:

- The dominating kinematic dependence of $A_{UT}^{\sin\phi}$ is on the transverse momentum of the hadron. The smooth dependence on x_F can be almost entirely attributed to the residual correlation between x_F and p_T due to the sizable width of the chosen bins of x_F. This can be also seen in Fig. 6.3, where the π^+ asymmetries are essentially independent of x_F. The same message holds for the K^+ case. However, a certain dependence on x_F is observed for the π^- data (and less significantly for the case of K^-), which is also reflected in the change of sign of the π^- asymmetry points for $p_T < 1$ GeV seen in Fig. 6.2 over the four slices in x_F. This feature of the π^+ data contrasts with the results for inclusive pion asymmetries from the BRAHMS collaboration [68] in proton-proton collisions, where the asymmetry was found to increase with x_F after binning the data in slices of p_T, both for positive and negative pions.
- The evolution of the $A_{UT}^{\sin\phi}$ amplitudes for pions as a function of x_F is similar to the one observed for A_N in hadronic collisions (see Fig. 2.8). However, larger asymmetries are found in the hadronic case. In addition, the measured π^- asymmetries are smaller in size than those for π^+, in contrast to the symmetric evolution seen for hadronic data.
- The two-fold structure of the π^+ data plotted against p_T suggests a mix of contributions. These (at least two) different mechanisms should also contribute to the asymmetries for the other hadron species, although the smaller size of $A_{UT}^{\sin\phi}$ measured for negative hadrons and the reduced statistical power at high p_T for K^+ data do not allow for a clear statement in this case.
- Eventually, we would like to establish a connection between the measured $A_{UT}^{\sin\phi}$ amplitudes and the two approaches for generating transverse SSAs discussed in Chapter 2, i.e., the TMD approach in Section 2.6.1 and the twist-3 collinear approach of Section 2.7.

[2]For some reason, the π^+ asymmetry for 04d1 data is small (with large error bars) for the overall large-p_T range, but large values are found for the other years. The compatibility tests of Section 5.4.8 show anyhow that the data are statistically compatible.

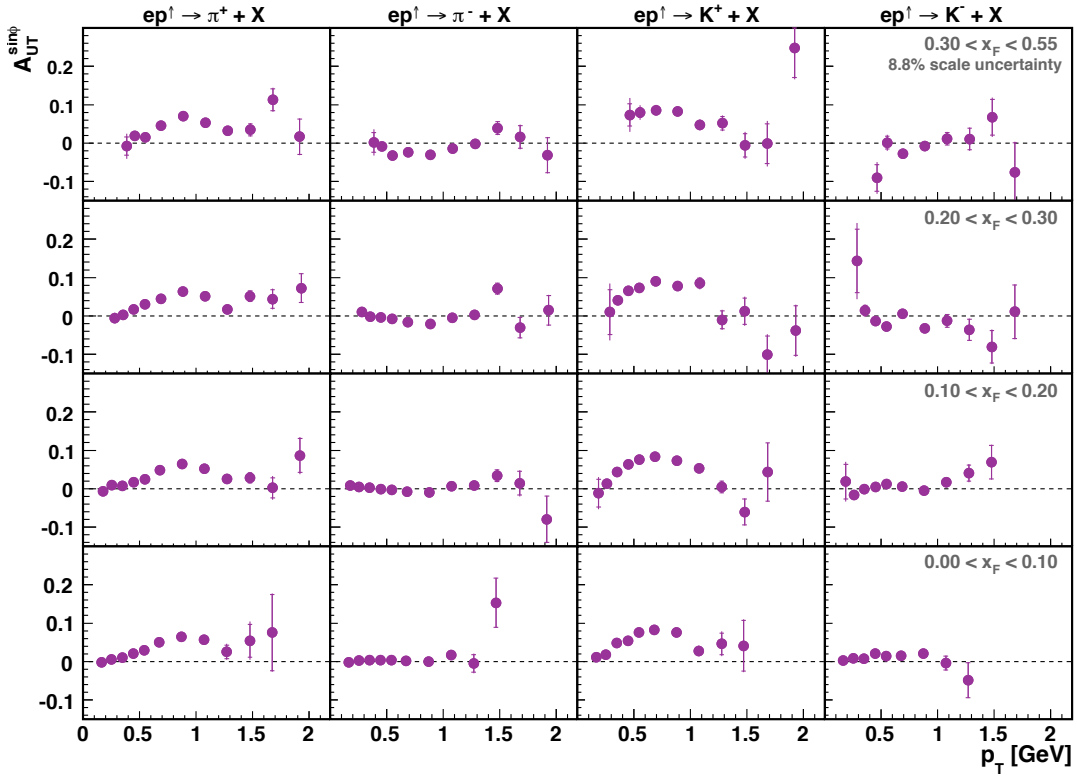

Figure 6.2. The $A_{UT}^{\sin\phi}$ amplitudes extracted as a function of p_T in four slices of x_F, for the four different hadron types. The inner error bars represent the statistical uncertainty of the measurement; the outer error bars indicate the total error obtained by adding the statistical and systematic uncertainties in quadrature.

Here some kinematic considerations must be kept in mind:

- The Sivers and Collins effects, and in general all TMDs, are only effective when $Q^2 \gg p_T^2$ and $Q^2 \gg \Lambda_{QCD}^2$, with $\Lambda_{QCD} \simeq 0.3$ GeV.
- The twist-3 collinear approach requires only the presence of one large scale (i.e., p_T), which should be larger than Λ_{QCD}.
- For $p_T \simeq \Lambda_{QCD}$, and assuming a very small Q^2, one enters in the **non-perturbative** regime, for which no precise theoretical knowledge presently exist.

- More information about the origin of the measured $A_{UT}^{\sin\phi}$ amplitudes can be obtained by examining different subprocesses independently. The total amount of analyzed data are selected simply by the detection of at least one charged pion or kaon with the requirements given in Section 4.2. These guarantee that the relevant properties (momentum, position and particle type) are well determined, but generally speaking, imply no constraints on the production channels of the hadrons[3]. In the kinematic range where the $A_{UT}^{\sin\phi}$ amplitudes were extracted, there exist several contributions to

[3]The only kinematical requirement is on the momentum of the hadron to be within 2 and 15 GeV, based on the optimal range for the RICH detector to provide a good PID. See Section 3.3.2.

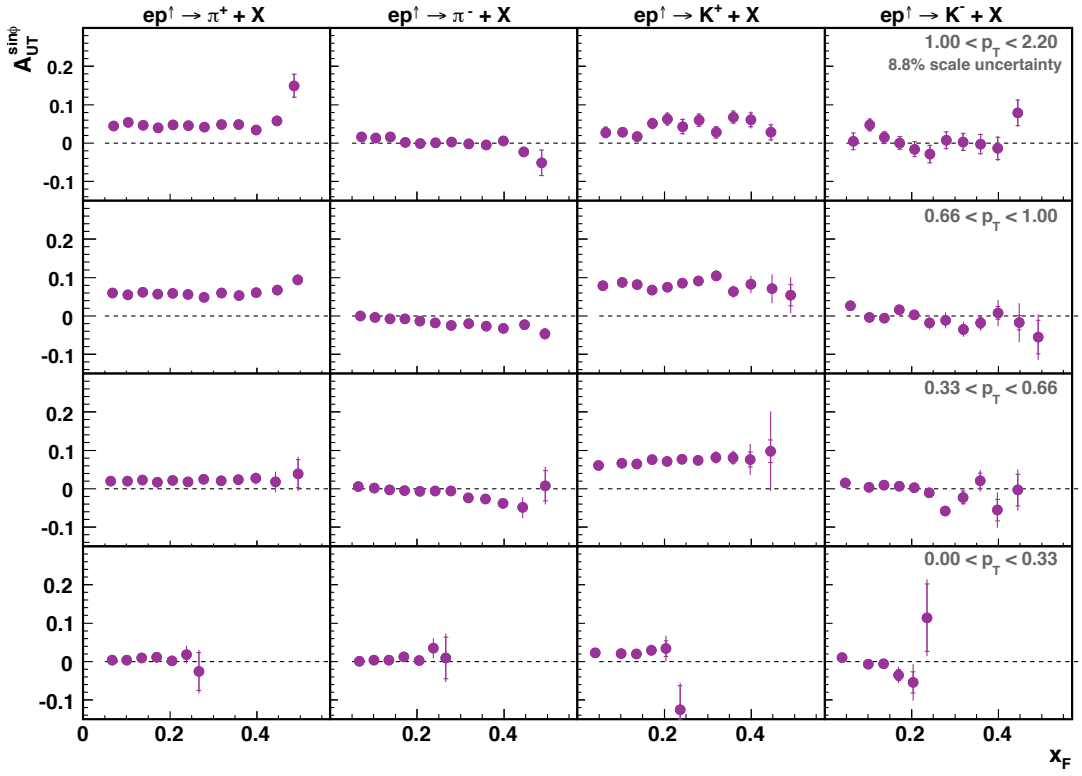

Figure 6.3. The $A_{UT}^{\sin\phi}$ amplitudes extracted as a function of x_F in four slices of p_T, for the four different hadron types. The inner error bars represent the statistical uncertainty of the measurement; the outer error bars indicate the total error obtained by adding the statistical and systematic uncertainties in quadrature.

the $ep^{\uparrow}$ cross section. The data are, nevertheless, expected to be dominated by events from *quasi-real photoproduction* ($Q^2 \to 0$). This can be understood considering that, since the scattered beam lepton is not required, many of the detected hadrons arise from collisions in which the beam lepton is scattered at low angles, i.e., low Q^2. On the other hand, at sufficiently large p_T, the proportion of hadrons resulting from DIS collisions (with $Q^2 > 1$ GeV) is expected to increase. These two type of processes may, in principle lead to different SSAs. In addition, other subprocesses exist that eventually produce a charged pion or kaon in the final state, e.g., vector-meson production.

- Therefore, in each kinematic bin, the measured $A_{UT}^{\sin\phi}$ amplitudes are presumed to be a sum of several contributions, i.e., from different **subsamples** of the inclusive data

$$A_{UT}^{\sin\phi}(p_T, x_F) = \sum_{i}^{\text{samples}} f_i \, A_{UT,i}^{\sin\phi}(p_T, x_F). \tag{6.1}$$

Here, $A_{UT,i}^{\sin\phi}$ is the asymmetry from the hadrons in each subsample, and $f_i \equiv N_i/N_{\text{inc}}$ is the fraction of tracks in the subsample (corrected by the trigger efficiency) with respect to the total number of inclusive data N_{inc}.

An estimation of the contributing processes, and the corresponding SSAs and hadron yields resulting from them, is thus essential to provide a deeper explanation of the measured asymmetries, and in order to use these data as input for theory calculations. This could be done for instance in a Monte Carlo simulation, where all necessary information about the originating reactions of the hadrons is kept. However, given the lack of a fully reliable Monte Carlo simulation, another approach was taken, based on the kinematical characterization of the collected data.

This is discussed in detail in the next section, where the $A_{UT}^{\sin\phi}$ amplitudes are extracted for several subsamples of the inclusive data. With the corresponding asymmetries in hand and also the relative yields in every kinematic bin of events in each subsample, we will try to provide a cleaner interpretation of the measured asymmetries.

6.2 Contributing subprocesses

Based on the previous discussion, the question arises naturally what the contribution to the measured $A_{UT}^{\sin\phi}$ amplitudes from the two main processes is: quasi-real photoproduction and semi-inclusive DIS reactions.

- Hadrons resulting from **quasi-real photoproduction** can be easily tagged by the absence of the scattered lepton in the spectrometer acceptance. Since these reactions imply very low momentum transfers ($Q^2 \to 0$ GeV^2), the beam lepton is scattered at very small angles, very close to the beam pipe, and remains undetected.

  Let us call these events (where only hadrons and no leptons are detected) *anti-tagged* events. Note that anti-tagged events can also result from beam leptons scattered at very large angles, and therefore (since Q^2 and the polar angle θ are correlated) at large Q^2. The fraction of events scattered at angles larger than the maximum angular acceptance of the HERMES spectrometer was determined in a Monte Carlo simulation. This turns out to be negligible for events with $p_T < 1$ GeV, for all values of x_F. However, a significant increase was seen for the tracks at both large p_T and x_F, being around 30% for the last bin of p_T (at largest x_F) for positive hadrons, and not bigger than 10% for negative hadrons. See Fig. E.34. Therefore, anti-tagged events can be effectively regarded as originating from photoproduction[4] reactions for low hadron transverse momentum, while at large p_T and large x_F, the anti-tagged sample consists of a mix of hadrons produced in photoproduction and DIS reactions.

- The **SIDIS** data set used in Refs. [91, 95] to extract the semi-inclusive SSAs related to the Sivers and Collins functions is *entirely* contained in the total inclusive data sample. This offers a remarkable opportunity to compare the measured $A_{UT}^{\sin\phi}$ amplitudes to the semi-inclusive SSAs associated to the Sivers and Collins effects, in the *same* kinematic regime. Note that this comparison is only approximate, as the SSAs imply different azimuthal modulations in each case.

[4] Let us, for brevity, omit the label *quasi-real*.

Hadrons produced in DIS collisions can be precisely determined by certain kinematic requirements (or *cuts*) on the lepton track detected in coincidence with the hadrons. These cuts are defined on Appendix C, and serve in three different ways: *(i)* maximize the probability that the detected lepton corresponds to the scattered beam lepton, *(ii)* enhance the proportion of hadrons resulting from hadronization of the struck quark, and *(iii)* require a minimum $Q^2 > 1$ GeV^2. It is worth mentioning that the lepton track is only used to *tag* the corresponding samples, i.e., the extraction of the $A_{UT}^{\sin\phi}$ amplitudes from these data is done otherwise in exactly the same way as for strictly inclusive data.

- In addition, a third group of events was considered: the *anti-SIDIS* events, i.e., those hadrons tracks for which a lepton was detected in coincidence, but rejected by the SIDIS kinematical cuts mentioned above. The two major contributions to this subsample were found to be

  - Hadrons with a **large energy fraction** ($z > 0.7$). These events are discarded in analyses of SIDIS data as they might originate in the decay of exclusive vector mesons. See Appendix C for more information.
  - Events with **small momentum transfer** ($Q^2 < 1$ GeV^2). These events are kinematically closer to the photoproduction regime, and therefore provide a good opportunity to explore it for the case where the virtual-photon variables can be reconstructed.
  - All other *residual* subsets, rejected by the remaining cuts on the SIDIS variables other than z or Q^2, were found to be very small ($z < 0.2$) or insignificant (see cuts on x, y and W^2) in comparison to the yields of total inclusive data in each kinematic bin.

Note that the sum of these three subsamples: anti-tagged, SIDIS and anti-SIDIS[5], represents the total amount of inclusive data. Thus, the value of the inclusive asymmetry in each kinematic bin is then

$$\begin{aligned} A_{UT}^{\sin\phi}(p_T, x_F) \;=\; & f_{\text{anti-tagged}}\, A_{UT,\,\text{anti-tagged}}^{\sin\phi}(p_T, x_F) \\ & + f_{\text{SIDIS}}\, A_{UT,\,\text{SIDIS}}^{\sin\phi}(p_T, x_F) \\ & + f_{\text{anti-SIDIS}}\, A_{UT,\,\text{anti-SIDIS}}^{\sin\phi}(p_T, x_F), \end{aligned} \tag{6.2}$$

which, taking into account the above considerations about every subset, can be rewritten in a more meaningful way (regarding the kinematical regimes) as

$$\begin{aligned} A_{UT}^{\sin\phi}(p_T, x_F) \;\simeq\; & f_{\text{photo}}\, A_{UT,\,\text{photo}}^{\sin\phi}(p_T, x_F) \\ & + f_{\text{SIDIS}}\, A_{UT,\,\text{SIDIS}}^{\sin\phi}(p_T, x_F) \\ & + f_{\text{large-z}}\, A_{UT,\,\text{large-z}}^{\sin\phi}(p_T, x_F) \\ & + f_{\text{low-}Q^2}\, A_{UT,\,\text{low-}Q^2}^{\sin\phi}(p_T, x_F), \end{aligned} \tag{6.3}$$

[5]The sum of SIDIS and anti-SIDIS data set is therefore the complete *tagged* sample.

in an obvious notation. The fractions and asymmetries obtained in each of the four cases of Eq. (6.4) are discussed in the next sections. The discussion will be centered only around the one-dimensional results as a function of p_T, which suffices for an interpretation. Other results for each subset are included in Appendix E.

6.2.1 Contribution from photoproduction

The fraction of anti-tagged events with respect to the total inclusive data is plotted in Fig. 6.4 for each bin of p_T. As can be seen in this figure, nearly 100% of the hadrons detected at low p_T are produced in photoproduction reactions. For the bins at higher p_T, this proportion decreases to a value of about 90% in the case of positive hadrons, while for negative hadrons it is on average larger and shows a less pronounced downtrend. As mentioned in Section 6.2, there is significant contribution to the anti-tagged category from events produced in DIS reactions on the last bins of p_T, see Fig. E.34.

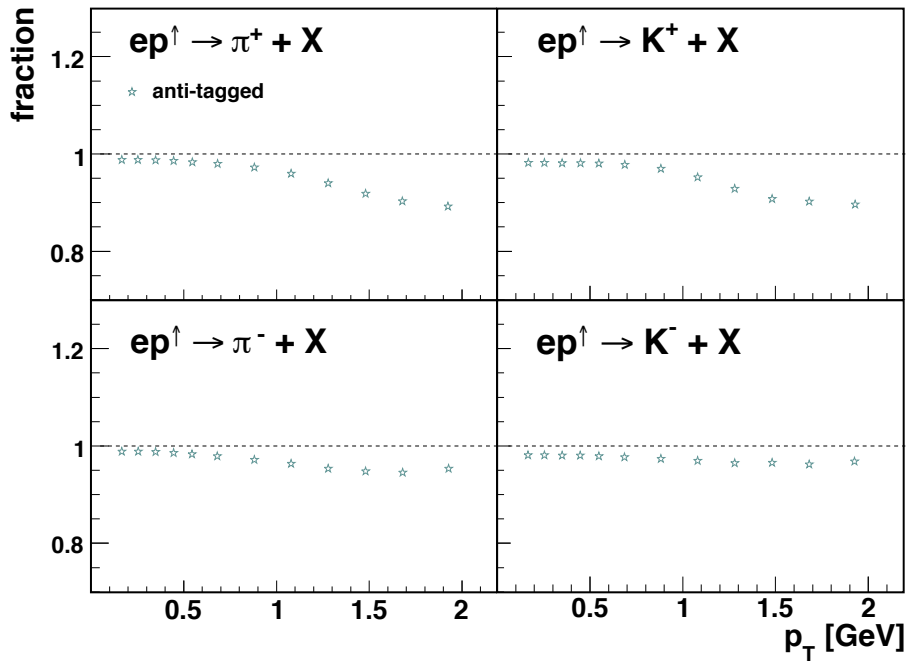

Figure 6.4. Fraction of collected hadrons for which no lepton track was detected in coincidence.

The $A_{UT}^{\sin\phi}$ amplitudes extracted only for the events in the anti-tagged sample are plotted with *star* symbols in Fig. 6.5, together with the inclusive asymmetries[6]. Only the corresponding statistical uncertainties are included in the error bars. For the low-p_T range, both asymmetries are nearly identical. At the bins of large-p_T, the anti-tagged asymmetries for positive (negative) hadrons are on average slightly smaller (larger) than the inclusive ones. The evolution of the last three points of the π^+ asymmetries, however, suggests that the asymmetry goes to zero. Note that, even if the results in this case are compatible with the

[6]The data points corresponding to the anti-tagged sample have been slightly shifted to the right.

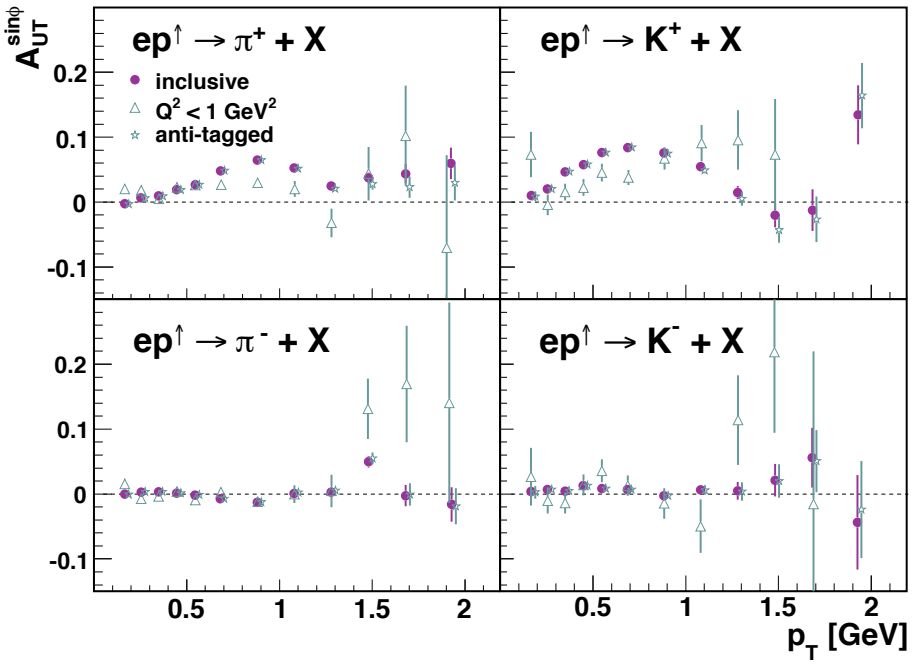

Figure 6.5. The $A_{UT}^{\sin\phi}$ amplitudes extracted from photoproduction events as a function of p_T, compared to the inclusive amplitudes.

inclusive $A_{UT}^{\sin\phi}$ within the error bars, the agreement in this case must be evaluated in the distance between the central values of the asymmetry in each case – both data samples are part of the same sample, and therefore their statistical uncertainties are correlated. As it is shown in next section, the asymmetry from the tagged subsamples are much larger than in this case, especially at large p_T. Therefore, and taking into account the mix of events from photoproductions and DIS reactions at large p_T, one can expect that the asymmetry from photoproductions vanishes at large transverse momentum.

The measured inclusive $A_{UT}^{\sin\phi}$ amplitudes are therefore dominated by the asymmetry resulting from photoproduction events over the entire p_T range explored (see Figs. E.19–E.15 in Appendix E for the results as a function of x_F, and the two-dimensional extractions.).

This is not surprising, provided that the ep cross section rises steeply towards low values of Q^2, such that the hadron-production rates increase considerably at these energies, becoming much larger than those from DIS collisions. At low values of Q^2, the mass spectrum of the virtual photon exchanged in the electron-proton collisions extends towards values of $Q^2 = 0$, which correspond to massless *real* photons. In this case, the outgoing hadrons can be effectively regarded as produced in photoproduction events. These low-Q^2 reactions are intrinsically different to the virtual photon-proton collisions which take place in DIS.

At leading order, two type of processes can contribute: *(i)* direct photon processes, where a real photon interacts itself with the proton (examples of these are the DIS, photon-gluon fusion, and QCD Compton processes), and *(ii)* hadronic photon processes, where the photon interacts with the proton via hadronic interactions. An example of the latter is the case of *diffractive scattering*, in which the photon fluctuates into a $q\bar{q}$ pair, and therefore the final collision is between one of these quarks and the quarks in the proton. Such process can

be calculated perturbatively provided that the transverse momentum of the quarks in the pair is large enough with respect to the photon direction. Below this scale, no perturbative calculations are possible and model estimates must be used instead to evaluate the cross section [10].

The very low-Q^2 data are therefore related to the hadronic component of the virtual photon. A mechanism able of generating a SSA in this non-perturbative regime is presumably similar to the case of the hadronic A_N. One could conjecture that the SSA for this region should originate from some unknown high-twist effect, i.e., related to a PDF appearing at twist-3 or larger, dominated by quark-gluon correlations and where higher-order loop corrections must be taken into account, given the low energy scale of the virtual photon. Such high-twist phenomena are expected to be suppressed by p_T [151]. This could be the reason for the tendency of the asymmetries towards zero values for the range $p_T \in [0.8, 1.3]$ GeV. On the other hand, any sizable effect related to the transverse spin is expected to vanish for $p_T \to 0$, which would explain why the asymmetries become zero at low p_T. For $p_T \gg \Lambda_{QCD} \sim 0.3$ GeV, the asymmetry could be related to a twist-3 PDF, as discussed in Section 2.7.

6.2.2 Contribution from SIDIS

The fraction of hadrons produced in SIDIS reactions is indicated with grey circles in Fig. 6.6. These are identified by the simultaneous detection of the hadron with the scattered beam lepton, as discussed in Appendix C. For all four hadron species, the fraction of events in the SIDIS regime is found to be less than 1% for the lowest p_T bins, rising with increasing value of the transverse momentum until $p_T \simeq 1.5$ GeV, after which it becomes smaller. The fraction reaches a maximum of 3% for π^+ and 2% for π^-, while it is less than 4% for K^+ and 2% for K^-. The $A_{UT}^{\sin\phi}$ amplitudes extracted from hadrons in the SIDIS subsample are plotted

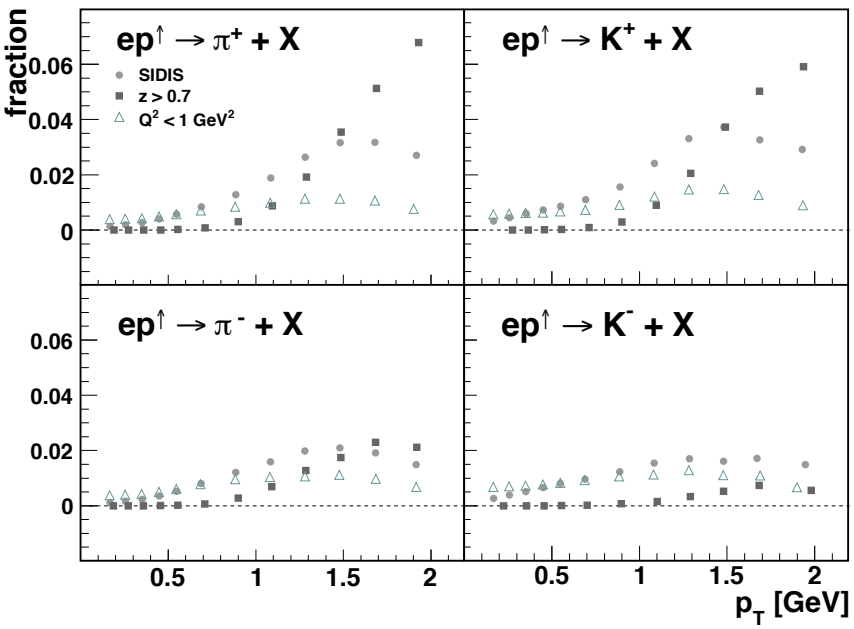

Figure 6.6. Fraction of collected hadrons for which a lepton track was detected in coincidence.

in Fig. 6.7, together with the inclusive asymmetries. Only the corresponding statistical uncertainties are included in the error bars. For positive pions, the measured $A_{UT}^{\sin\phi}$ amplitudes for the SIDIS events rise continuously with the hadron transverse momentum, reaching a value of about 20% for the largest bin in p_T. Except for the region at moderate p_T, these are significantly larger than the amplitudes from all inclusive data. For negative pions, the SIDIS amplitudes are clearly negative for almost the entire range in p_T, reaching a maximum value of about 5% at $p_T = 1.5$ GeV. For the two largest bins of the transverse momentum, the π^- asymmetries from SIDIS data show a trend towards positive values. The K^+ amplitudes for the SIDIS sample are compatible with those from the total sample in most of the explored kinematic range, showing a certain tendency towards larger values in the central p_T-region. No evident rise at large p_T is seen in this case, in contrast to the π^+ results. In the case of the K^- amplitudes, the smaller statistical power compared to the other samples, and the apparently random distribution of the amplitudes for the SIDIS over the p_T range, makes it difficult to conclude anything, except that they are compatible with zero.

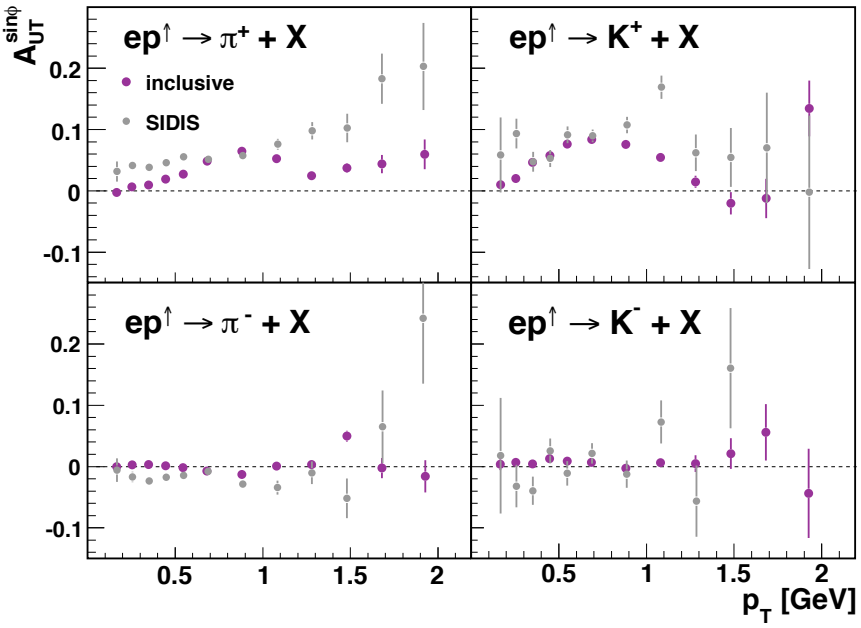

Figure 6.7. The $A_{UT}^{\sin\phi}$ amplitudes extracted from DIS events as a function of p_T, compared to the inclusive amplitudes.

This discussion holds also for the two-dimensional extractions of the amplitudes from SIDIS data, shown in Fig. E.19. However, the fraction of SIDIS events changes significantly with x_F, for a given p_T bin. This can be seen in Fig. E.18. For all hadron species, the largest fraction of SIDIS events is in the range $0.1 < x_F < 0.2$, at a value of $p_T \simeq 1.7$ GeV, being about 5% for π^+, 4% for π^-, 6% for K^+ and less than 3% for K^-. This effect is most noticeable at large values of the transverse momentum and seems to be correlated with the evolution of the fraction of events with large z, plotted with squares. In the case of the two-dimensional asymmetries, one subtle difference is found with respect to the one-dimensional results. For π^+, the two-dimensional amplitudes appear to reproduce the same tendency at moderate p_T, i.e., the rise-drop-rise trend, although in a smoother way.

One relevant observable for the interpretation of these asymmetries in terms of the TMDs is the ratio $p_{h\perp}^2/Q^2 \sim p_T^2/Q^2$. As discussed in Section 2.6.1, the factorization of the ep cross section into TMDs is only proven so far for the kinematic range in which $p_{h\perp} \ll Q^2$. One normally assumes that this is true if the ratio $p_{h\perp}^2/Q^2 < 1$. For the subsamples of inclusive data in which the scattered beam lepton was detected, it is possible to reconstruct the virtual photon and provide an estimation of this ratio, based on the average value of p_T and Q^2 in each kinematic bin. This is shown in Fig. 6.8, indicating that this condition is fulfilled for all data points, except for the last or two last points at large p_T, for which the ratio is slightly above 1. See Appendix E for more figures. In addition, the average Q^2 of the data in each bin is shown in Fig. 6.9.

The mechanism generating these asymmetries should therefore be related to some of the TMDs defined in Section 2.6.1. A natural candidate is the Sivers function $f_{1T}^{\perp}$, given that its azimuthal dependence on the target spin ($\sin(\phi_h - \phi_S)$) leads to a $\sin\phi$ dependence when integrated over ϕ_S, i.e., in the case where the scattered beam electron is not detected. This can easily be seen by comparing the definition of the azimuthal angles ϕ_S and ϕ_h for the SIDIS process, depicted in the right-hand side of Fig. 2.9, with the definition of ϕ for the inclusive production of hadrons in Fig. 2.15. The difference between ϕ_S and ϕ_h is precisely ϕ. Note, however, that ϕ_S and ϕ_h are defined with respect to the direction of the virtual photon $\mathbf{q}$, while ϕ is defined with respect to the direction of the incoming beam $\mathbf{k}$. Therefore, the relation between the azimuthal angles in both cases makes only sense under the assumption that $\mathbf{q}$ and $\mathbf{k}$ are collinear. The collinearity of the scattering process is related to the magnitude of the transverse momentum of the outgoing hadrons. For relatively low values of p_T, the approximation of $\phi_S - \phi_h = \phi$ should hold, whereas deviations between both quantities should be present at large p_T. This implies that, at large p_T, contributions to the measured asymmetries from other TMDs, like for instance the Collins fragmentation function $H_1^{\perp}$, are also expected.

The measured $A_{UT}^{\sin\phi}$ amplitudes for the SIDIS subsample are indeed quite similar to those measured in Refs. [91] for SIDIS data, supporting the idea that the Sivers effect could be the leading contribution. The smaller value of the measured asymmetries for π^- and K^- for this data subsample in comparison to those for positive hadrons could be interpreted as a cancellation of different contributions between favored and disfavored fragmentations functions[7], as pointed out in Ref. [91].

Similarly, these results could be interpreted in terms of the twist-3 collinear model (cf. Section 2.7), where the generating mechanism could be either a twist-3 chiral-odd fragmentation function coupled to the transversity distribution or a twist-3 chiral-even distribution function coupled to the ordinary twist-2 unpolarized fragmentation function.

[7] i.e., between a d-quark Sivers function opposite in sign to the dominant u-quark Sivers function. See the discussion given in Section 2.6.2 about the Sivers asymmetries from SIDIS data.

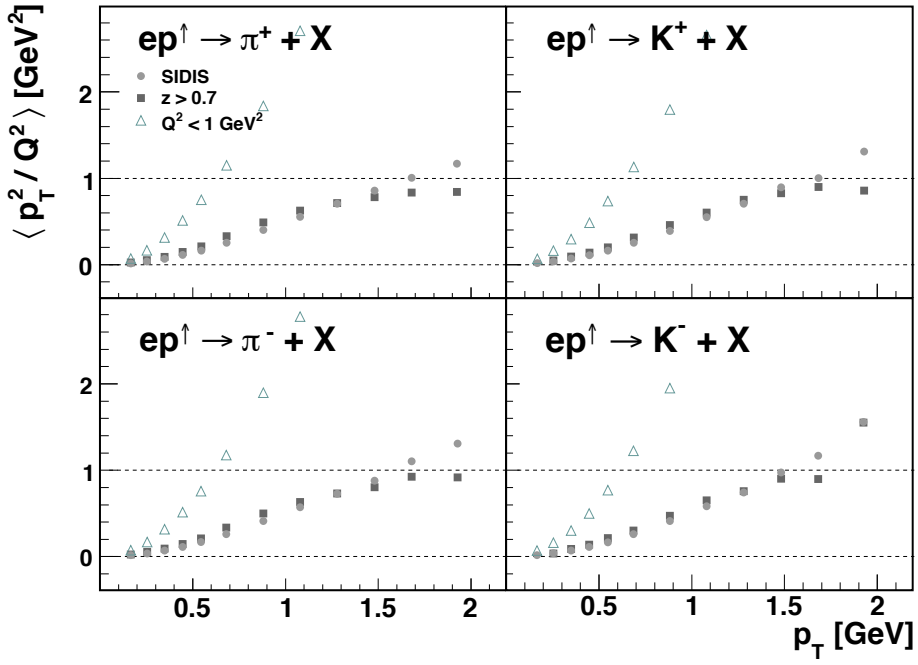

Figure 6.8. The ratio $\langle p_T^2/Q^2 \rangle$ calculated for each kinematic bin and different subsamples of the data.

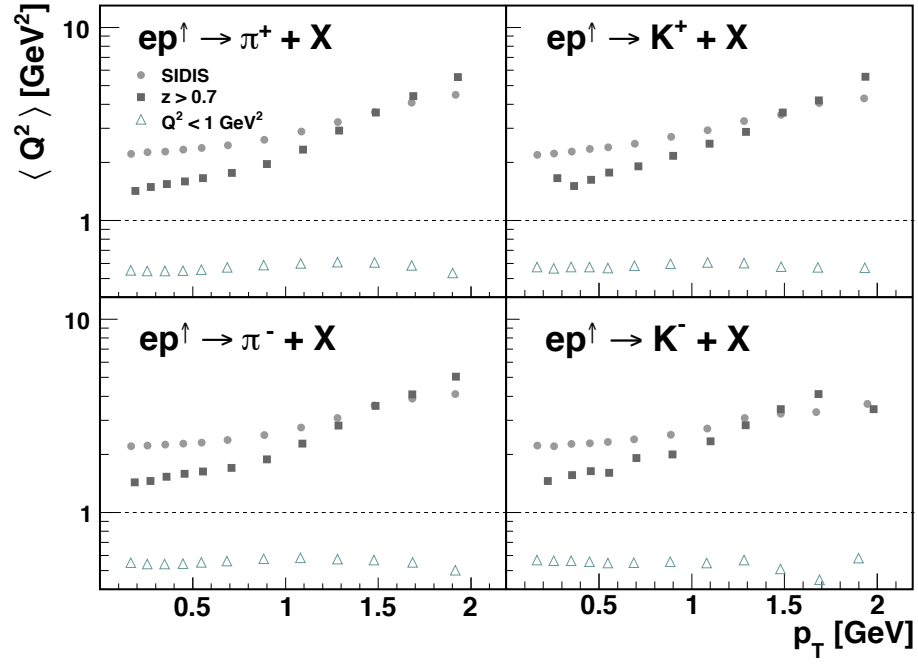

Figure 6.9. Average Q^2 calculated for each kinematic bin and different subsamples of the data.

Acceptance studies The measured asymmetries could be affected by the fact that an electron track is detected. This, as pointed out in Section 4.3, enhances the probability that the physics trigger fires and, therefore, that hadron tracks are collected. If these acceptance effects are large, the correction of the hadron yields by the trigger efficiency could not be sufficient. The estimation of acceptance effects for events with and without an electron can be done conveniently for the data in the SIDIS subsample, for which a fully-dimensional parametrization exist [147] in terms of the relevant SIDIS variables – let us call this the *SIDIS asymmetry function* $\mathcal{P}_{\text{SIDIS}}$, including azimuthal modulations due to the Sivers and Collins effects, as well as a $\sin\phi_S$ modulation

$$\begin{aligned}\mathcal{P}_{\text{SIDIS}}(x, Q^2, z, p_{h\perp}, \phi_h, \phi_S) \;=\; & 1 + S_\perp \cdot \mathcal{A}_{\text{Sivers}} \cdot \sin(\phi_h - \phi_S) \\ & + \mathcal{A}_{\text{Collins}} \cdot \sin(\phi_h + \phi_S) \\ & + \mathcal{A}_{\sin\phi_S} \cdot \sin\,\phi_S .\end{aligned} \tag{6.4}$$

Here, $\mathcal{A}_{\text{Sivers}}$, $\mathcal{A}_{\text{Collins}}$ and $\mathcal{A}_{\sin\phi_S}$ are Taylor expansions (up to with 44 parameters) in the relevant variables around the average kinematics of the SIDIS data sample. See Ref. [147] for more details, in particular Eq. (6.32) therein and related discussion. The procedure is the following: [8]

- Generate Monte Carlo events in the SIDIS kinematic regime, i.e., with the kinematic cuts defined in Appendix C for x, Q^2, y and W^2 applied to the electron track at *generation* level and hadrons in the spectrometer acceptance with the requirement $0.2 < z < 0.7$, but without applying any geometrical or angular cut to the scattered electron. The same PYTHIA production as described in Section 5.2 was used.
- Weight the events according to the probability function in Eq. (6.4), which introduces an azimuthal target spin dependence.
- Reconstruct the asymmetry for these events, which is affected by the geometrical acceptance for hadron tracks.
- Repeat the procedure but now applying the geometrical cuts also for the electron track, i.e., requiring the presence of an electron track in the final state within the geometrical acceptance.
- Reconstruct the asymmetry for these events with an electron, which is affected by the geometrical acceptance for both hadron and electron tracks. This asymmetry will have larger error bars than the previous case (only for reconstructed hadrons).
- Deviations between both cases are a hint of effects due to the geometrical acceptance.

The results of this test indicated a good agreement between the reconstructed asymmetries, apart from small statistical fluctuations of the data. Thus, it was concluded that the measured $A_{UT}^{\sin\phi}$ amplitudes are free of remarkable acceptance effects.

[8] The idea is similar to the one used in Chapter 5 to determine the *all-in-one* systematic uncertainty.

6.2.3 Contribution from large z

The results for this subsample are particularly interesting, since it is the fraction of the data for which largest asymmetries were measured. Events in this category are designated by the DIS cuts on x, y, Q^2 and W^2, defined in Appendix C, and having a large energy fraction $z > 0.7$ (in opposition to *conventional* SIDIS events, required to have $0.2 < z < 0.7$).

The fraction of SIDIS events with $z > 0.7$ is plotted in Fig. 6.6, denoted with square symbols. For the low-p_T range, this is found to be smaller than the fraction of SIDIS events, discussed in the previous section, whose z is in the range $0.2 < z < 0.7$. However, at large p_T, the fraction of events with $z > 0.7$ increases significantly up to 7% for π^+ and 6% for K^+. For π^-, this is found to be comparable to the events with $0.2 < z < 0.7$, while for K^-, it does not represent more than 1% of the inclusive yields at any given value of p_T.

The corresponding asymmetries for this data set are plotted in Fig. 6.10 with squared symbols. Very large positive asymmetries are found, exceeding 30%, in the case of π^+ and up to 40% for K^+. Also striking is the smooth, nearly non-existing dependence of these asymmetries on the transverse momentum. In the case of π^-, large negative asymmetries are found, increasing in size with p_T, exceeding 20%. This contrasts with the results for all other subsamples, where the measured π^- asymmetries are always suppressed in comparison to the π^+, pointing to possible cancellation effects. Moreover, the large negative asymmetries for π^- for these data resemble the predictions from Anselmino *et al.* in Ref. [89]. No relevant conclusions can be drawn from the K^- asymmetries at large z given the large error bars.

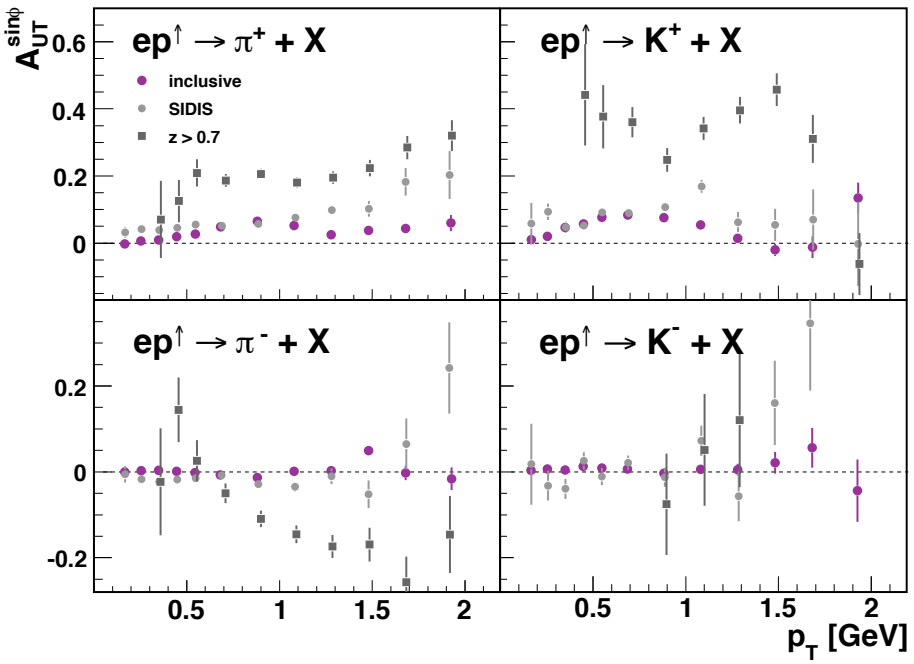

Figure 6.10. The $A_{UT}^{\sin\phi}$ amplitudes extracted from DIS events with $z > 0.7$ (squares) as a function of p_T, compared to the inclusive amplitudes, and the asymmetries from SIDIS events with $0.2 < z < 0.7$ (grey points).

The $\langle p_T^2/Q^2 \rangle$ corresponding to these data are plotted with squared symbols in Fig. 6.8. The situation is similar as to the SIDIS data. However, the average value of $\langle p_T^2/Q^2 \rangle$ in each bin is slightly higher, for $p_T < 1.3$ GeV, for the large-z events, and it does not become bigger than 1 in any case. This can be understood by examining the $\langle Q^2 \rangle$ of these data in Fig. 6.9.

The origin of these large asymmetries could be in different sources:

- **Dominance of struck quark** In a proton target, due to the dominance of u quarks, it is more likely to produce a meson containing an u quark, like π^+ and K^+ (*favored fragmentation*), than a meson containing a d quark, like π^- and K^-, which in many cases will originate from *unfavored fragmentation* of u quarks. This would explain why the Sivers asymmetries measured in SIDIS data [91] are bigger for positive than for negative mesons, as the latter would involve a dilution between the favored and unfavored fragmentation channels and this would lead to a cancellation of the Sivers effect for u and d quarks, with different sign. As a large value of z indicates a large correlation with favored fragmentation of the struck quark, one expects therefore a higher sensibility to the Sivers asymmetry inherent in the struck quark, without dilution from unfavored fragmentation of other quark species. This could explain the bigger size of the asymmetries measured for this sample, in particular for the π^-.
- **Exclusive vector meson production** Large z implies as well a higher probability that the hadron was produced in an exclusive channel. The decay of ρ mesons [153, 154] typically produces pions in the final state, e.g., in the reaction $e\,N \to e'\,\rho^0\,N' \to e'\,\pi^+\,\pi^-\,N'$, while ϕ mesons contribute to the kaon yield. The contributions from exclusive vector-meson decay to the SIDIS π^+ and K^+ yields are estimated in Ref. [91]. This is found to be much larger for π^+ (nearly 20%) than for K^+ (<4%). Note that in the cited reference, only data with $0.2 < z < 0.7$ are analyzed. For larger z, the contribution to π^+ rises to about 50% [155].
- **Exclusive single-pion or kaon production** Besides, large $A_{UT}^{\sin\phi_S}$ amplitudes, up to 80%, were observed for large z in the *direct* production of π^+ from exclusive reactions ($e\,p \to e\,n\,\pi^+$) [156]. A clear relation between these $A_{UT}^{\sin\phi_S}$ amplitudes and the measured $A_{UT}^{\sin\phi}$ amplitudes, however, has not yet been established. Also the $A_{UT}^{\sin(\phi_h-\phi_S)}$ amplitude for π^+, related to the Sivers effect, were measured in Ref. [156] and found to be negative and smaller in magnitude ($\sim 20\%$). The corresponding quasi-exclusive channel for direct π^- production is $e\,p \to e'\,\pi^-\Delta^{++}$, and for K^+ production is $e\,p \to e\,\Lambda\,K^+$. However, the contributions from these channels are expected to be small [157]. No exclusive channel that could contribute to the K^- asymmetries is known.

Missing mass One way of checking the possible contribution from exclusive channels to these large-z events is by looking at the spectrum of the missing mass M_X^2, defined as the squared mass of the undetected products X in the reaction $e\,p \to h\,e'\,X$. By applying conservation of energy and momentum, M_X^2 can be calculated from the relation

$$M_X = \sqrt{E_X^2 - |\mathbf{p}_X|^2}. \tag{6.5}$$

Here,

- $E_X = E_{\text{beam}} + M_P - \sqrt{M^2 + |\mathbf{p}|^2} - E_{e'}$, with M_P the mass of the proton, M and $\mathbf{p}$ the mass and momentum of the hadron, respectively, and $E_{e'}$ the energy of the scattered beam electron;
- the three components of the $\mathbf{p}_X$ vector are

$$\begin{aligned} p_{Xx} &= -p\ \sin\theta\ \cos\phi - p_{e'}\ \sin\theta_{e'}\ \cos\phi_{e'}, \\ p_{Xy} &= -p\ \sin\theta\ \sin\phi - p_{e'}\ \sin\theta_{e'}\ \sin\phi_{e'}, \\ p_{Xz} &= E_{\text{beam}} - p\ cos\theta_h - p_{e'}\ \cos\theta_{e'}, \end{aligned}$$

  where θ and ϕ are the polar and azimuthal angles of the hadron track, respectively, and $\theta_{e'}$ and $\phi_{e'}$ the corresponding ones of the scattered electron.

As the remnant of the proton target (usually a proton or a neutron resulting from reconversion of the quark lines) is never detected, a missing mass spectrum peaking at around 1 GeV (the nucleon mass), with a small tail towards higher mass values (i.e., little energy is available to produce other particles), would be an indication for an exclusive channel. The spectrum for M_X was calculated for the events in the large-z sample in every bin of p_T and x_F, from which it was concluded that these should not be dominated by exclusive production channels. Nevertheless, some of the high-p_T bins showed a small but significant peak around $M_X = 1$ GeV. Some examples of the resulting spectra can be seen in Fig. E.33. Notice, for instance, the peak around 1.8 GeV in the π^- spectrum (bottom left panel) indicating the production of Δ^{++}.

6.2.4 Contribution from low-Q^2

The contribution to the measured $A_{UT}^{\sin\phi}$ amplitude from *tagged* events with $Q^2 < 1$ GeV^2 was also considered. These data could be naively expected to have a similar behavior as the photoproduction data, which would offer a good opportunity to check their kinematic dependence given that, in this case, both scales (Q^2 and p_T) can be reconstructed. However, the resulting asymmetries contrast substantially with those from the anti-tagged sample.

This can be seen in Fig. 6.5, plotted with triangular symbols. A small but constant asymmetry of about 2% was found for the π^+ data, with only a light dependence on p_T. For K^+, the asymmetry was found to increase with p_T, being smaller than the inclusive (photoproduction) asymmetries at low-p_T, and larger than these after $p_T > 1$ GeV. The asymmetries for negative pions observed from these data are compatible with the ones from inclusive (photoproduction) data. The values for the fraction, $\langle p_T^2/Q^2 \rangle$ and $\langle Q^2 \rangle$ in each bin of p_T are correspondingly plotted in Figs. 6.6, 6.8, and 6.9.

In any case, one should be cautious with the interpretation of the results from this subsample. The tagged hadronic events with $Q^2 < 1$ GeV^2 correspond to electrons scattered at very low angles, just reaching the spectrometer geometry above and under the beam pipe, and one could expect that these events are strongly influenced by acceptance effects. This could be investigated in the same way as described for the events in the SIDIS subsample. Since these events represent a narrow *kinematic corner*, no additional studies were performed.

6.3 Conclusions

Transverse SSAs were measured for the first time in data from inclusive electroproduction of charged pions and kaons, resulting from $e\,p^{\uparrow}$ collisions with a 27.6 GeV unpolarized electron beam and a transversely polarized proton target. Positive asymmetries, reaching a value of 6% were observed for positive pions, and of 8% for positive kaons, exhibiting a clear dependence on the transverse momentum p_T of the hadrons. The asymmetries were found to become larger with p_T up to a maximum value around $p_T \in [0.7, 0.9]$ GeV, and then decrease to nearly zero for $p_T \sim 1.3$ GeV. After this value of p_T, the π^+ asymmetries were seen to increase again up to their maximum value, while for K^+ they were consistent with zero. In the case of negatively charged pions and kaons, the measured asymmetries were very small or consistent with zero within the statistical and systematic uncertainties over the entire range of the transverse momentum investigated. While there is no significant x_F-dependence for positive hadrons, the amplitudes for π^- change sign from small positive values at low x_F to negative values at high x_F, for $p_T < 1$ GeV. For K^-, the amplitudes are positive at low x_F, but appear to be consistent with zero at high x_F.

These data were manifestly dominated by events from quasi-real photoproduction, with very small, nearly zero, four-momentum transfer Q^2. The fraction of the inclusive yields corresponding to this regime was found to be larger than 95% for the range of transverse momentum 0 GeV $< p_T <$ 1 GeV, and to decrease to less than 90% for positively charged hadrons and about 95% for negatively charged hadrons in the range 1 GeV $< p_T <$ 2.2 GeV. Correspondingly, similar asymmetries (nearly identical) to the measured $A_{UT}^{\sin\phi}$ amplitudes were observed from hadrons in the photoproduction regime, for all values of the transverse momentum, being only slightly smaller (larger) than the inclusive asymmetries for positive (negative) hadrons at the highest p_T. In the case of π^+ data, a tendency of the asymmetries from photoproduction events to decrease to zero was seen at high p_T, in contrast to the results from the total inclusive sample.

The fraction of hadrons produced in DIS reactions represented only about 3% (2%) for positive (negative) charged hadrons for the bins of $p_T > 1.3$ GeV, while it was smaller than 2% for lower values of p_T, decreasing with it to nearly zero. Larger asymmetries were measured for this data set than for the total inclusive sample. The most remarkable case is the π^+, for which asymmetries as large as 20% were seen, continuously increasing with p_T. This fraction of the data constitutes the same hadron sample of semi-inclusive data used in Ref. [91] to measure the $A_{UT}^{\sin(\phi_h-\phi_S)}$ azimuthal moments associated with the Sivers parton distribution function, and in Ref. [95] to measure the $A_{UT}^{\sin(\phi_h+\phi_S)}$ moments related to the Collins fragmentation function. The measured $A_{UT}^{\sin\phi}$ amplitudes from hadrons produced in DIS events strongly resemble the semi-inclusive asymmetries of Ref. [91] associated with the Sivers effect, as it can be expected from elementary arguments, given the equivalence of the azimuthal modulations $\phi \simeq \phi_h - \phi_S$ in both cases.

Most striking were the contribution to the asymmetry from DIS events with large $z > 0.7$, with z being the fraction of the energy transferred to the proton carried by the outgoing hadron. Large positive asymmetries, up to 40%, were measured in this case for positive hadrons, with a smooth dependence on the transverse momentum, while negative

asymmetries with a largest value of 20% were found for π^-, increasing with p_T. Since a large value of z increases the correlation with the struck quark, these results can be interpreted as resulting from the Sivers effect, which is known to be strengthened with increasing z in semi-inclusive analyses [91]. A contribution to the measured asymmetries from vector-meson production or direct single -pion or single-kaon production in exclusive channels could not be excluded for these data. More studies should be done in this case.

Comparison to theory predictions In the kinematic region where predictions exist, i.e., $p_T > 1$ GeV, they agree relatively well with the results obtained in this analysis for positive pions, while the large negative amplitudes expected in Ref. [89] for negative pions, based on the contribution from the Sivers function, could not be confirmed. Such large asymmetries for π^- were found, though, for events at large z. The region below $p_T < 1$ GeV for photoproduction events lacks any theoretical framework at the moment, although a possible mechanism generating the asymmetry could be related to higher-twist effects, which are p_T suppressed and therefore could play a role at low p_T. No theoretical calculations for kaons exist. Both the higher-twist collinear approach and TMD approach, discussed in Chapter 2, predict that the asymmetries vanish for a sufficiently high value of the hadron transverse momentum. This is consistent with the dependence of the $A_{UT}^{\sin\phi}$ amplitudes for positive pions on p_T, for the range 0 GeV $< p_T <$ 1.5 GeV, and also with the amplitudes extracted for K^+ data over the entire kinematic range. However, in the latter case more data would be necessary to provide stronger evidence, most noticeably for $p_T > 2$ GeV. In contrast to this, a clear trend of the π^+ amplitudes to rise with $p_T > 1.5$ GeV is observed.

Comparison to hadronic data The $A_{UT}^{\sin\phi}$ amplitudes measured for charged pions for the photoproduction events have a similar kinematic evolution with x_F as the asymmetry A_N measured in the inclusive production of pions in hadron collisions. However, much smaller values of the asymmetries are obtained from ep data, and with larger values for π^+ than for π^- in this case, in contrast to the symmetrical evolution of A_N for these hadrons. The apparent independence from x_F, seen in the two-dimensional extraction of the $A_{UT}^{\sin\phi}$ amplitudes does not agree with the behavior observed in inclusive charged pion production by the BRAHMS experiment [68], where an increase with x_F was seen even after binning the data in slices of p_T.

The results presented in this thesis provide relevant information for a better understanding of the role of transverse-momentum dependent parton distribution and fragmentation functions and of higher-twist quark-quark and quark-gluon correlations in the generation of single-spin asymmetries. In particular, these data can be used to test the validity of the TMD factorization theorem, largely accepted for processes with two large scales (p_T and Q^2), but still under debate for processes with only one large scale (p_T), like the one studied here. Moreover, the measured $A_{UT}^{\sin\phi}$ amplitudes are closely related to the single-spin asymmetry A_N observed in transversely polarized hadron-hadron collisions which, since more than 40 years, represents a challenge to theoretical physics, and specifically to calculations based on perturbative QCD. The presented data could serve to study the transition region between the non-perturbative regime at low p_T, for which no precise calculations presently exist, and the perturbative domain.

7

Two-photon exchange in DIS

In this chapter, the measurement of transverse single-spin asymmetries (SSAs) in inclusive DIS ($e^{\pm}\,p^{up} \rightarrow e^{\pm}\,X$) is discussed and results are presented. Such an asymmetry can be unequivocally related to the exchange of two or more photons in the ep interaction. Experimentally, this measurement is very similar to the one described in Chapter 4, but comprising the analysis of the scattered beam lepton instead of hadron tracks in the final state. A brief motivation for two-photon physics is done in Section 7.1, while in Section 7.2 two experimental methods to determine two-photon exchange contributions are described together with an overview on existing measurements. The formalism for DIS including two-photon exchange effects is presented in Section 7.3. The actual measurement of transverse SSAs from HERMES data is reported in Section 7.4, and results are discussed in Section 7.5. These results were published in *Phys. Lett.* **B682** *(2010) 351* – see Ref. [158], and constitute the first precise measurement of SSAs from inclusive DIS data of $e\,p^{\uparrow}$ collisions[1].

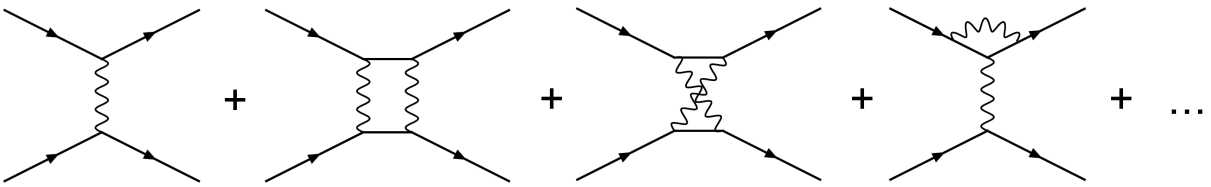

Figure 7.1. Feynman diagrams contributing to the electromagnetic interaction of two charged particles.

[1] In the time between the publication of Ref. [158] and the writing of this dissertation, preliminary results from the search of two-photon exchange in inclusive DIS from $e\,^3\mathrm{He}^{\uparrow} \rightarrow eX$ reactions at Hall A (Jefferson Lab) were also reported [190].

7.1 Motivation

The formalism for DIS, described in Chapter 2, is only valid under the assumption that no more than *one* photon is exchanged in the *ep* collision. This is normally referred to as the *Born approximation*, and it is equivalent of taking the first term in the diagrammatical expansion of the cross section depicted in Fig. 7.1. In most cases, such approximation suffices to understand the observed scattering phenomena. Corrections to the cross section from higher-order terms have been considered in the past [159], and were found to be not bigger than 2%. However, such estimates were based on contributions to inelastic scattering from the resonance region and are expected to be valid only for $Q^2 < 1$ GeV^2 [160].

On the other hand, the increasing precision of experiments over the last decades has provided sensibility to effects present at higher orders, with a consequent growth of the interest on studying higher-order contributions to the *ep* cross section, in particular in the case of two-photon exchange, depicted in the second diagram of the above figure. Note that with these corrections it is *not* meant the effect of *soft* (real or virtual) photons, i.e., radiative corrections, but the actual exchange of two or more *hard* photons between the lepton and the nucleon.

Mesurement of form factors Probably the best example where corrections beyond the Born level have received more attention is in the measurement of the proton electric (G_E) and magnetic (G_M) form factors[2]. Two-photon exchange has been proposed as a candidate to explain the differences in the determination of the ratio G_E/G_M by two independent methods:

- The **Rosenbluth method** [162], that relies on the linearity of the *reduced* unpolarized cross section σ_R with respect to polarization ϵ of the virtual photon [163]

$$\sigma_R \equiv \frac{\mathrm{d}\sigma}{\mathrm{d}\Omega}\frac{\epsilon\,(1+\tau)}{\sigma_{\text{Mott}}} = \tau\, G_M^2(Q^2) + \epsilon\, Q_E^2(Q^2), \tag{7.1}$$

$$\text{with} \qquad \epsilon = \frac{1}{1+2\,(1+\tau)\,\tan^2(\theta_e/2)} = \frac{\nu^2 - M^4\,\tau\,(1+\tau)}{\nu^2 + M^4\,\tau\,(1+\tau)}.$$

  Here, $\tau = -q^2/4M^2$, and σ_{Mott} is the Mott cross section, describing the elastic scattering from a point charge – see Eq. (A.24). At fixed Q^2 (fixed τ), the form factors are constant and σ_R depends only on ϵ. The Rosenbluth technique consists of measuring σ_R at different beam energies, keeping Q^2 fixed (i.e., measuring at different scattering angles) while varying ϵ. The electric form factor G_E^2 can be then extracted from the slope of σ_R, and the magnetic form factor G_M^2 from the constant term.

- The **polarization-transfer method** [164] utilizes polarization degrees of freedom to increase the sensitivity of the electric form factor at large Q^2 . In this case, longitudinally polarized electrons are scattered off unpolarized protons, such that a certain polarization is transferred to the recoiling proton $\vec{e} + p \to e + \vec{p}$. The ratio G_E/G_M of form factors

[2] See Appendix A for a definition, in particular Eq. (A.23).

can be directly related to the longitudinal (P_l) and transverse (P_t) components of the polarization of the recoiling proton [163]

$$\frac{G_E}{G_M} = -\frac{P_t}{P_l}\,\frac{(E_e + E'_e)\,\tan(\theta_e/2)}{2M}. \tag{7.2}$$

The outcome of extracting the ratio G_E/G_M from both methods is plotted in Fig. 7.2. Results from the Rosenbluth method are plotted with triangles, showing that the ratio is compatible with 1, and practically constant with Q^2. On the other hand, results from the polarization-transfer method are plotted with circles, indicating a clear linear evolution with the momentum-transfer. These results were calculated in Ref. [163], using data from Ref. [165], assuming one-photon exchange in both cases. The square symbols denote the G_E/G_M ratio extracted from Ref. [167] data with the Rosenbluth method corrected by two-photon exchange, as done in Ref. [166]. As it can be observed for the range $Q^2 \in [2, 3]$ GeV^2, the agreement between the results from both methods is better if two-photon exchange corrections are taken into account. The two-photon exchange corrections are rather significant for the Rosenbluth method (up to a few percents), while for the polarization-transfer method, they represent only a small correction – this can be understood from the corresponding version of Eqs. (7.1) and (7.2) including the two-photon exchange term [160, 166].

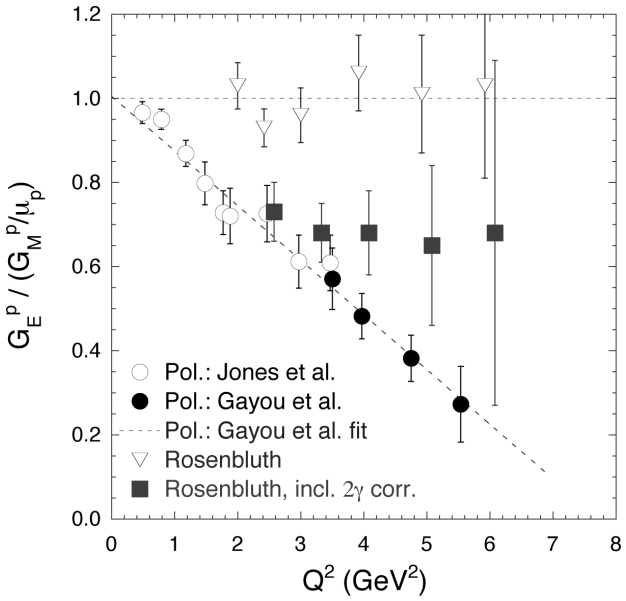

Figure 7.2. Ratio of electric and magnetic form factors of the proton, measured with the Rosenbluth method and the polarization-transfer method (Pol.). Figure taken from Ref. [166].

Further evidence The impact of the two-photon exchange correction to the measurement of form factors has motivated a deeper revision of other electron scattering measurements that require high precision. This is for instance the case of parity violation in elastic scattering of longitudinally polarized electrons off unpolarized protons, where corrections of several

percent to the parity-violating asymmetry were found [168]. A recent and complete review on the role of two-photon exchange in electron scattering can be found in Ref. [169].

7.2 Experimental access

In order to investigate contributions from two-photon exchange, it is necessary to find experimental observables that allow their isolation. Direct experimental evidence from two-photon exchange effects can be obtained, in particular, from two types of observables. One consists of differences in the cross section for different charges of beam particles (i.e., beam-charge asymmetries), and the other is related to the measurement of transverse single-spin asymmetries. All non-zero evidence to date of two-photon exchange effects in lepton-nucleon scattering comes from elastic scattering, while no hint of these effects was found for inelastic collisions.

- **Beam-charge asymmetries**. The ratio of **elastic** cross sections for positron e^+p and electron e^-p scattering is defined as [169]

$$R \equiv \frac{\sigma^{e^+p}}{\sigma^{e^-p}} \simeq \frac{|\mathcal{M}_\gamma^{e^+}|^2 + 2\,\mathcal{R}\mathrm{e}\left(\mathcal{M}_\gamma^{e^+ *}\mathcal{M}_{\gamma\gamma}^{e^+}\right)}{|\mathcal{M}_\gamma^{e^-}|^2 + 2\,\mathcal{R}\mathrm{e}\left(\mathcal{M}_\gamma^{e^- *}\mathcal{M}_{\gamma\gamma}^{e^-}\right)}, \tag{7.3}$$

  where $\sigma^{e^\pm p} \equiv d\sigma^{e^\pm p}/d\Omega$. Here, $\mathcal{R}\mathrm{e}$ stands for the real part of the cross section, and the $\mathcal{M}_\gamma$ and $\mathcal{M}_{\gamma\gamma}$ are the scattering amplitude for one- and two-photon exchange processes, respectively. The electron amplitude $\mathcal{M}_\gamma^{e^-}$ changes sign under the interchange $e^- \to e^+$, while $\mathcal{M}_{\gamma\gamma}^{e^-}$ does not [169]. The interference of both amplitudes ($\mathcal{M}_\gamma^* \mathcal{M}_{\gamma\gamma}$) has then opposite sign for the electron and positron scattering. This way, deviations of R from unity can be used as an indicator for two-photon exchange effects.

  Based on existing $e^\pm p$ data from early measurements at SLAC [170], Cornell [171], DESY [172], and Orsay [173] (see Ref. [174] for a compilation of measurements of $R^{e^+e^-}$), a deviation of the cross-section ratio of about 5% from unity was found [175]. These data were mainly for low Q^2, where two-photon exchange corrections to the cross section are known to be smaller than 1%. In recent years, other experiments have begun to collect data from $e^\pm p$ elastic collisions, with the goal of improving the precision of the measurement and extending the range in Q^2, like the VEPP-3 ring in Novosibirsk [176], the E07-005 experiment [177] at Jefferson Lab, and the OLYMPUS experiment [178] at DESY.

  Extractions of the cross section ratio R from **inelastic** scattering for both e^+/e^- and μ^+/μ^- beams have not supplied any signature of two-photon exchange effects so far [179] within their accuracy of a few percent.

- **Transverse SSAs**. Two-photon exchange effects also manifest as a single-spin asymmetry A_N in electron-nucleon scattering, when either the target or the beam spin are polarized normal to the scattering plane [180]. The combination of time-reversal invariance, parity conservation, and the hermiticity of the electromagnetic current operator forbids such asymmetry in the one-photon exchange approximation, as stated

in the Christ-Lee theorem [181], but a non-vanishing asymmetry can be obtained if two or more photons are exchanged, which makes this observable a clear indicator. The target spin asymmetry is defined as

$$A_N = \frac{\sigma^{\uparrow} - \sigma^{\downarrow}}{\sigma^{\uparrow} - \sigma^{\downarrow}}, \tag{7.4}$$

which, at order α in the electromagnetic coupling, can be written as

$$A_N = \frac{2\,\mathcal{I}m\left(\mathcal{M}_{\gamma}^{*}\,\mathcal{M}_{\gamma\gamma}\right)}{|\mathcal{M}_{\gamma}|^2}. \tag{7.5}$$

A measurement of A_N provides therefore direct access to the imaginary part of the interference between the one- and two-photon exchange amplitudes $\mathcal{I}m\left(\mathcal{M}_{\gamma}^{*}\,\mathcal{M}_{\gamma\gamma}\right)$. The size of such asymmetry can be expected to be of order α 1/137 $\mathcal{O}(10^{-2})$. In the case of a transverse beam asymmetry, the polarization of a relativistic particle in the direction normal to its momentum involves a suppression of m/E, with m and E the mass and energy of the particle. Therefore a beam normal asymmetry for $e^{\uparrow}\,p$ scattering in the range of 1 GeV must be of order 10^{-5}–10^{-6}.

On the experimental side, non-zero beam normal asymmetries of the order 10^{-5}–10^{-6} were measured in **elastic** scattering of transversely polarized electrons off unpolarized protons [182–184]. In **inelastic** scattering, however, no indication of two-photon exchange has been found to date. Transverse SSAs were measured at the Cambridge Electron Accelerator [185] and at SLAC [186], being compatible with zero within the precision of few percent of the experimental uncertainties.

Note that the leading contribution to the two-photon exchange effects is in all cases the interference between the one-photon and two-photon processes. Even if the effect is a sole consequence of the two-photon term, the interference with the one-photon term, that contributes with one factor of the coupling constant α, amplifies the effect. This is in contrast to the term $\mathcal{M}_{\gamma\gamma}^{*}\mathcal{M}_{\gamma\gamma}$, which is suppressed by α^2.

7.3 Formalism for DIS

The formalism for a transverse target SSA in DIS is presented in Ref. [187]. The derivation is equivalent to the Born cross section, derived in Section 2.1.2. However, the introduction of the extra photon in the interference term leads to a third index ρ, such that the cross section is proportional to

$$\sigma_{2\gamma} \propto L_{\mu\nu\rho} W^{\mu\nu\rho} \tag{7.6}$$

with the leptonic and hadronic tensors defined as [187]

$$L^{\mu\nu\rho} = \frac{1}{2}\,\mathrm{Tr}\Big((\not{k} + m)\gamma_5 \not{S}\,\gamma^{\mu}(\not{k}' + m)\gamma^{\nu}(\not{\ell} + m)\gamma^{\rho}\Big), \tag{7.7}$$

$$4\pi W^{\mu\nu\rho} = \sum_q e_q^3\,\frac{M\,x}{Q^2}\,\frac{1}{(p + k - \ell)^2 + i\epsilon}\,g_T^q(x) \times \mathrm{Tr}\Big(\gamma_5 \not{S}\,\gamma^{\mu}(\not{p} + \not{k} - \not{k}')\,\gamma^{\nu}(\not{p} + \not{k} - \not{\ell})\gamma^{\rho}\Big). \tag{7.8}$$

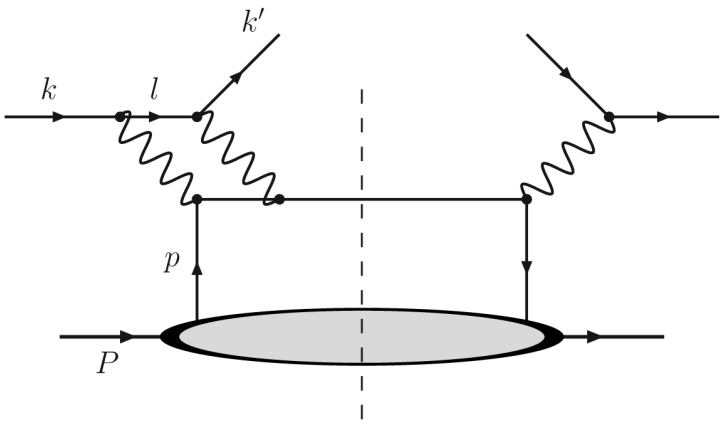

Figure 7.3. Contribution from two-photon exchange to DIS.

Here, k and k' are the momenta of the lepton before and after the interaction with the nucleon, p is the momentum of the quark in the nucleon p, and ℓ is the momentum of the lepton in the "intermediate" state between the emission of the two virtual photons, as indicated in Fig. 7.3. The Feynman *slash* notation stands for $\not{A} \equiv \gamma^\mu A_\mu$, where A_μ is a four-momentum. Furthermore, M and m are the masses of the proton and beam lepton, respectively, and g_T is the twist-3 quark distribution, defined through [187]

$$S^i g_T(x) = \frac{P^+}{M} \int \frac{d\xi^-}{4\pi} e^{ip\cdot\xi} \langle P, S|\bar{\psi}(0)\gamma^i\gamma_5\psi(\xi)|P, S\rangle\Big|_{\xi^+=\xi_T=0}, \tag{7.9}$$

with i denoting any transverse index.

For an unpolarized beam (U) and a transversely (T) polarized nucleon target, the spin-dependent part of the cross section is given by

$$\sigma_{UT} \propto e\,\alpha\,\frac{M}{Q}\,\epsilon_{\mu\nu\rho\sigma}\,S^\mu p^\nu k^\rho k'^\sigma\,C_T. \tag{7.10}$$

Here, e is the charge of the incident lepton, M is the nucleon mass, $-Q^2$ is the squared four-momentum transfer, p, k and k' are the four-momenta of the target, the incident and the scattered lepton, respectively, while $\epsilon_{\mu\nu\rho\sigma}$ is the Levi-Civita tensor. The term $\epsilon_{\mu\nu\rho\sigma}S^\mu p^\nu k^\rho k'^\sigma$ is proportional to $\mathbf{S}\cdot(\mathbf{k}\times\mathbf{k}')$, consequently the largest asymmetry is obtained when the spin vector $\mathbf{S}$ is perpendicular to the lepton scattering plane defined by the three-momenta $\mathbf{k}$ and $\mathbf{k}'$. Other kinematic dependences are included in the term C_T.

Note that the presence of the twist-3 quark correlation function g_T in the polarized cross section implies that target SSA is a twist-3 effect. In this formalism, only quark-quark correlations are considered, and a zero quark mass is assumed. If one would keep a quark mass, then a term proportional to the transversity distribution h_1 would also appear. Moreover, if one considers p_T-dependent terms in the quark-quark correlator, also the unintegrated g_{1T} parton density appears in the hadronic tensor [187]. The inclusion of quark-gluon-quark correlations can also be related to a combination of g_T and g_{1T} [187].

Predictions for SSAs The polarized cross section σ_{UT} is proportional to the electromagnetic coupling constant α, and therefore it is expected to be small. Due to the factor M/Q in Eq. (7.10), σ_{UT} is expected to become larger with decreasing Q^2. A calculation based on certain model assumptions [188] for a Jefferson Lab experiment [189] yields expectations for the asymmetry of order 10^{-4} at the kinematics of that experiment. The authors in Ref. [187], on the other hand, do not exclude asymmetries as large as 10^{-2} and point out that the term C_T in Eq. (7.10) cannot be completely evaluated at present. Given the dependence of σ_{UT} on the charge of the beam lepton e, the asymmetry is expected to have a different sign for opposite beam charges.

7.4 Measurement

The analyzed data were collected with the HERMES spectrometer (see Chapter 3) during the period 2002-2005. The data quality requirements for this analysis are described in Section 4.1 [3]. In this analysis, only tracks corresponding to the scattered leptons from reactions $e\,p^{\uparrow} \rightarrow e'\,X$ were selected. This was done by a combination of kinematical constraints on the lepton tracks, as discussed in Appendix C, and other requirements described in Section 4.2. In particular,

- Leptons were distinguished from hadrons by the PID detectors mentioned in Section 3.3.2, and with the algorithm discussed in Section 4.2.1. In this case, a PID value bigger than 2 was required to lepton tracks in order to exclude any contamination from a transverse hadron SSA in the lepton signal. This way, the contamination of hadrons in the lepton sample was smaller than 2×10^{-4}, with a lepton identification efficiency greater than 94%.
- Events were selected in the kinematic region $0.007 < x < 0.9$, $0.1 < y < 0.85$, $0.25\ \text{GeV}^2 < Q^2 < 20\ \text{GeV}^2$, and $W^2 > 4\ \text{GeV}^2$. See Section 2.1.1 for the definition of these variables.
- The minimum threshold for the energy deposition in the electromagnetic calorimeter was 1.4 GeV.
- All other requirements of Section 4.2 (not related to hadron tracks) apply.

The data productions used in this case were the 02c2, 04c2, 05c2 (see Section 3.5) [4]. No data from 2003 was included, which represented anyway just a small fraction of DIS events. The total collected statistics for each production is summarized in the right column of Table 7.1.

[3] Being identical to those for the analysis of inclusive hadron tracks.

[4] The main difference with respect to the *d1* productions mentioned in Chapter 4 is the use of a different tracking method (HRC instead of HTC).

Extraction of azimuthal moments The differential yield for a given target spin direction (↑ upwards or ↓ downwards) can be expressed as

$$\begin{aligned}\frac{\mathrm{d}^3N^{\uparrow(\downarrow)}}{\mathrm{d}x\ \mathrm{d}Q^2\ \mathrm{d}\phi_S} &= \\ &\left[L^{\uparrow(\downarrow)}\ \mathrm{d}^3\sigma_{UU} + (-)L_P^{\uparrow(\downarrow)}\ \mathrm{d}^3\sigma_{UT}\right]\ \Omega(x,Q^2,\phi_S) \\ &= \mathrm{d}^3\sigma_{UU}\left[L^{\uparrow(\downarrow)} + (-)\right. \\ &\left. L_P^{\uparrow(\downarrow)}\ A_{UT}^{\sin\phi_S}(x,Q^2)\sin\phi_S\right]\ \Omega(x,Q^2,\phi_S). \end{aligned} \tag{7.11}$$

Here, σ_{UU} is the unpolarized cross section, $L^{\uparrow(\downarrow)}$ is the total luminosity in the ↑ (↓) polarization state, $L_P^{\uparrow(\downarrow)} = \int L^{\uparrow(\downarrow)}(t)\ P(t)\ \mathrm{d}t$ is the integrated luminosity weighted by the magnitude P of the target polarization, and Ω is the detector acceptance efficiency. The angle ϕ_S is defined in this case as the azimuthal angle about the beam direction, between the upwards target spin direction and the lepton scattering plane, i.e., **opposite**[5] to the definition depicted in Fig. 2.1. The $\sin\phi_S$ azimuthal dependence follows directly from the form $\mathbf{S}\cdot(\mathbf{k}\times\mathbf{k}')$ of the spin-dependent part of the cross section; $A_{UT}^{\sin\phi_S}$ refers to its amplitude.

The asymmetry was calculated as

$$A_{UT}(x,Q^2,\phi_S) = \frac{\dfrac{N^{\uparrow}}{L_P^{\uparrow}} - \dfrac{N^{\downarrow}}{L_P^{\downarrow}}}{\dfrac{N^{\uparrow}}{L^{\uparrow}} + \dfrac{N^{\downarrow}}{L^{\downarrow}}}\ , \tag{7.12}$$

where $N^{\uparrow(\downarrow)}$ are the number of events measured in bins of x, Q^2, and ϕ_S. With the use of Eq. (7.11), it can be approximated[6], for small differences of the two average target polarizations $\langle P^{\uparrow(\downarrow)}\rangle = L_P^{\uparrow(\downarrow)}/L^{\uparrow(\downarrow)}$, as

$$A_{UT}(x,Q^2,\phi_S) \simeq A_{UT}^{\sin\phi_S}\sin\phi_S + \frac{1}{2}\frac{\langle P^{\downarrow}\rangle - \langle P^{\uparrow}\rangle}{\langle P^{\uparrow}\rangle\langle P^{\downarrow}\rangle}. \tag{7.13}$$

As shown in Table 7.1, $\langle P^{\uparrow}\rangle$ and $\langle P^{\downarrow}\rangle$ are the same to a good approximation for all data-taking periods.

year	beam	$\langle P^{\uparrow}\rangle$	$\langle P^{\downarrow}\rangle$	Events
2002	e^+	0.783±0.041	0.783±0.041	0.9 M
2004	e^+	0.745±0.054	0.742±0.054	2.0 M
2005	e^-	0.705±0.065	0.705±0.065	4.8 M

Table 7.1. Average target polarizations and total number of inclusive events for the three data sets used in this analysis.

[5] This "alternative" definition of ϕ_S led to an **error** in Ref. [158], where the angle is defined in the standard way, in contrast to the definition in analysis code.

[6] See derivation in Appendix B.

The advantage of using the fully-differential asymmetry $A_{UT}(x, Q^2, \phi_S)$ in Eq. (7.12) is that the acceptance function Ω cancels in each (x, Q^2, ϕ_S) kinematic bin, provided that the bin size is small. Assuming the ϕ_S dependence of σ_{UT} in Eq. (7.10) and Eq. (7.11), it can be easily shown[7] that the $\sin\phi_S$ amplitude $A_{UT}^{\sin\phi_S}$ and a left-right normal asymmetry A_N are related by

$$A_N = \frac{\sigma_L - \sigma_R}{\sigma_L + \sigma_R} = \frac{\int_0^\pi d\phi_S \; \mathrm{d}^3\sigma_{UU} \; A_{UT}^{\sin\phi_S} \; \sin\phi_S}{\int_0^\pi d\phi_S \; \mathrm{d}^3\sigma_{UU}} = \frac{2}{\pi} \; A_{UT}^{\sin\phi_S}, \tag{7.14}$$

where σ_L (σ_R) refers to the integrated cross section within the angular range $0 \leq \phi_S < \pi$ ($\pi \leq \phi_S < 2\pi$).

Kinematic binning The chosen bins for x and ϕ_S are summarized in Table 7.2. The Q^2 range was divided into a "DIS region" with $Q^2 > 1$ GeV^2 and a "low-Q^2 region" with $Q^2 < 1$ GeV^2 in order to test for a possible enhancement of the transverse-target SSA due to the factor M/Q appearing in Eq. (7.10) at low Q^2. The lowest reachable Q^2 at HERMES, for a minimum value of $x = 0.0073$, corresponds to 0.25 GeV^2 – see Appendix C for more information. These low-Q^2 data should be interpreted carefully, though, since strictly speaking, Eq. (7.10) may not be applicable to this range.

Variable	Bins	Bin borders
Q^2	1	[0.25, 20] GeV^2
x	5	[0.0073, 0.012, 0.017, 0.021, 0.030, 0.054]
Q^2	1	[1, 20] GeV^2
x	17	[0.0073, 0.012, 0.017, 0.021, 0.030, 0.036, 0.044, 0.054, 0.066, 0.08, 0.098, 0.12, 0.15, 0.19, 0.24, 0.35, 0.54, 0.9000]
ϕ_S	20	[0.0, 0.27, 0.54, 0.81, 1.08, 1.35, 2.02, 2.29, 2.56, 2.83, 3.10, 3.37, 3.64, 3.91, 4.18, 4.45, 5.17, 5.44, 5.71, 5.98, 6.29] rad

Table 7.2. Kinematic bins used in this analysis.

Fitting The $A_{UT}^{\sin\phi_S}$ amplitudes were extracted with a **binned** χ^2 fit of the functional form $p_1 \sin\phi_S + p_2$ to the measured asymmetry. Leaving p_2 as a free parameter or fixing it to the values given by Eq. (7.13) and Table 7.1 had no impact on the extracted $\sin\phi_S$ amplitude $A_{UT}^{\sin\phi_S}$, corresponding to parameter p_1.

[7] See derivation in Appendix B.

7.5 Results

The final results for the measured $\sin\phi_S$ amplitudes $A_{UT}^{\sin\phi_S}$ are shown in Fig. 7.4 as a function of x separately for electrons (two panels of the left side) and positrons (two panels on the right side). The results in the narrow panels at the left of each plot indicate the asymmetries integrated over the range of x. The open (closed) circles identify the data with $Q^2 < 1$ GeV^2 ($Q^2 > 1$ GeV^2). The error bars show the statistical uncertainties, while the error boxes show the systematic uncertainties.

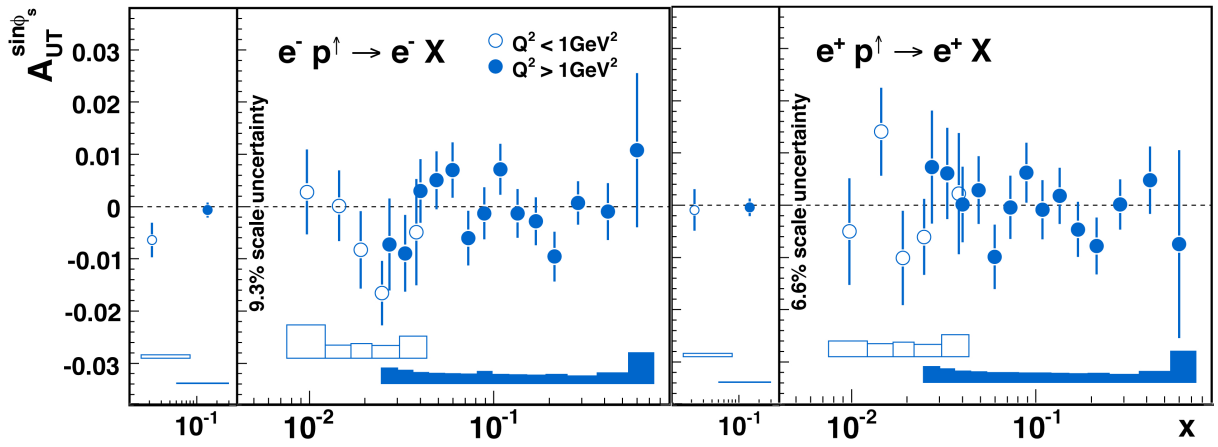

Figure 7.4. The x dependence of the $\sin\phi_S$ amplitudes $A_{UT}^{\sin\phi_S}$ measured with an electron beam (left) and a positron beam (right). The asymmetries integrated over x are shown on the left panel at the left of each case.

In both cases the asymmetries are consistent with zero within their uncertainties. Due to the kinematics of the experiment, the quantities x and $\langle Q^2 \rangle$ are strongly correlated, as shown in Fig. 7.5.

Fraction of elastic events The resulting amplitudes were not corrected for higher order QED effects or contamination by the radiative tail from elastic scattering. The latter correction requires knowledge of the presently unknown elastic two-photon asymmetry. From the definition of x and W^2 (see Section 2.1.1), it follows that for elastic reactions ($W = M$), x is equal to 1. For this reason, events with $x > 0.9$ are discarded from the data sample. The radiation of a photon by the lepton *before* the interaction with the proton, however, might provoke that elastic events (with x close to unity) end up being observed in the inelastic region. The contribution of the elastic radiative tail to the total event sample was estimated from a Monte Carlo simulation based on the LEPTO generator [191] together with the RADGEN [141] determination of QED radiative effects and with a GEANT [144] based simulation of the detector. The fraction of elastic events is shown in Fig. 7.4, denote with triangles. It reaches values as high as about 35% in the lowest x bin, where y is large ($\langle y \rangle \simeq 0.80$) and hence radiative corrections are largest [192]. The elastic fraction rapidly

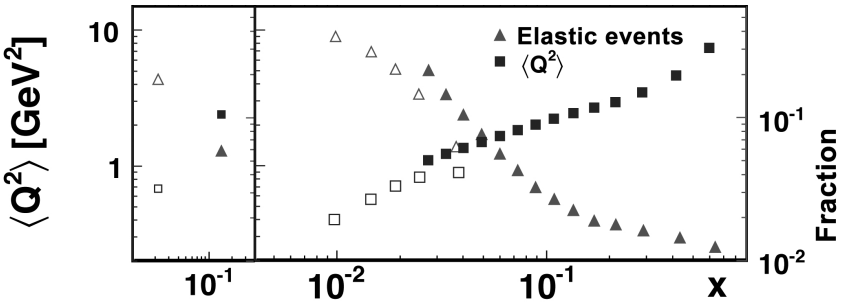

Figure 7.5. Average Q^2 vs. x from data (squares), and the fraction of elastic background events to the total event sample from a Monte Carlo simulation (triangles).

decreases towards high x, becoming less than 3% for $x > 0.1$.

Estimation of systematic uncertainties The systematic uncertainties, shown in the fourth column of Table 7.3 and as error boxes in Fig. 7.4, include contributions due to corrections for misalignment of the detector, beam position and slope at the interaction point and bending of the beam and the scattered lepton in the transverse holding field of the target magnet. They were determined from a high statistics Monte Carlo sample obtained from a simulation containing a full description of the detector, where an artificial spin-dependent azimuthal asymmetry was implemented [8]. Input asymmetries being zero or as small as 10^{-3} were well reproduced within the statistical uncertainty of the Monte Carlo sample, which was about five times smaller than the statistical uncertainty of the data. For each measured asymmetry point the systematic uncertainty was obtained as the maximum value of either *(i)* the statistical uncertainty of the Monte Carlo sample or *(ii)* the difference between the input asymmetry and the reconstructed one[9]. Systematic uncertainties from other sources like particle identification or trigger efficiencies were found to be negligible. The total estimated systematic uncertainty for the high (low) Q^2 data is about 50% (100%) for positrons and about 35% (50%) for electrons. Scale uncertainties from the target polarization (cf. Section 5.4.2) are not included in either case; these amount to 9.3% (6.6%) for the electron (positron) sample.

The transverse single-spin asymmetry amplitudes $A_{UT}^{\sin\phi_S}$ for electron and positron beams integrated over x are given separately for the "low-Q^2 region" and the "DIS region" in Table 7.3 along with their statistical and systematic uncertainties. All asymmetry amplitudes are consistent with zero within their uncertainties, which in the DIS region are of order 10^{-3}. The only exception is the low-Q^2 electron sample, where the asymmetry is 1.9 standard deviations different from zero. No hint of a sign change between electron and positron asymmetries is observed within uncertainties.

[8] Equivalently to the technique described in Chapter 5.
[9] See Section 5.3.

beam	$A_{UT}^{\sin\phi_S}$ $\times 10^{-3}$	$\delta A_{UT}^{\sin\phi_S}$(stat.) $\times 10^{-3}$	$\delta A_{UT}^{\sin\phi_S}$(syst.) $\times 10^{-3}$	$\langle x \rangle$	$\langle Q^2 \rangle$ [GeV^2]
e^+	-0.61	3.97	0.63	0.02	0.68
e^-	-6.55	3.40	0.63		
e^+	-0.60	1.70	0.29	0.14	2.40
e^-	-0.85	1.50	0.29		

Table 7.3. The integrated transverse single-spin asymmetry amplitude $A_{UT}^{\sin\phi_S}$ with its statistical and systematic uncertainties and the average values for x and Q^2 measured separately for electron and positron beams in the two Q^2 ranges $Q^2 < 1$ GeV^2 (upper rows) and $Q^2 > 1$ GeV^2 (lower rows).

7.6 Outlook

In this chapter, the first precise measurement of single-spin asymmetries in inclusive DIS (previously published in Ref. [158]) is reported, using data taken with the HERMES spectrometer with unpolarized electron and positron beams and a transversely polarized hydrogen target. This asymmetry is a direct indicator for two-photon exchange effects in the DIS collisions. No evidence for such effects was found within the experimental uncertainties, which are of order 10^{-3}.

Appendices

A
Scattering basics

Fermi Golden rule The cross section for the scattering of two point-like particles $ab \to X$ is given by

$$\sigma^{a+b\to X} = \sum_X \frac{1}{\mathcal{F}} \int \mathscr{P}\, |\mathcal{M}|^2, \tag{A.1}$$

- $\mathcal{M}$ is the *transition matrix element* related to the probability amplitude for the reaction. It can be calculated, separately for each particle, from the Feynman rules. Formally, it is defined as

$$\mathcal{M} = \langle \psi_f | \mathcal{V} | \psi_i \rangle = \int \psi_f^* \, \mathcal{V} \, \psi_i \mathrm{d}V, \tag{A.2}$$

  where $\mathcal{V}$ is the operator describing the interaction potential and the integral is over a finite volume V. The wave functions $\psi_{i,f}$ of the incoming and outgoing particles can be described, in Born approximation, by plane waves $\psi = e^{ipz}/\sqrt{V}$.

- $\mathcal{F}$ refers to the initial state particle flux, that depends on the initial particle energies and velocities $\mathcal{F} = 2\,E_a\,2\,E_b\,|\mathbf{v}_a - \mathbf{v}_b|$. In terms of the center of mass energy $s = (p_a + p_b)^2$, it can be expressed as a Lorentz invariant

$$\mathcal{F} = (s - m_a^2 - m_b^2)^2 - 4 m_a^2 m_b^2. \tag{A.3}$$

- $\mathscr{P}$ is the Lorentz invariant phase space. It accounts for the spherical interval $4\pi p^2 \mathrm{d}p$, in momentum space, that a particle occupies after scattering. For a final state with n_X particles and momenta $p_X = \sum_i k_i$, this is

$$\mathscr{P} = (2\pi)^4\, \delta^4(p_X - p_a - p_b) \prod_i^{n_X} \frac{\mathrm{d}^3\mathbf{k}_i}{(2\pi)^3 2k_i^0}, \tag{A.4}$$

  where the δ^4 arises from the condition of momentum conservation

$$\int e^{i\,x\,(p_f - p_i)} \mathrm{d}^4 x = (2\pi)^4 \delta^4(p_f - p_i). \tag{A.5}$$

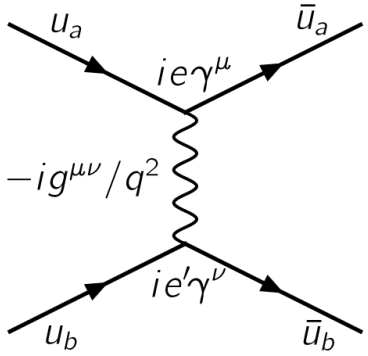

Figure A.1. Feynman diagram for the elastic scattering of two fermions.

Elastic scattering of point-like particles The electromagnetic interaction of two particles a and b with electric charges e and e', respectively, is described, at leading-order, by the Feynman diagram in Fig. A.1. The electromagnetic vertex joining the fermion lines defines the particle currents

$$j_a^\mu = ie\bar{u}_a\gamma^\mu u_a, \tag{A.6}$$
$$j_b^\nu = ie'\bar{u}_b\gamma^\nu u_b, \tag{A.7}$$

By means of the photon propagator $-ig^{\mu\nu}/q^2$, the matrix element can be written as

$$\mathcal{M} = \frac{iee'}{q^2}\,(\bar{u}_a\gamma_\mu u_a)\,(\bar{u}_b\gamma^\nu u_b) = \frac{iee'}{q^2}\,L_{\mu\nu} \tag{A.8}$$

where the *leptonic tensor* $L_{\mu\nu}$ is

$$L_{\mu\nu} = [\bar{u}(k',s')\ \gamma_\mu\ u(k,s)]^*[\bar{u}(k',s')\ \gamma_\nu\ u(k,s)], \tag{A.9}$$
$$= k_\mu k'_\nu + k'_\mu k_\nu - g_{\mu\nu}(k\cdot k' - m^2), \tag{A.10}$$
$$+m\ \epsilon_{\mu\nu\alpha\beta}\ s^\alpha\ q^\beta, \tag{A.11}$$

and only the last term (Eq. (A.11)) depends on the spin. If the spins of the particles are not taken into account, these must be averaged in the initial state and summed over the final state. The square of the matrix element involves then the contraction of two leptonic tensors

$$\frac{1}{4}\sum_{\text{spins}}|\mathcal{M}|^2 = \frac{e^2e'^2}{q^4}\,L_a^{\mu\nu}\,L^b_{\mu\nu} \tag{A.12}$$

which, after some non-trivial algebra using the Dirac trace techniques, and neglecting the particle masses, is given by

$$L_a\,L^b = 8[(k'\cdot p')\,(k\cdot p) + (k'\cdot p)\,(k\cdot p')],$$
$$= 2\,(s^2+u^2),$$
$$= s^2\,[1+(1-y)^2], \tag{A.13}$$

in terms of the Mandelstam variables $s = (k+p)^2 \simeq 2k\cdot p$, and $u = (k'-p)^2 \simeq -2k'\cdot p$, and using the relation $u/s = y-1$.

The expression for the cross section is given by Eq. A.1, after putting together the flux factor and phase space and performing the corresponding δ^4 integrations

$$\frac{\mathrm{d}\sigma}{\mathrm{d}Q^2} = \frac{e^2 e'^2}{8\pi Q^4}\,[1+(1-y)^2], \tag{A.14}$$

$$\text{or alternatively} \qquad \frac{\mathrm{d}\sigma}{\mathrm{d}y} = \frac{e^2 e'^2}{8\pi Q^4}\,[1+(1-y)^2]\,s, \tag{A.15}$$

We see that the scattering process is fully described by just *one* kinematic variable, i.e., Q^2 or y, related to the energy exchanged between both particles.

Electron-quark scattering The result above can be particularized for the elastic scattering of electrons and quarks inside a hadron, with the conversions

$$e' = e_q e, \qquad p \to xp, \tag{A.16}$$

since quarks carry a fractional charge and a fraction x of the hadron momentum. The same happens with the center of mass energy in the electron-hadron system, that now turns $s \to xs$. In addition, a distribution function $q(x)$ must be taken into account which gives the probability that the struck quark has a certain momentum fraction x. The assumption of *incoherent scattering* implies that one sums $\sum_i$ over all quarks with a specific value of x. From Eq. A.15 and the conversions above, it follows that

$$\frac{\mathrm{d}\sigma}{\mathrm{d}y} = \frac{e^2 e^2}{8\pi Q^4}\,[1+(1-y)^2]\,xs \sum_i e_i^2\, q_i(x), \tag{A.17}$$

and then, Eq. (A.14), with the conversion $\mathrm{d}/\mathrm{d}Q^2 = xs\ \mathrm{d}/\mathrm{d}y$, becomes

$$\frac{\mathrm{d}\sigma}{\mathrm{d}Q^2} = \frac{e^2 e^2}{8\pi Q^4}\,[1+(1-y)^2]\ \sum_i e_i^2\, q_i(x). \tag{A.18}$$

From Eqs. (A.14) and (A.18), the relationship for the DIS cross section in the naive parton model given in Eq. (2.11) becomes clear.

Notice that, for elastic scattering, one finds

$$p+q=p', \qquad x = \frac{Q^2}{2p\cdot q} = 1, \qquad Q^2 = sy, \tag{A.19}$$

and thus for inclusive DIS

$$p+q=p'+X, \qquad 0 < x = \frac{Q^2}{2p\cdot q} < 1, \qquad Q^2 = sxy. \tag{A.20}$$

Elastic electron-proton scattering The same formalism can be applied to the case of the elastic scattering of a charged particle off a composite object like the proton. In this case, the scattering amplitude is related to

$$|\mathcal{M}|^2 \sim \frac{\alpha^2}{q^4} L^{\mu\nu}\, K_{\mu\nu}, \tag{A.21}$$

where $K_{\mu\nu}$ is the *hadronic tensor*, describing the absorption of the virtual photon by the proton. This tensor cannot be derived from first principles, but it can be parametrized in terms of the so-called *elastic proton form factors* $K_{1,2}$ as

$$K^{\mu\nu} = K_1 \left(-g^{\mu\nu} + \frac{q^\mu q^\nu}{q^2}\right) + \frac{K^2}{M^2}\left(P^\mu + \frac{1}{2}\,q^\mu\right)\left(P^\nu + \frac{1}{2}\,q^\nu\right), \tag{A.22}$$

with M and P the mass and momentum of the proton, respectively. These form factors can be redefined in terms of the electric and magnetic form factors, related to the distribution of charge (G_E) and magnetic moment (G_M) of the proton. In terms of these form factors, the cross section for the elastic electron-proton scattering can be expressed as

$$\frac{\mathrm{d}\sigma}{\mathrm{d}\Omega} = \sigma_{\text{Mott}}\left(\frac{G_E^2 + \tau\, G_M^2}{1+\tau} + 2\tau\, G_M^2\, \tan^2(\theta/2)\right), \tag{A.23}$$

$$\text{with} \quad \sigma_{\text{Mott}} = \frac{4\alpha^2\, E^2\, \cos^2(\theta/2)}{q^4\,[1 + (2E/M)\, \sin^2(\theta/2)]}, \tag{A.24}$$

with $\mathrm{d}\Omega$ the differential of solid angle and θ the scattering angle, and $\tau = -q^2/4M^2$. This is known as the Rosenbluth formula, characterized by a typical $1/q^4$ dependence.

Inelastic electron-nucleon scattering The hadronic tensor for DIS can be expressed in terms of *four* scalar functions W_1, W_2, G_1 and G_2

$$W_{\mu\nu} = W^{\mathrm{S}}_{\mu\nu}(q;P) + iW^{\mathrm{A}}_{\mu\nu}(q;P,S), \tag{A.25}$$

with

$$\begin{aligned} W^{\mathrm{S}}_{\mu\nu} &= \left(-g_{\mu\nu} + \frac{q_\mu\, q_\nu}{q^2}\right) W_1 \\ &\quad + \frac{1}{M^2}\left(p_\mu - \frac{P\cdot q}{q^2}\, q_\mu\right)\left(p_\nu - \frac{P\cdot q}{q^2}\, q_\nu\right) W_2, \\ W^{\mathrm{A}}_{\mu\nu} &= M\epsilon_{\mu\nu\alpha\beta}\, q^\alpha\, S^\beta\, G_1 \\ &\quad + \frac{1}{M}\epsilon_{\mu\nu\alpha\beta}\, q^\alpha\, \left[(P\cdot q)\, S^\beta - (S\cdot q)\, P^\beta\right] G_2. \end{aligned}$$

Formally, another three terms associated to the unpolarized functions W_3, W_4 and W_5 are necessary to describe the structure of $W_{\mu\nu}$. Nevertheless, W_4 and W_5 are associated to current conservation of the hadron vertex ($q_\mu W^{\mu\nu} = q_\nu W^{\mu\nu}$) and can be expressed in terms of W_1 and W_2. The term related to W_3 violates parity and is therefore absent in ep scattering, since electromagnetic interactions conserve parity. In neutrino DIS, however, a contribution from W_3 cannot be excluded.

Helicity distribution The cross section for double-polarized DIS, following the parton model formula, cf. Eq. (2.11), in terms of the quarks PDFs and the proton and quarks helicities is

$$\mathrm{d}\sigma^{++} = \sum_q e_q^2 \left[q_+^+ \,\mathrm{d}\hat{\sigma}^{++} + q_-^+ \,\mathrm{d}\hat{\sigma}^{+-}\right] \qquad \text{proton "+"}, \tag{A.26}$$

$$\mathrm{d}\sigma^{+-} = \sum_q e_q^2 \left[q_+^- \,\mathrm{d}\hat{\sigma}^{+-} + q_-^- \,\mathrm{d}\hat{\sigma}^{+-}\right] \qquad \text{proton "}-\text{"}, \tag{A.27}$$

$$\tag{A.28}$$

where $\mathrm{d}\sigma \equiv \mathrm{d}\sigma/\mathrm{d}x\,\mathrm{d}y$, and $\mathrm{d}\hat{\sigma} \equiv \mathrm{d}\hat{\sigma}/\mathrm{d}y$; the superscripts $\mathrm{d}\sigma^{+-}$ refer to a beam electron with spin polarized along the direction of movement $(+)$, and a proton target polarized anti-parallel $(-)$ with respect to the incoming beam direction; for the eq hard scattering cross sections, $\mathrm{d}\hat{\sigma}^{+-}$ refers to the scattering of a "+" electron with a "−" quark.

Thus, the difference yields

$$\mathrm{d}\sigma^{++} - \mathrm{d}\sigma^{+-} = \sum_q e_q^2 [\Delta q \,\mathrm{d}\hat{\sigma}^{++} - \Delta q \,\mathrm{d}\hat{\sigma}^{+-}], \tag{A.29}$$

$$= \sum_q e_q^2 \,\Delta q \,(\mathrm{d}\hat{\sigma}^{++} - \mathrm{d}\hat{\sigma}^{+-}), \tag{A.30}$$

using $q_+^+ = q_-^-$, $q_-^+ = q_+^-$ and $\Delta q = q_+^+ - q_-^+$.

B

Derivation of formulae

Dependence of $\mathbf{A}_{\mathrm{UT}}$ on the polarizations The number of events in the two polarization states for each (p_T, x_F, ϕ) kinematic bin, with $N^{\uparrow(\downarrow)} \equiv \mathrm{d}^3 N^{\uparrow(\downarrow)}/\mathrm{d}p_T\ \mathrm{d}x_F\ \mathrm{d}\phi$, $\sigma_{UU} \equiv \mathrm{d}^3\sigma_{UU}$, and $\sigma_{UT} \equiv \mathrm{d}^3\sigma_{UT}$, is

$$\begin{aligned} N^{\uparrow} &= (L^{\uparrow}\sigma_{UU} + L_P^{\uparrow}\,\sigma_{UT})\;\Omega(p_T, x_F, \phi), \\ N^{\downarrow} &= (L^{\downarrow}\sigma_{UU} - L_P^{\downarrow}\,\sigma_{UT})\;\Omega(p_T, x_F, \phi). \end{aligned} \tag{B.1}$$

The definition of the asymmetry is

$$\begin{aligned} A_{UT} &= \frac{\dfrac{N^{\uparrow}}{L_P^{\uparrow}} - \dfrac{N^{\downarrow}}{L_P^{\downarrow}}}{\dfrac{N^{\uparrow}}{L^{\uparrow}} + \dfrac{N^{\downarrow}}{L^{\downarrow}}} \\ &= \frac{2\;\sigma_{UT} + \sigma_{UU}\;\left(\dfrac{L^{\uparrow}}{L_P^{\uparrow}} - \dfrac{L^{\downarrow}}{L_P^{\downarrow}}\right)}{2\;\sigma_{UU} + \sigma_{UT}\;\left(\dfrac{L_P^{\uparrow}}{L^{\uparrow}} - \dfrac{L_P^{\downarrow}}{L^{\downarrow}}\right)} \\ &= \frac{2\;\sigma_{UT} + \sigma_{UU}\;\left(\dfrac{1}{\langle P^{\uparrow}\rangle} - \dfrac{1}{\langle P^{\downarrow}\rangle}\right)}{2\;\sigma_{UU} + \sigma_{UT}\;\left(\langle P^{\uparrow}\rangle - \langle P^{\downarrow}\rangle\right)}\,, \end{aligned} \tag{B.2}$$

where we introduced the two averaged polarizations $\langle P^{\uparrow}\rangle$ and $\langle P^{\downarrow}\rangle$. Since σ_{UT} and $\langle P^{\uparrow}\rangle - \langle P^{\downarrow}\rangle$ are small we can do a Taylor expansion of A_{UT}:

$$
\begin{aligned}
A_{UT} &\simeq \left[2\,\sigma_{UT} + \sigma_{UU}\,\left(\frac{1}{\langle P^{\uparrow}\rangle} - \frac{1}{\langle P^{\downarrow}\rangle}\right)\right]\,\frac{1}{2\,\sigma_{UU}}\,\left[1 - \frac{\sigma_{UT}}{2\,\sigma_{UU}}(\langle P^{\uparrow}\rangle - \langle P^{\downarrow}\rangle)\right] \\
&= \frac{\sigma_{UT}}{\sigma_{UU}} + \frac{1}{2}\,\left(\frac{1}{\langle P^{\uparrow}\rangle} - \frac{1}{\langle P^{\downarrow}\rangle}\right) - \frac{\sigma_{UT}^2}{2\,\sigma_{UU}^2}(\langle P^{\uparrow}\rangle - \langle P^{\downarrow}\rangle) - \frac{1}{4}\frac{\sigma_{UT}}{\sigma_{UU}}(\langle P^{\uparrow}\rangle - \langle P^{\downarrow}\rangle)\,\left(\frac{1}{\langle P^{\uparrow}\rangle} - \frac{1}{\langle P^{\downarrow}\rangle}\right) \\
&= \frac{\sigma_{UT}}{\sigma_{UU}}\frac{(\langle P^{\uparrow}\rangle + \langle P^{\downarrow}\rangle)^2}{4\langle P^{\uparrow}\rangle\langle P^{\downarrow}\rangle} + \frac{1}{2}\,\left(\frac{\langle P^{\downarrow}\rangle - \langle P^{\uparrow}\rangle}{\langle P^{\uparrow}\rangle\langle P^{\downarrow}\rangle}\right) - \frac{\sigma_{UT}^2}{2\,\sigma_{UU}^2}(\langle P^{\uparrow}\rangle - \langle P^{\downarrow}\rangle) \\
&= \frac{\sigma_{UT}}{\sigma_{UU}}\,\left[1 + \left(\frac{\langle P^{\downarrow}\rangle - \langle P^{\uparrow}\rangle}{\langle P^{\downarrow}\rangle + \langle P^{\uparrow}\rangle}\right)^2\right] + \frac{1}{2}\,\left(\frac{\langle P^{\downarrow}\rangle - \langle P^{\uparrow}\rangle}{\langle P^{\uparrow}\rangle\langle P^{\downarrow}\rangle}\right) - \frac{\sigma_{UT}^2}{2\,\sigma_{UU}^2}(\langle P^{\uparrow}\rangle - \langle P^{\downarrow}\rangle) \\
&\simeq A_{UT}^{\sin\phi}\sin\phi + \frac{1}{2}\frac{\langle P^{\downarrow}\rangle - \langle P^{\uparrow}\rangle}{\langle P^{\uparrow}\rangle\langle P^{\downarrow}\rangle}\,,
\end{aligned}
\tag{B.3}
$$

where terms proportional to $\sigma_{UT}^2(\langle P^{\uparrow}\rangle - \langle P^{\downarrow}\rangle)$ and $\sigma_{UT}(\langle P^{\uparrow}\rangle - \langle P^{\downarrow}\rangle)^2$ have been neglected. In the case of same average polarizations for both target spin states, this leads to Eq. 4.35.

Relation between $A_{UT}^{\sin\phi}$ and A_N The definition of the normal left-right asymmetry is

$$
\begin{aligned}
A_N &= \frac{\sigma_L - \sigma_R}{\sigma_L + \sigma_R} \\
&= \frac{\int_{\pi}^{2\pi} d\psi\;(\sigma_{UU} + \sigma_{UT}) - \int_0^{\pi} d\psi\;(\sigma_{UU} + \sigma_{UT})}{\int_{\pi}^{2\pi} d\psi\;(\sigma_{UU} + \sigma_{UT}) + \int_0^{\pi} d\psi\;(\sigma_{UU} + \sigma_{UT})}\,.
\end{aligned}
\tag{B.4}
$$

Considering an anti-symmetric ψ-dependence of σ_{UT} $\left(\int_{\pi}^{2\pi} d\psi\;\sigma_{UT} = -\int_0^{\pi} d\psi\;\sigma_{UT}\right)$ and taking into account that σ_{UU} is independent of ψ, the asymmetry can be written as

$$
A_N = -\frac{\int_0^{\pi} d\psi\;\sigma_{UT}}{\int_0^{\pi} d\psi\;\sigma_{UU}}\,. \tag{B.5}
$$

In the case of a $\sin\psi$ modulation of σ_{UT}, this leads to Eq. (4.32)

$$
A_N = -\frac{\int_0^{\pi} d\psi\;\sigma_{UU}\;A_{UT}^{\sin\psi}\;\sin\psi}{\int_0^{\pi} d\psi\;\sigma_{UU}} = -\frac{2}{\pi}\;A_{UT}^{\sin\psi}. \tag{B.6}
$$

C

Selection of DIS events

The main physics trigger (21 or DIS trigger), discussed in Section 3.4, was originally designed to select inclusive DIS events. However, from these events, the sample of *real* DIS events, for which the scattered beam lepton is actually detected, represents only a small subset since most of the DIS trigger events contain only hadrons and no leptons[1]. In addition, some of the events containing a lepton are produced at $Q^2 < 1$ GeV^2 and should not be counted as DIS events.

inclusive DIS	semi-inclusive DIS	large-z
(0.25) 1 GeV^2 $< Q^2 <$ 20 GeV^2	1 GeV^2 $< Q^2 <$ (6 GeV^2)	1 GeV^2 $< Q^2 <$ (6 GeV^2)
4 GeV^2 $< W^2$	10 GeV^2 $< W^2$	10 GeV^2 $< W^2$
$0.1 < y < 0.85$	$(0.18) < y < 0.95$	$(0.18) < y < 0.95$
(0.007) $0.023 < x < 0.9$	$0.023 < x < 0.4$	$0.023 < x < 0.4$
	2 GeV $< p <$ 15 GeV	2 GeV $< p <$ 15 GeV
	$0.2 < z < 0.7$	$0.7 <$ z

Table C.1. Kinematic requirements for the inclusive DIS, SIDIS and large-z samples used in this analysis.

The selection of good DIS candidates is done by a set of kinematic requirements. These are listed in the left column of Table C.1. The boundaries of each kinematic variable were optimized in the past, and in most cases correspond to the limitations of the spectrometer acceptance. Additionally, the kinematics at HERMES are highly correlated (particularly x and Q^2), and therefore some of the boundaries depend on each other. This is better illustrated in Fig. C.1. The central column of Table C.1 corresponds to the selection of semi-inclusive DIS events, where at least one hadron is detected in coincidence with the scattered beam lepton. The right column indicates the criteria for the *large-z* region of the SIDIS events, discussed in Section 6.2.

[1] This is indeed shown in Section 6.2 and it has been studied several times in the past. See, e.g., Ref. [101].

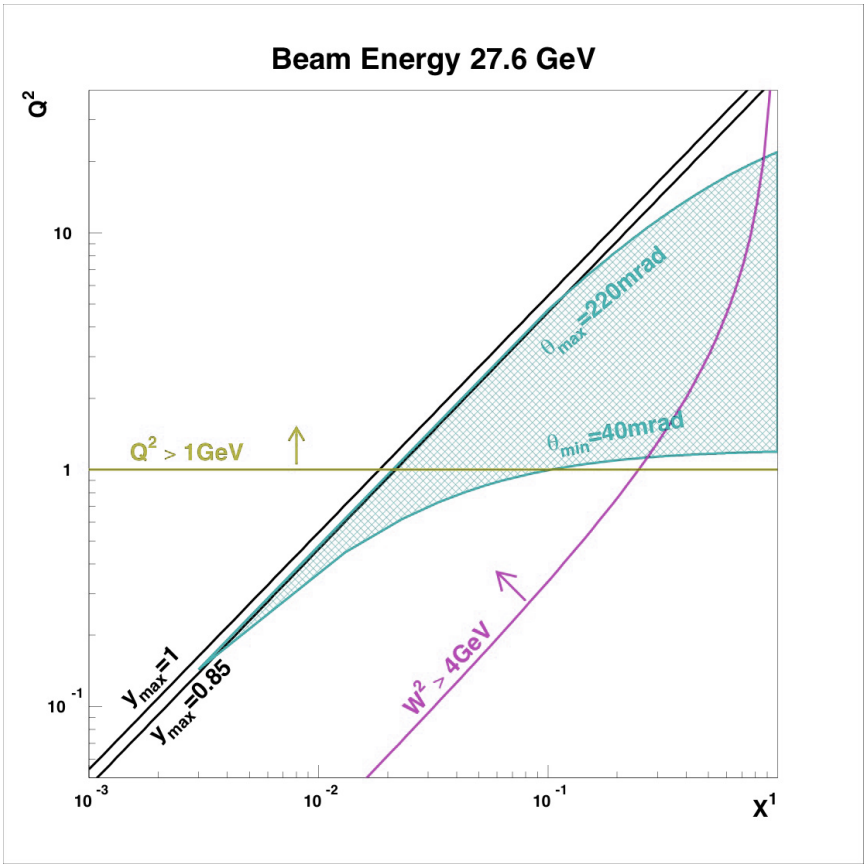

Figure C.1. Kinematic plane of DIS events at HERMES illustrating the boundaries on each variable.

- The cut on the squared mass of the final state W^2 discards events from the region of baryon resonances. In the case of SIDIS events, the higher cut improves the separation of the hadrons resulting from the hadronization of the struck quark from hadrons coming from the target remnant.
- The upper limit on the fractional energy transfer $y < 0.85$ removes events that may be affected by higher order QED radiation effects, i.e., bremsstrahlung. In semi-inclusive DIS events, the tagging of hadrons reduces these radiation effects and, thus, the upper limit can be raised up to $y < 0.95$. The upper cut on y also fixes the minimum momentum of the accepted lepton tracks. A value of $y < 0.85$ corresponds to 4.1 GeV, while for $y < 0.95$ leptons with energy as low as 1.38 GeV can be reconstructed. The lowest reachable value of the fractional energy transfer is $y = 0.07$, which is excluded by a minimum cut on $0.1 < y$. In the case of SIDIS events, the constraints on Q^2 and W^2 imply a minimum reachable value of $y = 0.18$, so that, in practice, no minimum cut is required for this case.
- The widest range in x that can be accessed at HERMES goes from $x \sim \mathcal{O}(10^{-3})$ to $x = 1$. The lower bound, related to the acceptance of the spectrometer, is given by the minimum scattering angle of about 40 mrad (which depends on the vertex position in the target cell) and the lowest accepted momentum due to the bending power of

the magnet. With the upper requirement of $y < 0.95$, the lowest reachable value of x corresponds to $x = 0.00124$. For the DIS data set, the constraints on $Q^2 > 1$ GeV^2 and $y > 0.85$ imply a minimum of $0.023 < x$. For the analysis of inclusive DIS data described in Chapter 7, in which data taken at low Q^2 were also analyzed, a minimum value of $x > 0.007$ was required in order to avoid the very low end of the distribution, where the population of bins at very low both x and Q^2 was found to be rather unstable and cut-dependent. The condition of $x > 0.007$ restricts the momentum transfer to be $Q^2 > 0.25\,\text{GeV}^2$.

The highest reachable value of x depends on the minimum W^2 required. For SIDIS analyses, the line $W^2 > 10$ GeV^2 crosses the $x = 0.5$ line around $Q^2 \sim 9$ GeV^2, and the $x = 0.4$ around $Q^2 \sim 6$ GeV^2. The population of events after $x > 0.4$ is however very small, and therefore this upper cut on x is used. For inclusive analyses, the condition $W^2 > 4$ GeV^2 implies that more events are found at higher x. Since $x = 1$ corresponds to elastic scattering, the cut on $x < 0.9$ is required in to reduce the background of events from elastic scattering. These cuts on x and W^2 determine the maximum value of 20 GeV^2 for Q^2 in the DIS data set.

- In the case of semi-inclusive analyses, the momentum of the selected hadron tracks is required to be in the range 2 GeV $< p <$ 15 GeV to ensure a reliable hadron identification by the RICH detector (See Section 3.3.2).
- The cuts on the hadron energy fraction z serve to enhance the semi-inclusive sample with hadrons originating from the struck quark. The lower limit of $0.2 < z$, in combination with the W^2 cut, discards hadrons resulting from the target remnant. The maximum limit $z > 0.7$ coincides with the region where exclusive vector meson production becomes bigger than 20% [147]. These exclusive channels typically decay in a pair of charged pions, which therefore have a large energy fraction.

If more than one lepton track is found to fulfill these requirements, only the one with larger momentum is taken as DIS candidate.

Charge symmetric background In addition to the scattered beam lepton, $e^+\,e^-$ pairs might be produced in several background processes, such as meson Dalitz decays or photon conversions, which in some cases, may end up being identified as DIS events. The rates for electrons and positrons from these charge symmetric background events are usually equivalent. Therefore, the real yield of DIS events in each kinematic bin is corrected for this background by subtracting the number of leptons with the charge opposite to that of the beam particle. The charge symmetric background reaches up to 25% at low x (i.e., low Q^2) and becomes negligible at large values of x. [16].

D

Wilson lines and universality

The Sivers function $f_{1T}^{\perp}$, nowadays one of the key parton distribution functions to understand the nucleon's transverse structure, did not have "*a happy childhood*". Not long after the original formulation by Sivers in Ref. [74], Collins (in the same paper [75] introducing the fragmentation function now carrying his name) proposed a proof of the vanishing of the Sivers function. Collins' argument was that the Sivers distribution function does not conserve time reversal invariance (a minus sign results after applying space- and time-reversal) and, thus, it should be forbidden in strong interactions

$$f_{1T}^{\perp}(x, k_{\perp}) \xrightarrow{T} -f_{1T}^{\perp}(x, k_{\perp}). \tag{D.1}$$

The reason why Collins argument was wrong, and why in fact we nowadays have experimental evidence of a non-vanishing Sivers function, relies on an incorrect definition of the quark-quark correlator in Eq. (2.40), ignoring the presence of a *Wilson line* in the operators defining the parton density [193].

What is a Wilson line? The strong coupling constant is large for the interaction of *soft* particles, i.e., particles with low energy. This implies that in scattering experiments involving hadrons, there is always soft gluon radiation. This radiation consists in principle of an infinite number of soft gluons, which would make their calculation in perturbation theory rather unmanageable[1]. In practice, in a diagrammatical approach, this soft radiation can be regarded as the exchange of a soft gluon between e.g., the quark-quark correlator Φ and the outgoing quark lines, or in the case of a hadron in the final state, in addition, between the fragmentation correlator Δ and the corresponding quark lines[2] Such extra diagrams, contributing to the tree-level process, can be resummed by means of an approximation somewhat equivalent to a path-ordered integral, *a path-ordered exponential*, also called a *gauge link* or *Wilson line*, that takes into account the radiation of soft gluons and ensures the color gauge invariance.

[1] An infinite amount of radiation would result into a infinite deflection of the particle trajectory!

[2] See, e.g., Figs. 1 and 2 from Ref. [194].

Thus, in order to make the correlation function Φ gauge invariant, a path-dependent Wilson line $W_{0\xi}$ must be inserted between the quark fields of Eq. (2.42)

$$\Phi_{ij}(k;P,S) = \frac{1}{(2\pi)^4}\int \mathrm{d}^4\,\xi\; e^{-i\,p\cdot\xi}\;\langle P,S|\bar{\psi}_j(\xi)\,W_{0\xi}\,\psi_i(0)|P,S\rangle, \tag{D.2}$$

where the Wilson line

$$W_{0\xi} = \mathcal{P}\exp\left(\;-i\,\sqrt{4\pi\alpha_S}\int_0^\xi \mathrm{d}s^\mu\,A_\mu(s)\;\right), \tag{D.3}$$

is a bilocal operator connecting the quark fields ψ in two different points in space and time, 0 and ξ. Here, $\mathcal{P}$ indicates the path-ordering integral over the gauge field A_μ, which is process-dependent. An analogous expression is found for the fragmentation correlator Δ, see e.g., Ref. [33].

Process dependence In the case of SIDIS, this soft radiation can be identified with the *final state interactions* mentioned in Section 2.6.2, and corresponds to the gluons interchanged between the struck quark (carrying a certain color charge c) and the proton remnant (which must then carry a color charge $\bar{c}$ as the original proton is a color-neutral object). This is schematically depicted in the right-hand side of Fig. D.1. In order to run over all exchanged gluons, which happens *after* the $\gamma^* q$ collision, the Wilson line must then go to future infinity, i.e., $W_{0\,\infty}$. This way, all soft-gluon radiation is absorbed into the parton densities and the corresponding fragmentation functions. Effectively, one considers only the case of Fig. 2.10 but now with a Φ and Δ that contain the gauge links [194].

The opposite case is found for Drell-Yan processes, in which two protons collide. One quark from each proton interacts with the other. These should have color charges c and $\bar{c}$, respectively. Therefore, the corresponding color-charged proton remnants interact with the quarks *before* the collision, leading to *initial state radiation*. The Wilson path must go therefore to the *past infinity*. See left-hand side of Fig. D.1.

Sivers revisited We can now reexamine the original Collins' proof for the vanishing of the Sivers function in Eq. (D.1). Once the parton distribution functions have been made gauge invariant, under time-reversal, the *future-pointing* Wilson line $W_{0\,\infty}$ is replaced by a *past-pointing* Wilson line $W_{-\infty\,0}$, so that the correct version of the proof gives

$$f_{1T}^{\perp}(x,k_\perp)|_{W_{0\,\infty}} \xrightarrow{T} f_{1T}^{\perp}(x,k_\perp)|_{W_{-\infty\,0}}. \tag{D.4}$$

Since the past-pointing Wilson lines are appropriate for factorization in the Drell-Yan process, the correct interpretation is not that the Sivers function vanishes, but rather that it has opposite sign in SIDIS and Drell-Yan

$$f_{1T}^{\perp}(x,k_\perp)|_{\text{DIS}} = -f_{1T}^{\perp}(x,k_\perp)|_{\text{Drell-Yan}}. \tag{D.5}$$

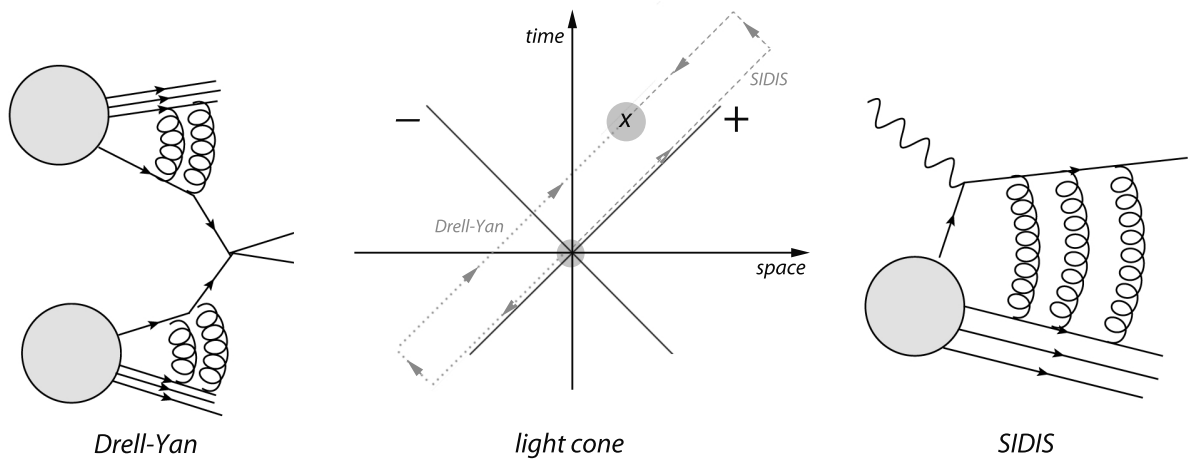

Figure D.1. Radiation of soft gluons between struck quark and proton remnants. In the central diagram, an schematic representation of the color gauge link, i.e., Wilson line, between $\psi(0)$ and $\psi(x)$ in the light cone is given.

Naive $T-$odd functions Parton distribution functions which in the absence of Wilson lines would not conserve time-reversal invariance are labelled as **T-odd** functions. The conservation of hermiticity, parity and time-reversal of the quark-quark correlator follows from the properties of the quark fields and it is expressed with the following relations [35]

$$\text{hermiticity:} \qquad \Phi(k;P,S) = \gamma_0\,\Phi^\dagger(k;P,S)\,\gamma_0, \tag{D.6a}$$

$$\text{parity:} \qquad \Phi(k;P,S) = \gamma_0\,\Phi(\bar{k};\bar{P},-\bar{S})\,\gamma_0, \tag{D.6b}$$

$$\text{time-reversal:} \qquad \Phi^*(k;P,S) = i\,\gamma^1\gamma^3\,\Phi(\bar{k};\bar{P},\bar{S})\,i\,\gamma^1\gamma^3, \tag{D.6c}$$

where the tilde four-vectors are defined as $\bar{p}^\mu = (p^0, -\mathbf{p})$. Parton distribution functions satisfying Eq. (D.6c) are said to be T-even, while for T-odd distribution functions, like the Sivers or Boer-Mulders functions, the time-reversal operation leaves a minus sign. These distribution functions are sometimes said to be **naive** T-odd, since in the relation (D.6c), the time-reversal operation is applied to the spins, momenta and field-operator combination without interchanging the initial and final states of the process [33]. A fragmentation function will be called T-odd if the corresponding distribution function is T-odd; e.g., the Collins fragmentation function $H_1^\perp$ is T-odd since the Boer-Mulders function $h_1^\perp$ is T-odd.

Universality The parton distribution functions are inherently non-perturbative objects and cannot be fully calculated from first principles. This would mean that expressions for cross sections involving TMDs have limited predictive value. For that reason one usually makes the proposition of *universality* of parton distribution functions. That is, the distribution of partons inside a certain hadron is assumed to be the same, regardless of the process in which it is probed. This allows to determine the PDFs from a certain process, e.g., DIS, and use them as input for the cross sections of other processes, like Drell-Yan. The assumption of universality, thus, makes the parton model, and QCD, a theory with predictive power.

The inclusion of Wilson lines, being process-dependent, in the definition of the distribution functions is therefore a crucial question regarding the validity of the assumption of universality

of these. In some processes, like the SIDIS and Drell-Yan commented above, the Wilson line implies a change of sign in the PDFs. In other processes, it can lead to much more complicated dependences, and further studies are needed to fully probe the universality of other PDFs. See Refs. [33, 194, 200] for more information.

Light-cone coordinates In the infinite momentum frame, where the partons and the proton can be considered quasi-collinear, it is convenient to express the relevant variables in terms of their components in the light cone. For example, the momentum $p = (p_0, \mathbf{p}) = (p_0, p_1, p_2, p_3)$ can be written as $p = (p_+, p_-, \mathbf{p}_T)$, where $p_\pm = p_0 \pm p_3)/\sqrt{2}$ and $\mathbf{p}_T = (p_1, p_2)$. If p is collinear with the boost direction, this implies that it points along the $+$ direction of the line cone $p \simeq (p_+, 0, \mathbf{0})$. Then, 4-vectors can be simply described with their $+$ component in the light cone.

E

Extra figures

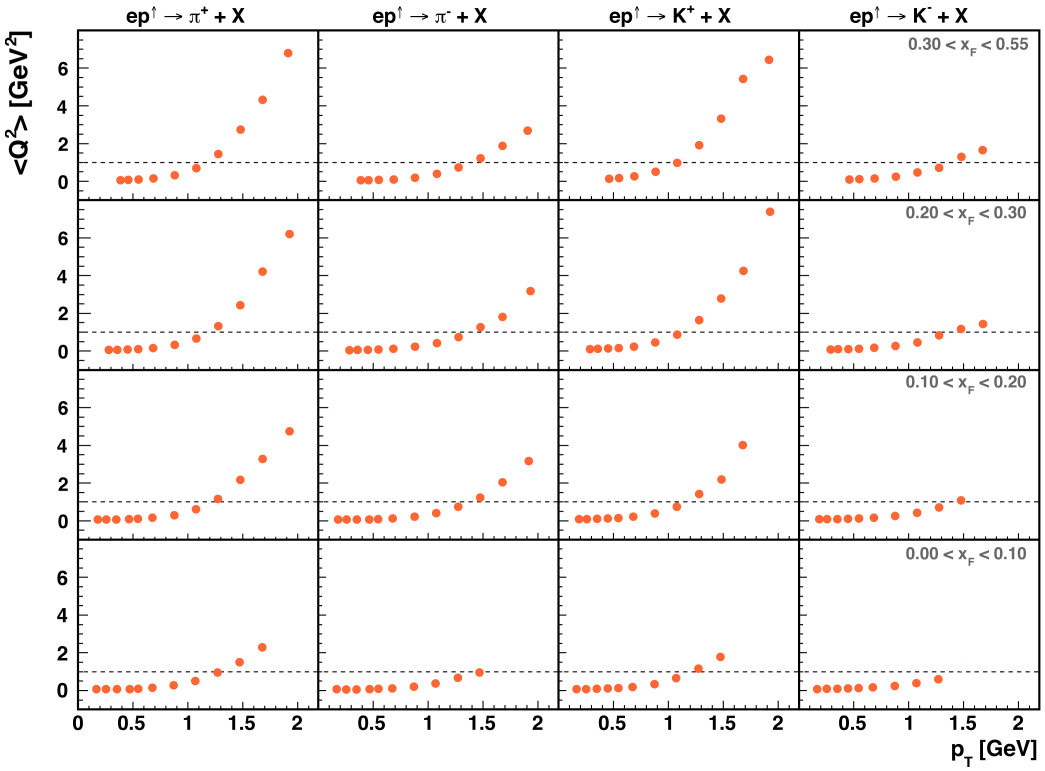

Figure E.1. Average Q^2 in every kinematic bin estimated from a Monte Carlo sample. As a function of x_F, all data points have $\langle Q^2 \rangle < 1\text{GeV}^2$.

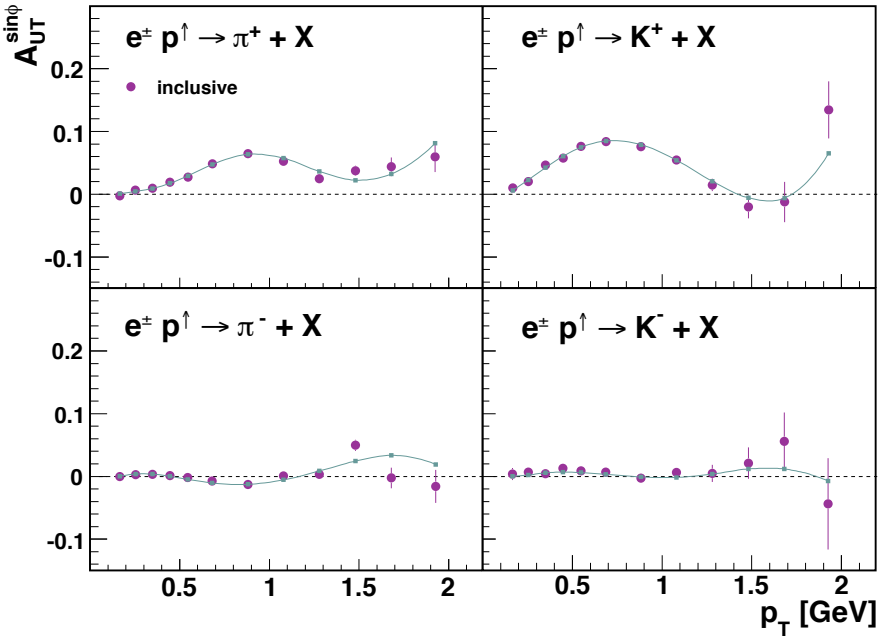

Figure E.2. The $\mathcal{A}_{UT}^{\sin\phi}$ fit function (with squares) evaluated at the average bin kinematics $\langle p_T \rangle$, plotted together with the $A_{UT}^{\sin\phi}$ amplitudes as a function of p_T. See Section 5.3.1.

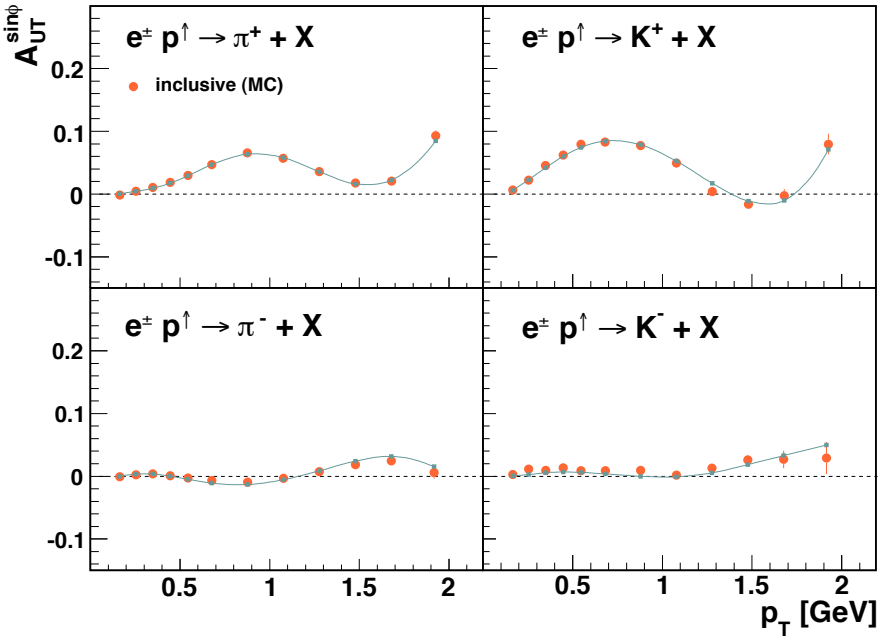

Figure E.3. The $A_{UT,MC}^{\sin\phi}$ amplitudes extracted from the polarized PYTHIA sample as a function of p_T. The $\mathcal{A}_{UT}^{\sin\phi}$ function is also shown for comparison; this is evaluated at the average bin kinematics $\langle p_T \rangle_{MC}$, $\langle x_F \rangle_{MC}$ for each hadron species. See Section 5.3.3.

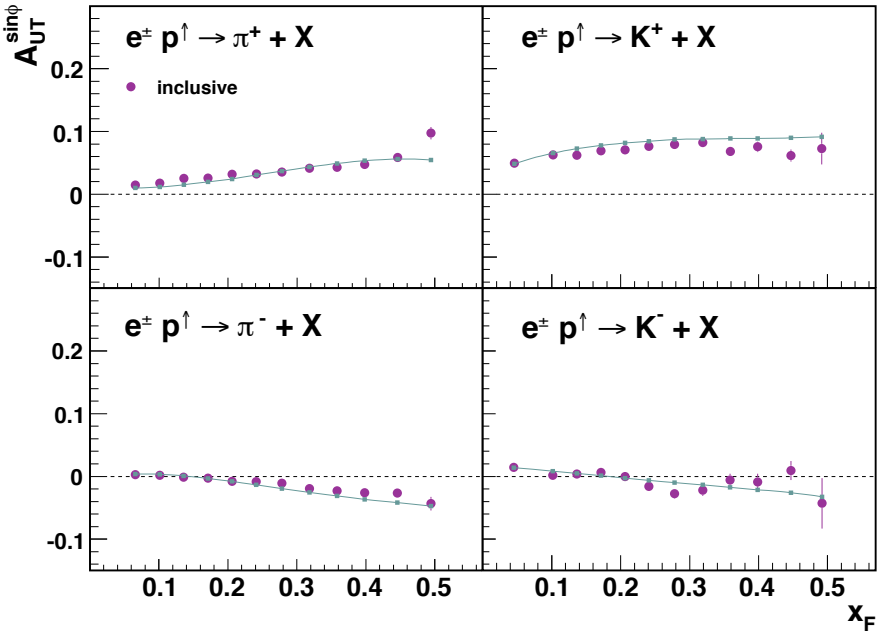

Figure E.4. The $\mathcal{A}_{UT}^{\sin\phi}$ fit function (with squares) evaluated at the average bin kinematics $\langle x_F \rangle$, plotted together with the $A_{UT}^{\sin\phi}$ amplitudes as a function of x_F. See Section 5.3.1.

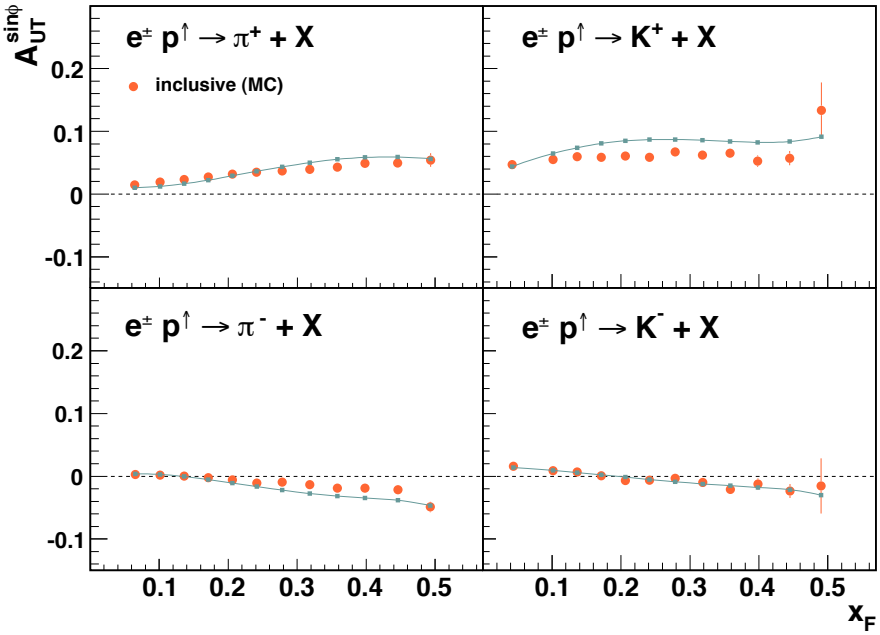

Figure E.5. The $A_{UT,MC}^{\sin\phi}$ amplitudes extracted from the polarized PYTHIA sample as a function of x_F. The $\mathcal{A}_{UT}^{\sin\phi}$ function is also shown for comparison; this is evaluated at the average bin kinematics $\langle p_T \rangle_{MC}$, $\langle x_F \rangle_{MC}$ for each hadron species. See Section 5.3.3.

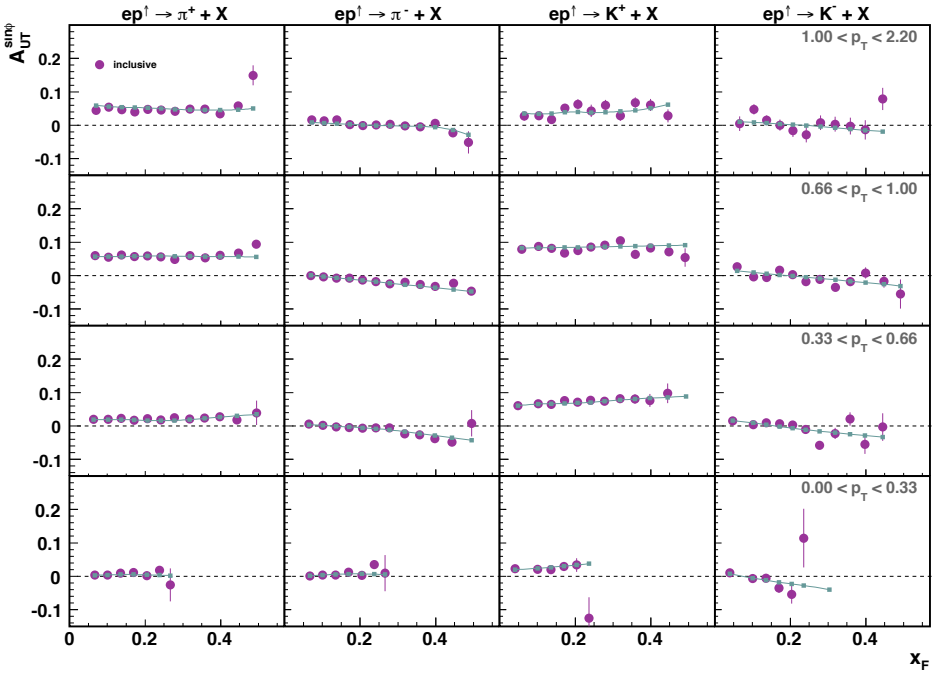

Figure E.6. The $\mathcal{A}_{UT}^{\sin\phi}$ fit function (with squares) evaluated at the average bin kinematics $\langle x_F \rangle$, plotted together with the $A_{UT}^{\sin\phi}$ amplitudes as a function of $x_F$in four different slices of p_T. See Section 5.3.1.

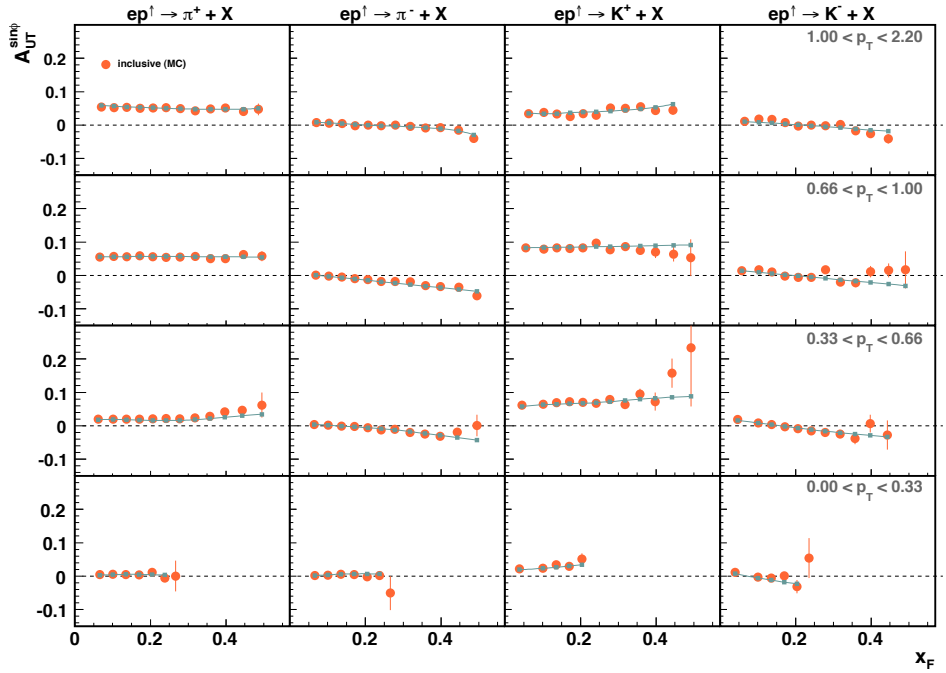

Figure E.7. The $A_{UT,MC}^{\sin\phi}$ amplitudes extracted from the polarized PYTHIA sample as a function of x_F in four slices of p_T. The $\mathcal{A}_{UT}^{\sin\phi}$ function is also shown for comparison; this is evaluated at the average bin kinematics $\langle p_T \rangle_{MC}$, $\langle x_F \rangle_{MC}$ for each hadron species. See Section 5.3.3.

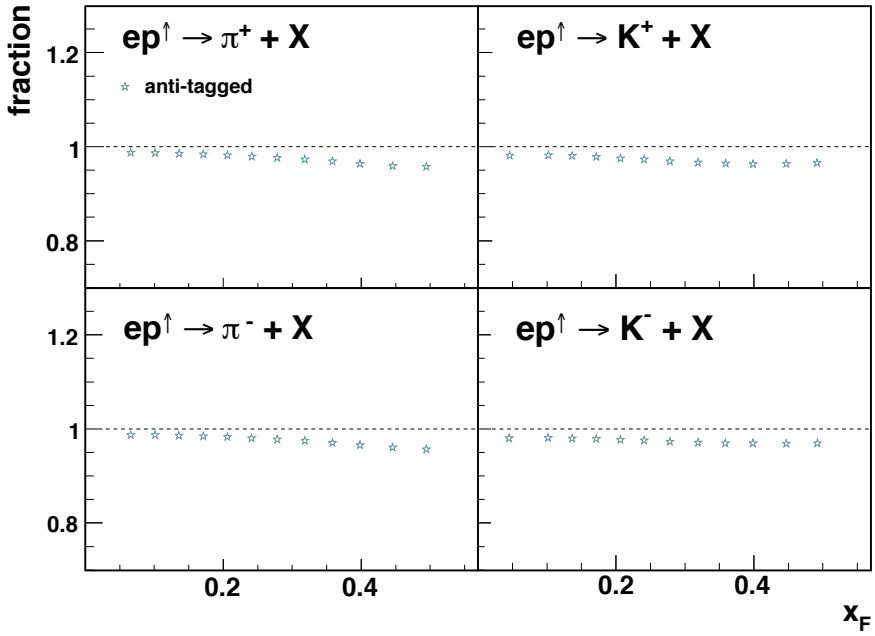

Figure E.8. Fraction of *anti-tagged* hadrons, i.e., for which no lepton track was detected in coincidence, in every bin of x_F. See Section 6.2.1.

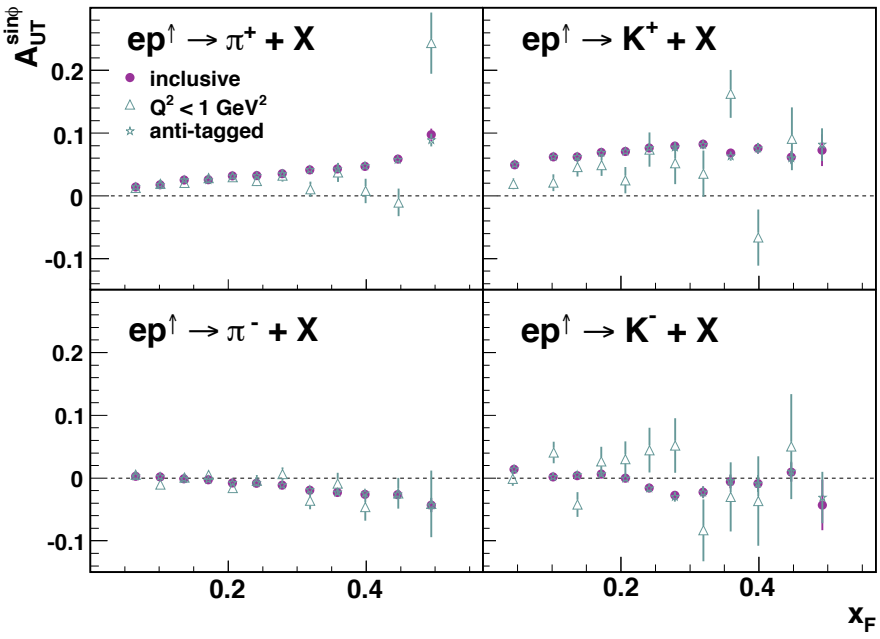

Figure E.9. The $A_{UT}^{\sin\phi}$ amplitudes extracted from photoproduction events as a function of x_F, compared to the inclusive amplitudes. See Section 6.2.1.

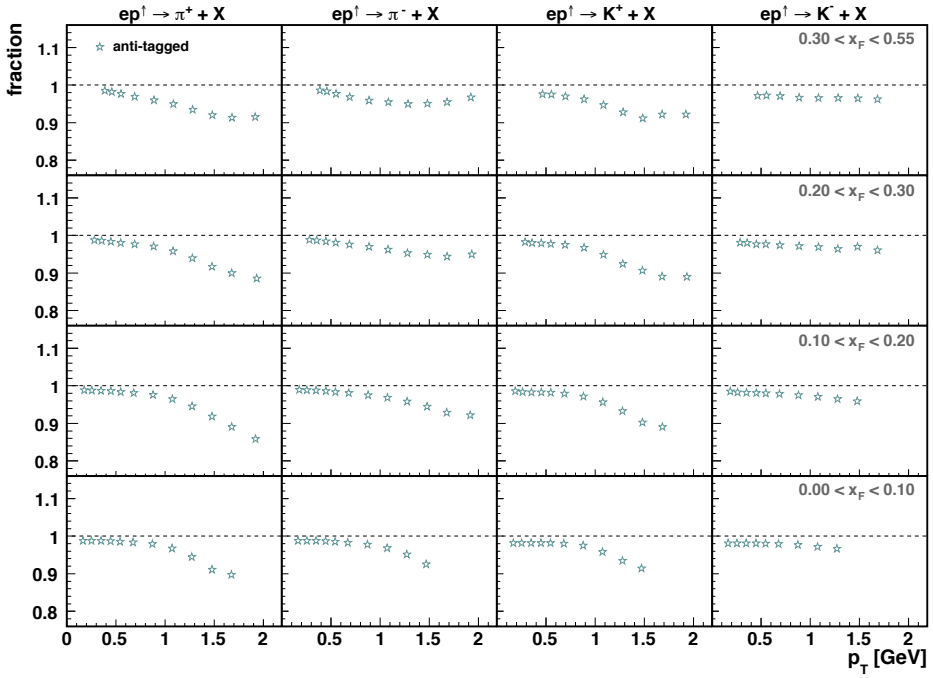

Figure E.10. Fraction of *anti-tagged* hadrons, i.e., for which no lepton track was detected in coincidence, in every bin of p_T. See Section 6.2.1.

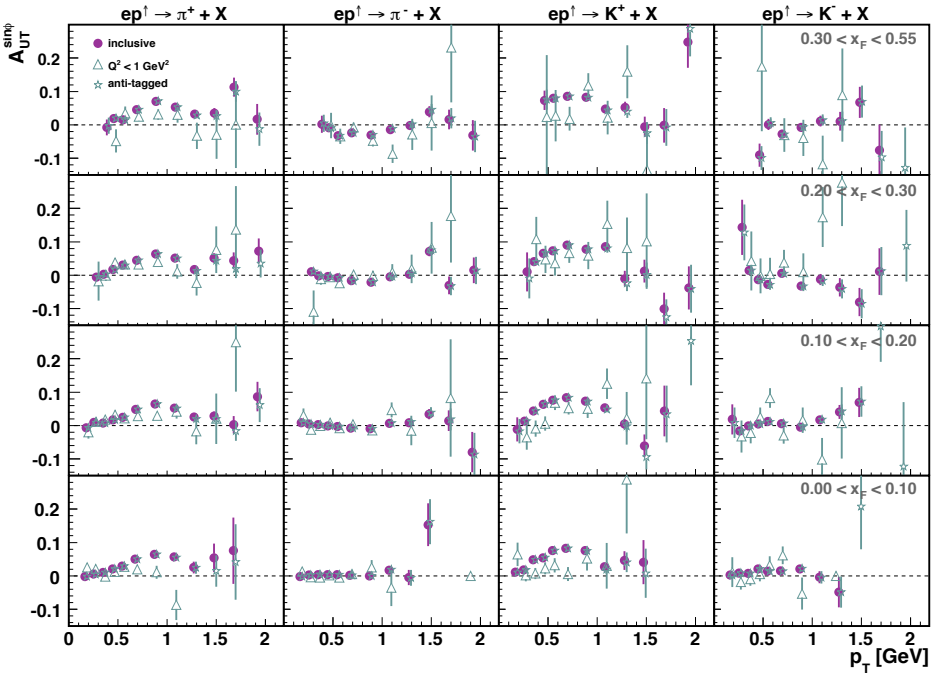

Figure E.11. The $A_{UT}^{\sin\phi}$ amplitudes extracted from photoproduction events as a function of p_T, compared to the inclusive amplitudes. See Section 6.2.1.

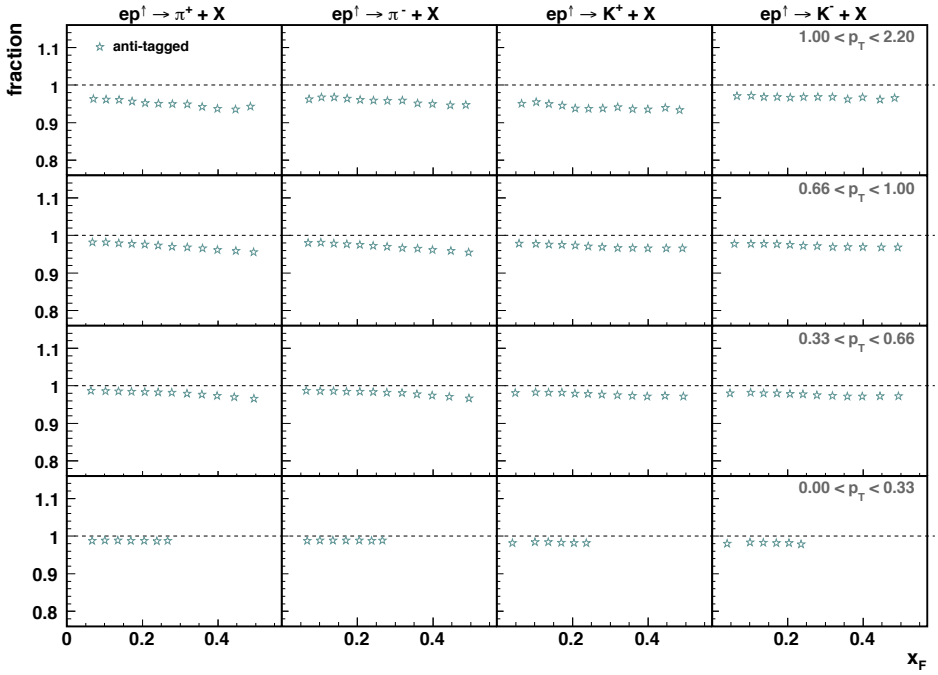

Figure E.12. Fraction of *anti-tagged* hadrons, i.e., for which no lepton track was detected in coincidence, in every bin of x_F. See Section 6.2.1.

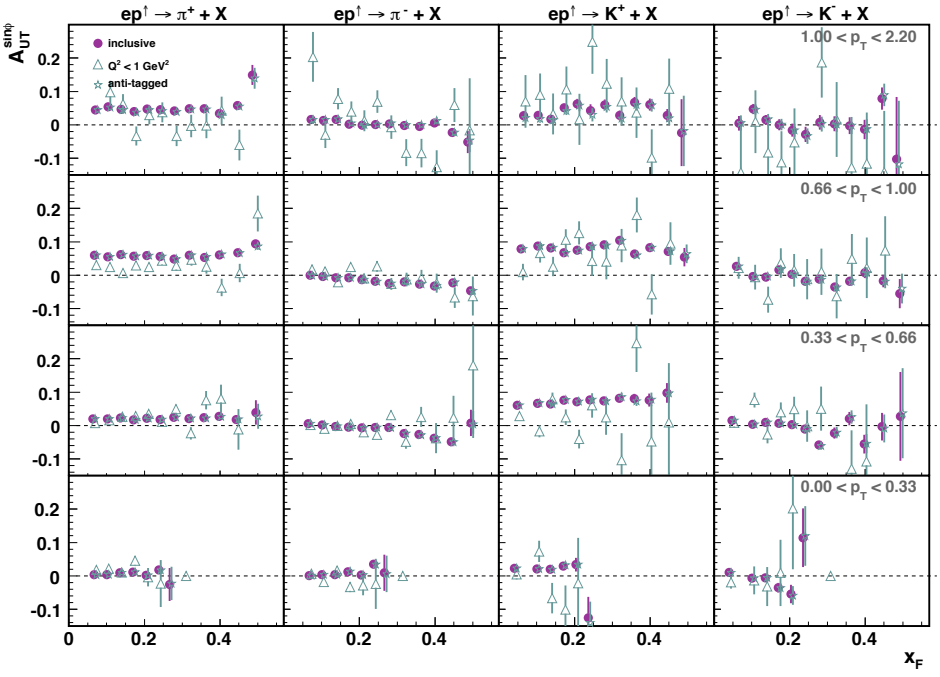

Figure E.13. The $A_{UT}^{\sin\phi}$ amplitudes extracted from photoproduction events as a function of p_T, compared to the inclusive amplitudes. See Section 6.2.1.

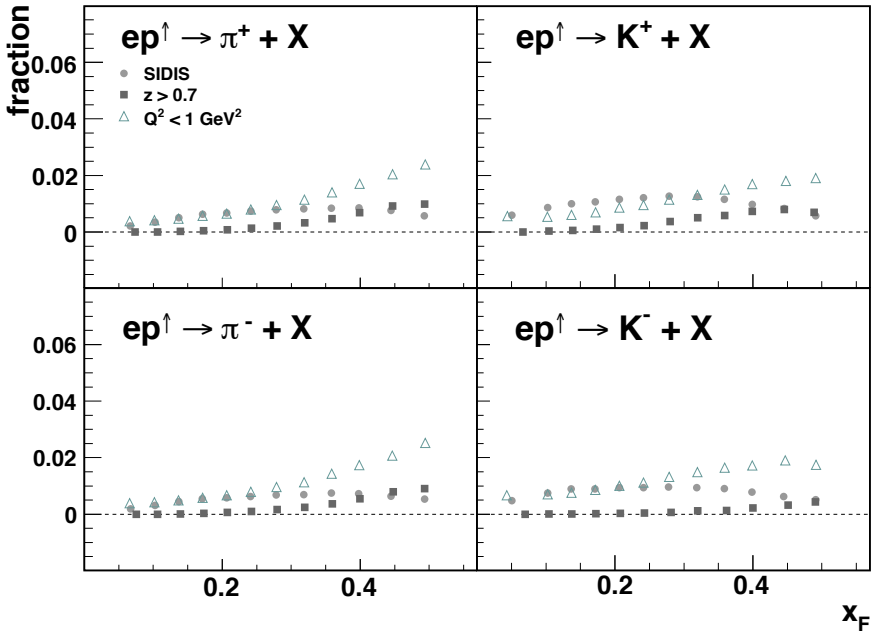

Figure E.14. Fraction of *tagged* hadrons, i.e., for which a lepton track was detected in coincidence, in every bin of x_F. See Sections 6.2.2 – 6.2.4.

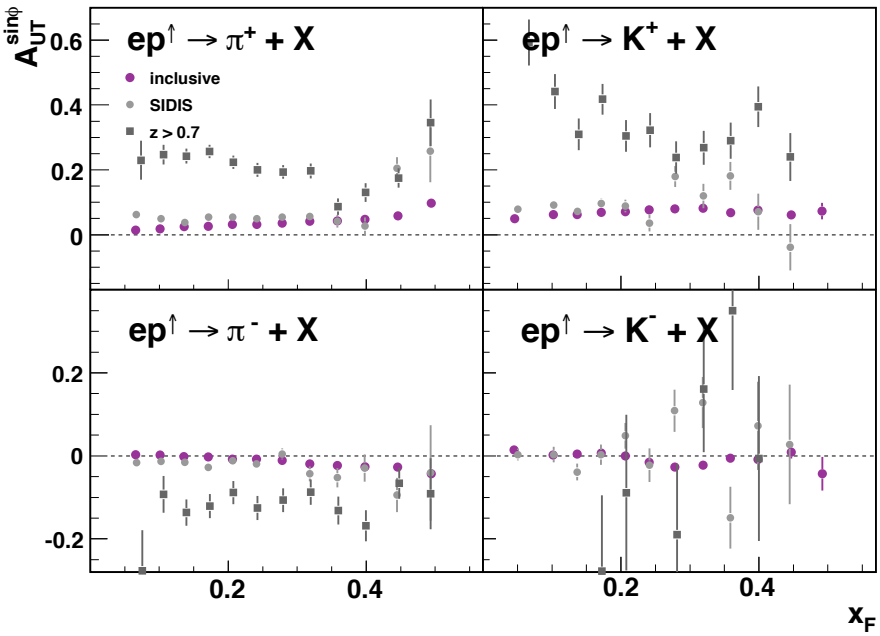

Figure E.15. The one-dimensional extraction of the $A_{UT}^{\sin\phi}$ amplitudes for DIS events as a function of x_F, compared to the inclusive amplitudes. See Sections 6.2.2 – 6.2.4.

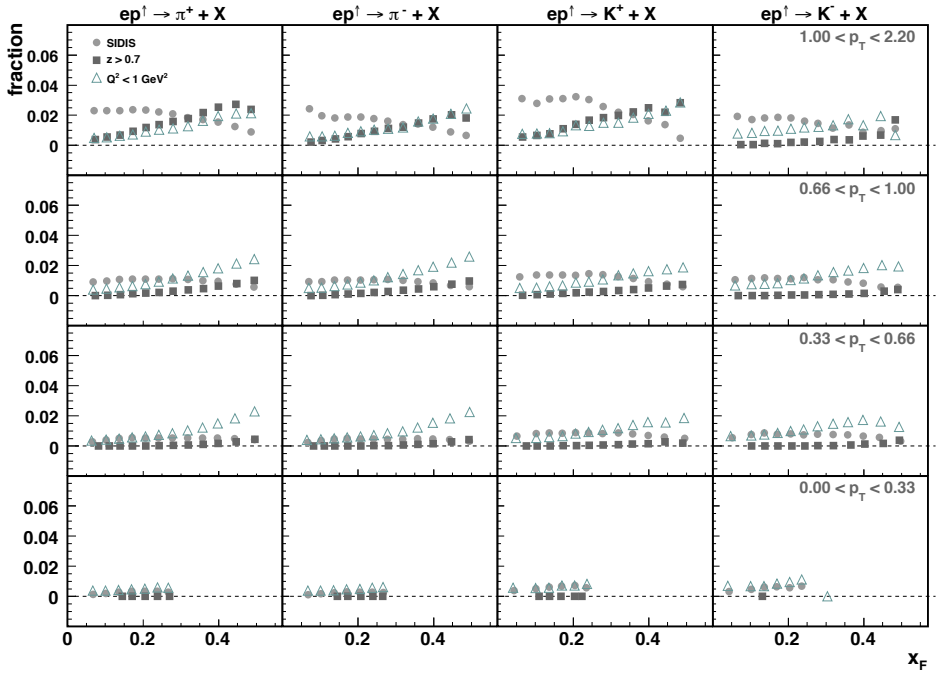

Figure E.16. Fraction of *tagged* hadrons, i.e., for which a lepton track was detected in coincidence, in every bin of x_F. See Sections 6.2.2 – 6.2.4.

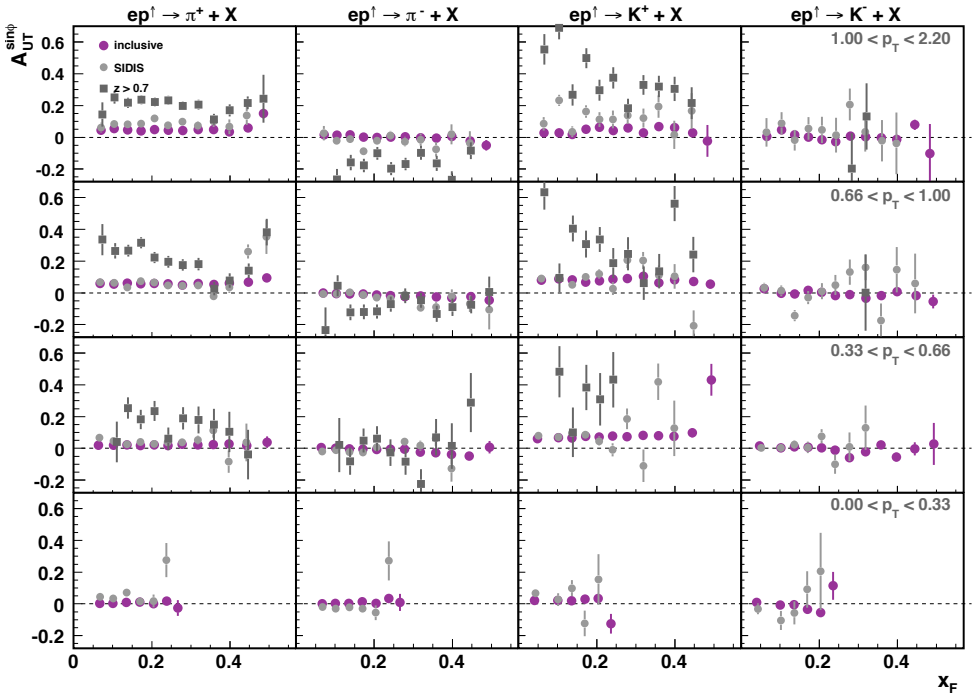

Figure E.17. The two-dimensional extraction of the $A_{UT}^{\sin\phi}$ amplitudes for DIS events as a function of x_F in four slices of p_T, compared to the inclusive amplitudes. See Sections 6.2.2 – 6.2.4.

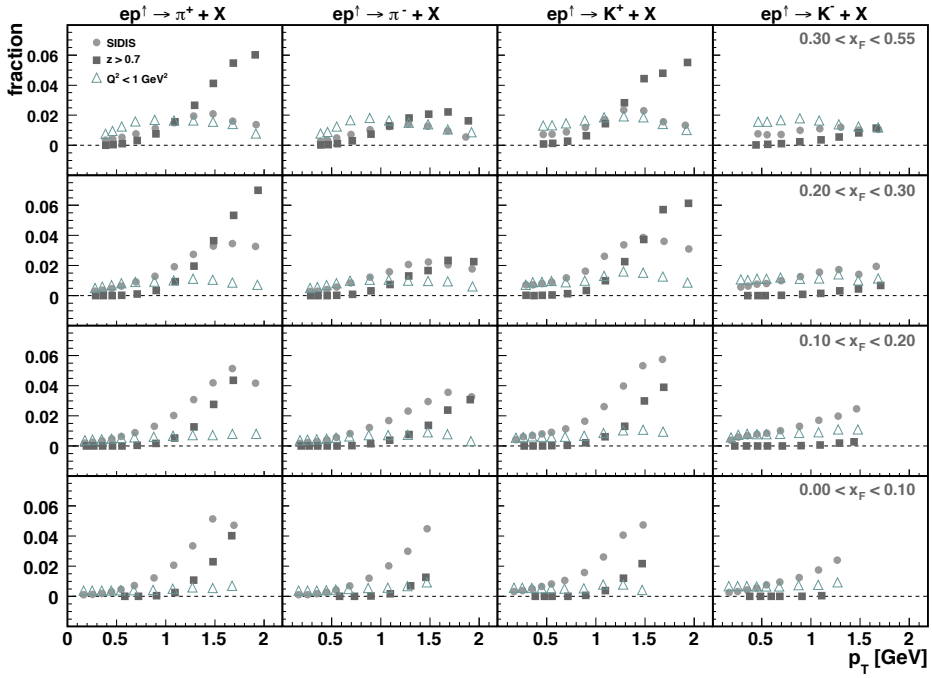

Figure E.18. Fraction of *tagged* hadrons, i.e., for which a lepton track was detected in coincidence, in every bin of p_T. See Sections 6.2.2 – 6.2.4.

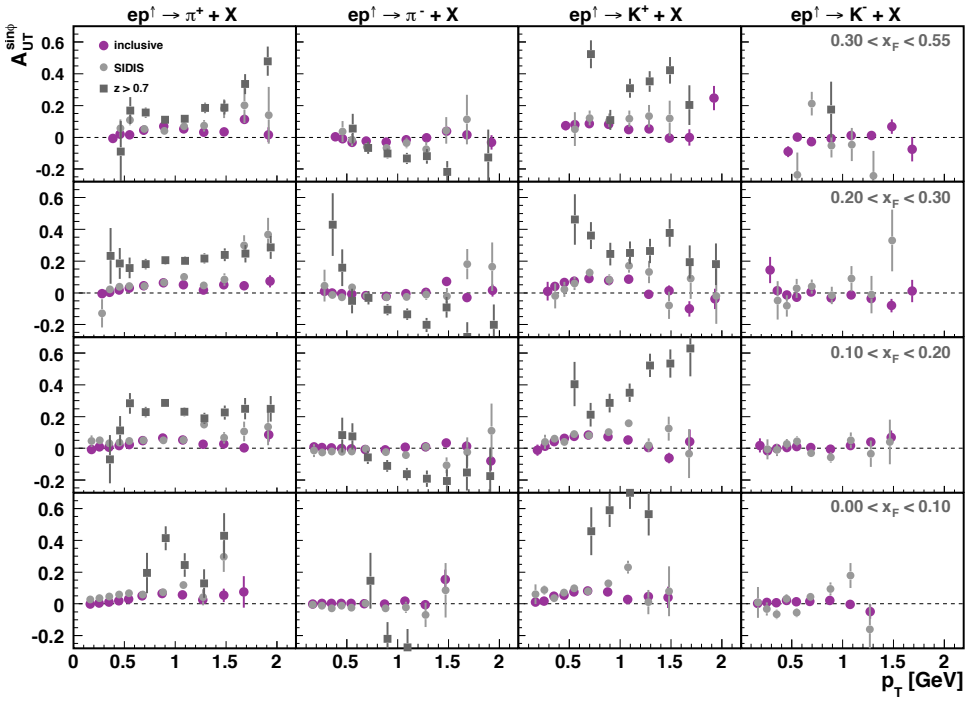

Figure E.19. The two-dimensional extraction of the $A_{UT}^{\sin\phi}$ amplitudes for DIS events as a function of p_T in four slices of x_F, compared to the inclusive amplitudes. See Sections 6.2.2 – 6.2.4.

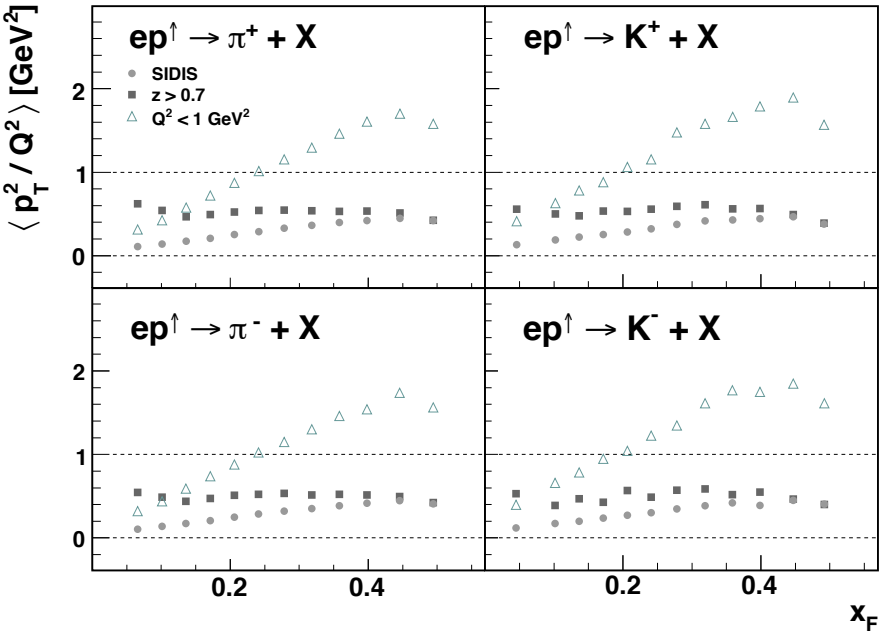

Figure E.20. The ratio $\langle p_T^2/Q^2 \rangle$ calculated for each x_F bin and different subsamples of the data. See Section 6.2.2 – 6.2.4.

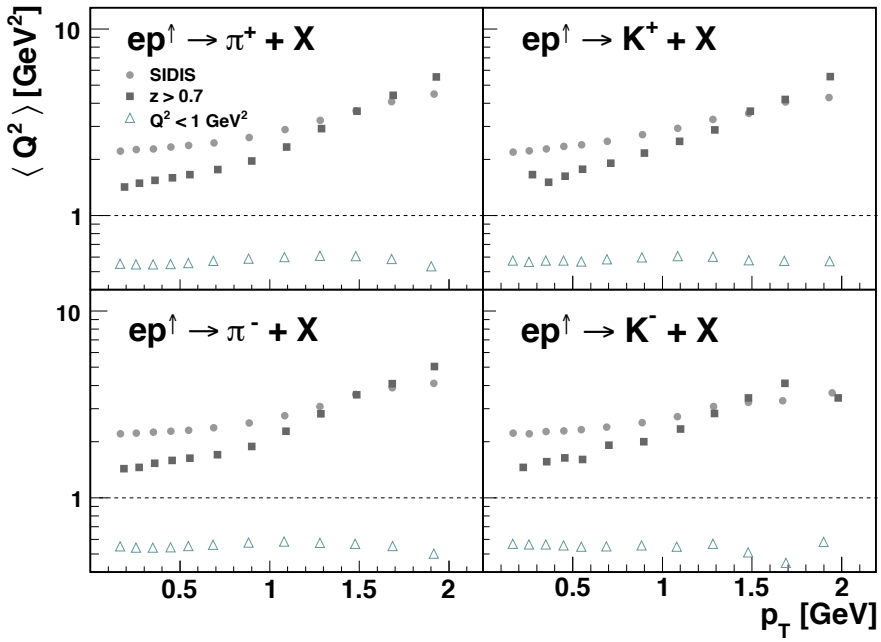

Figure E.21. Average Q^2 calculated for each x_F bin and different subsamples of the data. See Section 6.2.2 – 6.2.4.

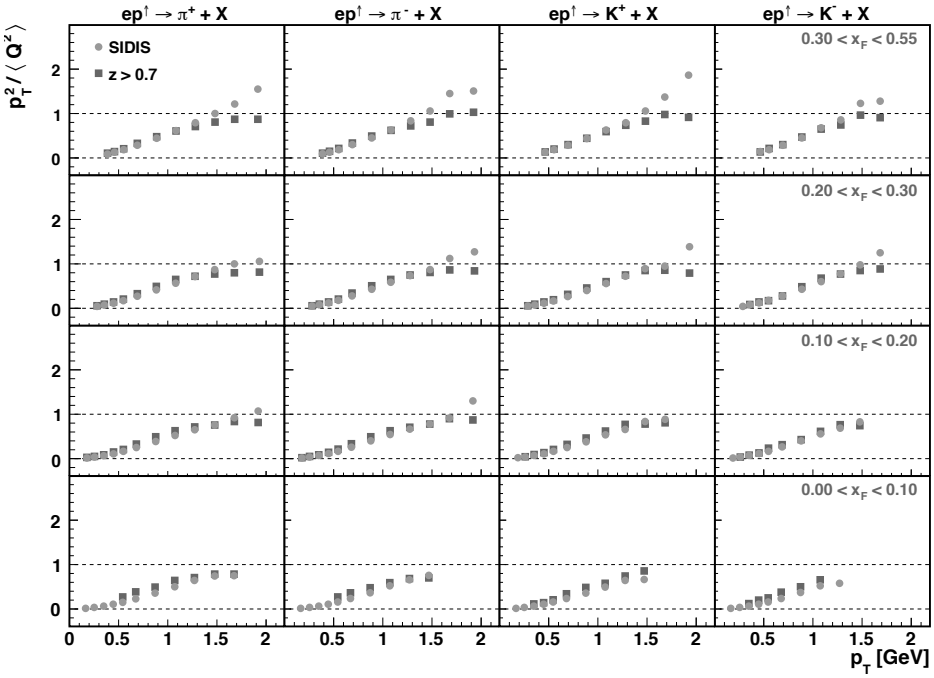

Figure E.22. The ratio $\langle p_T^2/Q^2 \rangle$ calculated for each p_T bin and different subsamples of the data. See Section 6.2.2 – 6.2.4.

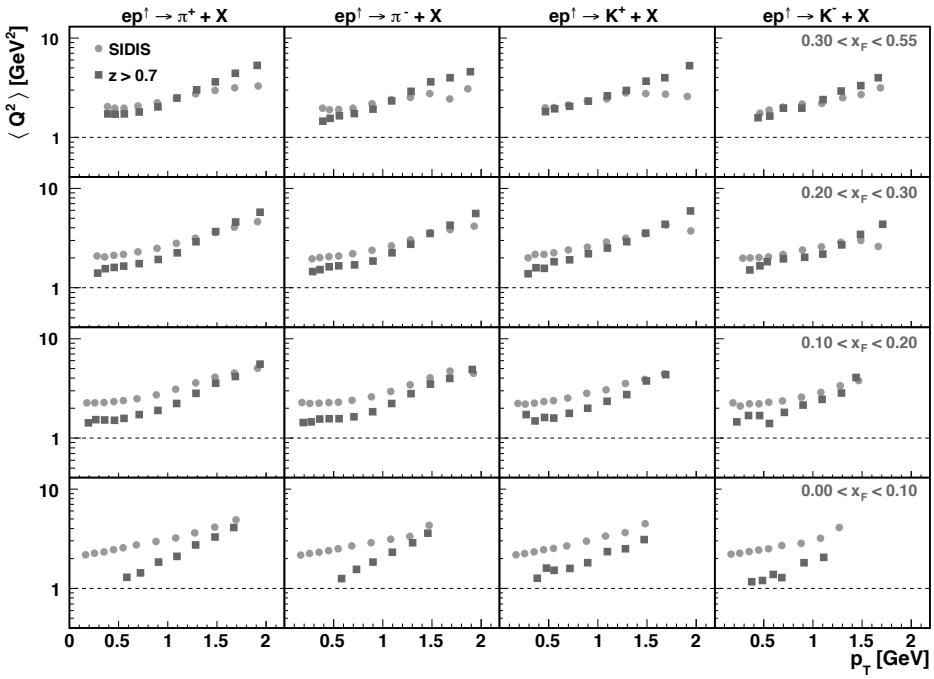

Figure E.23. Average Q^2 calculated for each p_T bin and different subsamples of the data. See Section 6.2.2 – 6.2.4.

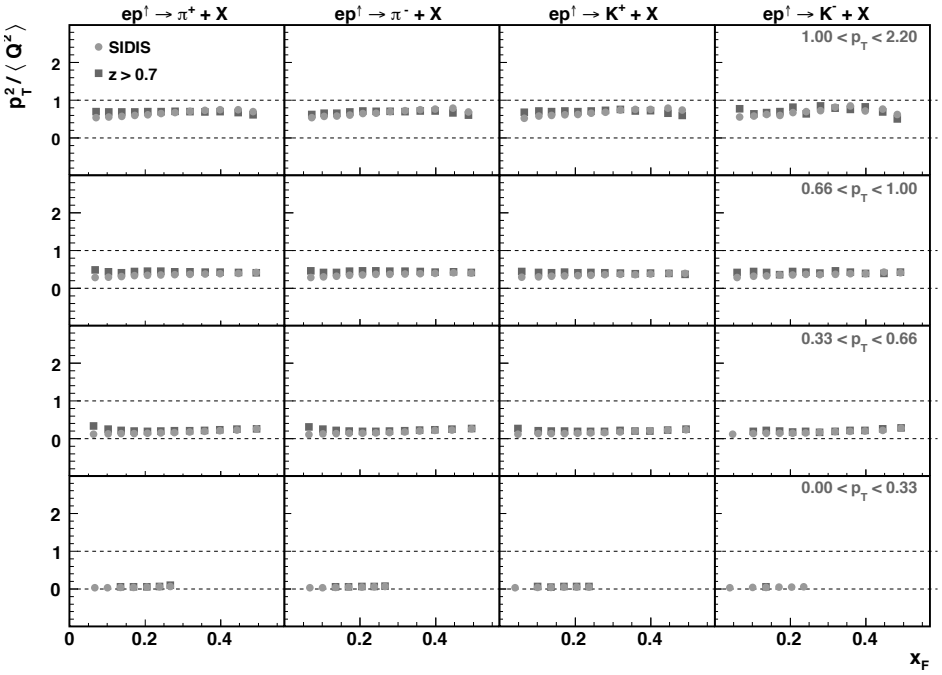

Figure E.24. The ratio $\langle p_T^2/Q^2 \rangle$ calculated for each x_F bin and different subsamples of the data. See Section 6.2.2 – 6.2.4.

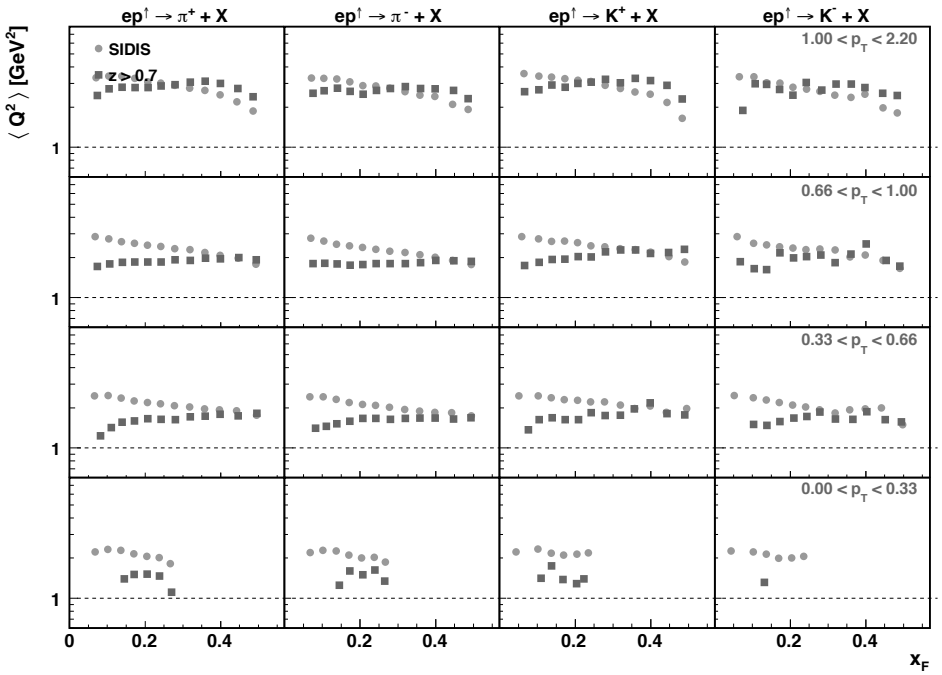

Figure E.25. Average Q^2 calculated for each x_F bin and different subsamples of the data. See Section 6.2.2 – 6.2.4.

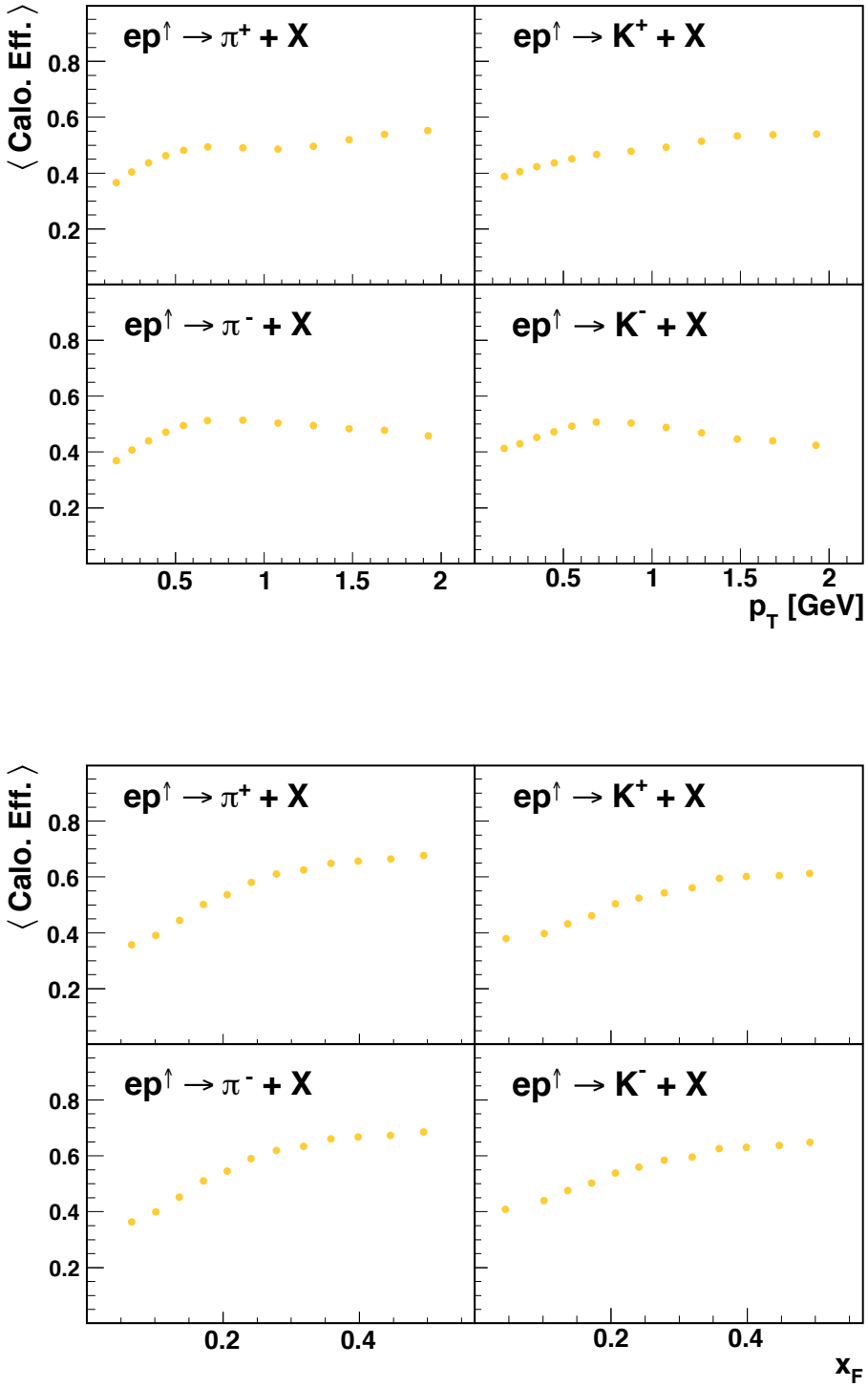

Figure E.26. Average calorimeter efficiency as a function of p_T (top) and as a function of x_F (bottom), including the effect of lepton tracks. See Section 4.3.

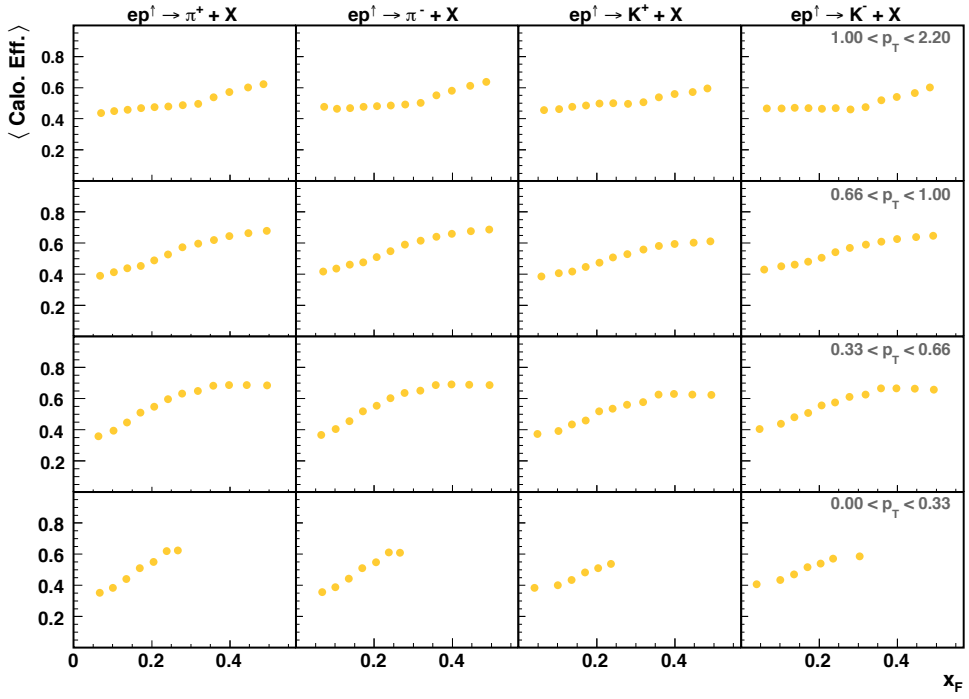

Figure E.27. Average calorimeter efficiency as a function of x_F, for the two-dimensional binning used in the analysis, including the effect of lepton tracks. See Section 4.3.

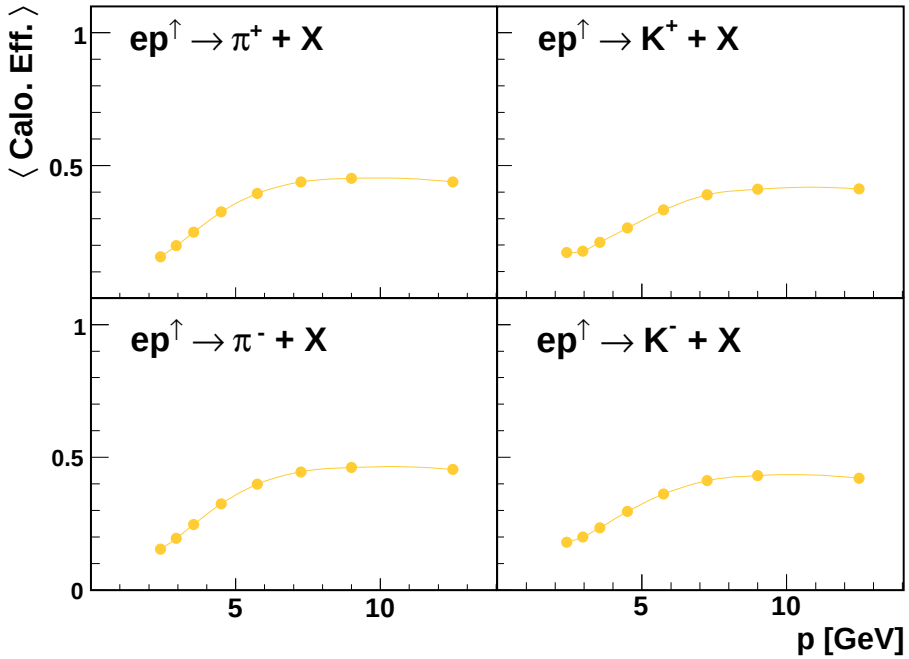

Figure E.28. Average calorimeter efficiency as a function of the hadron momentum. These values are a graphical representation of the *look-up* table described in Section 4.3, i.e., the effect of the lepton tracks is **not** included.

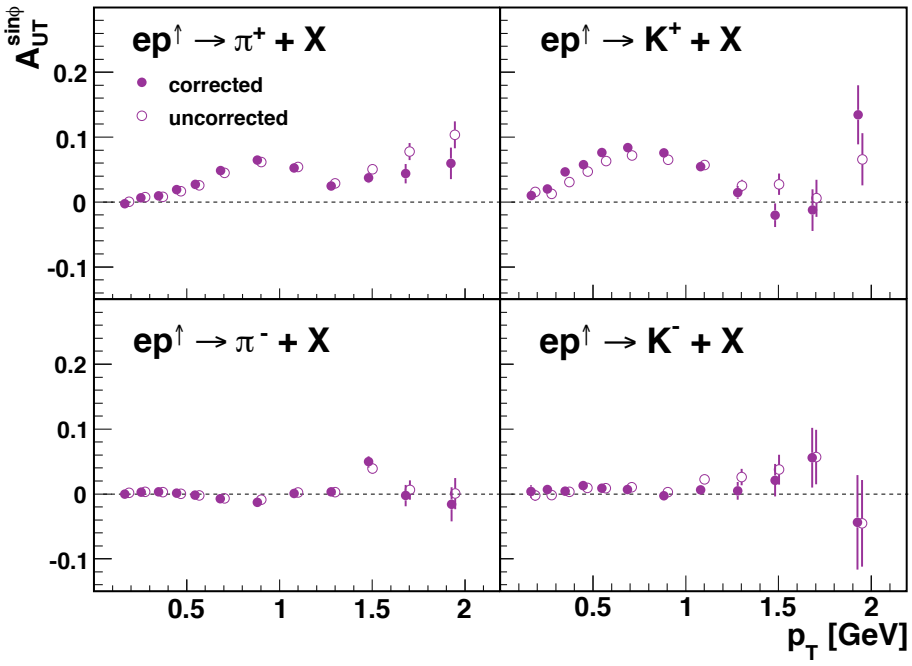

Figure E.29. The $A_{UT}^{\sin\phi}$ amplitudes as a function of p_T with and without the correction by the calorimeter efficiency. See Section 4.6.

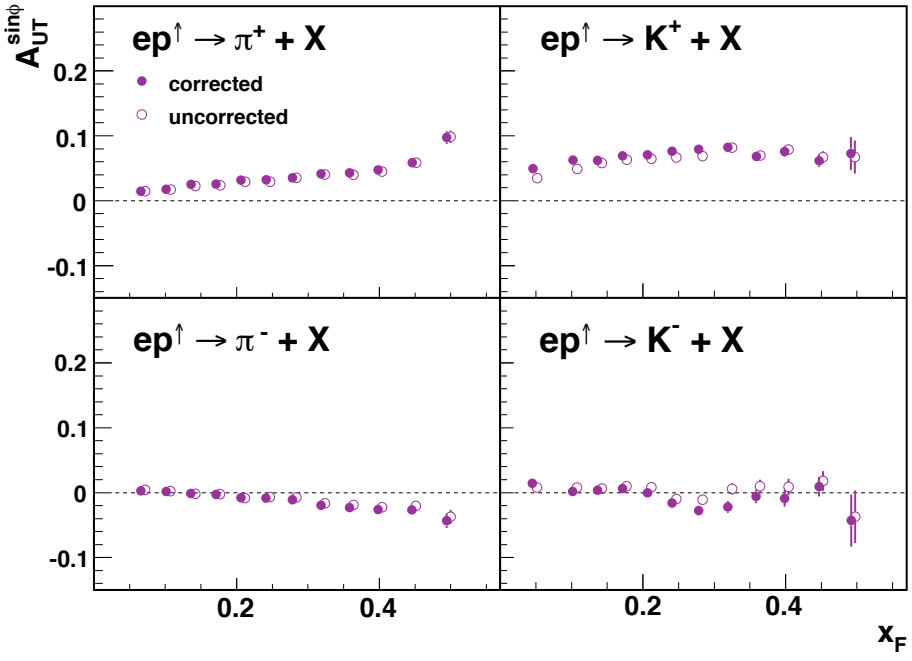

Figure E.30. The $A_{UT}^{\sin\phi}$ amplitudes as a function of x_F with and without the correction by the calorimeter efficiency. See Section 4.6.

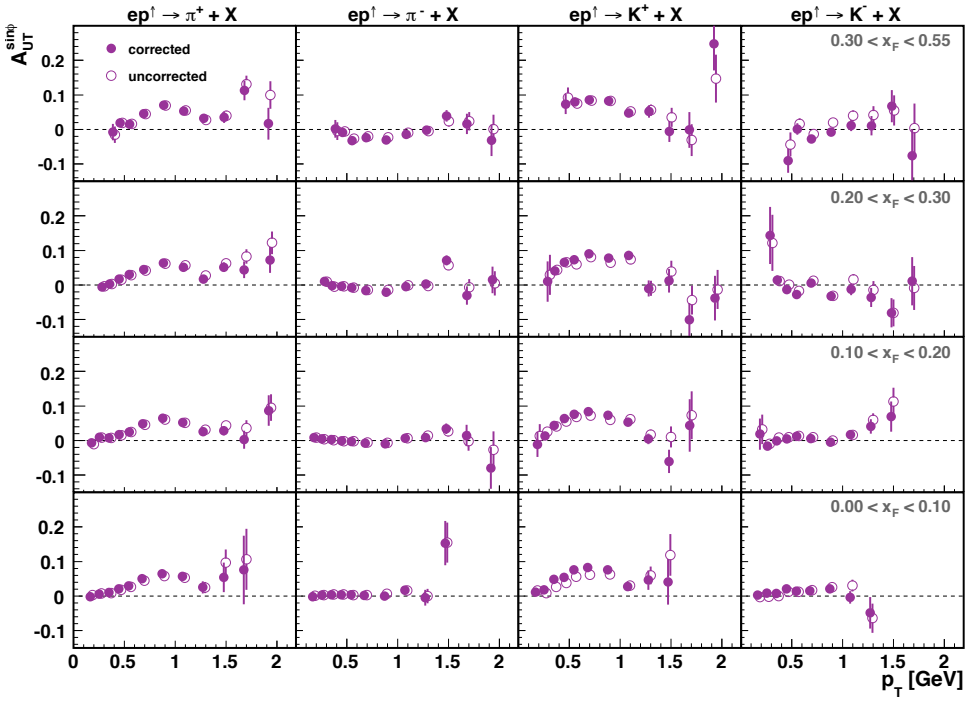

Figure E.31. The $A_{UT}^{\sin\phi}$ amplitudes as a function of p_T, in four slices of x_F, with and without the correction by the calorimeter efficiency. See Section 4.6.

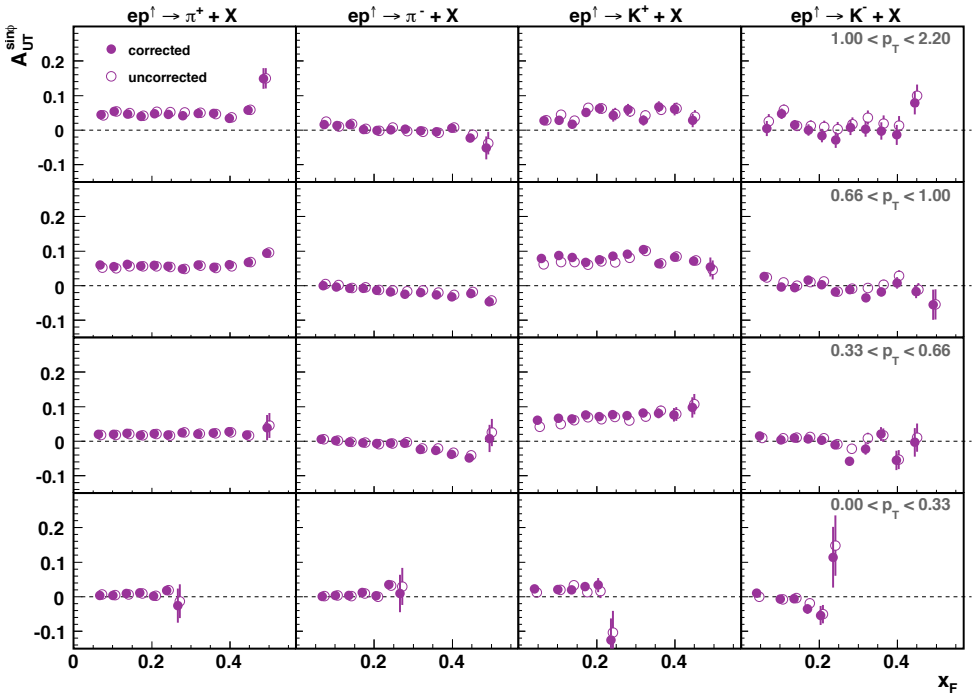

Figure E.32. The $A_{UT}^{\sin\phi}$ amplitudes as a function of x_F, in four slices of p_T, with and without the correction by the calorimeter efficiency. See Section 4.6.

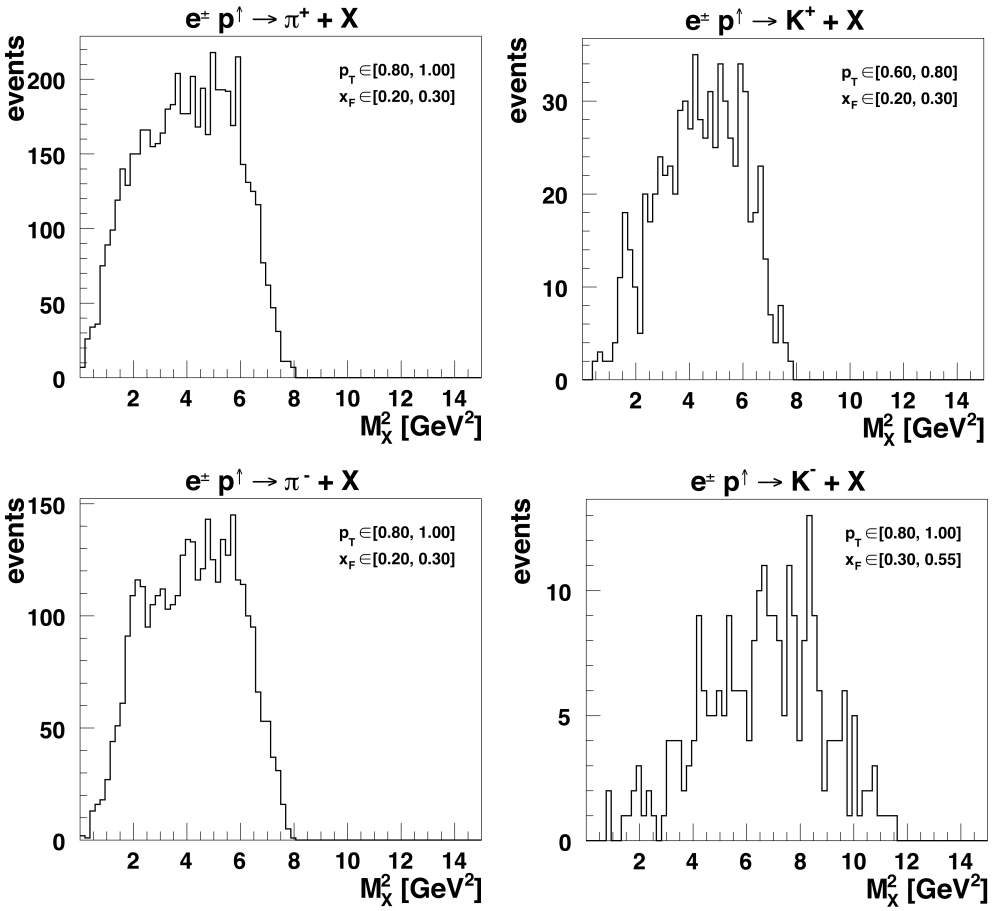

Figure E.33. Squared missing mass of events with $z > 0.7$ in different ranges of p_T and x_F, for the inclusive production of pions and kaons. See Section 6.2.3.

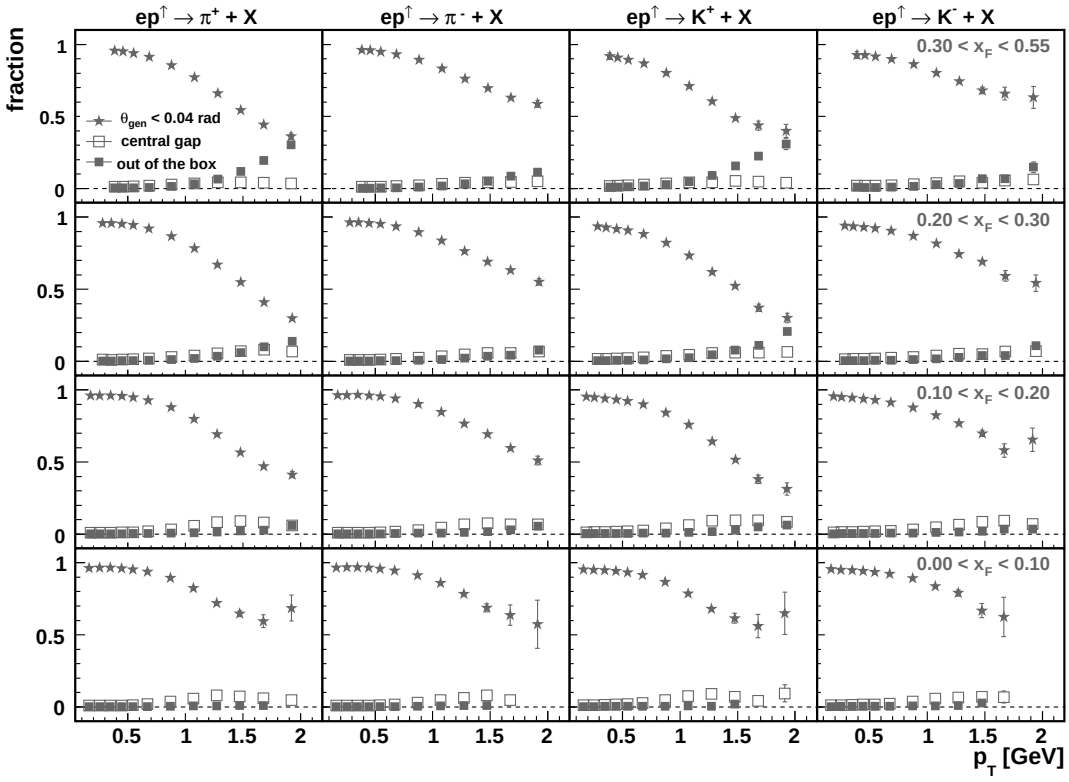

Figure E.34. Fraction of Monte Carlo generated hadron tracks in which the beam electron was scattered out of the acceptance of the HERMES spectrometer, with respect to the total number of inclusive hadron tracks. The star symbols denote events for which the electron is scattered on a cone with $\theta_e < 40$ mrad, i.e., very close to the beam pipe. The open squares indicate the fraction of hadrons for which the electron ended up in the central acceptance gap (40 mrad $< \theta_e <$ 140 mrad). The grey squares refer to the hadrons for which the corresponding beam electron was scattered at angles larger than the HERMES maximum acceptance.

Samenvatting

Na meer dan 60 jaar werken met "Diep Inelastische Verstrooiing" (Deep Inelastic Scattering, DIS) hebben fysici nu een indrukwekkend rijk beeld van de interne structuur van het proton, of meer in het algemeen, de nucleonen. Het idee achter DIS is eenvoudig: zeer hoog energetische leptonen (elektronen, positronen of muonen) worden in botsing gebracht met nucleonen. De impuls van het lepton moet hoog genoeg zijn opdat de golflengte van het foton dat de elektromagnetische wisselwerking overbrengt kleiner is dan de afmetingen van het nucleon. Op deze manier weten we dat het foton *diep* in het nucleon doordringt. Door het verstrooide lepton te meten, en zijn impuls en de strooihoek te bepalen, bekomt men informatie over de interne structuur van het nucleon.

Deze informatie is vervat in zogenaamde *parton distribution functions* (PDF) die de waarschijnlijkheid weergeven om een *parton* (letterlijk een deel van het nucleon) met welbepaalde eigenschappen in het nucleon aan te treffen. Op deze manier werden de bouwstenen van het nucleon, quarks en gluonen, ontdekt. Uit de vroegste metingen was al onmiddellijk duidelijk dat quarks spin 1/2 hebben. Een nucleon opgebouwd uit 3 quarks kan dan beschouwd worden als een systeem waarbij twee van de quarks hun spin parallel met de spin van het nucleon plaatsen, en de overblijvende quark met zijn spin anti-parallel. Maar in tegenstelling tot dit beeld vond een experiment van de EMC-samenwerking in de vroege jaren '80 dat de spin van de quarks slechts ongeveer 30% oplevert van de totale spin van het nucleon. Deze verrassende vaststelling werd de *spin crisis* genoemd, en leidde tot een hernieuwde belangstelling voor de substructuur van het nucleon en andere fenomenen gerelateerd aan de spin. Het HERMES experiment werd precies ontworpen en gebouwd met als primaire doel in meer detail de rol van de spin van de quarks te bepalen.

De precieze spin structuur van het nucleon is ook vandaag nog niet in detail gekend, alhoewel het beeld sedert het EMC-experiment veel duidelijker is. Zo weten we vandaag dat zowel de spin van de quarks, als die van de gluonen, en hun onderliggende dynamica allen een rol spelen in het opbouwen van de spin van het nucleon. Anderzijds zijn er nog polarisatie-fenomenen waargenomen die de rol van spin in deeltjesfysica sterk in de verf zetten. In het bijzonder denken we dan aan de grote asymmetrieën die waargenomen worden in experimenten met transversaal gepolariseerde nucleonen. Dergelijke transversale spin asymmetrie was een verrassing bij de ontdekking in de late '70er jaren, vooral omdat men dacht dat alle transversale spin effecten onderdrukt zouden zijn in een relativistisch proton. Maar we weten nu dat er binnen in een nucleon, zelfs een snel-bewegend proton, voldoende ruimte is voor transversale beweging van de quarks en gluonen. Hierdoor kunnen complexe correlaties ontstaan tussen de spin van het nucleon en de impuls van de quarks, waarbij er asymmetrische patronen kunnen voorkomen in de emissie van hadronen.

In DIS werden twee modellen uitgewerkt die leiden tot transversale asymmetrieën: respectievelijk het Sivers en het Collins-effect. Beide effecten werden waargenomen in semi-inclusieve DIS reacties, waarbij naast het verstrooide lepton ook een hadron gedetecteerd wordt. Om dit te vergelijken met de hadron-geïnduceerde reacties waarin enkel het geproduceerde hadron gemeten wordt, moet men inclusieve elektroproductie van hadronen aan een transversaal gepolariseerd proton meten met een ongepolariseerde lepton- bundel. Een dergelijke meting wordt voor het eerst gepresenteerd in deze thesis.

Transversale "single-spin" asymmetrieën (SSA) werden hier voor het eerste gevonden in gegevens voor inclusieve elektroproductie van geladen pionen en kaonen, afkomstig van $ep^{\uparrow}$ botsingen van een 27.6 GeV ongepolariseerde elektronbundel en een transversaal gepolariseerde protontarget. Positieve asymmetrieën tot een waarde van 6% werden gevonden voor positief geladen pionen, en tot 8% voor positieve kaonen. Deze SSA zijn ook duidelijk afhankelijk van de transversale impuls p_T van de hadronen. Ze nemen toe met stijgende p_T tot een maximum rond 0.7-0.9 GeV, en nemen dan af tot bijna nul voor $p_T \simeq 1.3$ GeV. Voorbij deze waarde van p_T nemen de π^+ asymmetrieën weer toe, terwijl ze voor K^+ consistent met nul blijven. In het geval van negatief geladen pionen en kaonen zijn de asymmetrieën zeer klein of consistent met nul binnen de fout, over het gehele bereik van de metingen.

De resultaten werden opgesplitst naar evenementen afkomstig van quasi-reële fotoproductie en DIS. Alhoewel de gemeten asymmetrieën bijna volledig afkomstig lijken te zijn van de dominante fotoproductie evenementen, werden effectief grotere asymmetrieën gevonden in het geval van DIS-kinematieken, waarbij de resultaten erop duiden dat ze afkomstig is van het Sivers-mechanisme.

In een laatste hoofdstuk wordt ook verslag gedaan van de eerste meting van een andere inclusieve single-spin asymmetrie, ditmaal inclusief over alle hadronen, d.w.z. enkel het verstrooide elektron werd gedetecteerd. Een dergelijke asymmetrie zou een directe aanwijzing zijn voor twee-foton uitwisseling in de DIS-botsingen. Er werd geen asymmetrie gevonden binnen de experimentele nauwkeurigheid. Als er een dergelijke asymmetrie bestaat, dan is ze kleiner dan 10^{-3}.

Bibliography

[1] A. López Ruiz, *Single-spin asymmetries in inclusive hadron production on transversely polarised protons*, 18th International Workshop on Deep Inelastic Scattering and Related Subjects (DIS2010), Florence, Italy (04/19/2010-04/23/2010), [link];
K. Rith, *Transverse single-spin asymmetries in inclusive hadron electroproduction at HERMES*, J. Phys.: Conf. Ser. **295** 012056, [link].

[2] A. Pich, *Quantum Chromodynamics*, Lectures at the 1994 European School of High-Energy Physics (Sorrento, 1994), hep-ph/9505231.

[3] I. Bird *et al.* [HERMES Collaboration], *A proposal to measure the spin-dependent structure functions of the neutron and proton at HERA*, DESY, PRC-90/01 (1990).

[4] M. Anselmino, *The transverse structure of protons and neutrons: TMDs*, Scholarpedia, **6(2)**:10209.

[5] Y. Koike, *Single transverse spin asymmetry in* $pp^{\uparrow} \to \pi X$ *and* $ep^{\uparrow} \to \pi X$, AIP Conf. Proc. **675** (2003) 449, hep-ph/0210396;
M. Anselmino *et al.*, AIP Conf. Proc. **1149** (2009) 465.

[6] M. Diehl, *Generalized parton distributions in impact parameter space*, Eur. Phys. J. C **25** (2002) 223 [Erratum-ibid. C **31** (2003) 277], hep-ph/0205208.

[7] S. Meissner, A. Metz, M. Schlegel and K. Goeke, *Generalized parton correlation functions for a spin-0 hadron*, JHEP **0808** (2008) 038, 0805.3165 [hep-ph];
C. Lorce, B. Pasquini and M. Vanderhaeghen, *Unified framework for generalized and transverse-momentum dependent parton distributions within a 3Q light-cone picture of the nucleon*, JHEP **1105** (2011) 041, 1102.4704 [hep-ph].

[8] D. L. Adams *et al.*, [E581/E704 Collaboration], *Comparison of spin asymmetries and cross-sections in* π^0 *production by 200-GeV polarized anti-protons and protons*, Phys. Lett. **B261** (1991) 201, [link].

[9] M. Anselmino, A. Efremov and E. Leader, *The theory and phenomenology of polarized deep inelastic scattering*, Phys. Rept. **261** (1995), hep-ph/9501369.

[10] A. M. Cooper-Sarkar, R. C. E. Devenish, *Deep Inelastic Scattering*, Oxford University Press (2011).
A. M. Cooper-Sarkar, R. C. E. Devenish and A. De Roeck, *Structure functions of the nucleon and their interpretation*, Int. J. Mod. Phys. A **13** (1998) 3385, hep-ph/9712301.

[11] J. D. Bjorken, *Current Algebra at Small Distances*, Proceedings of the International School of Physics Enrico Fermi Course XLI, J. Steinberger, ed., Academic Press, New

York, pp. 55-81, (1968).
J. D. Bjorken, *Asymptotic Sum Rules at Infinite Momentum*, Phys. Rev. 179, 1547-1553, (1969).

[12] J. Beringer *et al.* [Particle Data Group], *Review of Particle Physics*, Phys. Rev. D86, 010001 (2012), [link].

[13] A. Airapetian *et al.* [HERMES Collaboration], *Inclusive Measurements of Inelastic Electron and Positron Scattering from Unpolarized Hydrogen and Deuterium Targets*, JHEP **1105** (2011) 126, hep-ex/1103.5704.

[14] J. Ashman et al., [EMC Collaboration], Phys. Lett. **B206** (1988) 364.

[15] M. J. Alguard *et al.*, [E80 Collaboration], Phys. Rev. Lett. **41** (1978) 70; G. Baum *et al.* [E130 Collaboration], Phys. Rev. Lett. **51** (1983) 1135; V.W. Hughes *et al.*, Phys. Lett. **212** (1988) 511; J. Ashman *et al.* [EMC Collaboration], Phys. Lett. **B206** (1988) 364; J. Ashman *et al.* [EMC Collaboration], Nucl. Phys. **B328** (1989) 1; B. Adeva *et al.* [SMC Collaboration], Phys. Lett. **B302** (1993) 533; B. Adeva *et al.* [SMC Collaboration], Phys. Lett. **B320** (1994) 400; P.L. Anthony *et al.* [E142 Collaboration], Phys. Rev. Lett. **71** (1993) 759; P. L. Anthony *et al.* [E155 Collaboration], Phys. Lett. B **463** (1999) 339, hep-ex/9904002.

[16] A. Airapetian *et al.* [HERMES Collaboration], *Measurement of the proton spin structure function $g_1(p)$ with a pure hydrogen target*, Phys. Lett. B **442** (1998) 484, hep-ex/9807015;
A. Airapetian et al, [HERMES Collaboration], *Precise determination of the spin structure function g_1 of the proton, deuteron and neutron* Phys. Rev. **D75** (2007) 012007, hep-ex/0609039.

[17] K. Abe *et al.* [E154 Collaboration], *Next-to-leading order QCD analysis of polarized deep inelastic scattering data*, Phys. Lett. B **405** (1997) 180, hep-ph/9705344;
P.L. Anthony *et al.* [E155 Collaboration], *Measurement of the Proton and Deuteron Spin Structure Functions g_2 and Asymmetry A_2*, Phys. Lett. B **458**, 529, hep-ex/9901006.

[18] A. Airapetian, *et al.*, [HERMES Collaboration], *Measurement of the virtual-photon asymmetry A_2 and the spin-structure function g_2 of the proton*, hep-ex/1112.5584.

[19] R. Feynman, *Very High-Energy Collisions of Hadrons*, Phys. Rev. Lett. **23** (1969) 1415; J. D. Bjorken and E. A. Paschos, *Inelastic Electron-Proton and γ-Proton Scattering and the Structure of the Nucleon*, Phys. Rev. **185** (1969) 1975.

[20] M. Gell-Mann, *A Schematic Model Of Baryons And Mesons*, Phys. Lett. **8** (1964) 214; See also M. Gell-Mann, *The Eightfold Way: a Theory of Strong Interaction Symmetry*, Unpublished report for the California Institute of Technology (1961), CTSL-20.

[21] G. Zweig, *An $SU(3)$ model for strong interaction symmetry and its breaking*, Developments in the Quark Theory of Hadrons, pp.22-101, (1964), CERN-TH-401.

[22] C. G. Callan and D. J. Gross, *High-energy electroproduction and the constitution of the electric curent*, Phys. Rev. Lett. 33 (1969) 156.

[23] G. Zweig, *Origins of the Quark Model*, Invited talk at the *Baryon 1980* Conference, California Institute of Technology, (1980), CALT-68-805.

[24] E. Leader and M. Anselmino, *A crisis in the parton model: where, oh where is the proton's spin?*, Z. Phys. **C41** (1988) 239.

[25] J. Ashman *et al.* [European Muon Collaboration], *An Investigation of the Spin Structure of the Proton in Deep Inelastic Scattering of Polarized Muons on Polarized Protons*, Nucl. Phys. B **328** (1989) 1.

[26] M. Anselmino, Physics lecture at the International School of Physics "Enrico Fermi", 167th Course, 2007, Varenna, Italy.

[27] R. L. Jaffe, *Spin, twist and hadron structure in deep inelastic processes*, Proceedings of the conference "Erice 1995, The spin structure of the nucleon" 42-129 (1995) hep-ph/9602236.

[28] G. F. Sterman, *Partons, factorization and resummation, TASI 95*, Based on seven lectures at the Theoretical Advanced Study Institute, *QCD and Beyond*, Boulder, Colorado, (1995), hep-ph/9606312.

[29] Wu-Ki Tung, *Bjorken scaling*, Scholarpedia, **4(3)** (2009) 7412.

[30] V.N. Gribov and L.N. Lipatov, Sov.J.Nucl.Phys. **15** (1972) 438;
G. Altarelli and G. Parisi, Nucl. Phys. **B126** (1977) 298;
Yu. L. Dokshitzer, Sov.Phys. JETP **46** (1977) 641.

[31] G. Altarelli, *QCD evolution equations for parton densities*, Scholarpedia, **4(1)** (2009) 7124.

[32] A. D. Martin, R. G. Roberts, W. J. Stirling and R. S. Thorne, "NNLO global parton analysis," Phys. Lett. B **531** (2002) 216, hep-ph/0201127.

[33] C. J. Bomhof, *Azimuthal spin asymmetries in hadronic processes*, PhD thesis, Vrije Universiteit Amsterdam (2007), [link].

[34] V. Barone, A. Drago and P. G. Ratcliffe, *Transverse polarisation of quarks in hadrons*, Phys. Rept. **359** (2002) 1, hep-ph/0104283.

[35] A. Bacchetta, *Probing the transverse spin of quarks in deep inelastic scattering*, PhD thesis, Vrije Universiteit Amsterdam (2002), hep-ph/0212025.

[36] E. Leader, *Spin in particle physics*, Cambridge University Press, (2001).

[37] P. J. Mulders and R. D. Tangerman, , *The Complete tree level result up to order* $1/Q$ *for polarized deep inelastic leptoproduction*, Nucl. Phys. B **461** (1996) 197 [Erratum-ibid. B **484** (1997) 538], hep-ph/9510301.

[38] A. Bacchetta, U. D'Alesio, M. Diehl and C. A. Miller, *Single-spin asymmetries: The Trento conventions*, Phys. Rev. D **70** (2004) 117504, hep-ph/0410050.

[39] A. Airapetian *et al.* [HERMES Collaboration], *Quark helicity distributions in the nucleon for up, down, and strange quarks from semi-inclusive deep-inelastic scattering*, Phys. Rev. D **71** (2005) 012003, hep-ex/0407032.

[40] D. de Florian, R. Sassot, M. Stratmann and W. Vogelsang, *Global Analysis of Helicity Parton Densities and Their Uncertainties*, Phys. Rev. Lett. **101** (2008) 072001, 0804.0422 [hep-ph].

[41] A. Airapetian *et al.* [HERMES Collaboration], "Leading-Order Determination of the Gluon Polarization from high-p(T) Hadron Electroproduction," JHEP **1008** (2010) 130, hep-ex/1002.3921.
C. Adolph *et al.* [COMPASS Collaboration], *Leading order determination of the gluon polarisation from DIS events with high-p_T hadron pairs* (2012), hep-ex/1202.4064.

[42] V. Barone *et al.* [PAX Collaboration], *Antiproton-proton scattering experiments with polarization*, (2005), hep-ex/0505054;
M. Anselmino, V. Barone, A. Drago and N. N. Nikolaev, *Accessing transversity via J / psi production in polarized p vector anti-p vector interactions*, Phys. Lett. B **594** (2004) 97, hep-ph/0403114.

[43] M. Anselmino, M. Boglione, U. D'Alesio, A. Kotzinian, F. Murgia, A. Prokudin and C. Turk, *Transversity and Collins functions from SIDIS and e+ e- data*, Phys. Rev. D **75** (2007) 054032, hep-ph/0701006.

[44] A. Airapetian *et al.* [HERMES Collaboration], *Single-spin asymmetries in semi-inclusive deep-inelastic scattering on a transversely polarized hydrogen target,*, Phys. Rev. Lett. **94** (2005) 012002, hep-ex/0408013.

[45] V. Y. .Alexakhin *et al.* [COMPASS Collaboration], *First measurement of the transverse spin asymmetries of the deuteron in semi-inclusive deep inelastic scattering*, Phys. Rev. Lett. **94** (2005) 202002, hep-ex/0503002;
E. S. Ageev *et al.* [COMPASS Collaboration], *A New measurement of the Collins and Sivers asymmetries on a transversely polarised deuteron target*, Nucl. Phys. B **765** (2007) 31, hep-ex/0610068.

[46] K. Abe *et al.* [Belle Collaboration], *Measurement of azimuthal asymmetries in inclusive production of hadron pairs in e+ e- annihilation at Belle*, Phys. Rev. Lett. **96** (2006) 232002, hep-ex/0507063.

[47] L. Dick et al., *Spin Effects in the Inclusive Reactions π^+-Polarized $p \to \pi^+$ - Anything at 8 GeV/c* Phys. Lett. **B 57** (1975) 93.

[48] R.D. Klem et al., *Measurement of Asymmetries of Inclusive Pion Production in Proton Proton Interactions at 6 GeV/c and 11.8 GeV/c*, Phys. Rev. Lett. **36** (1976) 929.

[49] W. H. Dragoset et al., *Asymmetries in Inclusive Proton-Nucleon Scattering at 11.75 GeV/c*, Phys. Rev. **D 18** (1978) 3939.

[50] J. Antille et al., *Spin dependence of the inclusive reaction $p\,p^{\uparrow} \to \pi^0\,X$ at 24-GeV/c for high-p_T π^0 produced in the central region*, Phys. Lett. **B 94** (1980) 523.

[51] V.D. Apokin et al., *Observation of significant spin effects in hard collisions at 40-GeV/c*, Phys. Lett. **B 243** (1990) 461.

[52] D.L. Adams et al. [FNAL-E581 and E-741 Collaborations], *Comparison of spin asymmetries and cross sections in π^0 production by 200-GeV polarized anti-protons and protons*, Phys. Lett. **B 261** (1991) 201.

[53] D.L. Adams et al. [FNAL-E704 Collaboration], *Analyzing power in inclusive pi+ and pi- production at high x_F with a 200-GeV polarized proton beam*, Phys. Lett. **B 264** (1991) 462.

[54] D.L. Adams et al. [FNAL-E581 and E-704 Collaborations], *Large x(F) spin asymmetry in π^0 production by 200-GeV polarized protons*, Z. Phys. **C 56** (1992) 181.

[55] D.L. Adams et al. [FNAL-E581 and E-704 Collaborations], *High x(t) single spin asymmetry in π^0 and eta production at $x_F = 0$ by 200-GeV polarized anti-protons and protons*, Phys. Lett. **B 276** (1992) 531.

[56] A. Bravar et al. [FNAL-E704 Collaboration], *Analyzing power measurement in inclusive Λ^0 production with a 200-GeV/c polarized proton beam*, Phys. Rev. Lett. **75** (1995) 3073.

[57] D.L. Adams et al. [FNAL-E704 Collaboration], *Single spin asymmetries and invariant cross-sections of high transverse momentum inclusive π^0 production in 200 GeV/c $p\,p$ and $\bar{p}\,p$ interactions*, Phys. Rev. **D 53** (1996) 4747.

[58] A. Bravar et al. [FNAL-E704 Collaboration], *Single spin asymmetries in inclusive charged pion production by transversely polarized anti-protons*, Phys. Rev. Lett. **77** (1996) 2626.

[59] V. V. Abramov et al., *Production asymmetry measurement of high χ_T hadrons in $p^{\uparrow}\,p$ collisions at 40-GeV*, Nucl. Phys. **B 492** (1997) 3, hep-ex/0110011.

[60] D.L. Adams et al. [FNAL-E704 Collaboration], *Measurement of single spin asymmetry in eta meson production in $p^{\uparrow}\,p$ and $\bar{p}^{\uparrow}\,p$ interactions in the beam fragmentation region at 200 GeV/c*, Nucl. Phys. **B 510** (1998) 3.

[61] K. Krueger et al., *Large analyzing power in inclusive $\pi^{\pm}$ production at high x_F with a 22-GeV/c polarized proton beam*, Phys. Lett. **B 459** (1999) 412.

[62] C.E. Allgower et al., *Measurement of analyzing powers of π^+ and π^- produced on a hydrogen and a carbon target with a 22-GeV/c incident polarized proton beam*, Phys. Rev. **D 65** (2002) 092008.

[63] J. Adams et al. [STAR Collaboration], *Cross-sections and transverse single spin asymmetries in forward neutral pion production from proton collisions at s**(1/2) = 200 GeV*, Phys. Rev. Lett. **92** (2004) 171801, hep-ex/0310058.

[64] S.S. Adler et al. [PHENIX Collaboration], *Measurement of transverse single-spin asymmetries for mid-rapidity production of neutral pions and charged hadrons in polarized p p collisions at s**(1/2) = 200 GeV/c*, Phys. Rev. Lett. **95** (2005) 202001, hep-ex/0507073.

[65] A. Bazilevsky, *et al.*, *Single Transverse-Spin Asymmetry in Very Forward and Very Backward Neutral Particle Production for Polarized Proton Collisions at s**(1/2) = 200-GeV*, Phys. Lett. B **650** (2007) 325, hep-ex/0610030.

[66] M. Togawa [PHENIX Collaboration], *Measurement of the cross section and the single transverse spin asymmetry of forward neutrons from p p collisions at RHIC-PHENIX*, AIP Conf.Proc. **915** (2007) 689.

[67] I. Arsene *et al.* [BRAHMS Collaboration], Production of mesons and baryons at high rapidity and high p_T in proton-proton collisions at s**(1/2) = 200-GeV, Phys. Rev. Lett. **98** (2007) 252001, hep-ex/0701041.

[68] I. Arsene *et al.* [BRAHMS Collaboration], *Single Transverse Spin Asymmetries of Identified Charged Hadrons in Polarized p p Collisions at s**(1/2) = 62.4-GeV*, Phys. Rev. Lett. **101** (2008) 042001, 0801.1078 [nucl-ex].

[69] B. I. Abelev *et al.* [STAR Collaboration], *Forward Neutral Pion Transverse Single Spin Asymmetries in p p Collisions at s**(1/2) = 200-GeV*, Phys. Rev. Lett. **101** (2008) 222001, 0801.2990 [hep-ex].

[70] J. H. Lee *et al.* [BRAHMS Collaboration], *Cross-sections and Single Spin Asymmetries of Identified Hadrons in $p^{\uparrow}$ p at s**(1/2) = 200-GeV*, 0908.4551 [hep-ex].

[71] A. Adare *et al.* [PHENIX Collaboration], *Measurement of Transverse Single-Spin Asymmetries for J/ψ Production in Polarized p p Collisions at $\sqrt{s} = 200$ GeV*, Phys. Rev. D **82** (2010) 112008, 1009.4864 [hep-ex].

[72] G. L. Kane, J. Pumplin and W. Repko, *Transverse Quark Polarization in Large p(T) Reactions, e+ e- Jets, and Leptoproduction: A Test of QCD*, Phys. Rev. Lett. **41** (1978) 1689, [link].

[73] Z. -t. Liang and C. Boros, *Single spin asymmetries in inclusive high-energy hadron hadron collision processes*, Int. J. Mod. Phys. A **15** (2000) 927, hep-ph/0001330.

[74] D. W. Sivers, *Single-spin production asymmetries from the hard scattering of pointlike constituents*, Phys. Rev. D **41** (1990) 83, [link];
D. W. Sivers, *Hard-scattering scaling laws for single-spin production asymmetries*, Phys. Rev. D **43** (1991) 261, [link].

[75] J. C. Collins, *Fragmentation of transversely polarized quarks probed in transverse momentum distributions*, Nucl. Phys. B **396** (1993) 161, hep-ph/9208213;
J. C. Collins, S. F. Heppelmann and G. A. Ladinsky, *Measuring transversity densities in singly polarized hadron hadron and lepton - hadron collisions*, Nucl. Phys. B **420** (1994) 565, hep-ph/9305309.

[76] A.V. Efremov, L. Mankiewicz and N.A. Törnqvist, Phys. Lett. B **284** (1992) 394.

[77] J. -W. Qiu and G. F. Sterman, *Single transverse spin asymmetries in hadronic pion production*, Phys. Rev. D **59** (1999) 014004, hep-ph/9806356.

[78] Y. Koike, W. Vogelsang and F. Yuan, *On the Relation Between Mechanisms for Single-Transverse-Spin Asymmetries*, Phys. Lett. B **659** (2008) 878, 0711.0636 [hep-ph].

[79] H. Beppu, Y. Koike, K. Tanaka and S. Yoshida, *Contribution of Twist-3 Multi-Gluon Correlation Functions to Single Spin Asymmetry in Semi-Inclusive Deep Inelastic Scattering*, Phys. Rev. D **82** (2010) 054005, 1007.2034 [hep-ph];
H. Eguchi, Y. Koike and K. Tanaka, *Single Transverse Spin Asymmetry for Large-p(T) Pion Production in Semi-Inclusive Deep Inelastic Scattering*, Nucl. Phys. B **752** (2006) 1, hep-ph/0604003;
H. Eguchi, Y. Koike and K. Tanaka, *Twist-3 Formalism for Single Transverse Spin Asymmetry Reexamined: Semi-Inclusive Deep Inelastic Scattering*, Nucl. Phys. B **763** (2007) 198, hep-ph/0610314.

[80] P. B. van der Nat, *Transversity in two-hadron fragmentation*, PhD thesis, Vrije Universiteit Amsterdam (2007), [link].

[81] A. Bacchetta, M. Diehl, K. Goeke, A. Metz, P. J. Mulders and M. Schlegel, *Semi-inclusive deep inelastic scattering at small transverse momentum*, JHEP **0702** (2007) 093, hep-ph/0611265.

[82] S. Kretzer, E. Leader and E. Christova, *Fragmentation functions from semi-inclusive DIS pion production and implications for the polarized parton densities*, Eur. Phys. J. C **22** (2001) 269, hep-ph/0108055.

[83] A. Airapetian *et al.* [HERMES Collaboration], *Measurement of longitudinal spin transfer to Lambda hyperons in deep inelastic lepton scattering*, Phys. Rev. D **64** (2001) 112005, hep-ex/9911017;
A. Airapetian *et al.* [HERMES Collaboration], *Transverse Polarization of Lambda and anti-Lambda Hyperons in Quasireal Photoproduction*, Phys. Rev. D **76** (2007) 092008, hep-ex/0704.3133.

[84] O. Biebel, P. Nason and B. R. Webber, *Jet fragmentation in e+e- annihilation*, (2001), hep-ph/0109282;
K. Nakamura et al. [Particle Data Group], *Fragmentation functions in e^+e^-, ep and pp collisions*, JP **G 37** (2010) 075021, [link].

[85] M. Anselmino, *The transverse spin structure of the nucleon*, Proceedings of the International School of Physics "Enrico Fermi", 167th Course, 2007, Varenna, Italy.

[86] R. N. Cahn, *Azimuthal Dependence in Leptoproduction: A Simple Parton Model Calculation*, Phys. Lett. B **78** (1978) 269;
R. N. Cahn, *Critique Of Parton Model Calculations Of Azimuthal Dependence In Leptoproduction*, Phys. Rev. D **40** (1989) 3107.

[87] M. Anselmino, M. Boglione, U. D'Alesio, A. Kotzinian, F. Murgia and A. Prokudin, *The Role of Cahn and sivers effects in deep inelastic scattering*, Phys. Rev. D **71** (2005) 074006, hep-ph/0501196.

[88] K. Goeke, A. Metz and M. Schlegel, *Parameterization of the quark-quark correlator of a spin-1/2 hadron*, Phys. Lett. B **618** (2005) 90, hep-ph/0504130.

[89] M. Anselmino, M. Boglione, U. D'Alesio, S. Melis, F. Murgia and A. Prokudin, *Single spin asymmetries in l p —> h X processes: A Test of factorization*, Phys. Rev. D **81** (2010) 034007, 0911.1744 [hep-ph].

[90] D. Boer, M. Diehl, R. Milner, R. Venugopalan, W. Vogelsang, D. Kaplan, H. Montgomery and S. Vigdor *et al.*, *Gluons and the quark sea at high energies: Distributions, polarization, tomography*, nucl-th/1108.1713.

[91] A. Airapetian *et al.* [HERMES Collaboration], *Observation of the Naive-T-odd Sivers Effect in Deep-Inelastic Scattering*, Phys. Rev. Lett. **103** (2009) 152002, 0906.3918 [hep-ex].

[92] F. Bradamante [COMPASS Collaboration], *New COMPASS results on Collins and Sivers asymmetries*, 1111.0869 [hep-ex].

[93] D. Boer and P. J. Mulders, *Time reversal odd distribution functions in leptoproduction*, Phys. Rev. D **57** (1998) 5780, hep-ph/9711485.

[94] A. Airapetian *et al.* [HERMES Collaboration], *Azimuthal distributions of charged hadrons, pions, and kaons produced in deep-inelastic scattering off unpolarized protons and deuterons*, 1204.4161 [hep-ex].

[95] A. Airapetian *et al.* [HERMES Collaboration], *Effects of transversity in deep-inelastic scattering by polarized protons* Phys. Lett. B **693** (2010) 11, 1006.4221 [hep-ex].

[96] M. Anselmino, M. Boglione and F. Murgia, *Single spin asymmetry for p (polarized) $p \to \pi X$ in perturbative QCD*, Phys. Lett. B **362** (1995) 164, hep-ph/9503290;
M. Anselmino and F. Murgia, *Single spin asymmetries in transversely polarized proton anti-proton proton inclusive processes*, Phys. Lett. B **442** (1998) 470, hep-ph/9808426;
M. Anselmino, M. Boglione and F. Murgia, *Phenomenology of single spin asymmetries in p –polarized $p \to \pi X$*, Phys. Rev. D **60** (1999) 054027, hep-ph/9901442.

[97] U. D'Alesio and F. Murgia, *Parton intrinsic motion in inclusive particle production: Unpolarized cross sections, single spin asymmetries and the Sivers effect*, Phys. Rev. D **70** (2004) 074009, hep-ph/0408092;
U. D'Alesio and F. Murgia, *Azimuthal and Single Spin Asymmetries in Hard Scattering Processes*, Prog. Part. Nucl. Phys. **61** (2008) 394, 0712.4328 [hep-ph].

[98] L. Nogach [STAR Collaboration], *Measurements of Transverse Spin Effects with the Forward Pion Detector of STAR*, AIP Conf. Proc. **915** (2007) 543, hep-ex/0612030.

[99] M. Burkardt, *Impact parameter dependent parton distributions and transverse single spin asymmetries*, Phys. Rev. D **66** (2002) 114005, hep-ph/0209179.

[100] S. Meissner, A. Metz and K. Goeke, *Relations between generalized and transverse momentum dependent parton distributions*, Phys. Rev. D **76** (2007) 034002, hep-ph/0703176.

[101] U. Elschenbroich, *Transverse Spin Structure of the Proton Studied in Semi-inclusive DIS*, PhD thesis, Universiteit Gent (2006), [link].

[102] M. Anselmino, *et al.*, *Comparing extractions of Sivers functions*, hep-ph/0511017.

[103] X. Artru, *Proposals for measuring transversity distributions in deep inelastic electron scattering and a model for E-704 asymmetries*, hep-ph/9310323.

[104] L. Pappalardo, *Measurement of Collins and Sivers asymmetries at HERMES*, Proceedings of the Second Workshop on Transverse Polarization Phenomena in Hard Processes (Transversity 2008), Ferrara, Italy (2008).

[105] J. -W. Qiu and G. F. Sterman, *Single transverse spin asymmetries*, Phys. Rev. Lett. **67** (1991) 2264, [link];
J. -W. Qiu and G. F. Sterman, *Single transverse spin asymmetries in direct photon production*, Nucl. Phys. B **378** (1992) 52, [link].

[106] A. V. Efremov and O. V. Teryaev, Sov. J. Nucl. Phys. **36** (1982) 140 [Yad. Fiz. **36** (1982) 242];
A.V. Efremov and O.V. Teryaev, *QCD asymmetry and polarized hadron stucture function measurement*, Phys. Lett. **150B** (1985) 383, [link];
A.V. Efremov and O.V. Teryaev, Sov. J. Nucl. Phys. **36** (1982) 557 [Yad. Fiz. **36**(1982) 950];
A.V. Efremov and O.V. Teryaev, Sov. J. Nucl. Phys. **39** (1984) 962 [Yad. Fiz. **39** (1984) 1517].

[107] S. M. Troshin and N. E. Tyurin, *Spin content of constituent quarks and one spin asymmetries in inclusive processes*, Phys. Rev. D **52** (1995) 3862, hep-ph/9503275.

[108] M. Anselmino *et al.*, *Sivers Effect for Pion and Kaon Production in Semi-Inclusive Deep Inelastic Scattering*, Eur. Phys. J. **A39** (2009) 89, 0805.2677 [hep-ph].

[109] M. Anselmino *et al.*, *Update on transversity and Collins functions from SIDIS and e+ e- data*, Nucl. Phys. Proc. Suppl. **191** (2009) 98, 0812.4366 [hep-ph].

[110] M. Glück, E. Reya, and A. Vogt, *Dynamical Parton Distributions Revisited*, Eur. Phys. J. **C5** (1998) 461, hep-ph/9806404.

[111] D. de Florian, R. Sassot, and M. Stratmann, *Global analysis of fragmentation functions for pions and kaons and their uncertainties*, Phys. Rev. **D75** (2007) 114010, hep-ph/0703242.

[112] C.H. Llewellyn Smith and B.H. Wiik, *Physics with large electron-proton colliding beams*, DESY, 77/38 (1977), [link].

[113] I. Flegel and P. Söding, *Super microscope HERA: Gazing into the heart of matter*, DESY brochure (2002), [link].

[114] M. J. Alguard et al, *Deep inelastic scattering of polarized electrons by polarized protons*, Phys. Rev. Lett. **37**, 1261 (1976), [link].

[115] P. L. Anthony et al, [E142 Collaboration] *Determination of the neutron spin structure function,* Phys. Rev. Lett. **71**, 959 (1993); K. Abe et al., [E154 Collaboration] *Precision Determination of the Neutron Spin Structure Function* g_{1n}, Phys. Rev. Lett. **79**, 26 (1997), hep-ex/9705012.

[116] D. Adams et al, *Measurement of the spin dependent structure function* $g_1(x)$ *of the proton*, Phys. Lett. **B329**, 399 (1994), hep-ph/9404270.

[117] A. A. Sokolov and I. M. Ternov, *On Polarization and Spin Effects in Synchrotron Radiation Theory*, Sov. Phys. Doklady **8**, 1203 (1964);
A. A.Sokolov and I. M.Ternov, *Synchrotron Radiation* (Pergamon Press, New York, 1968; Akademie-Verlag, Berlin, 1968).

[118] A. Airapetian et al, [HERMES Collaboration], *The hermes polarized hydrogen and deuterium gas target in the hera electron storage ring*, Nucl. Instr. and Meth. A **540(1)**, 68 (2005), physics/0408137.

[119] A. Nass, *et al.*, *The HERMES polarized atomic beam source*, Nucl. Instrum. Meth. A **505** (2003) 633.

[120] HERMES target webpage, http://www-hermes.desy.de/groups/tgtgrp/www_target/

[121] K. Ackerstaff *et al.* [HERMES Collaboration], *The HERMES spectrometer*, Nucl. Instrum. Meth. A **417** (1998) 230, hep-ex/9806008.

[122] J. T. Brack, J. E. Belz, S. Clark, J. Ely, B. Fox, G. J. Hofman, E. R. Kinney and D. J. Mercer *et al.*, *The HERMES forward tracking chambers: Construction, operation, and aging effects*, Nucl. Instrum. Meth. A **469** (2001) 47.

[123] S. Bernreuther, A. B. Borissov, H. Bottcher, S. Brons, W. Bruckner, A. Buchsteiner, M. Ferstl and Y. Garber *et al.*, *The HERMES back drift chambers*, Nucl. Instrum. Meth. A **416** (1998) 45, hep-ex/9803005.

[124] A. Andreev, S. Belostotsky, G. Gavrilov, O. Grebenyuk, E. Ivanov, A. Kiselev, A. Krivshich and S. Kozlov *et al.*, *Multiwire proportional chambers in the HERMES experiment*, Nucl. Instrum. Meth. A **465** (2001) 482.

[125] H. E. Jackson [HERMES Collaboration], *The HERMES dual radiator RICH: Performance and impact*, Nucl. Instrum. Meth. A **553** (2005) 205.

[126] P. A. Cerenkov, *Visible radiation produced by electrons moving in a medium with velocities exceeding that of light*, Phys. Rev. **52**, 378 (1937), [link].

[127] R. De Leo et al, *Electronic detection of focused cherenkov rings from aerogel*, Nucl. Instr. and Meth. A **401(2-3)**, 187 (1997).

[128] J.P. Albanese et al., NIM 212 (1983) 111.

[129] V. L. Ginzburg and I. M. Franck, Soviet Phys. JETP **16**, 15 (1946).

[130] F. Harris et al, Nucl. Instr. and Meth. **107**, 413 (1973).

[131] D. M. Thiessen, *The Gas System for the HERMES Transition Radiation Detector*, Master's thesis, Simon Fraser University (1996), HERMES-96-028.

[132] K. Nakamura et al. [Particle Data Group], *Passage of particles through matter*, JP **G 37** (2010) 075021, [link].

[133] T. Benisch, S. Bernreuther, E. Devitsin, V. Kozlov, S. Potashov, K. Rith, A. Terkulov and C. Weiskopf, *The luminosity monitor of the HERMES experiment at DESY*, Nucl. Instrum. Meth. A **471** (2001) 314.

[134] Th. Bayes, *An essay towards solving a problem in the doctrine of chances* , Philosophical Transactions of the Royal Society of London, **53**, 370 (1763), [link].

[135] J. Wendland, *Improved particle identification at HERMES and polarised valence quark distributions in the proton*, Master's thesis, Simon Fraser University (1999), [link];
J. Wendland, *Polarized Parton Distributions Measured at the HERMES Experiment*, PhD thesis, Simon Fraser University (2003), [link].

[136] F. James, *MINUIT fitting package*, converted to C++ class, TMinuit for the ROOT software by R. Brun.

[137] F. T. Solmitz, *Analysis of Experiments in Particle Physics*, Annual Review of Nuclear Science (1964), [link].

[138] L. De Nardo, *Measurement of the Structure Function g1d at HERMES and Extraction of Polarized Parton Distributions*, PhD thesis, University of Alberta (2002), [link].

[139] *Can the Gluon Polarization in the Nucleon be extracted from HERMES Data on single high-pt Hadrons?*, PhD thesis, Universitäet Hamburg (2004), [link].

[140] T. Sjostrand, S. Mrenna and P. Z. Skands, *PYTHIA 6.4 Physics and Manual*, JHEP **0605** (2006) 026 hep-ph/0603175.

[141] I. Akushevich, H. Bottcher and D. Ryckbosch, *RADGEN 1.0: Monte Carlo generator for radiative events in DIS on polarized and unpolarized targets*, In *Hamburg 1998/1999, Monte Carlo generators for HERA physics* 554-565 hep-ph/9906408.

[142] B. Anderson *et al.*, *Parton Fragmentation and String Dynamics*, Phys. Rept. **97** 31, (1983).

[143] A. Hillenbrand, *Measurement and Simulation of the Fragmentation Process at HERMES*, PhD thesis, Friedrich-Alexander-Universität Erlangen-Nürnberg (2005) [link].

[144] GEANT manual - *Detector description and simulation tool*, (1993), GEANT web page.

[145] N. Makins, *GMC TRANS Manual*, HERMES Internal Report (2003), [link].

[146] A. Miller, *Extracting Fourier harmonics from sparse distributions*, HERMES Internal Report (2005), [link].

[147] L. L. Pappalardo, *Transverse spin effects in polarized semi-inclusive deep inelastic scattering*, PhD thesis, Universitá degli Studi di Ferrara (2008), [link].

[148] Rene Brun *et al.*, *ROOT Users Guide 5.26* (2009), [link].

[149] R. Lamb, *The Boer-Mulders and Cahn effects: Azimuthal modulations in the spin-independent SIDIS cross section at HERMES* , PhD thesis, University of Illinois at Urbana-Champaign (2010), [link].

[150] Wikipedia, *Student's t-test*, [link].

[151] A. Schäfer, *private communication*.

[152] D. Heesbeen, *Quasi-real photo-production of hyperons on polarized* $^{1,2}H$ *targets*, PhD thesis, Rijksuniversiteit Groningen (2003), [link].

[153] A. Airapetian *et al.* [HERMES Collaboration], *Exclusive rho-0 electroproduction on transversely polarized protons*, Phys. Lett. B **679** (2009) 100, 0906.5160 [hep-ex].

[154] A. Airapetian *et al.* [HERMES Collaboration], *Ratios of Helicity Amplitudes for Exclusive rho-0 Electroproduction*, Eur. Phys. J. C **71** (2011) 1609, 1012.3676 [hep-ex].

[155] A. Airapetian *et al.* [HERMES Collaboration], *Multiplicities of charged pions and kaons from semi-inclusive deep-inelastic scattering by the proton and the deuteron*.

[156] A. Airapetian *et al.* [HERMES Collaboration], *Single-spin azimuthal asymmetry in exclusive electroproduction of π^+ mesons on transversely polarized protons*, Phys. Lett. B **682** (2010) 345, 0907.2596 [hep-ex].

[157] M. Diehl, W. Kugler, A. Schafer and C. Weiss, *Exclusive channels in semi-inclusive production of pions and kaons*, Phys. Rev. D **72** (2005) 034034 [Erratum-ibid. D **72** (2005) 059902], hep-ph/0506171.

[158] A. Airapetian *et al.* [HERMES Collaboration], *Search for a Two-Photon Exchange Contribution to Inclusive Deep-Inelastic Scattering*, Phys. Lett. B **682** (2010) 351, 0907.5369 [hep-ex].

[159] S.D. Drell and S. Fubini, *Higher Electromagnetic Corrections to Electron-Proton Scattering*, Phys. Rev. **113** (1959) 741;
G.K. Greenhut, *Two-Photon Exchange in Electron-Proton Scattering*, Phys. Rev. **184** (1969) 1860.

[160] P. A. M. Guichon and M. Vanderhaeghen, *How to reconcile the Rosenbluth and the polarization transfer method in the measurement of the proton form-factors*, Phys. Rev. Lett. **91** (2003) 142303, hep-ph/0306007.

[161] C. E. Carlson and M. Vanderhaeghen, *Two-Photon Physics in Hadronic Processes*, Annual Review of Nuclear and Particle Science **57** (2007) 171, hep-ph/0701272.

[162] M. N. Rosenbluth, Phys. Rev. **79** (1950) 615.

[163] J. Arrington, *How well do we know the electromagnetic form factors of the proton?*, Phys. Rev. **C68** (2003) 034325, nucl-ex/0305009.

[164] A.I. Akhiezer, L.N. Rozentsveig and I.M. Shmushkevich, Sov. Phys. JETP **6** (1958) 588 ;
A.I. Akhiezer and M.P. Rekalo, Sov. Phys. Doklady **13** (1968) 572.

[165] R. C. Walker *et al.*, Phys. Rev. **D49** (1994) 5671;
M. K. Jones *et al.*, Phys. Rev. Lett. **84** (2000) 1398;
O. Gayou *et al.*, Phys. Rev. Lett. **88** (2002) 092301.

[166] A. V. Afanasev, S. J. Brodsky, C. E. Carlson, Y. -C. Chen and M. Vanderhaeghen, *The Two-photon exchange contribution to elastic electron-nucleon scattering at large momentum transfer*, Phys. Rev. D **72** (2005) 013008, hep-ph/0502013.

[167] L. Andivahis *et al.*, Phys. Rev. **D 50** (1994) 5491.

[168] A. V. Afanasev and C. E. Carlson, *Two-photon-exchange correction to parity-violating elastic electron-proton scattering*, Phys. Rev. Lett. **94** (2005) 212301, hep-ph/0502128.

[169] J. Arrington, P. G. Blunden and W. Melnitchouk, *Review of two-photon exchange in electron scattering*, Prog. Part. Nucl. Phys. **66** (2011) 782, 1105.0951 [nucl-th].

[170] A. Browman, F. Liu and C. Schaerf, *Positron-Proton Scattering*, Phys. Rev. **139** (1965) B1079.

[171] R. L. Anderson *et al.*, *Scattering of Positrons and Electrons from Protons*, Phys. Rev. Lett. **17** (1966) 407.

[172] W. Bartel *et al.*, *Scattering of positrons and electrons from protons*, Phys. Lett. **B 25** (1967) 242.

[173] B. Bouquet *et al.*, *Backward scattering of positrons and electrons on protons*, Phys. Lett. *B 26* (1968) 178.

[174] J. Mar *et al.*, *Comparison of Electron-Proton and Positron-Proton Elastic Scattering at Four-Momentum Transfers up to 5.0 (GeV/c)*^{2}, Phys. Rev. Lett. **21** (1968) 482.

[175] J. Arrington, *Evidence for two photon exchange contributions in electron proton and positron proton elastic scattering*, Phys. Rev. C **69** (2004) 032201, nucl-ex/0311019.

[176] J. Arrington, *et al.*, *Two-photon exchange and elastic scattering of electrons/positrons on the proton. (Proposal for an experiment at VEPP-3)*, (2004), nucl-ex/0408020;
D. M. Nikolenko *et al.*, *Experiments with internal targets at the VEPP-3 electron storage ring*, Phys. Atom. Nucl. **73** (2010) 1322.

[177] W. Brooks, J. Arrington, K. Joo, B. Raue, A. Afanasev, and L. Weinstein, *Beyond the Born approximation: A precise comparison of positron-proton and electron-proton elastic scattering in CLAS*, Approved by PAC31 (2006), [link].

[178] M. Kohl, *The OLYMPUS experiment at DESY*, AIP Conf. Proc. **1160** (2009) 19.

[179] H. Jostlein *et al.*, Phys. Lett. **B52** (1974) 485;
S. Hartwig *et al.*, Lett. Nuovo Cim. **15** (1976) 429;
D. L. Fancher *et al.*, Phys. Rev. Lett. **37** (1976) 1323;
L. S. Rochester *et al.*, Phys. Rev. Lett. **36** (1976) 1284;
S. Hartwig *et al.*, Phys. Lett. **B82** (1979) 297;
J. J. Aubert *et al.* [EMC Collaboration], Nucl. Phys. **B272** (1986) 158;
A. Argento *et al.* [BCDMS Collaboration], Phys. Lett. **B140** (1984) 142.

[180] A.O. Barut and C. Fronsdal, Phys. Rev. **120** (1960) 1871;
A. De Rujula, J. M. Kaplan and E. De Rafael, Nucl. Phys. **B 35** (1971) 365;
A. De Rujula, J.M. Kaplan, and E. de Rafael, Nucl. Phys. **B 53** (1973) 545.

[181] N. Christ and T. D. Lee, Phys. Rev. **143** (1966) 1310.

[182] S. P. Wells *et al.* [SAMPLE Collaboration], Phys. Rev. **C63** (2001) 064001.

[183] F. E. Maas *et al.* [A4 Collaboration], Phys. Rev. Lett. **94** (2005) 082001.

[184] D. S. Armstrong *et al.* [G0 Collaboration], Phys. Rev. Lett. **99** (2007) 092301.

[185] J. A. Appel *et al.*, Phys. Rev. **D1** (1970) 1285;
J. R. Chen *et al.*, Phys. Rev. Lett. **21** (1968) 1279.

[186] S. Rock *et al.*, Phys. Rev. Lett. **24** (1970) 748.

[187] A. Metz, M. Schlegel, K. Goeke, *Transverse single spin asymmetries in inclusive deep-inelastic scattering*, Phys. Lett. **B643** (2006) 319, hep-ph/0610112.

[188] A. Afanasev, M. Strikman and C. Weiss, *Transverse target spin asymmetry in inclusive DIS with two-photon exchange*, Phys. Rev. D **77** (2008) 014028, 0709.0901 [hep-ph].

[189] X. Jiang *et al.*, Jefferson Lab Hall A Experiment E-07- 013 (2007).

[190] J. Katich, *Measurement of the Target-Normal Single-Spin Asymmetry Any in the Deep Inelastic Region from the Reaction* $^3He^{\uparrow}(e, e')$, PhD thesis, The College of William and Mary (2011).

[191] G. Ingelman, A. Edin, and J. Rathsman, Comp. Phys. Commun. **101** (1997) 108.

[192] L. W. Mo and Y. S. Tsai, Rev. Mod. Phys. **41** (1969) 205.

[193] J. C. Collins, *Leading twist single transverse-spin asymmetries: Drell-Yan and deep inelastic scattering*, Phys. Lett. B **536** (2002) 43, hep-ph/0204004.

[194] D. Boer, P. J. Mulders and F. Pijlman, *Universality of T odd effects in single spin and azimuthal asymmetries*, Nucl. Phys. B **667** (2003) 201 hep-ph/0303034.

[195] R. Frederix, *Wilson lines in QCD*, Master's thesis, Universiteit Utrecht (2005) [link].

[196] A. V. Belitsky, X. Ji and F. Yuan, *Final state interactions and gauge invariant parton distributions*, Nucl. Phys. B **656** (2003) 165, hep-ph/0208038.

[197] M. Anselmino, M. Boglione, and F. Murgia, *Single spin asymmetry for* $p^{\uparrow}p \to \pi X$ *in perturbative QCD*, Phys. Lett. **B** 362 (1995) 164, hep-ph/9503290.

[198] M. Anselmino and F. Murgia, *Single spin asymmetries in transversely polarized proton(antiproton) - proton inclusive processes*, Phys. Lett. **B** 442 (1998) 470, hep-ph/9808426.

[199] K. G. Wilson, *The renormalization group and critical phenomena*, Nobel Lectures, Physics 1981-1990, World Scientific Publishing Co., Singapore (1993) [link].

[200] C. J. Bomhof and P. J. Mulders, *Non-universality of transverse momentum dependent parton distribution functions*, Nucl. Phys. B **795** (2008) 409 0709.1390 [hep-ph].